University of Cagliari University of Sassari

XXXIII Cycle

PhD Degree in

Chemical Science and Technology

PhD Thesis Title

Computer simulation studies of micro-heterogeneous liquid mixtures

Scientific Disciplinary Sector
CHIM/02

Grant funded by UNICA

PhD Student Dr. Leon de Villiers Engelbrecht

Supervisor Prof. Flaminia Cesare Marincola
Co-supervisor Prof. Francesca Mocci

PhD Coordinators Prof. Stefano Enzo
Prof. Carla Cannas

Final exam Academic Year 2019– 2020
Thesis defense: May 2021 Session

Acknowledgements

Firstly, I would like to thank Prof Francesca Mocci for the opportunity to pursue my PhD under her expert supervision; it would not have been possible without her guidance, enthusiasm and kind encouragement throughout my PhD studies.

I thank Prof Flaminia Cesare Marincola for her kind supervision, discussion and support.

I am grateful to Prof Aatto Laaksonen for his precious insight and discussion, for making available abundant computational resources, and for hosting me at Stockholm University.

I would also like to express my gratitude towards the following people:

- Prof Xiaoyan Ji, who kindly hosted me in her friendly research group at Luleå Technical University for two months;
- The HPC-Europa3 transnational access programme made possible a two-month long research visit to the Center for High Performance Computing (PDC), at KTH, Stockholm (application code HPC170K5MD) where I was granted access to substantial computational resources which has enabled an important component of this work; In particular, I'd like to thank Dr Lilit Axner of the PDC for her kind support;
- This work was performed, in part, using computational resources provided by the Swedish National Infrastructure for Computing (SNIC), project ID SNIC 2019/1-32.

This work was performed in collaboration with the follow persons, whom I wish to thank here: Dott. Riccardo Farris, Dr Alessandro Mariani, Dr Lorenzo Gontrani, Dr Tudor Vasiliu and Dr Sergiy Perepelytsya for their friendly collaboration on computational projects, and Prof Silvia Porcedda, Dr Alessandra Piras and Dott. Monica Demurtas for their experimental input and stimulating discussion.

I thank Prof Giuseppe Saba and Mr Andrea Ardu for their kindness and invaluable technical support. The kind support of my PhD course coordinators, Professors Carla Cannas and Stefano Enzo, is gratefully acknowledged.

I would like to express my deep gratitude towards the late Prof Klaus R Koch for his years of guidance and support.

My family for their support throughout my studies.

Eleonora, for her love and encouragement.

Contents

Abstract

Liquid mixtures are part of our everyday lives and are important in numerous chemical research and industrial applications. While often apparently featureless, uniform and uninteresting, kept in bottles and containers in the chemical laboratory, their molecular-level structure and physical properties can be completely the opposite, and are continually attracting scientific interest. Strong repulsive and attractive interactions between the molecules can create most intriguing local arrangements, molecular aggregates and complexes, whose spatial organisation is often difficult to characterise, or rationalise. Moreover, the same liquid components can behave completely differently depending on the mixing ratio, strongly affecting macroscopic properties, e.g. mass density, viscosity or melting/boiling points. To gain insight into the complex world of binary liquid mixtures, deep eutectic solvents and ionic liquids, a combination of experimental and theoretical, or computational, studies is necessary. In this thesis, the focus is on understanding how the microscopical molecular organization in organic solvent mixtures affects the physico-chemical and solvating properties. While in all of the presented studies the systems are investigated both experimentally and computationally, the main focus of my thesis is on computational modelling, primarily based on molecular mechanics. In this approach, the system of interest is modelled by interacting particles representing either single atoms of groups of atoms, and their interactions and movements are described by classical mechanics. This approximate method allows for the modelling of large molecular systems, e.g. liquid mixtures with structural heterogeneities on the nanometer length scale and microsecond time scale.

Specifically, my work has been devoted to the following problems: (1) Explaining how large anions in mixed liquid solvents can be apparently preferentially solvated by the less polar components, described in **Chapter 3**. (2) Explaining excess thermodynamics properties for relatively simple organic solvent liquid mixtures, described in **Chapter 4**, and extending the investigation approach to more complex "pseudo-binary" mixtures of DES with water or methanol, where it has not been applied before, described in **Chapter 6.** (3) Developing coarse grained model of charged liquid solvent, to be able to verify the long-range ordering effects connected to solvent micro-segregation, described in **Chapter 5**. The fundamental concepts and background are provided in **Chapter 1** & **2**.

1 Introduction

1.1 Overview

Liquid-liquid mixtures (or simply "liquid mixtures") are widely encountered in chemical research and industry, where they are routinely used as versatile solvents in chemical synthesis and chromatographic separation of mixtures of compounds. And they are part of our daily life as well, in the currently highly-used disinfectants, in household cleaning products, in alcoholic drinks, anti-freeze products, etc. When mixing two or more liquid substances, it is generally expected that if they are fully mutually soluble, or miscible, the final mixtures will possess intermediate behaviour between those of the separate components. Ideally, we can tailor the mixture's properties, such as density, polarity, viscosity, phase transition points, etc. by proper choice of the mixture components. However, in our non-ideal world, this is often not case: when mixing two liquids it might happen that the resulting mixture density is higher than that of the pure components, or that the liquid-solid transition point is lower than that of either neat liquids, or that the vapour pressure reaches a minimum value at a certain mixture composition. Knowing and predicting this non-ideal behaviour is of great importance for the many applications of liquid mixtures.

As for all chemical systems, the macroscopic properties depend on the nature of intra- and intermolecular interactions, and on the spatial organization of the molecules. In fact, many of the particular properties and applications of liquid mixtures are understood as due to specific molecular coordination or aggregation states or self-association of components, e.g. eluents and selective solvents, cryo-solvents and cryo-protectants. The study of the structure of liquids is more complex than that of solids, due to the highly dynamic nature of the spatial organization, and on the strong dependence on the thermodynamic conditions.

In combination with a variety of experimental techniques, computational molecular modelling, and in particular Molecular Dynamics (MD) simulations, are widely applied to study liquid structure, and are often a fundamental tool to explain the molecular-level origin of non-ideal mixing behaviour. Despite decades of simulations of liquids, analysing the spatial organization from MD simulation trajectories is still far from a trivial task. Indeed, a variety of tools for understanding the molecular aggregation behaviour are still being developed, also stimulated by the necessity of rationalizing the structures of emerging classes of solvents like ionic liquids (ILs) or deep eutectic solvents (DES), and there is still large room for the development of computational structure analysis tools.

Another challenge to be typically addressed when studying liquid mixtures is that of developing an appropriate computational molecular model. The spatial and dynamical properties of liquid mixtures and solutions are orchestrated by the complex interplay of the intermolecular forces, comprising van der Waals interactions, hydrogen bonds and electrostatic interaction. Thus, the proper modelling of such interactions is fundamental to obtain realistic simulations, and often some model parameters, especially the atomic charges, may need to be adjusted in order to reproduce the system properties of interest.

It is also important to mention that, depending on the property of interest, different molecular model "granularities", or resolutions, have to be considered. In particular, when long-range ordering is to be studied, systems dimensions of tens of Ångström may have to be modelled, and the molecules have to be simulated with a resolution larger than the atomic scale. This approach is required because the computational time increases rapidly with the number N of particles, approaching N*log$N$ when treating electrostatic interaction using the Particle Mesh Ewald method. By grouping several atoms in a single particle leads to a dramatic reduction in computation times. The development of such "coarse-grained" (CG) models is far from trivial, and different methods have been developed for their construction.

Coming from a previous experience of experimental studies of the solvating properties of mixtures, during which I came to realise the power of computational molecular modelling for rationalizing the liquid solvent mixtures properties, and especially their unusual behaviour, I devoted this PhD thesis work to the use of MD simulations to explain highly unusual properties experimentally detected in solvent mixtures. In this quest, I also worked on the development of a coarse-grained model for organic molecules, capable of reproducing the experimental properties of their mixtures. The work performed in this PhD thesis shows that behind the unusual properties of these systems is generally the microheterogeneity or some peculiar aggregation arrangement, typically through H-bonds.

Specifically, my work has been devoted to the following problems:

- explaining excess thermodynamics properties for relatively simple organic solvent liquid mixtures and extending the investigation approach to more complex "pseudo-binary" mixtures of DES with water or methanol, where it has not been applied before.
- explaining how large anions in mixed liquid solvents can be apparently preferentially solvated by the less polar solvent
- developing coarse grained model of charged liquid solvent, to be able to verify the long-range ordering effects connected to solvent micro-segregation.

In my studies I continuously reference to the relevant experimental techniques that were used to characterise the unusual properties of the studied liquid mixtures. Therefore, in the introductory chapter, I briefly introduce the experimental techniques that are often used to obtain information on liquid structure, and that were used as reference for the computational studies presented here: spectroscopy techniques – NMR in particular – and X-ray scattering experiments. A number of other experimental techniques, or variations of the essential techniques briefly introduced above, may be used to obtain structural information about liquids and their mixtures. Notable mentions include acoustic (speed of sound) measurements, mass spectrometry, and light scattering.

1.2 Properties of liquid mixtures

The solvent characteristics of liquid mixtures, and of binary mixtures (*i.e.* consisting of only two pure liquid components) in particular, are routinely and conveniently modified, or "tuned", by simply changing the ratio of the mixture components, referred to as the mixture composition. (Marcus, 2002) Naturally, the liquid mixture composition may be expressed in different ways, e.g. as a volume, weight or number ratio (mole fraction); the latter is often used in fundamental studies of liquid mixtures as it relates the molecular composition of the system. The mole fraction of a component A in a binary mixture of liquids A and B, for example, is given by $x_A = N_A/(N_A + N_B)$, where N_A and N_B are the total number of A and B molecules (normally expressed in moles) in the mixture. The composition of liquid mixtures also affects their observable bulk physical properties, e.g. polarity, density, viscosity or melting point. In fact, while variations of many such properties as a function of mixture composition (often expressed as a mole fraction, x_A) often appear smooth and regular (provided the mixture remains macroscopically fully miscible, *i.e.* no bulk liquid–liquid phase separation occurs), some binary liquid mixtures do exhibit intriguing deviations from the expected, ideal mixing behaviour.

Liquid mixtures involving water, *aqueous mixtures*, are ubiquitous in nature, as well as in industrial and research activities. One of the simplest aqueous mixture involving an organic solvent is that of methanol. This binary mixture (often referred to as "water–methanol" or "water + methanol"), for example, is of considerable importance both as solvent in applied research and as traditional model system for understanding hydrophobic solvation in aqueous environments from a theoretical point of view. (Gibson, 1935; Frank and Evans, 1945; Dixit *et al.*, 2002) These mixtures can therefore be used to introduce some relevant properties of the organic-aqueous mixtures in general. Water-methanol mixtures are macroscopically fully miscible at all mixture compositions at room temperature, with their mass densities (ρ) showing a smooth decrease with increasing methanol content, as shown in **Figure 1.1**. Upon closer inspection, the densities of these mixtures may be seen to be somewhat higher than expected (dotted black line) and may be seen to follow a specific curved trend between those of the pure components when plotted as a function of the *mass fraction* methanol.

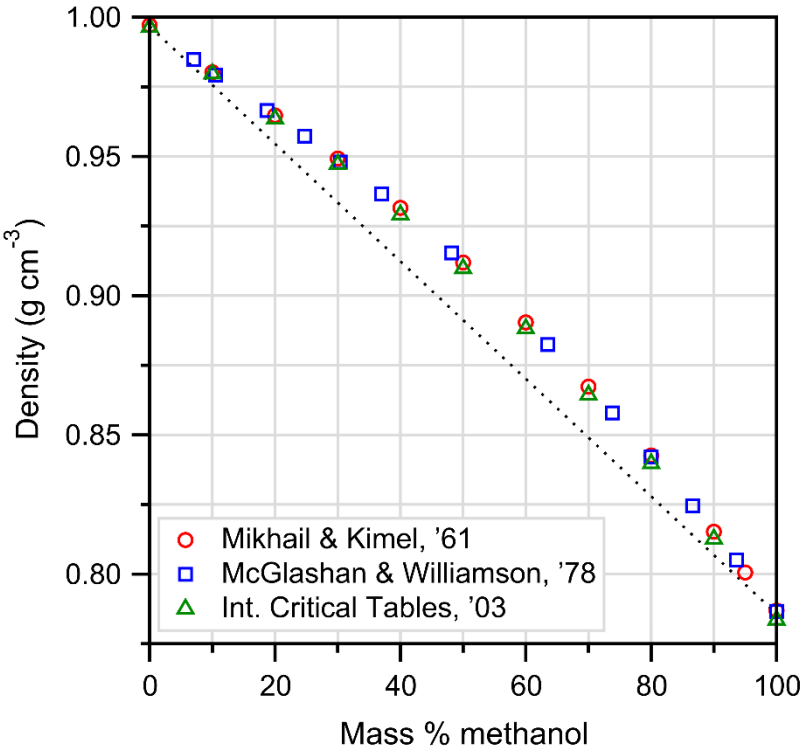

Figure 1.1 Literature mass density data for water-methanol liquid mixtures at 298.15 K (0.1 MPa), plotted as a function of the mass percentage methanol in the mixture. Data reproduced from Mikhail & Kimel, (Mikhail and Kimel, 1961) McGlashan & Williamson, (McGlashan and Williamson, 1976) and the *International Critical Tables of Numerical Data, Physics, Chemistry and Technology*. (Washburn, 2003; Wensink *et al.*, 2003)

In practice, such deviations from the expected, or "ideal", behaviour are best demonstrated, or characterised, by calculating *excess thermodynamic properties*, in this case the excess density or, more commonly, the excess molar volume, V^{E} (also commonly abbreviated V_m^{E}).The excess thermodynamic properties, Y^{E}, for binary liquid mixtures are essentially calculated according to the following equation:

$$Y^{E} = Y_{\text{mix.}} - (x_A Y_A + x_B Y_B) \qquad (1.1)$$

where Y is the property (e.g. volume V, or enthalpy H), Y_{mix} the value (measured) for the particular liquid mixture, Y_A and Y_B the property values for the pure liquids A and B (under the same conditions), and x_A and $x_B = (1 - x_A)$ their respective mole fractions. The term in brackets represents the property value for the hypothetical ideal mixture and may include and additional correction term (PV^{E}, which

is typically negligible for liquids and consequently omitted). In the case of V^E for an A-B binary mixture, the equation thus becomes:

$$V^{\mathrm{E}} = V_{\mathrm{m,mix.}} - \left(x_{\mathrm{A}} V_{\mathrm{m,A}} + x_{\mathrm{B}} V_{\mathrm{m,B}}\right) \tag{1.2}$$

with $V_{m,i}$ the molar volume of component i (i.e. A or B). In practice, V^E may be calculated as follows:

$$V^{\mathrm{E}} = \frac{\left(x_{\mathrm{A}} M_{\mathrm{A}} + x_{\mathrm{B}} M_{\mathrm{B}}\right)}{\rho_{\mathrm{mix.}}} - \frac{x_{\mathrm{A}} M_{\mathrm{A}}}{\rho_{\mathrm{A}}} - \frac{x_{\mathrm{B}} M_{\mathrm{B}}}{\rho_{\mathrm{B}}} \tag{1.3}$$

Here, $\rho_{mix.}$ is the measured density of the mixture, ρ_A and ρ_B the densities of pure liquids A and B under the same conditions, and M_A and M_B the molar masses of components A and B. The V^E of the water–methanol mixtures are plotted in Figure 1.2 and are negative for all mixtures, from which it follows that these mixtures have smaller volumes than expected based on those of the corresponding pure water and methanol fractions, i.e. volume "contraction" occurs upon mixing. (Stouten and Kroon, 1990)

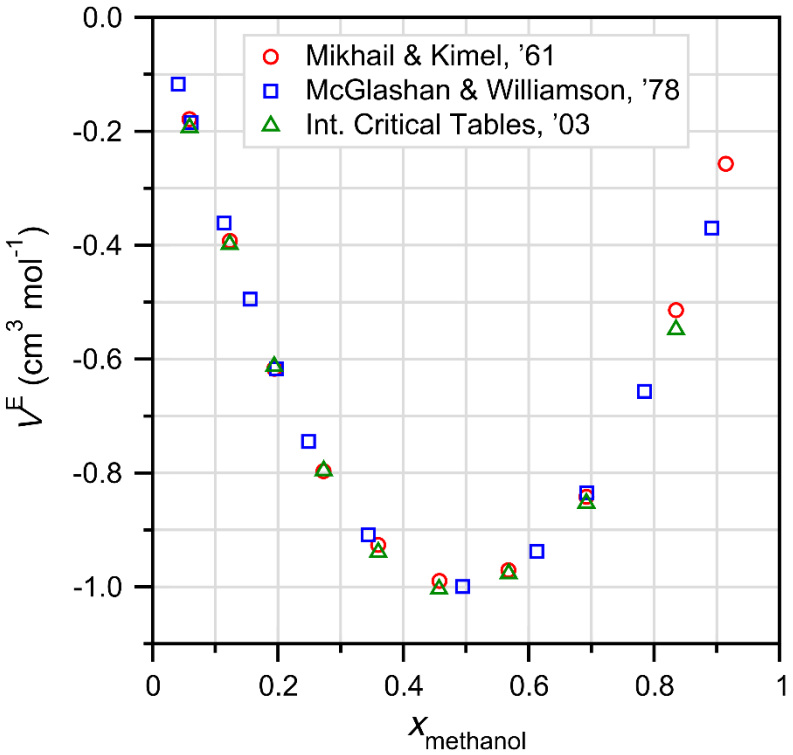

Figure 1.2 Excess molar volumes, V^E, of water-methanol at 298.15 K (0.1 MPa), calculated from literature density data in **Figure 1.1**. (Mikhail and Kimel, 1961; McGlashan and Williamson, 1976; Washburn, 2003; Wensink *et al.*, 2003)

Water-methanol mixtures exhibit many other interesting non-ideal mixing properties, e.g. large positive excess viscosities with a curious viscosity maximum at $x_{\text{methanol}} \approx 0.3$. (Wensink *et al.*, 2003) Understanding the molecular-level origin of these interesting observations has been the subject of sustained research activity, as is the case for numerous other aqueous binary mixtures.

For example, numerous experimental studies spanning nearly a century, e.g. (Gibson, 1935; Dixit *et al.*, 2002), have concluded that the water-methanol mixtures introduced above are not uniformly mixed at the molecular level as one might expect based on their featureless and macroscopically fully miscible nature, but instead have a complex molecular-level structure characterised by water self-association *via* strong hydrogen bonding ("H-bonding") interactions. Some experimental techniques frequently employed in studies of liquid molecular-level structures, and those of liquid mixtures in particular, are briefly introduced below.

1.3 Experimental studies of the structure of liquid mixtures

1.3.1 Spectroscopic techniques

Spectroscopic techniques, which monitor the interaction of electromagnetic radiation with matter, can provide information the local environment of molecules and inter- or intramolecular interactions, and as such can be used to study the molecular-level structures of liquid mixtures. In particular, vibrational (infra-red, IR, or Raman) (Bertie and Lan, 1997; Murdoch *et al.*, 2002; Burikov *et al.*, 2010) and nuclear magnetic resonance (NMR) spectroscopies (Yoshida, Kitajo and Yamaguchi, 2006; Corsaro *et al.*, 2008, 2018) have proven to be very powerful, non-invasive techniques to either study solvent molecules directly, or to probe the solution environment of a solute (i.e. an ion or molecule dissolved in the liquid mixture of interest). Examples of the latter include IR pump-probe spectroscopic techniques, (Sando, Dahl and Owrutsky, 2007) NMR chemical shift (δ) measurements, (Stengle *et al.*, 1984; Morgado *et al.*, 2013; Morgado, Martins and Filipe, 2019) and advanced NMR experiments, e.g. nuclear spin relaxation times and diffusion measurements. (Odelius, Holz and Laaksonen, 1997; Bagno, 2002; Mocci and Laaksonen, 2015)

As NMR chemical shift measurements for solutes in liquid mixtures are discussed later in this thesis, a brief example of this approach and its rationale is presented below. As described in standard introductory NMR spectroscopy texts, (Farrar and Becker, 1971) the magnetic shielding (σ) of a nucleus placed in an external/applied magnetic field is, in broad terms, dependent on the local electron distribution. For a probe nucleus located in a solute molecule in solution, the magnetic shielding and the related NMR chemical shift parameter δ (essentially the magnetic shielding relative to that of a reference, as is commonly used in practical NMR spectroscopy) are dependent on the nature of the local solution environment, or "solvation shell", through the effect of intermolecular interactions on the solute electron distribution. (Jameson, 1996) As such, the solute nucleus δ may be employed (with certain approximations/idealisations, which may or may not hold for a particular system) as a descriptor of the solvent composition surrounding the solute. (Ben-Naim, 1990) This approach has been shown to work particularly well for simple solutes (e.g. monoatomic) containing probe nuclei with large δ ranges, typically heavier (NMR active) nuclei. (Frankel, Langford and Stengle, 1970; Dechter and Zink, 1975)

Naturally, the presence of a solute in a liquid mixture affects, or modifies, the local solution structure/composition compared to that characteristic of the mixture itself; as such, in order to probe the latter, it is preferable that the solute interacts only weakly with the surrounding solvent molecules,

or otherwise in such a way that the inherent solution structure is essentially preserved (or elements thereof sampled); a prime example is ^{129}Xe, which is introduced in the form of a neutral, monoatomic solute. (Stengle *et al.*, 1984) In fact, ^{129}Xe NMR chemical shift measurements have been extensively employed to obtain information on the structure of pure liquids and their mixtures, (Jameson, Sears and Murad, 2004; Morgado *et al.*, 2013; Morgado, Martins and Filipe, 2019) including, more recently, ionic liquids. (Castiglione *et al.*, 2020) The $\delta(^{129}\text{Xe})$ data of Morgado *et al.* (Morgado, Martins and Filipe, 2019) for Xe atoms dissolved in binary liquid mixtures of *n*-hexane and perfluorohexane are reproduced in **Figure 1.3** as example. The non-first order variation of $\delta(^{129}\text{Xe})$ as a function of bulk composition and, importantly, its temperature dependence, was shown to be due to Xe atoms predominantly located (or *preferentially solvated*) in perfluorohexane-rich regions in these inherently nanoscale phase-separated (though macroscopically miscible) liquid mixtures.

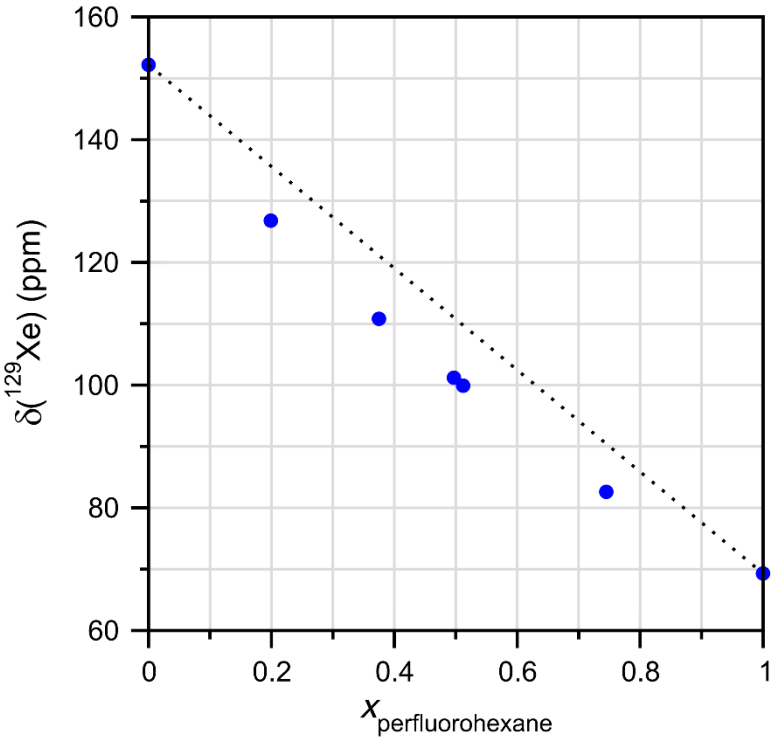

Figure 1.3 ^{129}Xe NMR chemical shift, $\delta(^{129}\text{Xe})$, raw data in *n*-hexane – perfluorohexane liquid mixtures at 313 K, plotted using data from Morgado *et al.* (Morgado *et al.*, 2013). Such data are typically corrected for bulk magnetic susceptibility changes with composition, which may be small relative to medium shifts, depending on the probe nucleus. The data, plotted as blue circles, may be seen to exhibit a non-linear variation as a function of perfluorohexane mole fraction, $x_{\text{perfluorohexane}}$. The black dotted line connects the $\delta(^{129}\text{Xe})$ limiting values in the respective pure liquids.

1.3.2 X-ray and neutron scattering

Information on the molecular structures of liquid systems may be obtained by measuring the intensity modulation spectrum of an incident neutron (Dixit *et al.*, 2002; Dougan *et al.*, 2004) or X-ray beam. (Nishikawa and Iijima, 1993; Nishikawa, Kasahara and Ichioka, 2002; Takamuku *et al.*, 2005) The reader is referred to the book chapter by Mariani *et al.* (Mariani *et al.*, 2021) for a more complete exposition of these techniques, with only essential information presented below as it relates to work contained in this thesis.

Considering only the elastic component of the X-rays interacting with matter (i.e. no kinetic energy is lost), the scattered intensity of an isotropic sample depends exclusively on the moment modulus variation of the beam, indicated by the scalar q (or Q) defined as:

$$q = 2k \sin(\theta) \tag{1.4}$$

with k the modulus (dependent on the incident photon wavelength λ) of both scattered and non-scattered radiation wave vectors, and 2θ the scattering angle. The observed scattering pattern is the superposition of the photons scattered by the molecules' electron density. This physical process takes place only if the incident wavelength λ is comparable with the atoms' characteristic size, from which it follows that X-rays may be used as a structural probe.

The result of a scattering experiment is the structure function, $S(q)$, which may be expanded as

$$S(q) = \sum_{i=1}^{N} x_i f_i^2(q) + I(q) \tag{1.5}$$

where f_i are the atomic scattering factor for each type of atom i, and x_i its number density; the second term, $I(q)$, is the *total static* structure function (or *reduced intensity*) and contains information about the molecular structure and distribution due to interference contributions from atom pairs.

$$I(q) = \sum_{i \neq j} x_i x_j f_i f_j H_{ij}(q) \tag{1.6}$$

Here, as before, x and f are the known number densities and atomic scattering factors of atoms i and j, and $H_{ij}(q)$ is the *partial structure function*, which is determined by the i-j distance distribution. Specifically, they are related through a Fourier integral to the radial pair distribution function, $g_{ij}(r)$, which describes the distribution of components i and j in real space (see Chapter 2). (Mariani *et al.*,

2021) In this way, neutron and X-ray scattering experiments can provide information on interatomic distributions, and hence liquid structure. (Soper and Phillips, 1986; Nishikawa and Iljima, 1993) Additional computational tools are often employed for the elucidation of complex liquid structures, e.g. empirical potential structure refinement, (Dougan et al., 2004) which makes use of computer simulation techniques.

1.4 Computer simulations of liquid mixtures

Molecular models and computer simulations can provide detailed information on the molecular-level structure and dynamics of liquids. (Allen and Tildesley, 1987) Since the early computer simulations of binary liquid mixtures of monoatomic particles in the 1970's, (McDonald, 1972) molecular simulation has become an invaluable complement to experiment for understanding of the interesting macroscopic behaviour of liquid mixtures on the molecular scale.

The binary water-methanol mixtures introduced in the previous sections, for example, have been extensively studied using various computational molecular models and simulation techniques in order to understand the properties of these mixtures under different physical conditions; see, for example, (Stouten and Kroon, 1990; Tanaka and Gubbins, 1992; Laaksonen, Kusalik and Svishchev, 1997; Wensink *et al.*, 2003). Such modelling efforts, details of which will be introduced in the next chapter, have confirmed that water molecules tend to self-associate *via* strong H-bonding interactions, with methanol methyl groups clustered together, resulting in a *percolated* liquid structure represented in **Figure 1.4** (Dixit *et al.*, 2002; Dougan *et al.*, 2004) Knowledge of this molecular-level structure (or "micro-structure") is important for understanding the anomalous physical properties of these liquid mixtures, e.g. densities and viscosities, mentioned in Section 1.1.

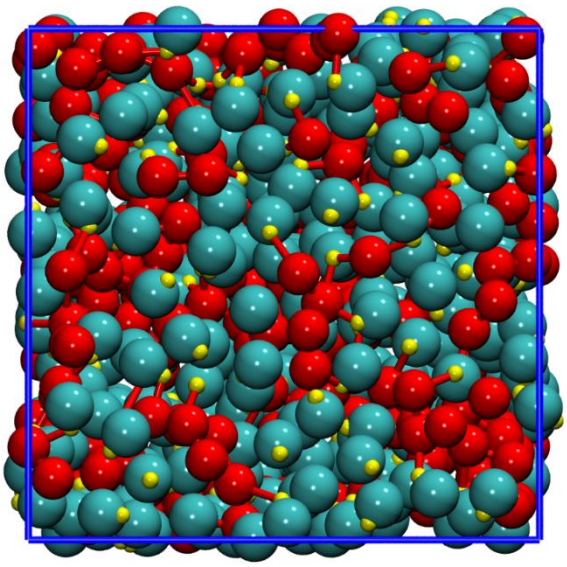

Figure 1.4 Computer simulation configuration of a water-methanol mixture, containing 276 water and 324 methanol molecules ($x_{\text{methanol}} = 0.54$). (Wensink *et al.*, 2003; Dougan *et al.*, 2004) The configuration representation, prepared with VMD, (Humphrey, Dalke and Schulten, 1996) shows water oxygen atoms as red spheres, methanol carbon atoms in cyan, and methanol oxygen atoms as small yellow spheres; H-bonds involving water molecules are indicated by red bars ("bonds"). All hydrogen atoms have been omitted. The representation, which effectively shows water self-association and the resulting percolated liquid structure, was prepared after those of Soper and co-workers. (Dixit *et al.*, 2002; Dougan *et al.*, 2004)

2 Computer simulations

2.1 Background

The first computer simulations of liquid systems were performed in the 1950's, (Allen and Tildesley, 1987) starting with the "Monte Carlo" work of Metropolis *et al.* (Metropolis *et al.*, 1953) considering collections of single particles, which was followed by computer simulations of molecular liquid systems, first diatomic molecules (Harp and Berne, 1968, 1970) and liquid water. (Barker and Watts, 1969; Rahman and Stillinger, 1971) These early computer simulations made use of classical mechanical molecular models, in which each atom (or even a group of atoms) is represented by a single particle with fixed partial electronic charge located at the particle centre (i.e. electrons are not explicitly considered), the behaviour and interactions of which are described by classical mechanics. Such "Molecular Mechanics" (MM) models still represent a computationally-affordable approximation that allows for the simulation of relatively large molecular models (order 10^6 atoms, and larger) representing the bulk liquid molecular structure and dynamics.

In this chapter, fundamental concepts of Molecular Mechanics force field models, MD computer simulation techniques and the alternative "coarse-grained" modelling approach, intended for the study of exceedingly large systems, will be introduced.

2.2 Molecular Mechanics force fields

The interactions and conformational mobility of molecules in classical molecular simulations are described by an effective potential energy expression and corresponding parameters for all atoms contained in the model, together constituting an MM force field (sometimes abbreviated "FF"). The MM effective potential, $V(r)$, is computed as a sum of contributions, Eq. (2.1), which may be classified as "bonded" (describing interactions between covalently bonded atoms, or atoms that are located in close proximity in the same molecule) and "non-bonded" (intermolecular interactions, or interactions between otherwise distant atoms) terms. The bonded terms consist of covalent bond stretching, angle bending and dihedral angle (torsional) potentials that are typically described by harmonic oscillator-type functions ("springs"). Dihedral angle potentials are more involved, (Ryckaert, Ciccotti and Berendsen, 1977) and a number of different functions have been developed for the description interactions between atoms separated by two three chemical bonds, often including

reduced non-bonded interactions. The effective potential functional form for the Amber force field is as follows: (Case *et al.*, 2018)

$$V(r) = \sum_{bonds} k_b(d - d_0)^2 + \sum_{angles} k_\theta(\theta - \theta_0)^2 + \sum_{dihedrals} k_\varphi[1 + \cos(n\varphi + \delta)] + \sum_{non-bonded\ pairs} \left\{ \varepsilon_{ij} \left[\left(\frac{\sigma_{ij}}{r_{ij}} \right)^{12} - \left(\frac{\sigma_{ij}}{r_{ij}} \right)^{6} \right] + \frac{q_i q_j}{4\pi\epsilon_0 r_{ij}} \right\} \quad (2.1)$$

The non-bonded potential energy component (terms in curly brackets in Eq. (*2.1*) is computed as a sum of pair-wise contributions, i.e. one for each pair of atoms located in different molecules, or that are otherwise considered distant (i.e. the interactions if which are not included in the "bonded" potential energy component). These additive pair-wise non-bonded contributions, in turn, are a sum of terms accounting for van der Waals and electrostatic interactions and described by, respectively, Lennard-Jones and Coulomb potential functions. The parameters included in the force field, i.e. harmonic force constants (k_b, k_θ etc.) and equilibrium bond lengths and angles (d_0, θ_0 etc.), atomic partial charges (q_i) and Lennard-Jones potential parameters (σ_i, ε_i), are derived from experiment and/or quantum chemical calculations. Force field parameterisation strategies may differ depending on its intended application, e.g. simulation of liquids and their mixtures, e.g. (Jorgensen *et al.*, 1983; Jorgensen, 1986), or biological macromolecules. (Weiner and Kollman, 1981; Brooks *et al.*, 1983; Dauber-Osguthorpe and Hagler, 2019) As such, computer simulation results are dependent, at least to some extent, on the particular MM force field used to describe the model system.

In practice, MM force fields usually contain LJ parameters for each type of atom ("atom type") treated, e.g. O and H atoms of water (which may differ from those for the same element in methanol, or other alcohols), which describe the van der Waals' interactions between atoms of the *same* atom type, i.e. *like* types. The LJ potential for the SPC water model oxygen atom type is shown in **Figure 2.1** as example of the nature of this function. (Berendsen, Grigera and Straatsma, 1987)

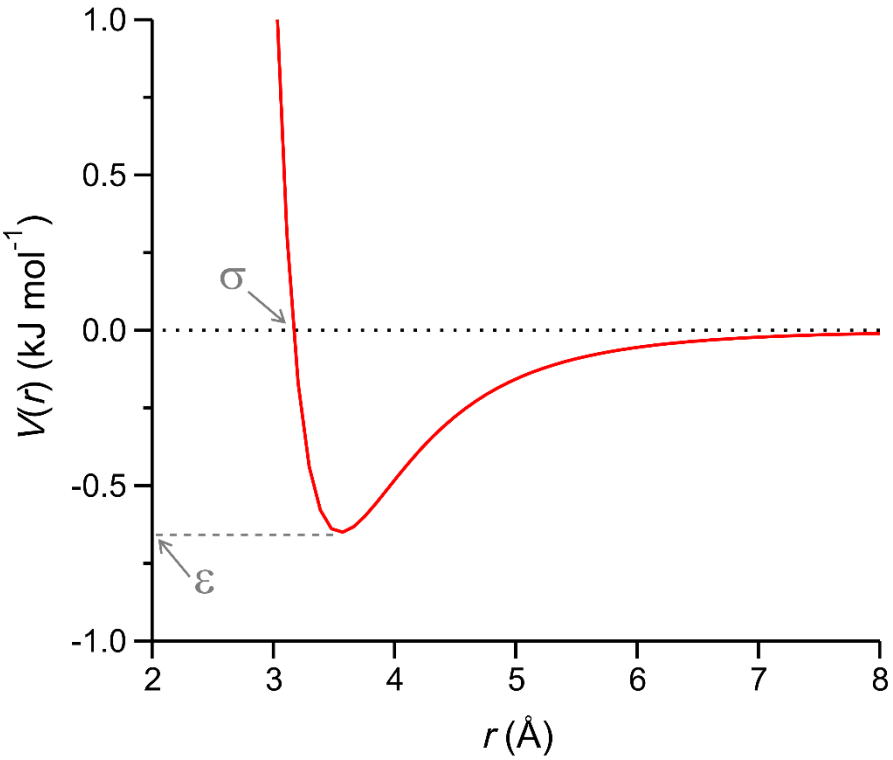

Figure 2.1 Partial Lennard-Jones (LJ) potential for SPC water model oxygen atoms. The LJ parameters σ (Å) and ε (kJ mol^{-1}) are indicated in grey, while $V(r)$ = 0 kJ mol^{-1} is indicated with a horizontal dotted black line to show the LJ potential's asymptotic approach with increasing particle separation r.

The LJ parameters for describing interactions between *unlike* types (e.g. O and C atoms in methanol, often also referred to as "cross-terms") are typically calculated from those of the two types in question, say i and j, by a set of "combining rules" (or "combination" or "mixing" rules). (Schnabel, Vrabec and Hasse, 2007) The Amber simulation software, for example, makes use of the Lorentz-Berthelot rules: (Case *et al.*, 2018)

$$\sigma_{ij} = \frac{1}{2}\left(\sigma_{ii} + \sigma_{jj}\right) \tag{2.2}$$

$$\varepsilon_{ij} = \sqrt{\varepsilon_{ii} \cdot \varepsilon_{jj}} \tag{2.3}$$

The "atom type"-concept is fundamental in Molecular Mechanics. It arises from the fact that the force field parameters, such as bonding constant or equilibrium bonding distances for a given element, e.g. carbon, with another element, e.g., should reasonably differ depending on the chemical environment, e.g. C=O bond force constant/length will be different than those in R_3C-O-H. This imply classifying the sp^2 carbon in the carbonyl as a different atom type than an sp^3 carbon bound to a hydroxyl group. A list of the common atom types of the general AMBER force field (GAFF) (Wang *et al.*, 2004) is reported in **Table 2.1**. Partial atomic charge development/parameterisation is a crucial step, for which each established force field has its own rationale and methodology, notably since it affects strong electrostatic interactions (including H-bonding).

Table 2.1 Selection of basic atom types in GAFF (Wang *et al.*, 2004)

Atom type	Description	Atom type	Description
c	sp^2 C in C=O, C=S		
c1	sp^1 C	o	sp^2 O in C=O, COO-
c2	sp^2 C, aliphatic	oh	sp^3 O in hydroxyl group
c3	sp^3 C	os	sp^3 O in ether and ester
ca	sp^2 C, aromatic		
hc	H on aliphatic C		
ha	H on aromatic C		
hn	H on N		
ho	H on O		
hs	H on S		
hp	H on P		

2.3 Computer simulation methods and techniques

2.3.1 Monte Carlo and Molecular Dynamics

The most widely used methods for performing classical molecular simulations are Monte Carlo (MC) and Molecular Dynamics (MD). (Allen and Tildesley, 1987) MC, the older of the two, stochastically moves particles (atoms, or groups of atoms) essentially by randomly choosing a particle and moving it to a randomly-chosen new position; the move is accepted if it results in an energy decrease or fulfils the Boltzmann distribution (at the specified target temperature). The MC method effectively samples configurational space and is still commonly used in molecular simulation. Differently, MD is a fully deterministic method in which the time evolution of the system is computed by solving Newton's equations of motion for large numbers of particles at each simulation step. Essentially, the potential energy is calculated for a given system configuration, from which the force acting on each classical particle, and consequently its acceleration, may be obtained. (Allen and Tildesley, 1987) The essential relationship is given in Eq. (*2.4*), where $a_i(t)$ is the time-dependent acceleration of particle *i*, obtained from the force $F(r)$ acting on *i* (note m_i is the particle mass), which, in turn, is computed from the effective potential $V(r)$ gradient: (Mariani *et al.*, 2021)

$$a_i(t) = \frac{1}{m_i} F[r_i(t)] = -\frac{1}{m_i} \nabla V[r_i(t)] \tag{2.4}$$

This information may be used to propagate the positions and velocities of the particles by application of an appropriate algorithm for integrating the equations of motion, i.e. to determine the position and velocity of *i* at time $t + \Delta t$ (where Δt is the simulation *time step*) . (Allen and Tildesley, 1987) The particle positions and velocities may be stored at chosen intervals (i.e. every time step Δt, or every 100 Δt, etc.), and this time-dependent data is referred to as the simulation trajectory. MD simulations, unlike MC, can provide information on the dynamic properties of molecules, e.g. translational and rotational diffusion characteristics, (Mocci and Laaksonen, 2015) which is highly desirable, and has become the most widely-used classical molecular simulation method.

2.3.2 Periodic boundary conditions

Simulated systems, which are typically of dimensions 10-100's Å, are routinely intended as models for a larger, "macroscopic" material samples, e.g. a liquid or gas. Due to the high surface-to-volume ratio of simulated systems, a large percentage of simulated atoms/molecules occur at, or near, the system boundary with the surrounding vacuum, much larger than that in macroscopic samples. (Allen and Tildesley, 1987) As such, small simulated systems are not representative of the real target, since the boundary-region molecules (which, as described above, account for a significant percentage of the total simulated molecules) will exhibit a different distribution/behaviour, which is not characteristic of the target.

In order to avoid, or limit, this effect, it is common practice, in computer simulations of condensed phases in particular, to employ periodic boundary conditions ("PBC"). The essential concept is illustrated schematically below: particles approaching the system boundary interact with molecules located on the opposite side of the simulated system, before crossing the boundary, at the same time re-entering from the opposite side. Effectively, this procedure allows for mimicking of a continuous phase, with the simulated system itself a small volume "sample".

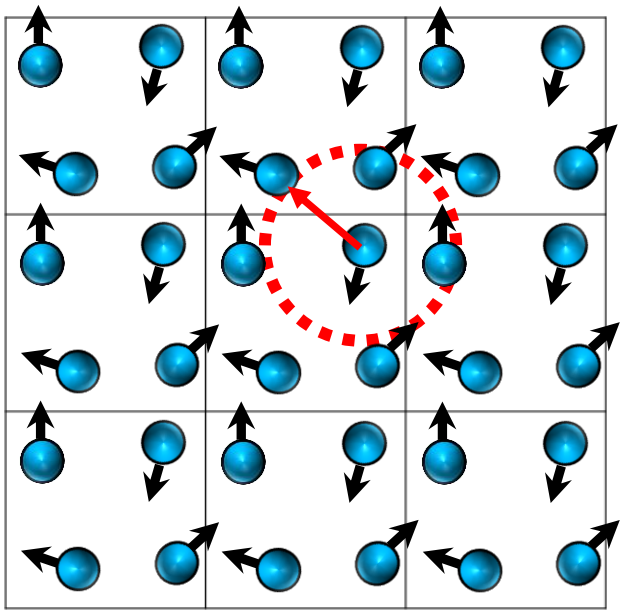

Figure 2.2 Schematic representation of the PBC concept in two dimensions: the central square represents the essential simulation cell, the boundaries through which molecules can freely pass and re-enter from the opposite side. The red dashed circle illustrates how each particle interacts only with the closest image of the other particle in the system. Image courtesy of F. Mocci.

2.3.3 Treatment of long-range electrostatic interactions

The intermolecular ("non-bonded") component of the effective potential energy expression in **Eq. (2.1)** decreases with increasing particle separation r_{ij}. The Lennard-Jones ("van der Waals") component, in particular, decreases rapidly as a function of distance, as seen in **Figure 2.1**.

At larger interparticle separations, e.g. 10-12 Å, the non-bonded potential becomes very small, yet its calculation presents a substantial computational load (since the number of pairwise interactions to be computed increase); for this reason, it is common practice to set the intermolecular potential to a constant zero, or to "cut" it, beyond a chosen separation limit ($r \geq r_{\text{cut}}$). Long-range corrections for energy and pressure are typically applied to truncated van der Waals interactions. (Case *et al.*, 2018)

Nevertheless, electrostatic interactions decrease more gradually with increasing particle separation, the Coulomb potential being proportional to r^{-1} in **Eq. (2.1)**, and standard long-range correction terms are not sufficiently accurate to account for this effect. To this end, electrostatic interactions in periodic systems are typically treated using Particle mesh Ewald Methods as described by Darden, Essmann and co-workers. (Darden, York and Pedersen, 1993; Essmann *et al.*, 1995)

2.3.4 Temperature and pressure coupling

MD simulations can be carried out under different physical conditions corresponding to constant volume, temperature, pressure, chemical potential, etc. based on statistical mechanical microcanonical, canonical, isobaric, etc ensembles. MD in the microcanonical (E, N, V) ensemble corresponds to pure Newtonian dynamics while for canonical (N, V, T) ensemble a thermostat is needed to keep temperature constant and for isobaric (N, P, T) ensemble also a barostat needed to have a constant pressure. Popular MD thermostats/barostats include the Berendsen weak coupling algorithm, (Berendsen *et al.*, 1984), Nosé-Hoover (Nosé, 1984; Hoover, 1985) and Parrinello-Rahman (Parrinello and Rahman, 1981), to name a few.

2.4 Structure of simulated liquids

2.4.1 General considerations

When performing computer simulations of liquids, it is important to be able to evaluate the structure of the simulated system by comparing it with experimental structural results. The simplest observable that can be extracted by the simulations and easily compared with experimental data is the average density, provided the simulation is not performed at fixed volume. At a higher level of detail, there are the structural information that can be compared with spectroscopic techniques, or from scattering experiment, which typically require a more elaborate analysis of the simulation data, and more sophisticated experiments. The analysis methods used for comparing simulated average liquid structures with structure factors from scattering experiments, or local molecular arrangements inferred from spectroscopic experiments, are briefly introduced in the following sections.

2.4.2 Radial distribution functions (RDFs)

The molecular structure of a liquid system is described by a series of particle distribution functions, the simplest of which is the pair distribution function, $g^2(r_{ij})$ or simply $g(r_{ij})$, which describes the probability of finding a pair of particles *i* and *j* separated by a distance *r*, relative to that based on a completely random particle distribution at the same bulk particle density. (Allen and Tildesley, 1987) In fact, $g(r)$, is a radially-averaged derivative of the original pair distribution function and is often simply referred to as a *radial distribution function*, or RDF. The probability of finding a particle *B* at distance *r* from particle *A* is given by the following general density-density correlation expression:

$$g_{AB}(r) = \frac{\rho_A(r|r_A = 0)}{\rho_B}, \tag{2.5}$$

in which ρ_B is the bulk (uniform) particle density of *B*, and ρ_A the average "microscopic" density of *B* in a small volume around a distance *r* from *A* (see below).

While technically applicable to a system of isotropically-distributed monoatomic (single) particles, RDFs are also commonly used for the description of molecular liquid structures, (Allen and Tildesley, 1987) often by consideration of selected molecular sites, e.g. molecule centre of mass or, more commonly, selected atomic sites.

In practice, RDFs are calculated from molecular simulation configurations by considering a central particle *A*, dividing the space around *A* (up to a certain distance) into spherical slices ("bins") of width Δr, and calculating a histogram for the *B* particle count in these slices. Defining $N_B(r,\Delta r)$ as the average number of *B* particles found within the interval r-½Δr and r+½Δr from the central particle *A*, and $V_B(r,\Delta r)$ as the volume of the spherical slice between interval r-½Δr and r+½Δr from the central particle *A*, then the radial distribution function can be calculated as:

$$g_{AB}(r) = \left(\frac{V}{N_B}\right)\frac{N_B(r,\Delta r)}{V_B(r,\Delta r)} = \left(\frac{V}{N_B}\right)\frac{N_B(r,\Delta r)}{4\pi\, r^2\, \Delta r}\ , \tag{2.6}$$

where N_B is the *total* number of *B* particles and *V* the overall volume of the configuration. This calculation is done for all particles *A* in each saved simulation configuration (or "frame"), so as to obtain the simulation average distribution which may be compared with experimental measurements, e.g. from neutron scattering structure functions, $S(q)$.

The water oxygen-oxygen RDF, $g_{OO}(r)$, computed from the simulated equimolar water-methanol mixture described in Section 1.4, is shown in **Figure 2.3**. The intense peak in the function is associated with H-bonded water molecules, i.e. due to all the H-bonded direct neighbours of a given water molecule in the mixture. This *coordination number*, $n(r)$, may be determined by integration of the RDF up to its first minimum, r_{min}, which is assumed to indicate the effective boundary between direct neighbours, and "next-nearest" neighbours (the second solvation shell). The formula for determining the coordination number of particle A by surrounding particles B is given in **Eq. (2.7)**. (Ben-Naim, 1990)

$$n_{AB}(r) = \rho_B \int_0^r g_{AB}(r) 4\pi r^2 dr \tag{2.7}$$

The $n(r)$ function is also plotted in **Figure 2.3**, from which the coordination number $n_{OO}(r_{min})$ may be read as approximately 2, i.e. on average, each water molecule in the mixture is H-bonded to two other water molecules, consistent with significant water self-association.

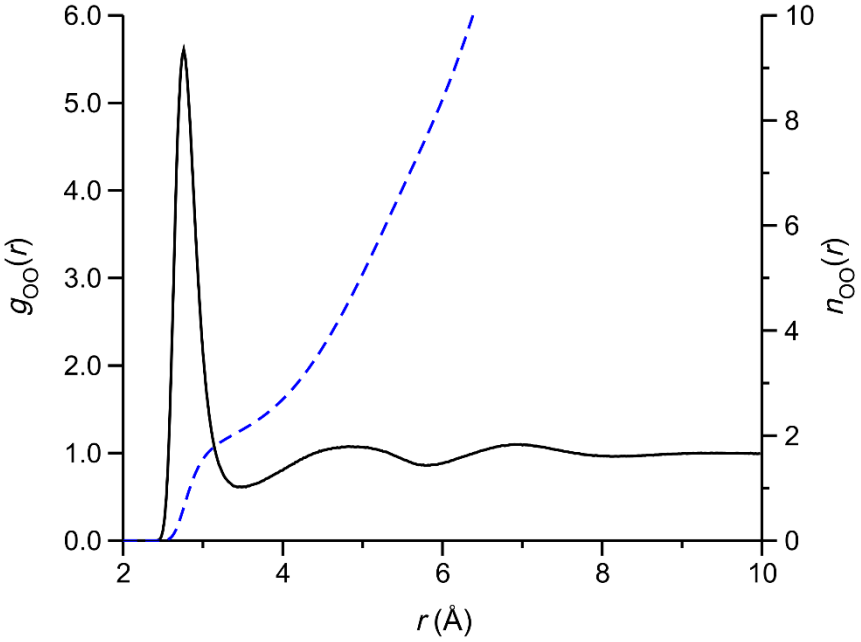

Figure 2.3 Water O-O RDF, $g_{OO}(r)$, for simulated equimolar water-methanol mixture: black solid line, primary axis. Also shown is the O-O coordination number, $n_{OO}(r)$, in dashed blue line, with values on the *secondary axis*.

2.4.3 Spatial distribution functions (SDFs)

For strongly interacting, e.g. H-bonded, liquid systems, it has been shown that much of the detailed three-dimensional local liquid structure may be lost by radial averaging of the pair distribution function, $g^2(r)$, due to cancellation of contributions from regions of low and high probability at the same distance r (or range Δr), but with different relative positions in the local structure. (Svishchev and Kusalik, 1993; Kusalik and Svishchev, 1994) Strictly speaking, the RDFs introduced above provide a complete structural picture only for liquids of spherical particles.

Spatial distribution functions (SDF) are defined in a similar way as RDFs, but there is no radial averaging of the pair distribution function:

$$g_{AB}(\vec{r}) = \frac{\rho_B \langle \vec{r} | \vec{r}_A = 0 \rangle}{\rho_B} \tag{2.8}$$

Here, symbols are as defined in Eq. (2.5), however, there is one important difference: SDFs use vectors instead of scalar distance values. Furthermore, since SDFs are a function of three variables, they have to be represented keeping one variable frozen, either by representing the iso-surfaces corresponding to a given SDF value, or by freezing one of the spatial variables. For further details on

SDFs, the interested reader is referred to original works by Kusalik and co-workers, (Svishchev and Kusalik, 1993; Kusalik and Svishchev, 1994) which includes a computational study of water-methanol mixtures. (Laaksonen, Kusalik and Svishchev, 1997)

2.4.4 Hydrogen bond analysis

The RDFs introduced above are routinely employed in computer simulation studies of the structures of H-bonded liquids. However, it is often desirable to introduce more stringent conditions for the identification of H-bonds, as these have been shown to be of a highly directional nature, i.e. geometrically well-defined. (Stillinger, 1980; Luzar and Chandler, 1996) A number of H-bond criteria have been proposed, both geometric and energetic, and these are often combined; a widely cited set of geometric H-bond criteria for water and alcohols are as follows: (Andanson *et al.*, 2005)

1. The distance between H-bond donor and acceptor oxygen atoms, O_D and O_A, should be smaller than a certain value, typically chosen as the corresponding O_D-O_A RDF first minimum, hereafter R_{OO}.

2. The distance R_{OH} between donor H and acceptor O atoms, should be smaller than a certain limit, similarly taken as the O_A-H_D RDF first minimum,

3. An angle criterion defining the relative orientations of donor and acceptor groups; in this study we define the H-bond O_D-H_D … O_A obtuse angle $\geq 135°$

In practical H-bond definitions, at least one of the above distance criteria (typically criterion 1) are combined with an angle criterion, allowing for the development of algorithms that provide detailed information on simulated H-bond topologies.

2.4.5 Cluster analysis

The structures of H-bonded liquids, such as water or alcohols, and their mixtures with other liquids, are often characterised by the presence of H-bonded aggregates (“clusters”) or even extended networks which continually break up and recombine, shedding and adding H-bonded members. (Stillinger, 1980; DeBolt and Kollman, 1995) Depending on the system studied, such H-bonded molecular clusters may consist of tens to hundreds of members, such that RDFs and SDFs, which

describe local structure, do not provide detailed information on their structure, size distributions or dynamics.

The binary water-methanol mixtures discussed in the preceding sections, for example, have been shown to have micro-heterogeneous liquid structures, (Dixit *et al.*, 2002; Dougan *et al.*, 2004) in which water molecules tend to self-associate (cluster) *via* strong H-bonding interactions. Similar molecular clustering is found in other binary mixtures of H-bonding or polar liquids, and detailed knowledge of the nature of this phenomenon may help to explain their anomalous physical properties, e.g. higher/lower than expected densities, (Stouten and Kroon, 1990; Engelbrecht *et al.*, 2021) and have important implications for their solvent characteristics. (Saielli *et al.*, 2005; Bragg, Kanu and Schwartz, 2011; Engelbrecht *et al.*, 2018) In computer simulations of aqueous mixtures, the formation of H-bonded water clusters may be studied by choosing a suitable H-bond definition, (Kumar, Schmidt and Skinner, 2007) and iteratively applying this definition to a given water molecule, its newly-found H-bonded neighbours, then their neighbours, and so on, combining this information in order to identify all unique H-bonded water clusters in the particular simulation configuration. A simplistic H-bond definition may be as follows: water molecules are considered H-bonded if their oxygen atoms are separated by a distance $r \leq R_{OO}$, where R_{OO} is the position of the first minimum of the *water-water* $g_{OO}(r)$; additional geometric or energetic H-bond criteria are typically implemented. (Stillinger, 1980; Kumar, Schmidt and Skinner, 2007)

Once established, a cluster identification algorithm may be applied to other simulation frames in order to determine the average size of H-bonded water clusters, their average size distribution, etc. (DeBolt and Kollman, 1995; Bergman and Laaksonen, 1998) The partial histogram below, **Figure 2.4 (top)**, shows the average count for H-bonded *water* clusters of given size (number of members), n_c, for a simulated equimolar water-methanol mixture in **Figure 1.4** using the simplistic distance criterion (1) described in the previous section; note that much larger water clusters are occasionally found. Such cluster count histograms are easily converted to show the fraction of water molecules participating in clusters of size n_c, which allows for comparison with experimental results; this data is show in **Figure 2.4 (bottom)**.

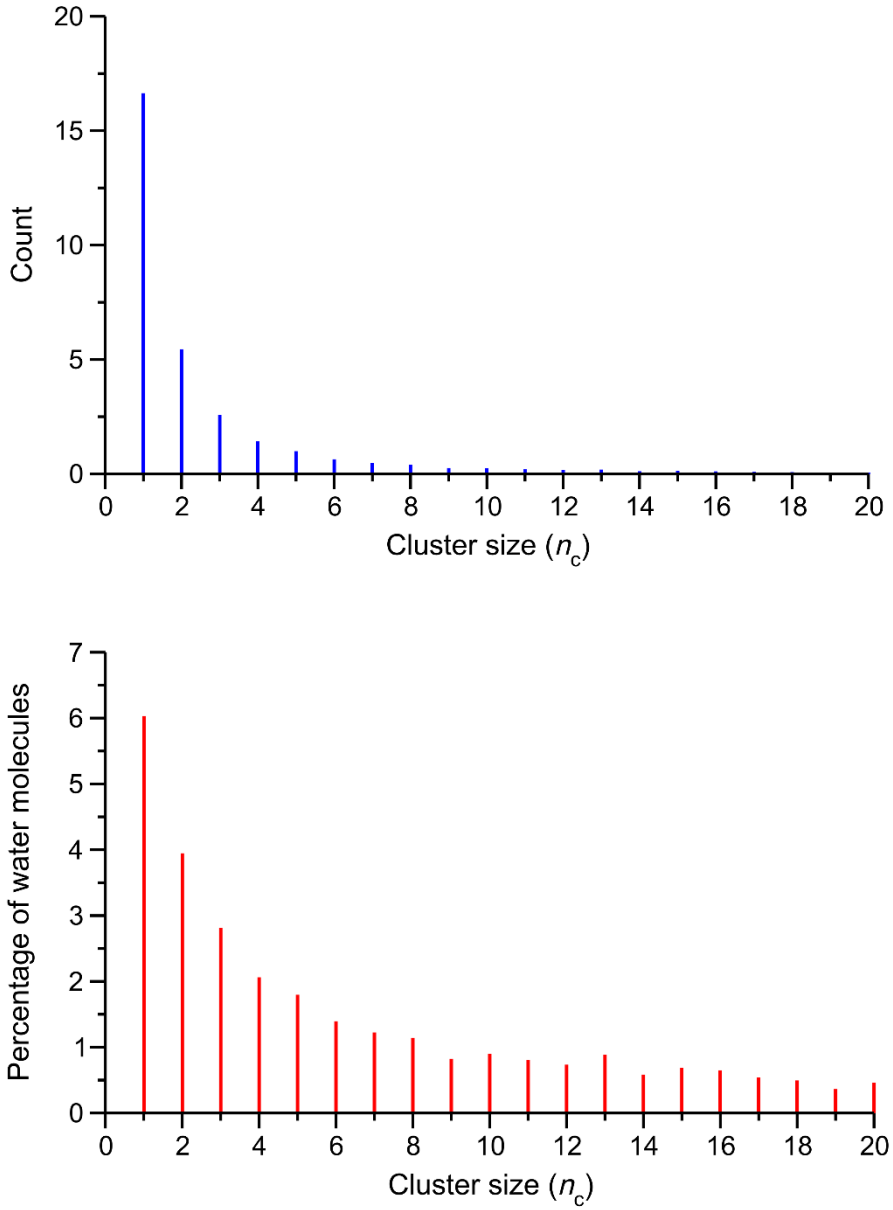

Figure 2.4 (Top) Partial water cluster count histogram, based on a simple O-O distance criterion, for a simulated equimolar water-methanol mixture. **(Bottom)** Histogram showing corresponding percentage of water molecules contributing to clusters of given size n_c.

2.5 Coarse-grained (CG) models

2.5.1 Background

The classical MD computer simulations considered in preceding sections, in which atoms are represented by a unique classical particles, are commonly referred to as "all-atom" (AA, also "atomistic", or atomic-resolution), and are routinely used to for the study of a wide variety of molecular systems, ranging from liquids, biological macromolecules and membranes, to solid materials. A number of popular force field packages have been developed for the simulation of such AA model systems, often representing up to tens of thousands of atoms, and usually for tens to hundreds of nanoseconds. (Jorgensen, Maxwell and Tirado-Rives, 1996; Wang *et al.*, 2004; Vanommeslaeghe *et al.*, 2010) However, the study of certain experimental observations or problems may require much larger models, consisting of millions of atomic particles, to be simulated over long timescales, perhaps hundreds of nanoseconds. Often such simulations are not practically attainable using conventional AA MD force field models; the sheer number of particles to be considered may simply be too high to complete the desired simulation in a reasonable time using available computational resources.

The traditional approaches for reducing the high computational cost presented by the now-conventional AA models essentially amount to reducing of the number of particles to be considered by introducing certain model simplifications. (Jorgensen and Tirado-Rives, 1988; Yang *et al.*, 2006) Such model simplifications include description of the solvent surrounding a macromolecule of interest by a continuum solvent model, (Weiner and Kollman, 1981; Brooks *et al.*, 1983) or simplifying the description of certain atomic groups, the detailed structures of which are thought to be of lesser importance, e.g. reducing the description of a methyl functional group in methanol to a single, large "united atom" (UA) interaction site. (Haughney, Ferrario and McDonald, 1987)

In recent years, coarse-graining modelling methods (CG, referring also to the "coarse-grained" models themselves) have become popular for the study of diverse molecular processes occurring over ever-larger length- and time scales, notably in studies of biological macromolecular systems and aggregation processes. (Lyubartsev *et al.*, 2010; Rebič *et al.*, 2017; Wang *et al.*, 2018; Wang *et al.*, 2020) The essential CG concept is quite similar to the UA force fields mentioned above, in the sense that they combine selected groups of atoms into single interaction sites, thus reducing the number of interactions to be computed. While established CG force fields are now available for study of certain problems, e.g. the Martini biomolecular CG FF, (Marrink and Tieleman, 2013) other systems may

require substantial CG model development, (Mariani *et al.*, 2021) which includes the decision of how to effectively assign atoms to unique CG particles. (Noid *et al.*, 2008; Dunn and Noid, 2015, 2016)

2.5.2 CG mapping

While the CG approach is conceptually highly intuitive, the choice of the number of CG particles (commonly referred to as *beads*) required to represent a given system, their relative positions with respect to the average atomic coordinates (together referred to as the *CG mapping scheme*), and, critically, the development of appropriate CG interaction potentials, are often far from trivial. (Noid *et al.*, 2008) Consider, for example, a simple CG model of the water molecule consisting of a single CG bead, (Lyubartsev *et al.*, 2010) located at the centre-of-mass (COM) of the water molecule. This CG model does not explicitly include electrostatic interactions, and is described by a *single* interaction potential, plotted in **Figure 2.5**. This potential, obtainable by different methods (discussed in more detail below), may be used to perform a CG MD simulation of pure water, from which the water-water intermolecular radial pair distribution function (RDF) may be computed. The CG water-water RDF is in reasonable agreement with $g_{OO}(r)$ obtained from neutron scattering experiments, (Soper and Phillips, 1986) and, as will be discussed below, virtually identical to that of the SPC water model under the same conditions. (Berendsen, Grigera and Straatsma, 1987; Mark and Nilsson, 2001)

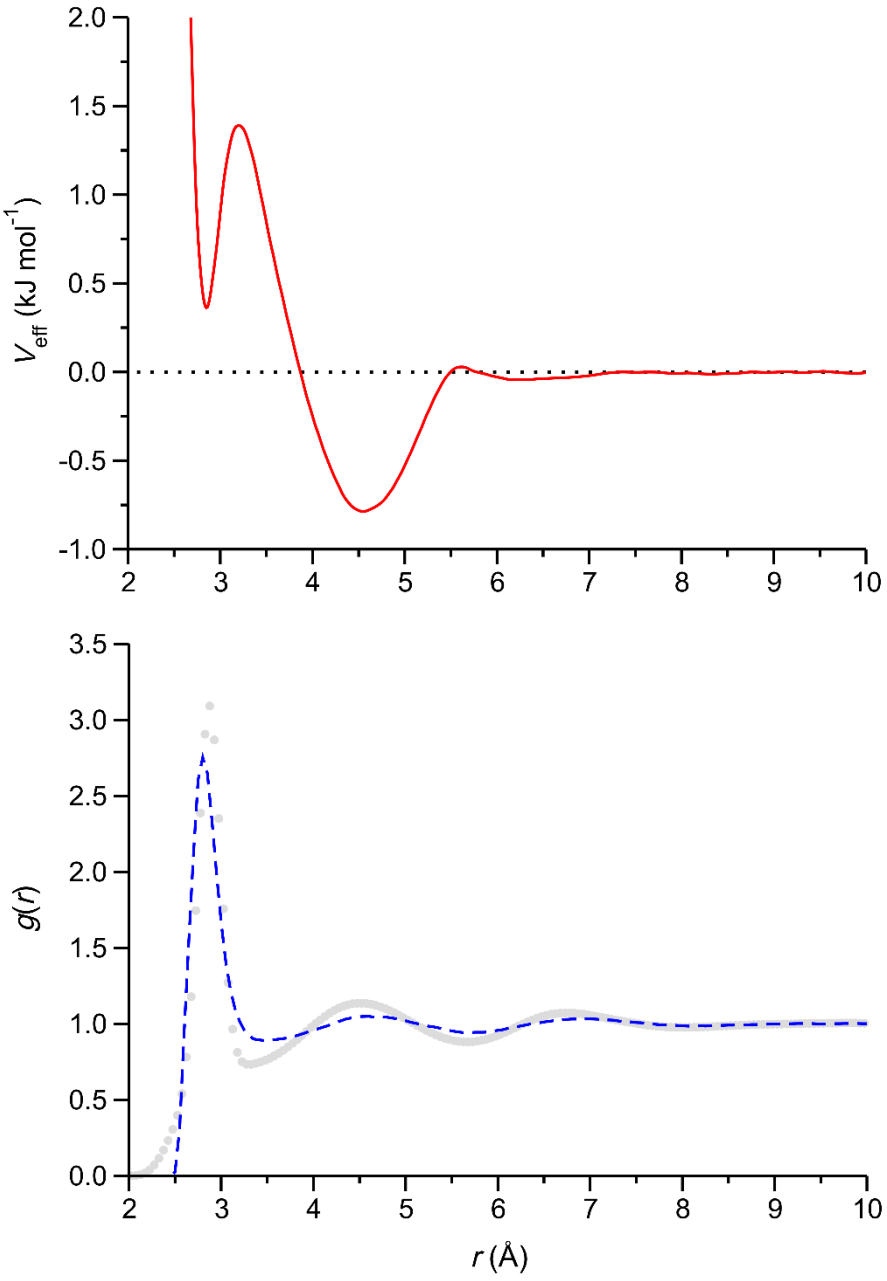

Figure 2.5 Effective potential, $V_{\text{eff}}(r)$ (**top panel**, solid red line), and RDF, $g(r)$ (**bottom**, dashed blue line) of single-bead CG water model. (Lyubartsev et al., 2010) Also shown in the bottom panel for comparison is the experimental $g_{OO}(r)$ of water, grey data points, from neutron diffraction experiments by Soper & Phillips. (Soper and Phillips, 1986)

2.5.3 CG model development

There exist two fundamentally different approaches for the development of CG interaction potentials, commonly referred to as "top-down" and "bottom-up" approaches. (Noid, 2013) In the former, the CG potential (or potential set, in the more general case of multiple CG bead types) is optimized in order to reproduce target thermodynamic properties or other experimental observables of the system to be simulated; the Martini biomolecular CG FF is an example of an FF parameterized using this approach. (Marrink and Tieleman, 2013) The alternative "bottom-up", or systematic multi-scale (MS), CG approach makes use of a suitable detailed, high-resolution model of the system of interest (typically an AA MD simulation) to derive interaction potentials for a low-resolution (CG) description of the system. (Noid *et al.*, 2008) This MS CG approach has different practical implementations, (Lyubartsev and Laaksonen, 1995; Chaimovich and Shell, 2011; Brini and Van Der Vegt, 2012; Noid, 2013) aimed at reproducing a set of target distributions obtained from the high-resolution model. The CG water model described in **Figure 2.5**, for example, was developed using a systematic structure-based method, (Lyubartsev and Laaksonen, 1995; Lyubartsev *et al.*, 2010) in which an AA MD simulation of the established SPC water model provides the reference water structure (COM RDF) to be reproduced by the CG model.

The systematic structure-based CG method, shown schematically in **Figure 2.6**, essentially starts from a chosen approximation ("guess") of the effective CG interaction potential set, which is then used to sample CG model configurations by the Monte Carlo (MC) algorithm, (Lyubartsev and Laaksonen, 1995; Mirzoev and Lyubartsev, 2013) or by MD. The performance of the trial CG potential set is evaluated by comparison of the sampled RDFs with the reference structure. The starting CG potential set is then modified, and the new set similarly tested. This potential update/test procedure is iteratively applied until a satisfactory reproduction of the reference structure is obtained. A selected set of trial potentials and resulting RDFs from the development of the single-particle CG water model described in **Figure 2.5** is shown as example in **Figure 2.6**.

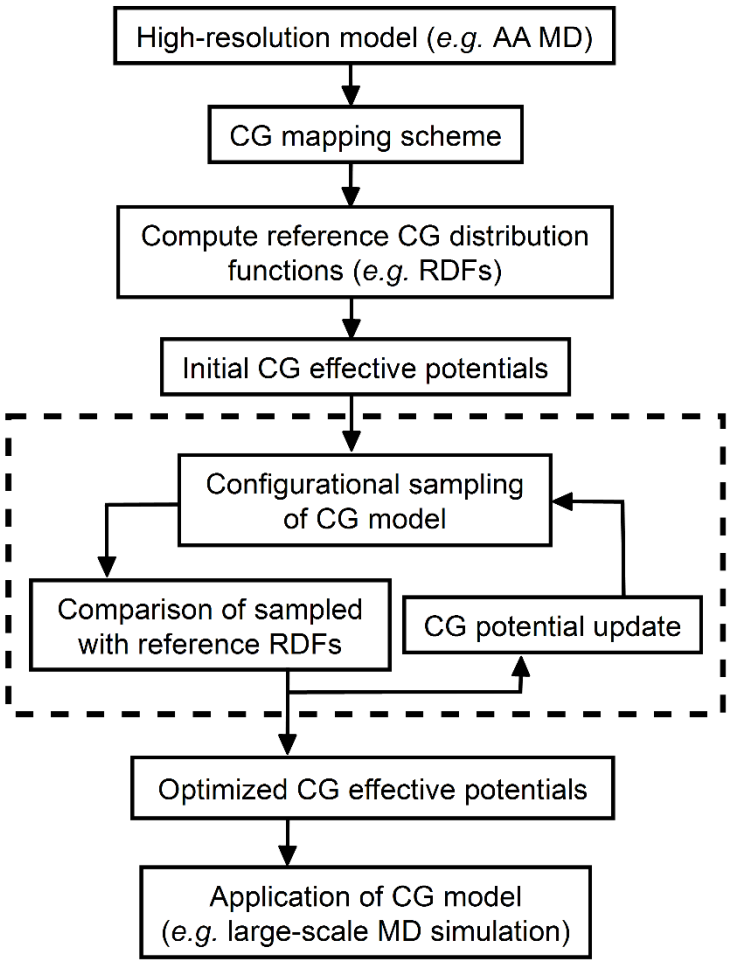

Figure 2.6 Essential steps in the structure-based MS CG method. (Mirzoev and Lyubartsev, 2013) The steps enclosed in dashed box constitute the iterative CG potential refinement process. Reproduced from (Mariani *et al.*, 2021). Copyright 2021 Springer.

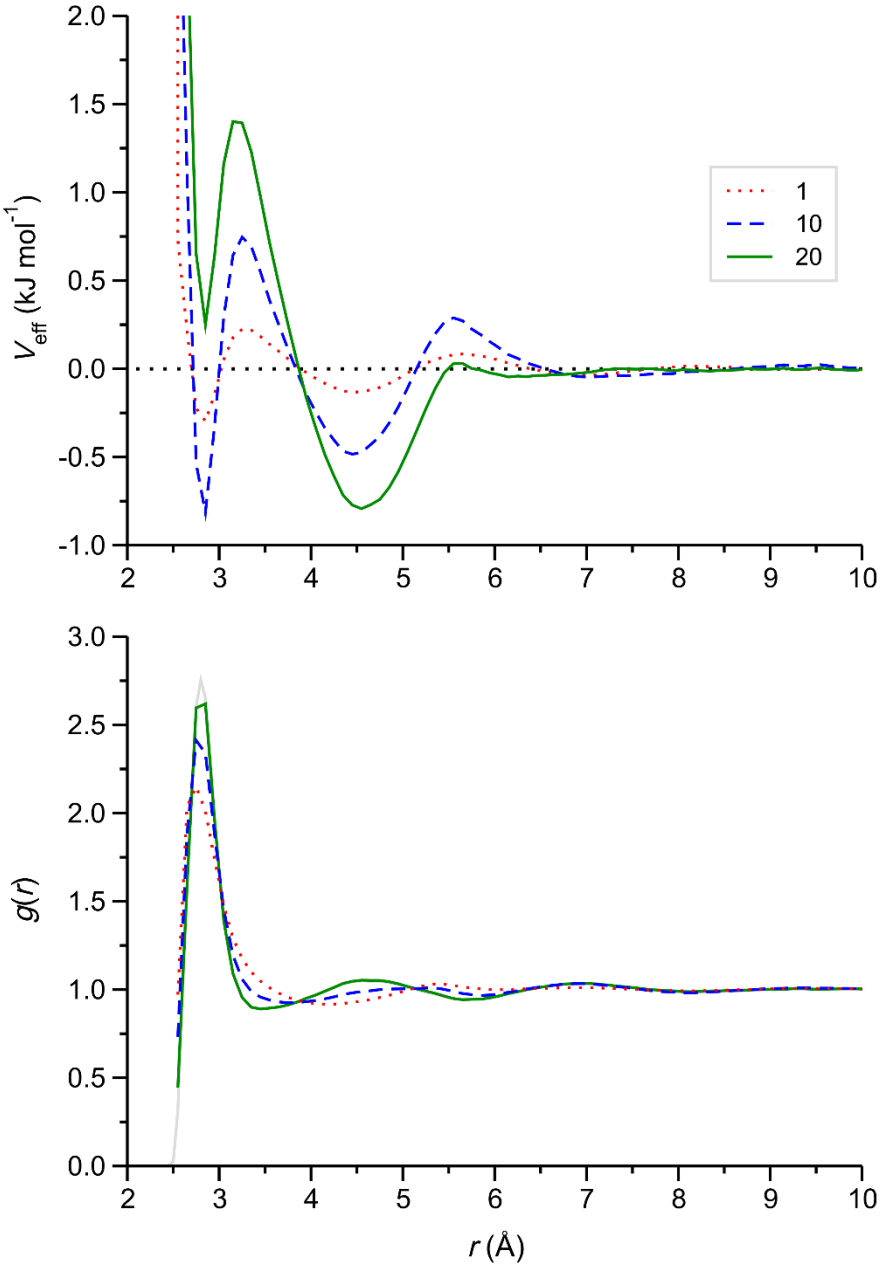

Figure 2.7 Top: Single-bead CG water interaction potential at different stages of structure-based CG procedure; (Lyubartsev *et al.*, 2010) numbers in legend indicate IMC iteration number: 1 red dotted line, 10 blue dashed line, and 20 (final iteration) solid green line. **Bottom:** Sampled CG water-water RDFs at different stages of CG procedure, compared with reference RDF from AA MD simulation of water (grey solid line). Note that these raw data (rather sparse grid) are interpolated (and smoothened) and extended prior to use. (Mirzoev and Lyubartsev, 2013) Data reproduced from Mariani *et al.* (Mariani *et al.*, 2021)

3 Preferential solvation in binary aqueous liquid mixtures

The work presented in this chapter has been published in *Inorganic Chemistry* (ACS). (Engelbrecht *et al.*, 2018)

Unsurprisingly, one of the main use of solvent mixtures is to dissolve other molecules and ions. In aqueous-organic solvent mixtures, we would expect that charged species should be preferentially solvated by water, the most polar solvent, with electrostatic interactions between the solvent and the solute being a determinant factor in the solvation. In this work however, we face the challenge of rationalizing how a large anion in a fully miscible aqueous-organic binary mixture could be preferentially solvated by the organic component.

The chapter is organized as follows. In Section 3.1 the relevance of the studied systems is presented, as well as the NMR experimental reference data that were to be rationalized by this study. Previous investigations on related systems are also briefly reviewed. Section 3.2 is devoted to the computational details. In Section 3.3 the liquid mixture structure of the studied is discussed, with particular emphasis on microheterogeneity, while Section 3.4 is focused on the concept of preferential solvation, and on how it was studied in the present investigations. Finally, in Section 3.5, the main conclusions from the presented computational study are highlighted.

3.1 Introduction

The platinum group metals (PGMs: Pt, Pd, Rh, Ir, Ru, and Os) are employed in numerous modern technological applications, the industrially most important of which is arguably the extensive use of Pt, Pd, and Rh in automobile emission control catalytic converters. (Glaister and Mudd, 2010) The large-scale industrial refining of PGMs involves a complex separation process from aqueous solutions using a variety of chemical processes and techniques, ranging from classical precipitation methods and oxidative distillation to selective solvent extraction, molecular recognition, and ion-exchange techniques. (Berfeld, Bird and Edwards, 1986) The selective solvent extraction of platinum $[PtX_x]^{n-x}$ complexes (X = Cl or Br and n is the Pt oxidation state of II or IV, x = 4 (square-planar) or 6 (octahedral complex geometry)) requires the favourable transfer of the appropriate chemical species, typically the octahedral $[PtCl_6]^{2-}$ anion, from an acidic, halide-rich aqueous phases into appropriate organic receptor phases. (Berfeld, Bird and Edwards, 1986; Bernardis, Grant and Sherrington, 2005; Koch *et al.*, 2006; Kramer and Koch, 2006, 2007)

^{195}Pt NMR spectroscopy is a powerful technique for determining the chemical speciation of Pt(II/IV) due to ligand-exchange reactions that may occur in aqueous solutions as relevant to the platinum refining industries. (Preetz, Peters and Bublitz, 1996; Kramer and Koch, 2006, 2007) The highly-sensitive NMR shielding of the ^{195}Pt nucleus, resulting in an extremely large chemical shift range of Pt(II/IV) complexes, allows for the unambiguous characterization of platinum complexes in solution by ^{195}Pt NMR, under suitably-controlled conditions. (Koch *et al.*, 2006) The remarkably-resolved $^{35/37}$Cl and $^{16/18}$O isotope effects present in the ^{195}Pt NMR profiles of the $[PtCl_{6-n}(H_2O)_n]^{n-2}$ (n = 0−6) and $[PtCl_{6-m}(OH)_m]^{2-}$ (m = 0−6) species in aqueous solution best illustrate the extraordinary sensitivity of the ^{195}Pt nuclear shielding, and may be used as unique "fingerprints" for these complexes in solution. (Engelbrecht, Murray and Koch, 2015; Koch and Engelbrecht, 2017)

Moreover, ^{195}Pt NMR chemical shifts are known to be highly sensitive to the solution environment of platinum complex, e.g. solvent, (Freeman *et al.*, 1976; Pesek and Mason, 1977) solute concentration, (Naidoo *et al.*, 2003; Koch *et al.*, 2006) and temperature. (Cohen and Brown, 1974) In binary mixtures of water and water-miscible organic solvents, very significant changes in the ^{195}Pt NMR chemical shift of the $[PtCl_6]^{2-}$ anion at constant concentration and temperature are observed, ranging from *ca.* 90 to >400 ppm as a function of the mole fraction of organic solvent (x_A). (Westra, 2005) Evidently, the ^{195}Pt NMR shielding is a remarkably sensitive probe of solute−solvent interactions in macroscopically miscible (single-phase) binary liquid mixtures, presumably reflecting subtle changes in the solvation shell composition of particularly the $[PtCl_6]^{2-}$ anion, (Freeman *et al.*, 1976; Westra, 2005) and other effects, such as ion-pairing interactions. (Naidoo *et al.*, 2003)

Several computational studies of the fundamental nature of hydration (solvation by water) of simple PGM complexes have appeared in the past two decades, (Lienke *et al.*, 2001; Naidoo *et al.*, 2002; Truflandier and Autschbach, 2010; Matthews, Venter and Naidoo, 2011) notably of the square-planar Pt and Pd complexes, (Beret *et al.*, 2008; Bowron *et al.*, 2012; Aono, Mori and Sakaki, 2016) considering the important biological activity of such compounds. (Fu and Tian, 2010; Truflandier, Sutter and Autschbach, 2011; Melchior *et al.*, 2015) Naidoo and co-workers (Lienke *et al.*, 2001; Naidoo *et al.*, 2002, 2003; Matthews, Venter and Naidoo, 2011) have developed classical force field models for the square-planar $[PtCl_4]^{2-}$ and octahedral $[PtCl_6]^{2-}$ (as well as $[PdCl_4]^{2-}$ and $[RhCl_6]^{3-}$) anionic Pt complexes, with the specific aim of investigating the hydration shell structures of these anions and their dynamic characteristics (e.g. translational and rotational diffusion) by MD computer simulation. Few detailed computational studies of the solvation of $[PtCl_6]^{2-}$ in solvents *other* than water have been reported, apart from pure methanol, (Naidoo *et al.*, 2003) and none in liquid mixtures.

In the context of developing novel and highly efficient, industrially relevant separation schemes for PGMs, such as potential chromatographic or solid-phase extraction methods, (Schmuckler and Limoni-Relis, 1995; Bernardis, Grant and Sherrington, 2005) it is expected that a deeper understanding of the detailed nature of solvation of $[PtCl_6]^{2-}$ anions not only in water, but also in organic solvents and binary liquid mixtures, including water-immiscible organic phases, will be necessary. (Koch *et al.*, 2006)

The significant, non-linear variations of in the ^{195}Pt NMR chemical shift, $\delta(^{195}Pt)$, of the octahedral $[PtCl_6]^{2-}$ complex in aqueous mixtures of methanol or 1,2-dimethoxyethane (DME), are plotted as a function of the mole fraction (x_A) of the organic component in **Figure 3.1**. (Westra, 2005)

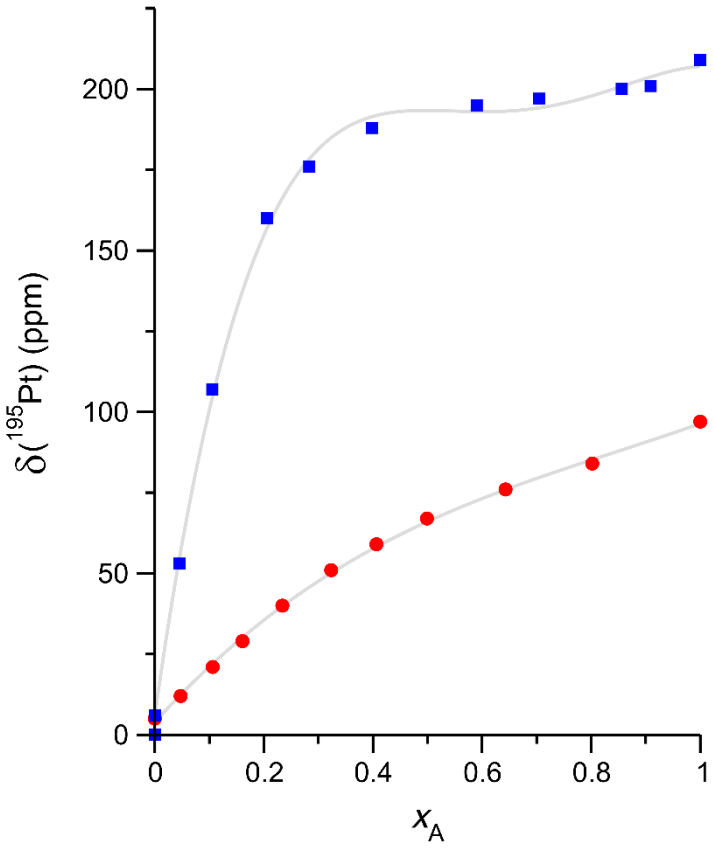

Figure 3.1 Experimental ^{195}Pt NMR (128 MHz, 303 K) chemical shifts, $\delta(^{195}Pt)$/ppm, of $[PtCl_6]^{2-}$ in solutions of $H_2PtCl_6 \cdot H_2O$ (~0.1 M) in binary mixtures of methanol (red circles) or 1,2-dimethoxyethane (DME, blue squares) with D_2O; grey solid curved lines are polynomial best fits intended as a guide to the eye. (Westra, 2005)

These $\delta(^{195}Pt)$ variation trends have been tentatively interpreted as suggesting preferential solvation of $[PtCl_6]^{2-}$ by the organic component, (Westra, 2005) a notion based on the well-established interpretation of preferential solvation of cations in binary liquid mixtures. (Burgess, 1978; Harris and Mann, 1978) To elucidate the origin of the pronounced non-linearity of the $\delta(^{195}Pt)$ variations in these mixtures, and those involving DME in particular, for which the trend which effectively plateaus at high x_{DME}, classical MD computer simulations employing a previously-developed $[PtCl_6]^{2-}$ force field (Matthews, Venter and Naidoo, 2011) were performed at selected water-methanol (as reference) and water-DME mixture compositions. The results of these simulations indicate that more subtle effects are at play: spatial micro-heterogeneity characterising the water-DME mixtures, particularly at higher x_{DBE}, are found to be important in this case. It follows that the traditional notion of preferential ion solvation, as implied from studies of monatomic cations in particular, (Burgess, 1978; Harris and Mann, 1978) may not necessarily be applicable to the polyatomic $[PtCl_6]^{2-}$ anions in water-DME and related solvent mixtures.

3.2 Computational details

3.2.1 Force field

The revised metal solution force field ("MSFF"), developed by Naidoo and co-workers, (Matthews, Venter and Naidoo, 2011) was used to model the $[PtCl_6]^{2-}$ complex. The classical hydronium (H_3O^+) model of Sagnella and Voth (Sagnella and Voth, 1996) was adopted, with the TIP3P water model (Jorgensen *et al.*, 1983) (CHARMM type) and CHARMM General force field (CGenFF) for methanol. (Vanommeslaeghe *et al.*, 2010; Lin, He and MacKerell, 2013) The specifically-developed CHARMM ether force field was used to model DME. (Vorobyov *et al.*, 2007; Lee *et al.*, 2008) The original full ionic charges of $[PtCl_6]^{2-}$ and H_3O^+ were scaled according to the "Molecular Dynamics in Electronic Continuum" (MDEC) model proposed by Leontyev and Stuchebrukhov. (Leontyev and Stuchebrukhov, 2009, 2010, 2011) This scaling procedure, also known as the "Electronic Continuum Correction" (ECC), accounts approximately for the effect of electronic dielectric screening of ionic charges in classical MD simulations of condensed phases including liquid solutions. The full ionic charges are multiplied by $1/\sqrt{\varepsilon_{el}}$, where ε_{el} is the high-frequency (optical) dielectric constant of the medium: 1.78 for pure water and ~2 for many organic media. (Leontyev and Stuchebrukhov, 2010) The model is strictly applicable to systems having uniform electronic polarization properties ("electronically uniform"), although the approach has been shown to be successful for simulations involving ions in the presence of immiscible liquid phases, such as water-oil interfacial preferences

of halide ions, as studied by Jungwirth and co-workers. (Vazdar *et al.*, 2012) In these interfacial studies, the ionic charges scaled using the ε_{el} value of pure water gave good results. Accordingly, in the present work, all ionic charges were similarly scaled using $\varepsilon_{el} = 1.78$, resulting in a reduction of the charge of the hydronium ion from +1 to +0.75, and that of $[PtCl_6]^{2-}$ from −2 to −1.5. For comparison, a set of simulations were also performed for solutions in water−DME mixtures using the original full ionic charges.

3.2.2 MD simulations

All MD simulations were performed, processed and analysed using the GROMACS software package (ver. 5.0.5), (Van Der Spoel *et al.*, 2005; Pronk *et al.*, 2013) with simulation parameters recommended for use of the CHARMM force field in GROMACS. (Bjelkmar *et al.*, 2010; Lee *et al.*, 2016) Simulated systems consisted of approximately 1000−7000 solvent molecules, depending on the particular mixed solvent composition, in cubic simulation cells with edge lengths of *ca.* 50-60 Å. Mixed solvent configurations were generated using the "gmx insert-molecules" routine of GROMACS. These starting configurations were equilibrated using a mixed minimization and MD simulation procedure similar to that described below in detail for the *solution* systems. Following a steepest-descent energy minimization step, NPT simulations (303 K, 0.1 MPa target temperature and pressure) were performed under periodic boundary conditions, using a leap-frog integrator (2 fs simulation time step). All bonds involving hydrogen were constrained to specified equilibrium distances using LINCS (Hess *et al.*, 1997) (or SETTLE (Miyamoto and Kollman, 1992) for water), and configurations were saved every 1 ps. Other simulation settings are summarised in **Table 3.1**.

Table 3.1. Selected simulation settings for solvent mixtures (GROMACS 5.0.5)[a]

Simulation parameter	Equilibration stage	Production stage
Total simulation time (ns)	2	40
Temperature coupling method	Berendsen [b]	Nosé-Hoover [c]
Temperature coupl. time constant (ps)	0.1	1.0
Pressure coupling method	Berendsen [b]	Parrinello-Rahman [d]
Pressure coupl. time constant (ps)	0.5	5.0
LJ interaction cut-off scheme	Force-switch	Force-switch
LJ switching range (Å)	10-12	10-12
Long-range electrostatic treatment	PME [e]	PME
Short-range Coulomb cut-off (Å)	12	12

[a] (Van Der Spoel *et al.*, 2005; Pronk *et al.*, 2013); [b] (Berendsen *et al.*, 1984); [c] (Nosé, 1984; Hoover, 1985); [d] (Parrinello and Rahman, 1981); [e] (Darden, York and Pedersen, 1993; Essmann *et al.*, 1995).

Solution configurations containing 12 $[PtCl_6]^{2-}$ complex anion and 24 H_3O^+ cation units were generated by randomly substituting solvent molecules in equilibrated mixed solvent configurations; the resulting compositions approximately match the experimental salt concentration (0.1 M). Details of the simulated systems are reported in **Table 3.2**. The solution systems were simulated following a protocol similar to that described by Naidoo and co-workers. (Matthews, Venter and Naidoo, 2011) Following a steepest-descent energy minimization, MD simulations were performed using a leap-frog integrator (1 fs time step) with bonds involving hydrogen atoms constrained to specified equilibrium distances using LINCS/SETTLE, (Miyamoto and Kollman, 1992; Hess *et al.*, 1997) as described above. All simulations made use of periodic boundary conditions. Lennard-Jones (LJ) potentials were truncated using the recommended LJ force-switching method (Bjelkmar *et al.*, 2010; Lee *et al.*, 2016) between 14 and 16 Å; electrostatic interactions were cut off at 16 Å, with long-range electrostatic interactions treated using the Particle-Mesh Ewald method (PME, 1 Å grid spacing). (Essmann *et al.*, 1995) System equilibration consisted of three consecutive MD simulation steps: (1) a 2 ns *NPT* ensemble MD simulation (303 K, 0.1 MPa) using the Berendsen temperature/pressure coupling (time constants τ_T = 0.1 ps, τ_P = 1 ps); (Berendsen *et al.*, 1984) (2) 2 ns in the *NPT* ensemble using the Nosé−Hoover temperature coupling (τ_T = 1 ps), (Nosé, 1984; Hoover, 1985) and Parrinello−Rahman pressure coupling (τ_P = 5 ps, with isothermal compressibility estimated for each specific solvent mixture); (Parrinello and Rahman, 1981) (3) 5 ns *NVT* ensemble MD simulation with the same Nosé−Hoover thermostat settings. Finally, 40 ns production simulations were similarly performed in the *NVT* ensemble (303 K), with trajectories stored every 1 ps.

Table 3.2. Simulated solution details, with x_A the mole fraction co-solvent, N_A and N_w the total numbers of co-solvent and water molecules, and the system size (cubic simulation cell edge length). All systems contained 12 $[PtCl_6]^{2-}$ and 24 H_3O^+ model units.

Co-solvent (A)	x_A	N_A	N_w	Size (Å)
None	0.0	0	6783	58.8907
Methanol	0.2	1103	4414	59.2865
	0.5	2040	2040	58.7277
	0.8	2701	675	59.2448
	1.0	2843	0	58.9232
DME	0.2	682	2889	59.0370
	0.5	940	940	57.8544
	0.8	1085	279	58.5949
	1.0	1178	0	59.5451

3.3 Liquid mixture structure

The liquid structures of the water-methanol and water-DME mixtures considered in the present work have been studied before in some detail, both experimentally (Bedrov *et al.*, 2000; Nickolov, Goutev and Matsuura, 2001; Douhéret *et al.*, 2004; Das Mahanta *et al.*, 2016) and by computer simulation, (Bedrov, Borodin and Smith, 1998; Bedrov, Pekny and Smith, 1998; Hezaveh *et al.*, 2011; Gujt *et al.*, 2017) These mixtures have been found to be characterised by water self-association, resulting in *micro-heterogeneous* liquid structures. The tendency of water molecules to self-associate appears to be more pronounced in the DME mixtures. In a preliminary attempt to compare the degree of structural micro-heterogeneity in these liquid mixtures, two additional simulations were performed, each system containing 500 water molecules and an appropriate number of co-solvent molecules (1500 methanol; 570 DME) so as to ensure that the simulated system volumes were comparable; i.e. structural micro-heterogeneity was evaluated (in view of the size difference between methanol and DME) by comparing the extent to which water molecules self-associate in a given binary liquid mixture volume. The representative simulation configurations in **Figure 3.2** clearly show larger water clusters in the DME mixture, which is confirmed by a radical Voronoi tessellation-based (VP) domain analysis using the TRAVIS simulation trajectory analysis software package; (Brehm and Kirchner, 2011; Brehm *et al.*, 2015) only water oxygen atoms were considered in this analysis, results of which are reported in **Figure 3.3**.

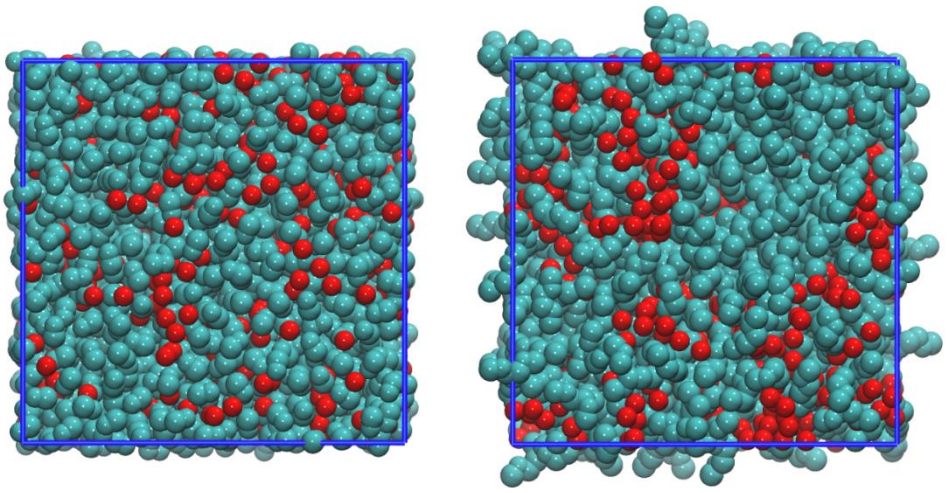

Figure 3.2 Final MD simulation configurations of water-methanol (left) and water-DME (right) mixtures, showing only water molecule oxygen atoms (red spheres) and co-solvent in cyan (all hydrogen atoms omitted in the interest of clarity). Both simulated systems contain 500 water molecules (with 1500 methanol and 570 DME molecules, respectively), and were simulated under *NVT* conditions at 303 K.

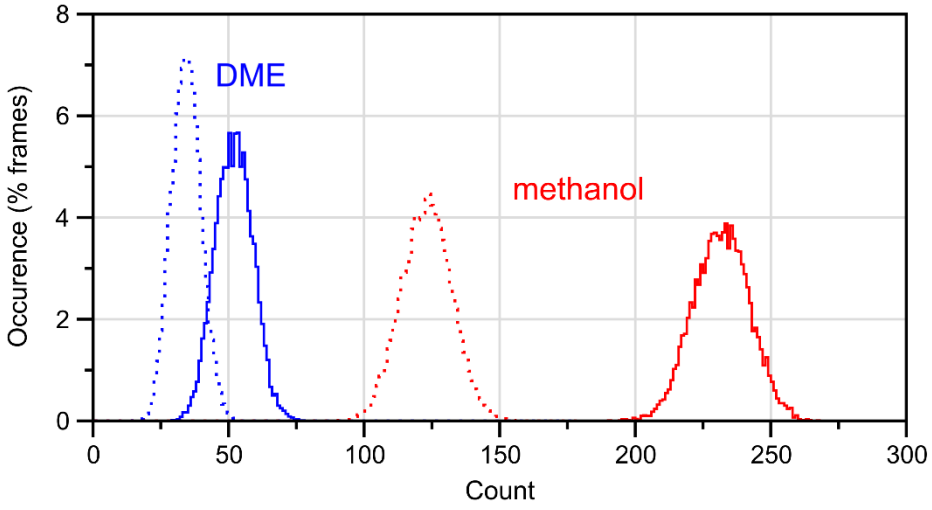

Figure 3.3. Voronoi tessellation-based (VP) water oxygen atom domain count distributions in simulated water-methanol (red dotted line) and water-DME (blue dotted line) mixtures. (Brehm and Kirchner, 2011; Brehm *et al.*, 2015) Shown in solid line are corresponding cluster analysis results (based on a water O-O distance criterion, $r_{OO} \leq 3.5$ Å) for the same simulated systems (10,000 configurations each). (Pronk *et al.*, 2013)

This VP domain analysis provides as standard output, among other quantities, the number of pre-defined VP domains (in this case composed of water O atoms) in histogram format (i.e. the total domain number distribution over all configurations sampled). This number includes "isolated" water oxygen atoms, i.e. domain size = 1. At any rate, it is clear from **Figure 3.3** that the average number of isolated water oxygen domains, to be identified with water clusters (approximately), in the methanol mixture is more than twice that in the DME-water mixture, indicative of a larger number of small clusters/isolated water molecules.

For comparison, a simplistic water oxygen cluster analysis, using a single $r_{OO} \leq 3.5$ Å distance criterion, was performed using the "gmx clustsize" algorithm included in the GROMACS 5.0.5 software package. (Pronk *et al.*, 2013) The resulting water cluster count histogram data plotted in **Figure 3.3**, while different from the VP-results (see below), confirm a significantly higher count in the methanol mixture; the average water cluster *sizes* $\langle n_c \rangle$ obtained by this procedure are as follows: water-methanol mixture, 3.7; water-DME mixture, 17.9. The VP and distance criterion-based data in **Figure 3.3** are clearly different, though this is not unexpected, since the methods are fundamentally different: VP analysis of liquid water configurations typically results in apparently high neighbour counts, (Shih, Sheu and Mou, 1994) but includes more distant water molecules (sharing small VP faces; in principle, neighbours could be "filtered" based on the shared VP face size).

The liquid structures of the simulated water-methanol and -DME binary mixture may be further characterised by computing appropriate pair distribution functions, e.g. RDFs which may be integrated in order to estimate the number of H-bonded neighbours etc. As such functions have been reported previously for both water-methanol [see, e.g. (Laaksonen, Kusalik and Svishchev, 1997) and DME mixtures (Bedrov, Borodin and Smith, 1998; Hezaveh *et al.*, 2011; Gujt *et al.*, 2017; Engelbrecht *et al.*, 2018), these will not be reported or discussed here; the interested reader is referred to the above-cited literature.

3.4 Preferential solvation

3.4.1 General considerations

The experimental $\delta(^{195}Pt)$ of $[PtCl_6]^{2-}$ dissolved in selected binary aqueous mixtures plotted in Figure 3.1 exhibit different degrees of non-linear variation as a function of the bulk mixture composition, expressed as the mole fraction organic solvent, x_A. Similar deviations from linearity of the NMR chemical shift variations of other solutes, notably monatomic metal cations, in binary liquid mixtures (i.e. from a straight line connecting their limiting δ values in the respective pure solvents) are traditionally interpreted as indicative of *preferential solvation* of the solute by one of the liquid mixture components. (Frankel, Langford and Stengle, 1970; Ben-Naim, 1990; Marcus, 1990) The preferential solvation of a solute in a binary solvent mixture may be defined as a condition in which the molecular composition of its local solution environment, specifically its primary, or "contact" solvation shell, differs from that characterising the bulk binary solvent mixture, as opposed to the "ideal" behaviour, in which the local composition is identical to that of the bulk mixture. (Marcus, 1985; Ben-Naim, 1990) The latter situation is expected, provided certain simplifying approximations, to result in a linear variation of the solute chemical shift as a function of bulk mixed solvent composition, expressed as a mole fraction, $x_A = N_A/(N_A + N_B)$, where N_A and N_B are the total number of solvent molecules A and B, respectively. (Ben-Naim, 1990) Within this model, the significant curvature of both experimental $\delta(^{195}Pt)$ trends as a function of the solvent composition shown in **Figure 3.1** suggests $[PtCl_6]^{2-}$ to be preferentially solvated by the organic solvent component in these aqueous mixtures.

Preferential solvation phenomena are often evaluated experimentally with reference to the "equi-solvation point" (or "iso-solvation point"), a concept defined by Frankel *et al.* (Frankel, Stengle and Langford, 1965) as that bulk binary mixture composition at which the NMR chemical shift of the solute lies exactly midway between the respective limiting chemical shift values in the pure solvents. At this equi-solvation point, both mixed solvent components are considered to participate equally in forming the solvation shell of the solute (on average), assuming short solvation shell residence times on the NMR time scale. The derivation of the equi-solvation point for $[PtCl_6]^{2-}$ in water-methanol mixtures, based on its $\delta(^{195}Pt)$ data and the methodology of Dechter and Zink, (Dechter and Zink, 1975) is shown in **Figure 3.4**. The equi-solvation points of the complex in the remaining binary mixtures, derived by this procedure, are reported in **Table 3.3**. The $[PtCl_6]^{2-}$ equi-solvation point occurs at $x_A < 0.5$ for both mixtures studied, suggesting preferential solvation of the complex by the

organic component. In fact, the equi-solvation point in water-DME mixtures occurs at only x_{DME} = 0.11, with $\delta(^{195}Pt)$ effectively levelling-off above $x_{DME} \approx 0.38$ (suggesting a constant local solution environment with increasing x_{DME} beyond this point), which, perhaps counter-intuitively, would suggest a pronounced preferential solvation of $[PtCl_6]^{2-}$ by DME, as opposed to water.

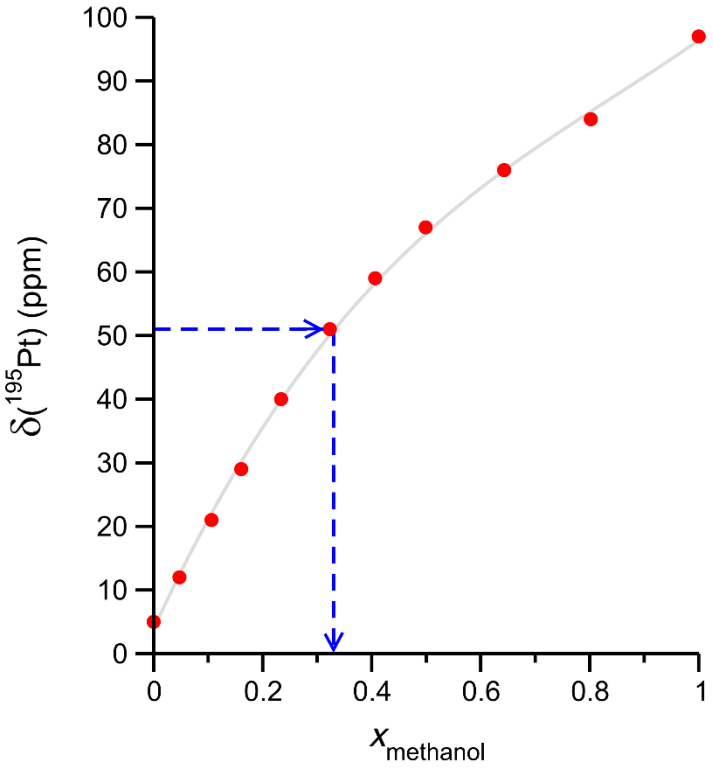

Figure 3.4 Estimation of equi-solvation point of $[PtCl_6]^{2-}$ in aqueous methanol solutions: experimental $\delta(^{195}Pt)$ data in red, with best-fit polynomial in grey solid line. The equi-solvation point is estimated by moving horizontally from exactly half the limiting $\delta(^{195}Pt)$ in pure methanol, and then vertically down from the intercept with the experimental data/fit to read the equi-solvation point-abscissa ($x_{methanol}$). Experimental $\delta(^{195}Pt)$ were taken from (Westra, 2005)

Table 3.3. Equi-solvation points, and their corresponding ^{195}Pt NMR chemical shifts ($\delta(^{195}Pt)$, 128 MHz, 303 K) for $[PtCl_6]^{2-}$ in solutions of $H_2PtCl_6 \cdot H_2O$ (~0.1 M) in binary mixtures of D_2O and co-solvents methanol and 1,2-dimethoxyethane (DME)

Co-solvent (A)	**$\delta(^{195}Pt)$ (ppm) at equi-solvation point**	**Equi-solvation point composition (x_A)**
Methanol	51	0.33
DME	108	0.11

No further information about the detailed solvation shell structures and the actual solvation numbers can be inferred from these $\delta(^{195}Pt)$ data; in principle, $\delta(^{195}Pt)$ may be computed (though this is not a straightforward task in general, considering substantial relativistic effects and the need to consider many solvation configurations), (Sterzel and Autschbach, 2006) provided, in addition to the availability of substantial computational resources/time, that a representative sample of solvation shell configurations can be identified, typically obtainable by computer simulation. (Bühl *et al.*, 2005; Lindgren, Laaksonen and Westlund, 2009; Truflandier and Autschbach, 2010; Aidas *et al.*, 2013) Moreover, these aqueous mixtures, and those involving DME in particular, are known to be highly non-ideal, exhibiting varying degrees of molecular self-association, or micro-heterogeneity under conditions similar to those considered in the present work. (Bedrov *et al.*, 2000; Nickolov, Goutev and Matsuura, 2001; Dixit *et al.*, 2002; Dougan *et al.*, 2004; Douhéret *et al.*, 2004; Gubskaya and Kusalik, 2004; Corsaro *et al.*, 2008; Joshi and Kumbharkhane, 2011; Zhang *et al.*, 2013) Indeed, the inherent micro-heterogeneity of binary aqueous mixtures are thought to have potentially important implications in the context of preferential solvation phenomena, notably for anionic solutes. (Hawlicka and Swiatla-Wojcik, 1998; Saielli *et al.*, 2005; Bragg, Kanu and Schwartz, 2011)

3.4.2 Simulation configurations

Selected simulation snapshots of solutions in water-methanol and water-DME binary mixtures are shown in **Figure 3.5** & **Figure 3.6**, respectively. In these figures, the system volumes occupied by the two solvent components (water and organic co-solvent) are represented by two separate, non-intersecting surface representations; (Humphrey, Dalke and Schulten, 1996) also shown are similar renderings of corresponding solvent mixture configurations (i.e. in the absence of the solute) to allow for visual comparison of solvent component distributions. Considering first the water-methanol solution configurations in **Figure 3.5**, it may be noted that the distribution of water and methanol molecules appears to be essentially similar to that of the corresponding simulated mixtures in the absence of the solute, i.e. characterised by clustering of water molecules. The $[PtCl_6]^{2-}$ complex may be seen to interact with both water and methanol, with water molecules in the contact shell often forming part of H-bonded water clusters.

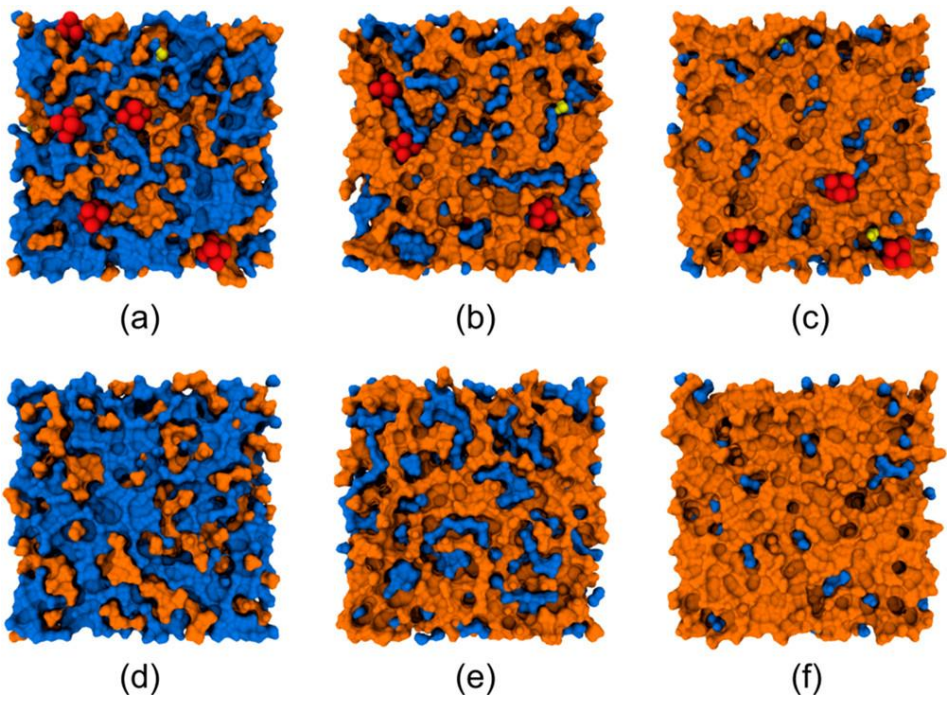

Figure 3.5 Final MD simulation configuration representations (15 Å-think "slices") of $(H_3O)_2[PtCl_6]$ in water-methanol mixtures: $x_{methanol}$ = (a) 0.2, (b) 0.5, and (c) 0.8. Water and methanol molecules are represented by blue and orange surfaces, respectively. The solute is shown in space-filling representation ("van der Waals"), with $[PtCl_6]^{2-}$ red and H_3O^+ yellow. Shown in panels (d)-(f) are corresponding representation of solvent mixture simulation configurations (no solute). All images produced using VMD. (Humphrey, Dalke and Schulten, 1996) Reproduced with permission from (Engelbrecht *et al.*, 2018). Copyright 2018 American Chemical Society.

In the water-DME solution configurations, **Figure 3.6**, where larger H-bonded water clusters are evident, $[PtCl_6]^{2-}$ complexes also interact with both solvents, but in such a way that the complex tends to localise at the edges, or borders, of water clusters. Bragg *et al.*, (Bragg, Kanu and Schwartz, 2011) in their MD simulations of water-tetrahydrofuran (THF) mixtures, reported that iodide anions (I^-) are similarly located at the edges of small water clusters, or "pools", which are a characteristic structural feature of these water-THF mixtures; this solvation behaviour was noted to be related to the preferential localisation of I^- at air-water interfaces in previous computer simulations. (Jungwirth and Tobias, 2006)

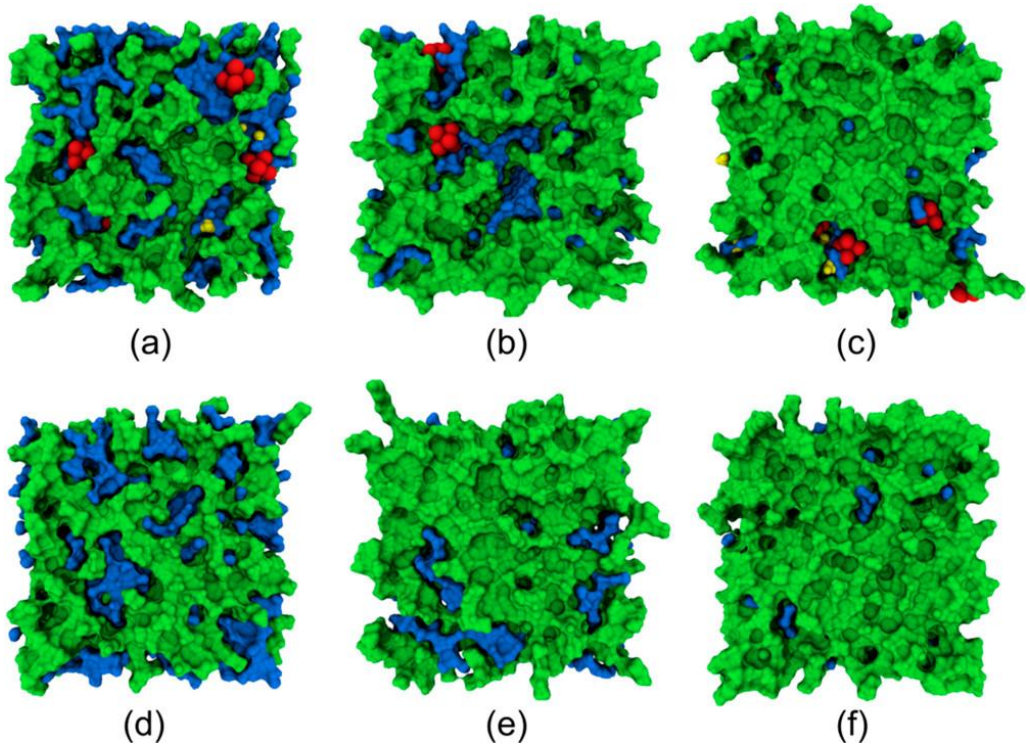

Figure 3.6 Final MD simulation configuration representations (15 Å-think "slices") of $(H_3O)_2[PtCl_6]$ in water-DME mixtures: x_{DME} = (a) 0.2, (b) 0.5, and (c) 0.8. Water and DME molecules are represented by blue and green surfaces, respectively. The solute is shown in space-filling representation ("van der Waals"), with $[PtCl_6]^{2-}$ red and H_3O^+ yellow. Shown in panels (d)-(f) are corresponding representation of solvent mixture simulation configurations (no solute). All images produced using VMD. (Humphrey, Dalke and Schulten, 1996) Reproduced with permission from (Engelbrecht *et al.*, 2018). Copyright 2018 American Chemical Society.

3.4.3 RDFs

Previous MD simulation studies of the hydration of the chloro-complex anions of Pt, Pd, Rh, and Ir in pure water, have made extensive use of metal-water oxygen (O_w) RDFs to obtain information about the nature of hydration, and to estimate the average numbers of interacting water molecules, or "hydration numbers", of these complexes. (Lienke *et al.*, 2001; Naidoo *et al.*, 2002; Truflandier and Autschbach, 2010; Matthews, Venter and Naidoo, 2011) The Pt-O_w RDFs for $[PtCl_6]^{2-}$ in all water-methanol and water-DME mixtures simulated are plotted in **Figure 3.7 (a)** & **Figure 3.8 (a)**, respectively. In pure water, the first Pt-O_w peak occurs at r = 4.55 Å, followed by a second peak (second shell) at ~5.4 Å. (Truflandier and Autschbach, 2010; Matthews, Venter and Naidoo, 2011) In the solvent mixtures, the Pt-O_w RDF second maximum moves closer (shorter r_{PtO}), partially merging with the more intense first maximum, the position of which remains essentially constant with changing solvent composition. Naidoo and co-workers (Matthews, Venter and Naidoo, 2011) reported apparently similar, convoluted/partially-"merged" metal-O_w RDFs for the more highly-charged, but structurally similar, $[RhCl_6]^{3-}$ and $[IrCl_6]^{3-}$ complexes in water; these merged first/second RDF peak structures were explained as due to tighter, more compact second hydration shells compared to that of $[PtCl_6]^{2-}$. In view of this explanation, it would follow that the water clustering observed in these liquid mixtures, and the resulting localisation of $[PtCl_6]^{2-}$ at the borders of such clusters (**Figure 3.5** & **Figure 3.6**), leads to a more compact second hydration shell of the complex as compared to that in pure water. Naturally, Cl-O_w (or Cl-H_w, the water hydrogen) RDFs can also be computed, however these have been shown to provide essentially similar information on simulated $[PtCl_6]^{2-}$ - water interactions. (Naidoo *et al.*, 2002; Matthews, Venter and Naidoo, 2011)

The solvation of $[PtCl_6]^{2-}$ by methanol may be similarly evaluated by computing Pt-O_m (methanol oxygen) RDFs, plotted in **Figure 3.7 (b)**. The Pt-O_m RDF in the pure methanol solution shows a well-defined first peak at r = 4.70 Å; this first maximum decreases in intensity and moves gradually to shorter distances with decreasing methanol content (r_{max} = 4.66 Å at $x_{methanol}$ = 0.2), while the broader, apparently convoluted second peak intensity increases, also moving closer. The Pt-O_m RDF first minimum (separating these two peaks), also shifts gradually to shorter r_{PtO}; this point and its implications will be discussed in some detail below. Key RDF parameters are collected in **Table 3.4**.

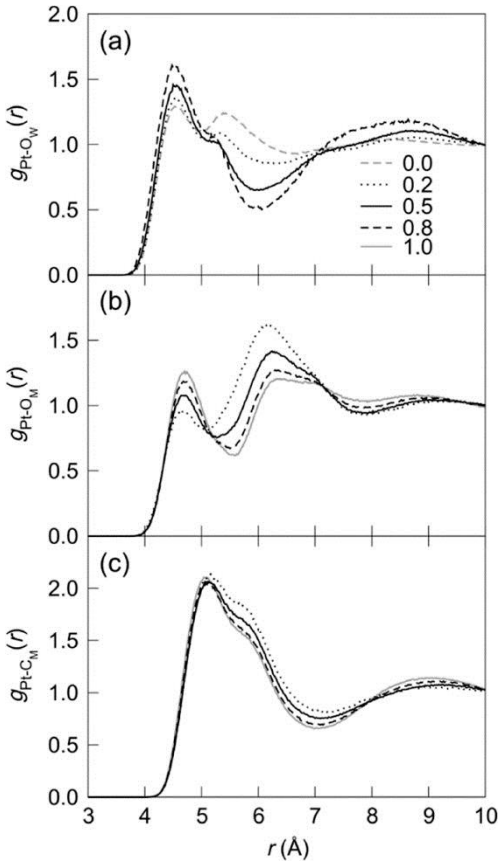

Figure 3.7 (a) Pt−O_w, **(b)** Pt−methanol oxygen (O_m), and **(c)** carbon (C_m) RDFs, $g(r)$, from MD simulations of $(H_3O)_2[PtCl_6]$ in water-methanol mixtures. Legend indicates the mixed solvent composition as mole fraction of methanol, $x_{methanol}$. Reproduced with permission from (Engelbrecht *et al.*, 2018). Copyright 2018 American Chemical Society.

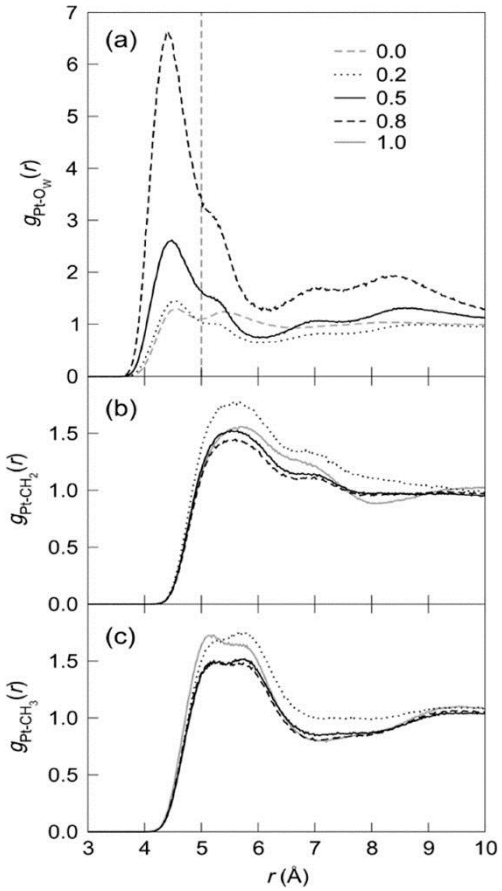

Figure 3.8 RDFs, $g(r)$, from MD simulations of $(H_3O)_2[PtCl_6]$ in water-DME mixtures for pairs Pt-water oxygen (O_w) **(a)**, DME methylene (CH_2) **(b)**, and methyl (CH_3) **(c)** carbon atoms. Legend indicates the mixed solvent composition as mole fraction DME, x_{DME}. Vertical grey dashed line in panel (a) indicates Pt-O_w RDF integration range, as discussed in the text. Reproduced with permission from (Engelbrecht *et al.*, 2018). Copyright 2018 American Chemical Society.

Table 3.4. Pt-*X* RDF key parameters and derived data for simulated water-methanol solutions.

RDF parameter	Mole fraction methanol, $x_{methanol}$				
	0.0	**0.2**	**0.5**	**0.8**	**1.0**
Pt-O_w					
r_{max} (Å)	4.55	4.55	4.55	4.52	–
r_{min} (Å)	5.0	5.1	6.0	6.0	–
n_{PtO} (r = 5.0 Å)	8.8	5.8	2.9	1.1	–
n_{PtO} (r = 6.0 Å)	23.5	13.8	6.2	2.0	–
Pt-O_m					
r_{max} (Å)	–	4.66	4.69	4.70	4.70
r_{min} (Å)	–	5.1	5.3	5.5	5.6
n_{PtO} ($r = r_{min}$)	–	1.2	2.7	4.4	5.3
n_{PtO} (r = 6.0 Å)	–	2.7	5.5	7.9	7.2
Pt-C_m					
r_{max} (Å)	–	5.16	5.12	5.10	5.06
r_{min} (Å)	–	7.2	7.1	7.1	7.0
n_{PtC} (r = 5.5 Å)	–	2.9	5.4	7.0	7.9
n_{PtC} (r = 6.0 Å)	–	4.9	8.9	11.2	12.5

Interestingly, methanol molecules are found to adopt different relative orientations in the $[PtCl_6]^{2-}$ solvation shell region, as shown in the representative simulation configuration in **Figure 3.9**. In addition to the expected interaction mode in which methanol hydroxyl (-OH) group dipoles are directed towards the anionic complex (i.e. O-H … Pt effectively linear), with methyl ($-CH_3$) groups pointing outwards (orientation 1), two further general orientations are found: (2) both -OH and $-CH_3$ of the methanol molecules within the solvation shell, i.e. -OH and $-CH_3$ approximately equidistant from Pt, and (3) only $-CH_3$ in solvation shell, with -OH directed outwards. The latter interaction modes (orientations 2 and 3), are evaluated by Pt-C_m (methanol carbon) RDFs, plotted in **Figure 3.7 (c)**. These functions, with their first maxima occurring at *ca.* 5 Å, are curiously invariant with increasing methanol content and all show a characteristic "shoulder" on their more distant slope (~5.8 Å). It may be noted that, while Naidoo and co-workers reported Pt-C_m SDFs for $[PtCl_6]^{2-}$ in pure methanol, (Naidoo *et al.*, 2003) no RDFs for such pairs, nor for any other organic solvents, have been reported for comparison.

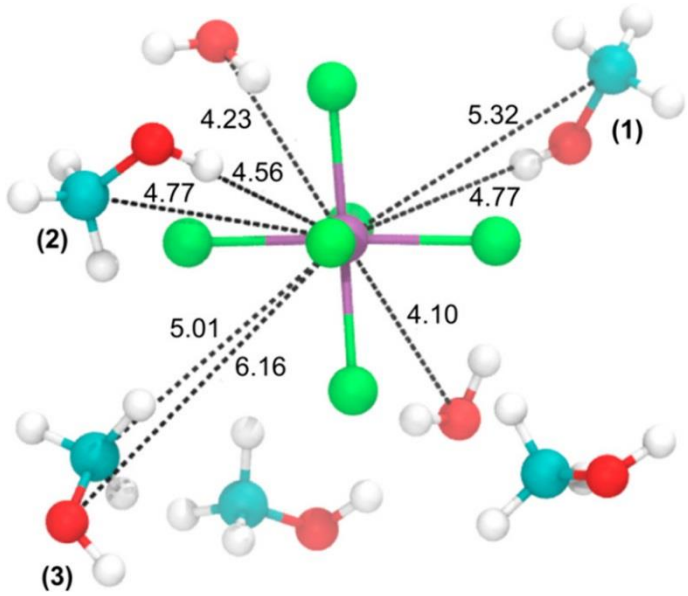

Figure 3.9 Representative solvation shell arrangement of [PtCl6]2− in a simulated water-methanol mixture ($x_{methanol}$ = 0.5). Colouring scheme: C in cyan, O red, Pt violet, Cl green. Water molecules with oxygen atoms within 5.0 Å, and methanol molecules with O atoms within 5.3 Å and/or C within 5.5 Å of the Pt centre (violet) are shown. Selected typical Pt−O and Pt−C distances (in Å) are given as indicated by the black-labelled, dotted lines. Methanol molecules labelled (1-3) are discussed in the main text. Reproduced with permission from (Engelbrecht *et al.*, 2018). Copyright 2018 American Chemical Society.

Table 3.5. Pt-*X* RDF key parameters and derived data for simulated water-DME solutions

RDF parameter	Mole fraction DME, x_{DME}				
	0.0	**0.2**	**0.5**	**0.8**	**1.0**
Pt-O_w					
r_{max} (Å)	4.55	4.53	4.45	4.42	–
r_{min} (Å)	5.0	6.1	6.1	6.2	–
n_{PtO} (r = 5.0 Å)	8.8	4.2	2.6	1.8	–
n_{PtO} (r = 6.0 Å)	23.5	8.6	4.8	3.0	–
Pt-CH_2					
r_{max} (Å)	–	5.60	5.56	5.56	5.70
r_{min} (Å)	–	6.7	6.7	6.7	6.7
n_{PtC} (r = 5.5 Å)	–	2.6	3.4	3.5	3.8
n_{PtC} (r = 6.0 Å)	–	5.0	6.4	6.7	7.3
Pt-CH_3					
r_{max} (Å)	–	5.25 (5.78)	5.20 (5.73)	5.20 (5.72)	5.17 (5.73)
r_{min} (Å)	–	5.7	5.5	5.5	5.5
n_{PtC} (r = 5.5 Å)	–	2.8	3.8	4.2	5.1
n_{PtC} (r = 6.0 Å)	–	5.2	6.8	7.5	8.8

The interactions between $[PtCl_6]^{2-}$ and DME are characterised by two sets of Pt-C RDFs, (1) Pt-CH_2 (DME methylene carbon), and (2) Pt-CH_3 (DME methyl carbon), shown in **Figure 3.8 (b)** and **(c)**, respectively. The Pt-C RDFs in pure DME are characterised by broad first peaks in the range r_{PtC} = 5-6 Å, with that of the methyl carbons (Pt-CH_3) showing a distinct indentation (*ca.* 5.5 Å), with closest maximum at ~5.2 Å. This indented Pt-CH_3 first peak shape essentially persists in the DME-water mixtures, though subtle changes in the relative peak heights may be noted. The broad Pt-C_{DME} RDF first maxima, occurring at greater distances than those of Pt-$O_{w/m}$ RDFs, in pure DME and its mixtures are consistent with the lower partial atomic chargers (and consequently weaker electrostatic attraction; e.g. the hydroxyl H partial charges of the TIP3P water model are +0.417 e each, while those of the DME model methylene and methyl group H atoms are only +0.09 e each), and the larger steric bulk of these aliphatic groups. Indeed, inspection of simulated $[PtCl_6]^{2-}$ solvation shell configurations in water-DME mixtures, e.g. **Figure 3.10**, shows that DME molecules adopt various orientations and configurations in this region.

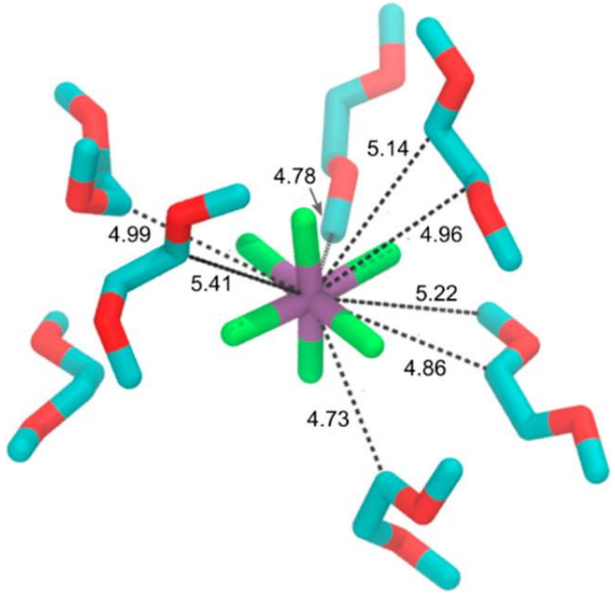

Figure 3.10. Representative conformations of DME molecules in the solvation shell of [PtCl6]2− in water-DME mixture (x_{DME} = 0.5), using a standard atom colouring scheme (C atoms in cyan, O red, Pt violet, Cl green). The "liquorice" representation, with hydrogen atoms omitted in the interest of clarity, shows that solvating DME molecules may adopt various conformations and orientations within this region. Pt−C distances (in Å) to carbon atoms within 5.5 Å of Pt are indicated using labelled dotted black lines. Reproduced with permission from (Engelbrecht *et al.*, 2018). Copyright 2018 American Chemical Society.

3.4.4 Coordination numbers

As described in Chapter 2, RDFs may be suitably integrated, typically their intense first peaks (i.e. up to first discernible minimum) in order to determine the number of directly interacting neighbouring particles (by some interaction type, e.g. H-bonding). The Pt-*X* RDFs in **Figure 3.7** & **Figure 3.8** present potential complications in this regard, as many exhibit complex, convoluted first peaks which complicates the choice of first-peak integration limit. Consider, for example, the Pt-O_w RDFs in **Figure 3.7 (a)** & **Figure 3.8 (a)**: while in pure water this functions has a well-defined first minimum at $r \approx 5.0$ Å, the second Pt-O_w peak increasingly merges with the more intense first peak in both methanol and DME mixtures, resulting in a "shoulder", or hump. These convoluted structures naturally pose a problem for defining the first hydration shell of the complex. Consequently, *two* integration limits (or radii) were considered for the Pt-O_w RDFs: (1) the first minimum in *pure* water, $r_{min}(1) = 5.0$ Å; (2) the first actual minimum in the liquid mixtures, $r_{min}(2) = 6.0$ Å. The results of this procedure are reported in **Table 3.4** & **Table 3.5** and plotted in **Figure 3.11** & **Figure 3.12**.

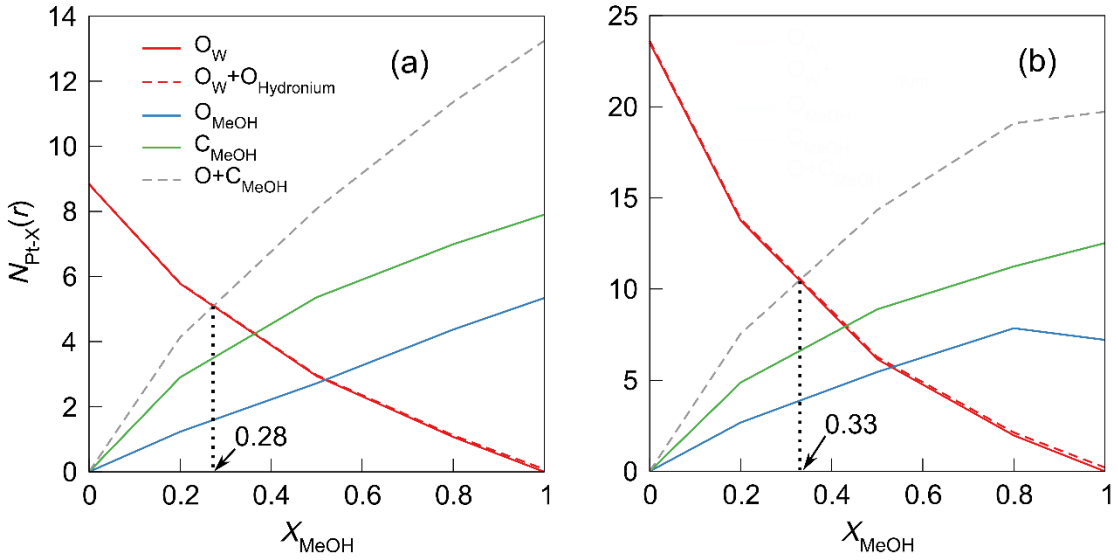

Figure 3.11 Pt−O_w (red), O_m (blue), and C_m (green) coordination numbers, $N(r)$, for $[PtCl_6]^{2-}$ in water-methanol mixtures (composition $x_{methanol}$), obtained by integration of appropriate RDFs with integration radii **(a)** $r_{min}(1) = 5.0$ Å (Pt−O_w), r_{min} (Pt−O_m), and 5.5 Å (Pt− C_m); **(b)** $r_{min}(2) = 6.0$. Dashed red and grey lines indicate respectively the *total* Pt−O_w (water and H_3O^+) and Pt−methanol (O_m + C_m) coordination numbers. The vertical black dotted lines indicate the positions of the total Pt−O_w and Pt−(O_m + C_m) coordination number intercepts, used for the estimation of the equi-solvation points. Adapted with permission from (Engelbrecht *et al.*, 2018). Copyright 2018 American Chemical Society.

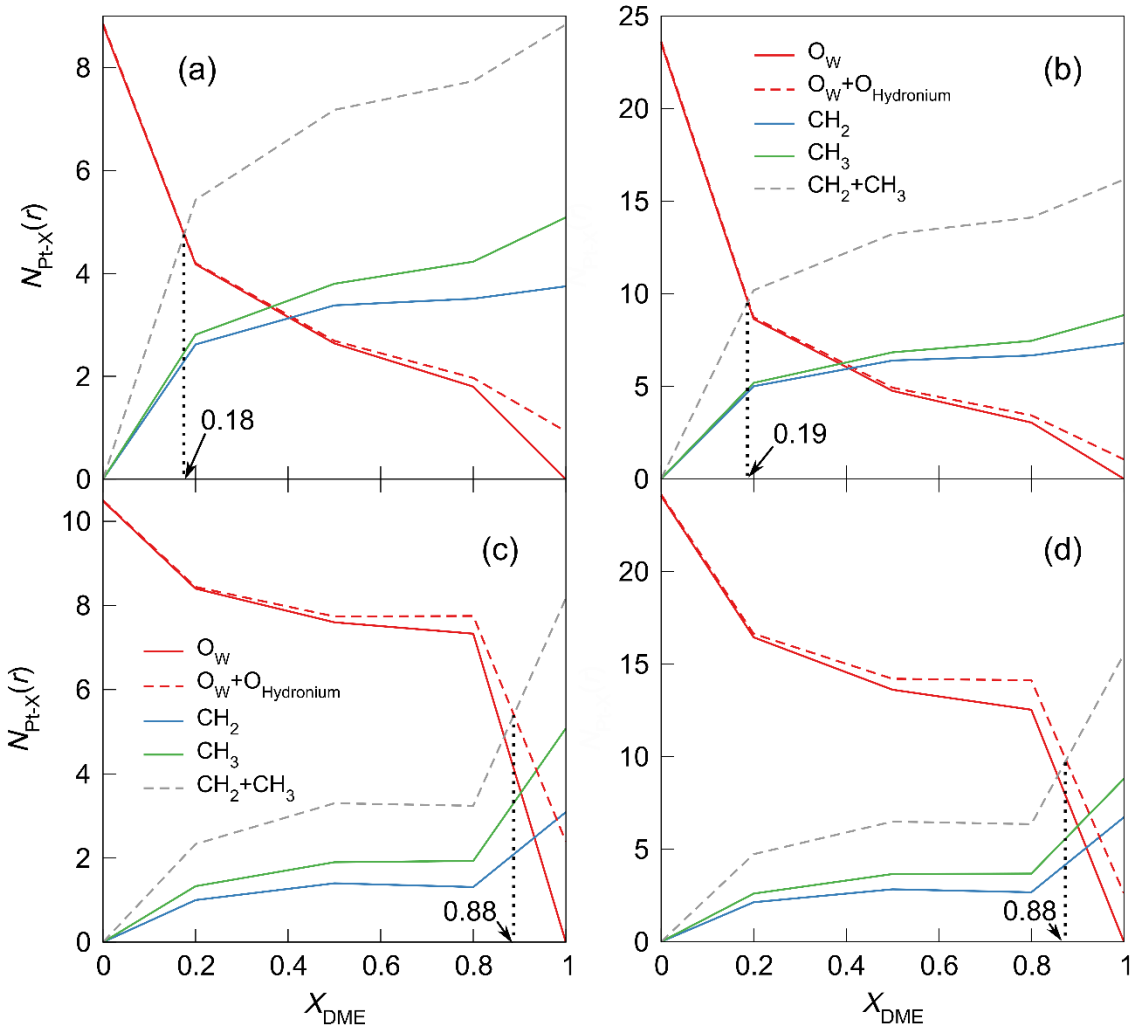

Figure 3.12. Pt−O_w (red), CH_2 (blue), and CH_3 (green) coordination numbers, $N(r)$, for $[PtCl_6]^{2-}$ in water-DME mixtures (composition x_{DME}), obtained by integration of appropriate RDFs with integration radii **(a)** $r_{min}(1)$ = 5.0 Å (Pt−O_w) and 5.5 Å (Pt− C); **(b)** $r_{min}(2)$ = 6.0. Dashed red and grey lines indicate respectively the total Pt−O_w (water and H_3O^+) and Pt−DME (CH_2 + CH_3) coordination numbers. The vertical black dotted lines indicate the positions of the total Pt−O_w and Pt−(CH_2 + CH_3) coordination number intercepts, used for the estimation of the equi-solvation points. Panels (c) and (d) show corresponding coordination numbers for simulations in which ions have *full ionic charges*, as discussed in Section 3.4.6. Adapted with permission from (Engelbrecht *et al.*, 2018). Copyright 2018 American Chemical Society.

The Pt-O_w coordination numbers, n_{PtOw}, obtained using Pt-O_w RDF integration limits $r_{min}(1)$ and (2) described above, while obviously different, show very similar variation trends as a function of mixed solvent composition, x_A. For the simulated water-methanol solutions (**Figure 3.11**), n_{PtOw} decreases gradually with increasing $x_{methanol}$, showing an apparent moderate downward curvature; for the water-DME solutions (**Figure 3.12**), on the other hand, n_{PtOw} decreases sharply between $x_{DME} = 0 - 0.2$, then

more gradually with increasing x_{DME} = 0.2 – 0.8. In fact, the simulated n_{PtOw} variations in **Figure 3.11** & **Figure 3.12** bear a striking, though "mirrored" (w.r.t. intensity), resemblance to the corresponding experimental $\delta(^{195}Pt)$ trends in **Figure 3.1**.

The evaluation of Pt-C coordination numbers (reflecting the participation of aliphatic groups -CH_2 and -CH_3 in the $[PtCl_6]^{2-}$ solvation shell) are similarly complicated by broad and convoluted first peaks for both methanol and DME systems. As noted in the preceding section, these features likely reflect the orientational variability and conformational flexibility of these weakly-interacting sites. For all Pt-C RDFs (i.e. both methanol and DME) a primary integration radius of $r_{int}(1)$ = 5.5 Å was chosen (position of the first peak indentation in Pt-CH_3 RDF in DME), with an alternative $r_{int}(2)$ = 6.0 Å taken for consistency with the $r_{min}(2)$ of the Pt-O_w RDFs described above. The resulting Pt-C coordination numbers are reported in **Table 3.4** & **Table 3.5**.

3.4.5 Equi-solvation points

The Pt-*X* coordination number variations in allow for estimation of the equi-solvation points of $[PtCl_6]^{2-}$ in the simulated water-methanol and water-DME solutions. Starting with the water-methanol solutions, the total Pt-O_w coordination number trend (n_{PtOw}, which includes an effectively negligible contribution from hydronium cations) may be seen in **Figure 3.11** to intercept the total Pt-methanol site trend (i.e. $n_{PtOm} + n_{PtCm}$) at a bulk composition $x_{methanol}$ = 0.28 (integration radii 1) or 0.33 (radii 2). These values are in excellent agreement with the experimental equi-solvation point of $x_{methanol}$ = 0.33. (Westra, 2005)

The above approach to estimating the equi-solvation point effectively identifies the total number of methanol sites (i.e. -OH and -CH_3) with the average number of methanol molecules participating to the $[PtCl_6]^{2-}$ solvation shell; as is evident in Fig. 10, this is not necessarily the case (since some methanol molecules are oriented such that *both* sites are located/counted in this region). It should be stressed that this apparent limitation is not restricted to the computational approach, but also applies to the experimental NMR chemical shift-based method (Dechter and Zink, 1975); as such, the equi-solvation point estimated from simulated coordination numbers may be said to reproduce that obtained from the corresponding experimental $\delta(^{195}Pt)$ trends, the techniques having similar limitations in how they relate to the actual equi-solvation point.

A similar procedure for the simulated water-DME mixtures (**Figure 3.12**) yields an equi-solvation point estimate of x_{DME} = 0.18 (both integration radii sets 1 & 2), again in good agreement with that

obtained from the experimental $\delta(^{195}Pt)$-based value, x_{DME} = 0.11, (Westra, 2005) considering the limited number of simulation data points. Finally, a note on the contribution of H_3O^+ counter-ions to the $[PtCl_6]^{2-}$ solvation shell, i.e. ion-pairing: (Naidoo *et al.*, 2003) a similar procedure based on Pt-H_3O^+ oxygen atom RDF integrations has revealed an effectively negligible contribution by this species. Only at high DME content, x_{DME} = 0.8 & 1.0, does H_3O^+ make an appreciable contribution to the Pt-O coordination number, and the inclusion of this contribution does not make a detectable difference to the estimated equi-solvation point in the simulated water-DME (or water-methanol) solutions. (Engelbrecht *et al.*, 2018)

3.4.6 Ionic charge scaling considerations

The ionic charge-scaling method (MDEC) employed in this study has been shown to account approximately for the important effect of electronic polarizability, specifically the electronic dielectric screening of ionic charges in condensed phases. (Leontyev and Stuchebrukhov, 2009, 2010, 2011) To date, very few studies of the solvation of inorganic polyatomic ions using the MDEC charge scaling method have been reported to our knowledge, and none for $[PtCl_6]^{2-}$. Pegado *et al.* (Pegado *et al.*, 2012), in their comparative MD simulation study of the hydration of the sulphate (SO_4^{2-}) anion, demonstrated that the MDEC model provides results comparable to those obtained with a fully polarizable shell model (charge-on-spring model), as well as to *ab initio* MD (AIMD) simulations.

In view of the limited use of the MDEC method for polyatomic ions, the series of simulations of $[PtCl_6]^{2-}$ in water-DME mixtures (including the respective pure solvents) were repeated using the original full ionic charges for $[PtCl_6]^{2-}$ and H_3O^+, which were previously successfully implemented for simulations of the respective ions in pure water. (Sagnella and Voth, 1996; Matthews, Venter and Naidoo, 2011) The Pt-O_w and Pt-C_{DME} coordination numbers, obtained by RDF integration are plotted in **Figure 3.12 (c)** & **(d)**. The coordination number variations shown there are clearly different from those obtained using scaled ionic charges, **Figure 3.12 (a)** & **(b)**, resulting in a $[PtCl_6]^{2-}$ equi-solvation point estimate of x_{DBE} = 0.88, significantly different from that obtained from the experimental $\delta(^{195}Pt)$ trend (0.11). (Westra, 2005) As shown in the representative simulation snapshots in **Figure 3.13**, the $[PtCl_6]^{2-}$ complex is strongly hydrated in the full ionic charge-simulations, and does not exhibit the interfacial solvation preference described in Section 3.4.2; in fact, extensive ion-pairing is observed, with large ionic aggregates forming at high x_{DME} (0.8, 1.0) (essentially precipitate formation), which is incompatible with the high experimental solubility. (Pluhařová, Mason and Jungwirth, 2013)

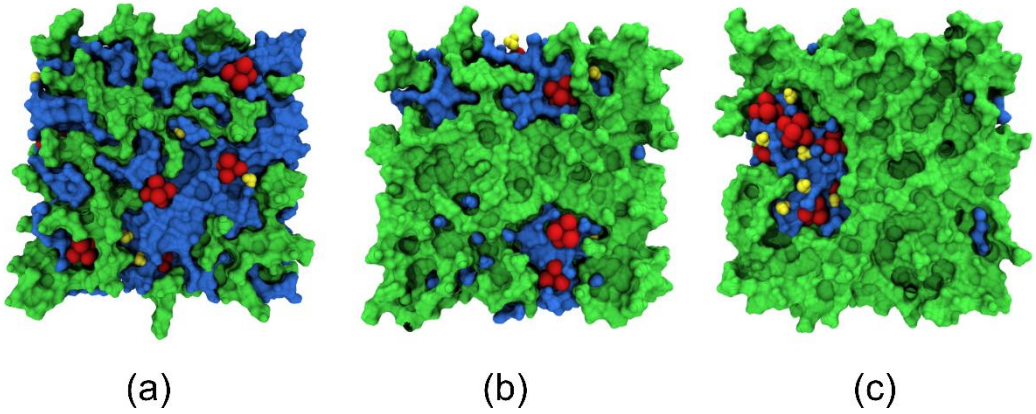

Figure 3.13 Final MD simulation configuration representations (15 Å-think "slices") of $(H_3O)_2[PtCl_6]$ in water-DME mixtures with *original full ionic charges*: (Sagnella and Voth, 1996; Matthews, Venter and Naidoo, 2011) x_{DME} = (a) 0.2, (b) 0.5, and (c) 0.8. Water and DME molecules are represented by blue and green surfaces, respectively. The solute is shown in space-filling representation ("van der Waals"), with $[PtCl_6]^{2-}$ red and H_3O^+ yellow. All images produced using VMD. (Humphrey, Dalke and Schulten, 1996) Reproduced with permission from (Engelbrecht *et al.*, 2018). Copyright 2018 American Chemical Society.

As described by Leontyev and Stuchebrukhov, (Leontyev and Stuchebrukhov, 2010) full ionic charge-models work well in aqueous solutions (high-dielectric medium), however fail in low-dielectric media e.g. organic solvents and, conceivably, their aqueous mixtures. In this context it may be noted that Bagno and co-workers, (Saielli *et al.*, 2005) in their investigation of the apparent preferential solvation of tetramethylammonium (TMA^+) and Cl^- ions in water-acetonitrile binary mixtures, specifically reported an overestimation in the strength of chloride-water interactions in their classical simulations, which was ascribed to the neglect of electronic polarizability effects and the use of point charges on atoms. More recent computational studies emphasize the importance of the use of appropriate polarizable models for accurate classical modelling of ion solvation, and their distribution at aqueous interfaces in particular. (Petersen *et al.*, 2005; Caleman *et al.*, 2011; Vazdar *et al.*, 2012)

3.5 Conclusions

The ^{195}Pt NMR chemical shifts, $\delta(^{195}Pt)$, of the industrially relevant $[PtCl_6]^{2-}$ complex anion in binary mixtures of water and the water-miscible solvents (A) methanol and 1,2-dimethoxyethane (DME) exhibit significant, non-linear variations as a function of bulk mixture composition, x_A. According to the established view concerning the effect on the NMR chemical shift of ions in binary mixed solvents, (Frankel, Langford and Stengle, 1970; Marcus, 1985; Ben-Naim, 1990) these $\delta(^{195}Pt)$ trends

are consistent with varying degrees of preferential solvation of $[PtCl_6]^{2-}$ complex by the organic solvent component. In water-DME mixtures, in particular, the large $\delta(^{195}Pt)$ variation exhibits a pronounced deviation from linearity, suggesting significant preferential solvation of $[PtCl_6]^{2-}$ by DME. Classical MD computer simulations were performed to help understand the nature of solvation of $[PtCl_6]^{2-}$ in these water-DME mixtures, leading to the following general conclusions:

1. The water-DME mixtures themselves are microscopically heterogeneous (micro-heterogeneous).

2. $[PtCl_6]^{2-}$ complexes tend to localize near, or at, the interface between the water and DME-rich solution regions, where they are partially solvated by both components.

3. The $[PtCl_6]^{2-}$ solvation shell composition changes sharply between bulk compositions x_{DME} = 0-0.2, and then more gradually with increasing x_{DME}, reflecting the sharp initial increase and subsequent plateau of the corresponding experimental $\delta(^{195}Pt)$ data.

The preferential location of $[PtCl_6]^{2-}$ within DME-rich regions, at the edge of H-bonded water clusters, initially seems counter-intuitive considering the lack of appropriate positively-charged interaction sites in the DME model. However, Kudin and Car, (Kudin and Car, 2008) in their computational study of the interfacial preferences of hydronium and hydroxide ions, noted that while simple electrostatic considerations may dictate that ions should prefer to be located in bulk water as opposed to interfaces with low-dielectric media, this is not necessarily the case: experiments reveal that water interfaces with oil droplets and hydrophobically assembled structures are usually electrically charged. Similar interfacial ion solvation phenomena have been reported by other workers, (Jungwirth and Tobias, 2006) including the preference of halide anions to locate at water-oil interfaces, as studied by Jungwirth and co-workers. (Vazdar *et al.*, 2012) Caleman *et al.* (Caleman *et al.*, 2011) investigated the preference of halide anions (excluding F^-) for surface *vs.* bulk water solvation in water droplets in a vapor phase. The authors demonstrated that while the phenomenon is caused by a complex interplay between energetic components, it is driven by favourable water-water interactions. Our MD simulations results suggest that similar phenomena may be operative in the apparent "preferential solvation" of $[PtCl_6]^{2-}$ by DME in its aqueous mixtures. As the bulk water content in these mixtures is reduced to water-rich regions, and eventually dynamic, small water clusters with increasing DME content (x_{DME}), the $[PtCl_6]^{2-}$ complex anions remain associated with these water clusters at the borders of bulk DME, affording minimal additional perturbation of the hydrogen-bonded water network. This finding is consistent with the experimentally-observed

plateauing of $\delta(^{195}Pt)$ with increasing x_{DME}, indicating no further changes in the local solvation environment of the $[PtCl_6]^{2-}$ anion. As such, the $\delta(^{195}Pt)$ trend is strongly connected to the evolution of the mixed solvent micro-heterogeneous structure with changing composition.

In water-methanol mixtures, on the other hand, MD simulations indicate more gradual changes in the $[PtCl_6]^{2-}$ solvation shell composition with increasing $x_{methanol}$, consistent with the more moderately-curved experimental $\delta(^{195}Pt)$ trend. (Westra, 2005) Interestingly, methanol molecules in the $[PtCl_6]^{2-}$ solvation shell region tend to adopt orientations allowing them to participate in hydrogen bonding interactions with surrounding solvent molecules, with their less-polarized, weakly-interacting methyl groups directed towards the anionic complex. This observation, together with fact that water self-association occurs in these mixtures, (Laaksonen, Kusalik and Svishchev, 1997; Dixit *et al.*, 2002; Dougan *et al.*, 2004; Corsaro *et al.*, 2008) suggests that the apparent preferential solvation of $[PtCl_6]^{2-}$ by methanol may, similarly, be essentially driven by the need for maximal preservation of energetically favourable H-bonded solvent structures, e.g. water clusters. (Hawlicka and Swiatla-Wojcik, 1998)

Finally, application of the MDEC ionic charge scaling method to account for the electronic dielectric screening of ionic charges (an important consequence of electronic polarizability in condensed phases) (Leontyev and Stuchebrukhov, 2010) results in simulations which are both qualitatively and quantitatively consistent with the interpretation of the corresponding experimental $\delta(^{195}Pt)$ NMR data; by contrast, similar MD simulations performed for H_3O^+ and $[PtCl_6]^{2-}$ in water-DME mixtures using the full ionic charges, originally intended for modelling of these ions in pure water, (Sagnella and Voth, 1996; Matthews, Venter and Naidoo, 2011) results in strong hydration of the anionic complex and, notably at high x_{DME}, extensive ion-association (precipitation), which is not consistent with experiment. (Pluhařová, Mason and Jungwirth, 2013) These observations support the current contention that accurate modelling of ion solvation phenomena mandates an account of the electric polarization and dielectric screening effects. (Jungwirth and Tobias, 2006; Caleman *et al.*, 2011) Jungwirth *et al.* (Pluhařová, Mason and Jungwirth, 2013) demonstrated that MDEC ionic charge-scaled models derived from non-polarizable classical force fields may benefit from additional parameter adjustment. It follows that the MDEC ion models used in the present study must be regarded as a necessary first step toward incorporating the effects of electronic polarizability for bulky anions, such as the $[PtCl_6]^{2-}$; moreover, such models may similarly benefit from further optimization for use in non-aqueous solution environments in future computational studies.

4 Excess thermodynamic properties of binary liquid mixtures of butanol isomers with di-*n*-butyl ether

The work presented in this chapter has been published in the *Journal of Physical Chemistry B* (ACS), (Engelbrecht et al., 2021) and presented as an oral contribution at the "XI Conference of Young Scientists: Problems of Theoretical Physics" (December 21 – 23, 2020, online) international conference, organised by the Bogolyubov Institute for Theoretical Physics of the National Academy of Sciences of Ukraine.

While in Chapter 3 the attention focused on aqueous binary mixtures, in the present chapter considers binary mixtures of two organic solvents, of which only one can self-associate with H-bonding: alcohol-ether mixtures. The systems studied here are the binary mixture with DBE of the two butanol isomers, which are characterized large difference in the excess thermodynamic properties.

This chapter is organized as follows: In Section 4.1 the relevance of the particular systems studied in this work, including their practical applications and a short review of previous experimental studies performed on this type of mixture. In Section 4.2 the details of the preparation of the modelled system and of the simulation protocols are described. Section 4.3 is dedicated to the calculations of the excess thermodynamic properties and in Section 4.4 to 4.8 we discuss how RDFs, H-bond and cluster analyses allow for explanation of the large difference in the thermodynamics properties between the studied mixtures. Some concluding remarks are presented in the final section.

4.1 Introduction

The physical properties of binary liquid mixtures of alcohols with either alkanes or ethers have been the subject of sustained research interest over the past few decades due to both their increasing practical importance as fuel additives in internal combustion engines and fundamental interest as model mixtures of self-associating and non-self-associating components. (Treszczanowicz and Benson, 1977; Awwad and Pethrick, 1982; Pathak and Pradhan, 1988; Patil, Pathak and Pradhan, 1989; Kammerer and Lichtenthaler, 1998; Bernazzani *et al.*, 2006; Alaoui *et al.*, 2011)

In fuel applications, oxygenated compounds e.g. alcohols and ethers, are employed and investigated as additives with the aim of reducing pollutants from vehicle exhaust emissions by altering combustion characteristics.(Rezanova, Kammerer and Lichtenthaler, 1999; Alaoui *et al.*, 2011; Dakkach *et al.*, 2015, 2017) Higher alcohols, and butanol isomers (**Figure 4.1**, top) in particular, are

increasingly studied for applications as biofuels, since they have been proposed to offer potential advantages over the traditional biofuel, ethanol, including better compatibility with existing engine designs at 85% per volume compared with the corresponding ethanol-based fuel (E85), and higher energy content per unit volume.(Alaoui *et al.*, 2011; Dakkach *et al.*, 2015) Indeed, butanol isomers are included in the international regulation on the promotion of the use of energy from renewable sources. (*Directive 2009/28/EC of the European Parliament and of the Council of 23 April 2009 on the promotion of the use of energy from renewable sources and amending and subsequently repealing Directives 2001/77/EC and 2003/30/EC*, 2015) The related di-*n*-butyl ether (DBE), the structure of which is also shown in **Figure 4.1** (bottom), has also been investigated as fuel additive. (Alaoui *et al.*, 2011) Consequently, there is a considerable interest in understanding the physical properties of these compounds and their mixtures, e.g. mixture excess thermodynamic properties.(Rezanova, Kammerer and Lichtenthaler, 1999; González *et al.*, 2000)

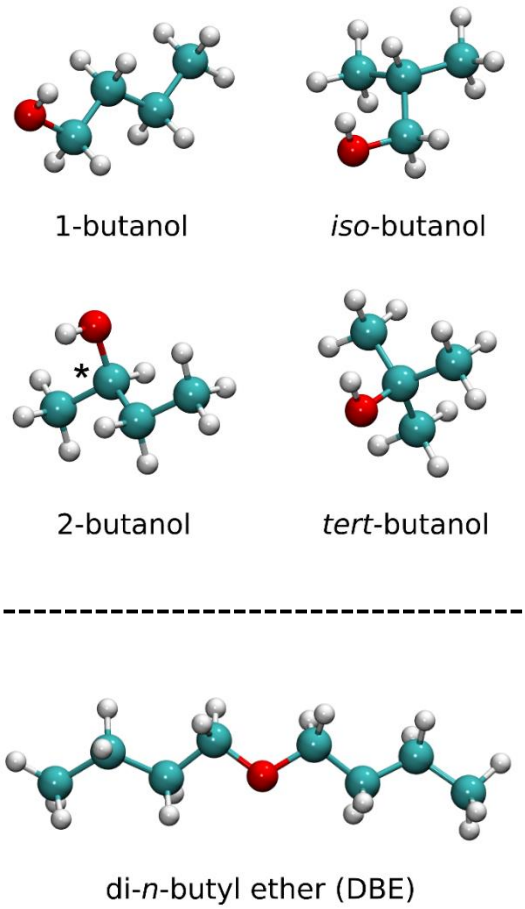

Figure 4.1 (Top) Molecular models of butanol isomers. Note that 2-butanol, having a chiral centre (*), exists as a racemic mixture of *R*/*S* stereoisomers. **(Bottom)** Structure of di-*n*-butyl ether (DBE). Representations were prepared using VMD, (Humphrey, Dalke and Schulten, 1996) with carbon atoms coloured cyan, oxygen red, and hydrogen white.

Measurements of the molar enthalpies of mixing, $\Delta_{mix}H$, a property identified with excess molar enthalpy, H^E, and the excess molar volumes, V^E, of binary mixtures of butanol isomers with DBE have been reported by several groups over the past three decades. (Pathak and Pradhan, 1988; Patil, Pathak and Pradhan, 1989; Kammerer and Lichtenthaler, 1998; Bernazzani *et al.*, 2006) Both the H^E and V^E of these mixtures have been found to increase (become more positive) in the order 1-butanol (*n*-butanol) < 2-methyl-1-propanol (*iso*-butanol) < 2-butanol (*sec*-butanol) < 2-methyl-2-propanol (*tert*-butanol; *t*-butyl alcohol), with the V^E values showing an interesting change in sign from negative at all compositions for 1-butanol and *iso*-butanol, to predominantly positive for 2-butanol and positive at all compositions for *t*-butyl alcohol-DBE mixtures; **Figure 4.2**.

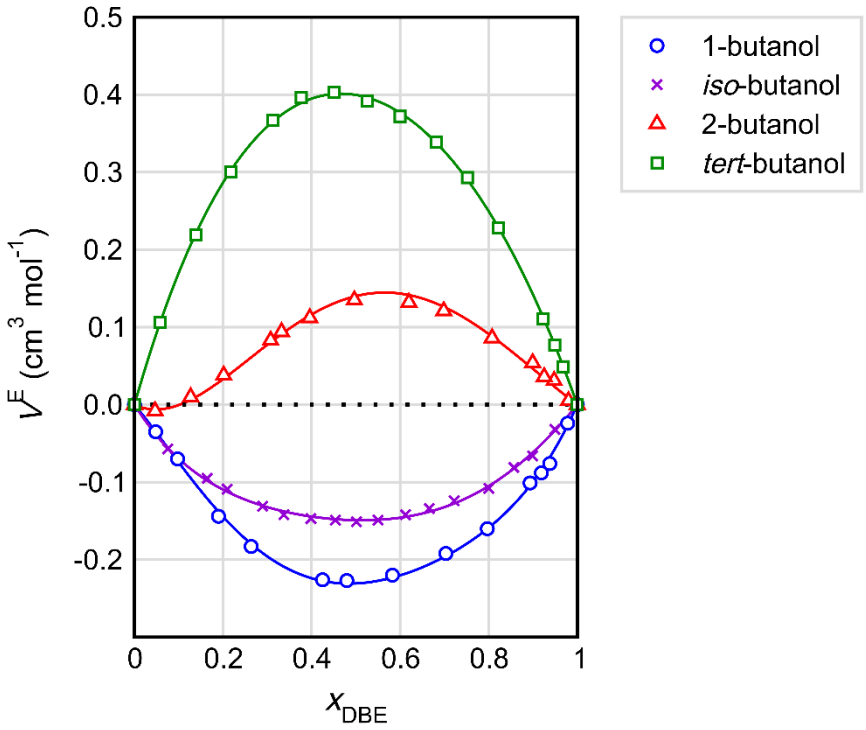

Figure 4.2 Excess molar volumes, V^E, of butanol isomer-di-*n*-butyl ether (DBE) binary mixtures at 298.15 K (0.1 MPa). Data reproduced from Patil *et al.* (Patil, Pathak and Pradhan, 1989)

These excess thermodynamic property trends have been interpreted as resulting from a difference in the balance of contributions arising from the breakage of alcohol-alcohol H-bonds upon mixing, the formation of new alcohol-DBE H-bonds within the mixtures, and other non-specific intermolecular interactions. For example, the observed V^E trend of the mixtures are thought to be largely due to differences in alcohol-DBE H-bonding, where the alkyl chain branching in the vicinity of the

hydroxyl groups of 2- and *tert*-butanol sterically hinder H-bonding with DBE, resulting in a smaller negative V^E contribution from this interaction type compared to 1- and *iso*-butanol. (Patil, Pathak and Pradhan, 1989; Kammerer and Lichtenthaler, 1998; Bernazzani *et al.*, 2006)

Kammerer *et al.* (Kammerer and Lichtenthaler, 1998) applied the ERAS (Extended Real Association Solution) model to 1-butanol and 2-butanol + DBE mixtures with the aim to obtain the simultaneous description of H^E and V^E expressed by a set of system-specific parameters. As, both the mixtures exhibit strong hydrogen bonding, the chemical contribution was assumed dominant, with respect to the physical contribution (non-specific), in the calculation of each excess properties under examination and a fixed value for the physical parameter was used. A good representation of the experimental data was obtained by using the parameters previously obtained by a least-square treatment. For 2-butanol + DBE the model calculations result in much lower value for the association constant between alcohol and ether, KAB, than for the system with 1-butanol.

Numerous experimental studies of alcohol-alkane mixtures by ultrasonic measurements, (Awwad and Pethrick, 1982) vibrational (Murdoch *et al.*, 2002; Sassi *et al.*, 2007), or NMR spectroscopic (Abdel Hamid *et al.*, 2013; Flores *et al.*, 2014; Balanay, Kim and Fan, 2016) techniques and neutron scattering, (Mhanna *et al.*, 2016; Požar *et al.*, 2016) have revealed varying degrees of alcohol self-association *via* H-bonding. In addition, computational molecular modelling studies, notably Monte Carlo (MC) (Stubbs *et al.*, 2001; Stubbs and Siepmann, 2005; Gómez-Álvarez, Romaní and González-Salgado, 2013) and Molecular Dynamics (MD) simulations, (Fouad *et al.*, 2015; Požar *et al.*, 2016; Essafri and Ghoufi, 2019) have produced detailed molecular-level information on the nature of alcohol self-association in such mixtures, e.g. H-bonded alcohol cluster size distributions.

Interestingly, alcohol-ether binary liquid mixtures have received considerably less computational consideration than those of alcohol and alkanes; (Kgagodi and Mbaiwa, 2017) in fact, a literature survey reveals that no computer simulation studies have been reported for the butanol isomer-DBE mixtures described above. In view of the evident importance of alcohol-ether mixtures, AA MD simulations were performed for binary mixtures containing one of the two representative butanol isomers, 1- or 2-butanol, with DBE, spanning the entire mixture composition range, specifically with the aim of studying H-bonded alcohol self-association, its dependence on hydroxyl position in the linear hydrocarbon skeleton, and how it relates to existing explanations of the interesting excess thermodynamic properties of these mixtures.(Pathak and Pradhan, 1988; Patil, Pathak and Pradhan, 1989; Kammerer and Lichtenthaler, 1998; Bernazzani *et al.*, 2006; Alaoui *et al.*, 2011)

4.2 Computational details

4.2.1 MD force field

The General Amber Force Field (GAFF) (Wang *et al.*, 2004) was used to model 1- and 2-butanol (a racemic *R*/*S* stereoisomer mixture was used throughout) and DBE; i.e. all intramolecular (bonded) and Lennard-Jones non-bonded parameters (Lorentz-Berthelot combing rules). Atomic partial charges were derived according to the GAFF protocol (Wang *et al.*, 2004) by performing a fit to the molecular electrostatic potential (Restrained Electrostatic Potential, RESP, model), (Bayly *et al.*, 1993; Cieplak *et al.*, 2000) with electron densities obtained by quantum chemical calculations at the HF/6-31G* theory level. All electronic structure calculations were performed using Gaussian 09. (Frisch *et al.*, 2009)

4.2.2 MD simulations

Starting configurations for MD simulations were prepared by randomly placing a total of 400 molecules in a periodic cubic simulation cell, with dimensions chosen such that the configuration is close to the target density, using the Packmol software. (Martínez *et al.*, 2009) As noted above, all 2-butanol fractions consisted of a racemic mixture of 2-butanol stereoisomer (*R*/*S*) models.

All MD computer simulations were performed with the AMBER 18 simulation package, (Case *et al.*, 2005, 2018) using both CPU and GPU versions of PMEMD. (Le Grand, Götz and Walker, 2013) A simulation time step of 2 fs was used in all simulations, with bonds involving hydrogen were constrained to equilibrium distances using SHAKE (default tolerance). (Ryckaert, Ciccotti and Berendsen, 1977) Non-bonded interactions were cut off at distance of 12 Å, with long-range electrostatic interactions treated using the particle-mesh Ewald (PME) method. (Darden, York and Pedersen, 1993; Essmann *et al.*, 1995). The system temperature (target 298.15 K) and pressure (0.1 MPa) were maintained using the Berendsen weak coupling algorithm, (Berendsen *et al.*, 1984) with coupling times of 0.1 and 0.5 ps, respectively. (Smith, Berendsen and Van Gunsteren, 2004) Appropriate isothermal compressibility, κ_T, values for the mixtures, which are used in the pressure coupling, were obtained by interpolation of the data reported by Montero and co-workers. (Alaoui *et al.*, 2011; Dakkach *et al.*, 2015) Periodic boundary conditions were employed in all simulations.

Starting configurations were subjected to 10,000 steps of steepest-descent energy minimization prior to 1 ns MD simulations under constant temperature (NVT) and pressure (NPT) conditions, during which the system temperature and density were monitored, and equilibrated. Following this initial equilibration stage, a further NPT MD simulation of at least 50 ns was performed, storing the system configurations and properties every 1 ps and 0.1 ps, respectively.

4.3 Calculation of excess thermodynamic properties

4.3.1 Excess thermodynamic properties

The excess molar enthalpies (H^E) and volumes (V^E) of the simulated systems were calculated as described in Chapter 1 (Section 1.1). Average potential energies were employed in the calculation of H^E, and the PV^E correction term was neglected as it makes a negligible contribution in liquid systems. The simulation excess thermodynamic results are tabulated in **Table 4.1** & **Table 4.2** for simulated 1- and 2-butanol mixtures respectively; statistical uncertainties (standard deviations, indicated by ±) reported in the tables were estimated by the block-averaging method, as described in Section 4.3.2.

Table 4.1. Excess molar enthalpies (H^E), excess molar volumes (V^E) and densities (ρ) of simulated 1-butanol-DBE binary mixtures at 298.15 K, 0.1 MPa.

x_{DBE}	H^E (J mol^{-1})	V^E (cm^3 mol^{-1})	ρ (kg m^{-3})
0.000	-	-	801.04 ± 0.07
0.125	141 ± 10	-0.07 ± 0.01	791.91 ± 0.07
0.250	299 ± 10	-0.11 ± 0.01	784.17 ± 0.07
0.375	449 ± 9	-0.09 ± 0.01	777.34 ± 0.06
0.500	569 ± 10	-0.08 ± 0.01	771.56 ± 0.06
0.625	588 ± 10	-0.08 ± 0.01	766.68 ± 0.06
0.750	626 ± 10	-0.06 ± 0.02	762.33 ± 0.06
0.880	500 ± 11	-0.03 ± 0.02	758.33 ± 0.07
0.940	380 ± 10	-0.03 ± 0.02	756.71 ± 0.06
1.000	-	-	755.04 ± 0.06

Table 4.2. Excess molar enthalpies (H^E), excess molar volumes (V^E) and densities (ρ) of simulated 2-butanol-DBE binary mixtures at 298.15 K, 0.1 MPa.

x_{DBE}	H^E (J mol^{-1})	V^E (cm^3 mol^{-1})	ρ (kg m^{-3})
0.000	-	-	798.80 ± 0.07
0.125	484 ± 14	0.06 ± 0.01	789.13 ± 0.07
0.250	848 ± 14	0.11 ± 0.01	781.31 ± 0.08
0.375	1116 ± 13	0.19 ± 0.01	774.56 ± 0.07
0.500	1261 ± 11	0.21 ± 0.01	769.15 ± 0.06
0.625	1325 ± 11	0.28 ± 0.01	764.22 ± 0.06
0.750	1155 ± 11	0.20 ± 0.02	760.69 ± 0.06
0.880	855 ± 10	0.15 ± 0.02	757.33 ± 0.06
0.940	570 ± 10	0.10 ± 0.02	756.06 ± 0.05
1.000	-	-	755.04 ± 0.06

The H^E and V^E data computed from the MD simulations are compared with those measured experimentally in **Figure 4.3** & **Figure 4.4**, respectively. In these figures, both the data obtained by our experimental collaborators, Prof Silvia Porcedda and Dr Alessandra Piras (Engelbrecht *et al.*, 2021) and the latest literature data are plotted for comparison. (Kammerer and Lichtenthaler, 1998; Alaoui *et al.*, 2011) These experimental datasets may be seen to be in good agreement, as is the measurements from previous workers under the same conditions. (Pathak and Pradhan, 1988; Patil, Pathak and Pradhan, 1989; Bernazzani *et al.*, 2006)

The H^E from simulations of the 2-butanol mixtures are in excellent agreement with experiment, while those for corresponding 1-butanol mixtures are notably lower. While this difference is interesting (as discussed in more detail below), the discrepancies observed for the 1-butanol mixtures are not uncommon in magnitude among similar classical computer simulation studies using established general-purpose force fields, e.g. OPLS-AA. (Tanaka and Gubbins, 1992; Wensink *et al.*, 2003; Dai *et al.*, 2010) Moreover, the simulated 1-butanol mixtures' H^E variation trend reasonably reproduces the experimental trend symmetry, with maximum in the mixture composition range $x_{DBE} \approx 0.6$-0.7.

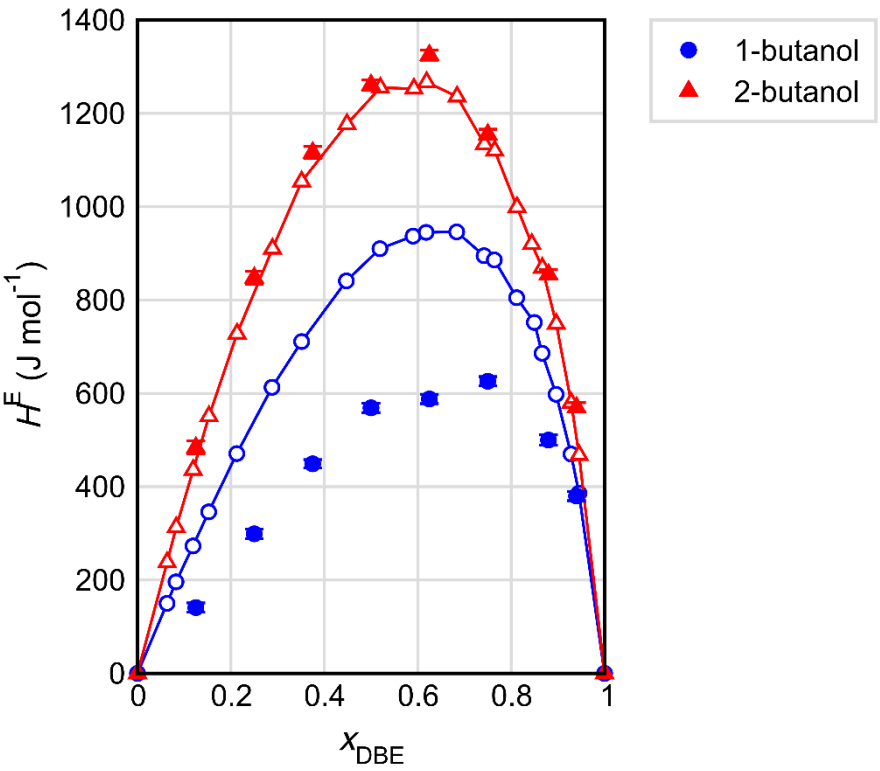

Figure 4.3 Excess molar enthalpies (H^E) of 1- and 2-butanol-DBE binary mixtures, at 298.15 K, 0.1 MPa, from experiment (open symbols) and MD computer simulation (solid symbols). Solid lines simply connect experimental data and are intended as guide for the eye. Statistical errors in simulated data are included, but effectively smaller than the data marker size. (Engelbrecht *et al.*, 2021)

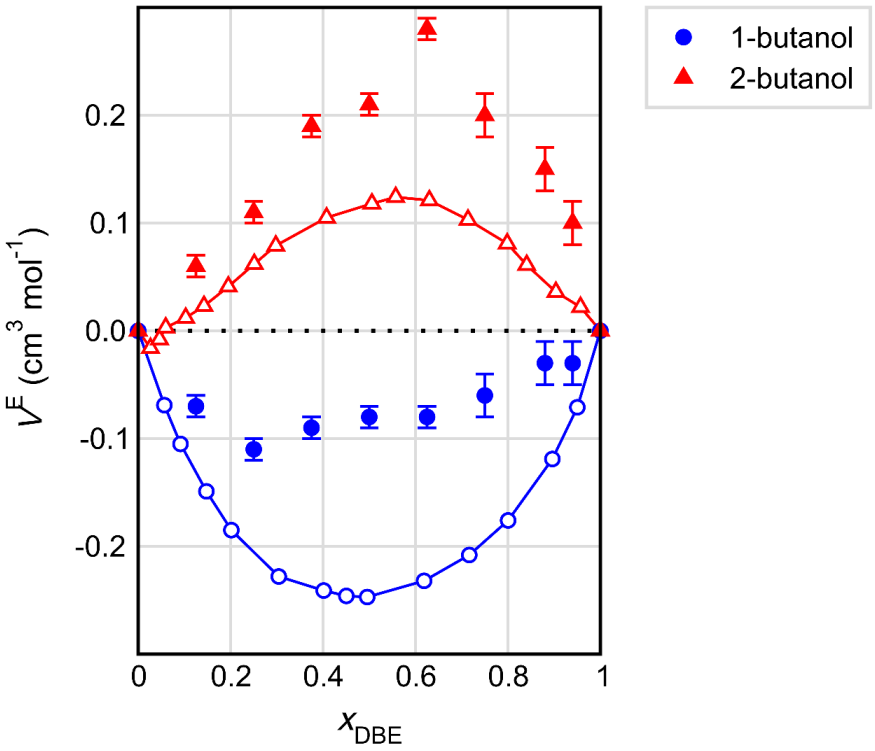

Figure 4.4 Excess molar volumes (V^E) of 1- and 2-butanol-DBE binary mixtures, at 298.15 K, 0.1 MPa, from experiment (open symbols) and MD computer simulation (solid symbols). As in **Figure 4.3**, solid lines simply connect experimental data and are intended as guide for the eye. (Engelbrecht *et al.*, 2021) Error bars on simulated data represent one standard deviation of the mean. (Flyvbjerg and Petersen, 1989)

The overall experimental V^E trend differences are reasonably reproduced by the MD simulations, with all-negative values for the 1-butanol-DBE mixtures, and all-positive for the corresponding 2-butanol mixtures. The simulated V^E values are higher (more positive) than experiment for both butanol isomers at all mixture compositions, with 1-butanol mixtures again showing larger discrepancies between simulated and experimental data. The simulation V^E trend is also noticeably more asymmetric than experiment. Nevertheless, it may be noted that the reproduction of small experimental V^E values is evidently challenging using standard classical force fields, often resulting in qualitative differences; the reader is referred to the simulation study of S-shaped excess thermodynamic properties by Miroshnichenko and Vrabec, (Miroshnichenko and Vrabec, 2015) and references therein. Deviations between experimental and simulated excess properties for binary liquid mixtures are often ascribed to limitations of classical force field combination (or combining) rules for describing interactions among unlike molecules, and it has been demonstrated that this agreement may be improved by application of certain scaling procedures to the computation of intermolecular

interactions. (Miroshnichenko and Vrabec, 2015) Overall, the present simulated excess thermodynamic results reasonably reproduce the main features of the experimental observations, as shown in **Figure 4.3** & **Figure 4.4** , and, in view of this validation, the simulations may be considered acceptable models for a deeper understanding the molecular-level liquid structure of these mixtures.

4.3.2 Evaluation of statistical errors

The statistical errors in the average simulated system potential energies and volumes were estimated using the block-averaging method described by Flyvbjerg and Petersen, (Flyvbjerg and Petersen, 1989) and by Berendsen. (Berendsen, 2011) Essentially, the full property data time series, e.g. N total datapoints (e.g. for the system volume), recorded at every n^{th} simulation timestep, are grouped, or "blocked", into successively larger blocks of consecutive datapoints by repeatedly doubling the block size. For each blocking operation, the individual block averages are calculated, and, finally, the standard deviation of these block averages around the unique mean value of full dataset (using standard methods for uncorrelated data). For example, the first blocking operation would calculate the (block) average values for sequential datapoints 1 and 2, 3 and 4, 5 and 6, etc. This operation results in a total number of blocks $n_b = N/2$. The next blocking operation would assign blocks as sequential datapoints 1-4, 5-8, 9-12, …, resulting in $n_b = N/4$, etc. In other words, the block size is doubled with each successive blocking operation. In the event that not all datapoints can be assigned to blocks of the required size (e.g. a full dataset consisting of 100 points cannot be divided into blocks of size 8 datapoints, i.e. the third blocking operation cannot be completed), the remaining data (datapoints 97-100, in this case) would be omitted from the calculation. An example of this procedure is shown in **Figure 4.5**.

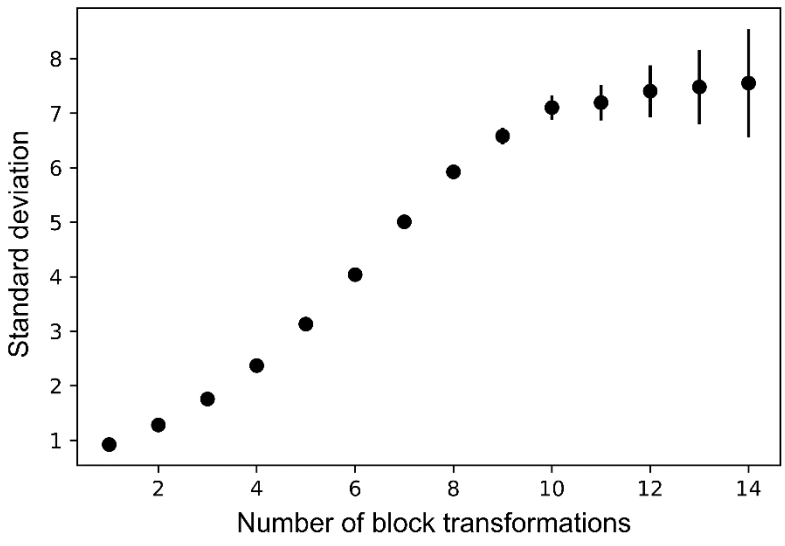

Figure 4.5 Block average standard deviations of the system volume data for an *NPT* simulation of 1-butanol-DBE mixture (x_{DBE} = 0.5) at 298.15 K, 0.1 MPa. The standard deviation units are Å^3, and error bars calculated using the relative uncertainty formula $1/\sqrt{(n_b - 1)}$, where n_b is the number of blocks. Reproduced from (Engelbrecht *et al.*, 2021) Copyright 2021 American Chemical Society.

4.3.3 Discussion

The H^E measurements of butanol isomer-DBE binary liquid mixtures have been interpreted as due to a balance between two energetic contributions of opposite sign: (Pathak and Pradhan, 1988; Kammerer and Lichtenthaler, 1998)

1. a **positive** (endothermic) contribution from the breakage of the characteristic H-bonded structure of the pure butanol isomer liquids upon mixing with DBE, and,
2. a **negative** (exothermic) contribution from the formation of new butanol-DBE H-bonds in the mixture.

The positive H^E values of butanol isomer-DBE mixtures have been taken to indicate that the energetic cost associated with breaking of the particular H-bonded structure of the pure butanol isomers upon mixing with DBE is not fully compensated by the formation of new butanol-DBE H-bonds. As regarding the actual H^E values, Kammerer and Lichtenthaler ascribe the larger positive H^E of 2-butanol compared to 1-butanol-DBE mixtures to a more pronounced formation of H-bonds between 1-butanol and DBE upon mixing, [contribution (2)] whereas the formation of such cross-species H-bonds in the corresponding 2-butanol mixtures would be more sterically hindered and thus less favourable. (Kammerer and Lichtenthaler, 1998) Interestingly, Lafuente and co-workers, (Valén *et al.*, 2002; Giner *et al.*, 2003) in their study of the excess thermodynamic properties of the related binary mixtures of 1- and 2-butanol with the cyclic ethers tetrahydrofuran (THF) and 2-methyl-THF, proposed the larger H^E values of the 2-butanol mixtures to be predominantly due to a greater degree of breakage of the pure 2-butanol H-bond associated structure upon mixing, i.e. contribution (1) described above. Indeed, it has been proposed that, for a given alcohol-ether binary mixture, the H-bond enthalpy of two self-associated alcohol molecules is greater than that between the alcohol and ether, (Murthy and Rao, 1968; Pathak and Pradhan, 1988) from which it would follow that the measured H^E do not necessarily reflect (in the absence of more detailed energetic information) the extent to which alcohol-alcohol H-bonds broken upon mixing are replaced by new alcohol-ether H-bonds.

Patil *et al.* (Patil, Pathak and Pradhan, 1989) first reported the excess molar volumes, V^E, of all butanol isomer-DBE binary mixtures, interpreting this quantity as resulting from three contributions, the first two of which are similar to that described above for H^E:

1. a **positive** contribution from the breaking of butanol-butanol H-bonds in the pure butanol isomer structure upon mixing (structure-breaking),

2. a **negative** contribution from the formation of new butanol-DBE H-bonds in the mixture, and,

3. a **positive** contribution due to the disruption of orientationally-ordered structure of pure DBE (through van der Waals interactions)

The authors ascribe the V^E order 1-butanol (negative) < iso-butanol (negative) < 2-butanol (predominantly positive) < tert-butanol (positive) to the same-order increased steric hindrance at the butanol isomer hydroxyl (OH) site, correlating the deviation of the butanol isomer molecular shape from linearity with the reduction of H-bonding and van der Waals interactions with the effectively linear DBE molecule, i.e. contribution (2). Similar interpretations were presented in subsequent reports of the V^E of these butanol isomer-DBE mixtures by Kammerer and Lichtenthaler (Kammerer and Lichtenthaler, 1998) and Bernazzani *et al.* (Bernazzani *et al.*, 2006). Chaudhari and Katti, (Chaudhari and Katti, 1985) in their study of the volumetric properties of butanol isomer-*n*-octane binary mixtures, reported a similar V^E order, but with all-positive values.

While it is generally accepted that pure liquid 1-butanol is more extensively associated *via* H-bonding compared to the other butanol isomers, including 2-butanol, (Rytting, Anderson and Higuchi, 1978) and that it is also more strongly self-associated in mixtures with alkanes, (Chaudhari and Katti, 1985) it appears that differences in the detailed H-bonded structures of pure 1- and 2-butanol, the H-bond topologies in their binary mixtures with DBE, and the precise role of such differences in determining the excess thermodynamic properties of such mixtures have not been studied by computer simulations.

4.4 RDFs

Computational studies of H-bonded liquid structure routinely make use of oxygen-oxygen radial pair distribution functions (RDFs), $g_{OO}(r)$, which describe the radially-averaged distribution of oxygen atoms around a given oxygen atom; naturally, these may belong to the same type of molecule, e.g. in pure water, or different molecules, e.g. the distribution of water oxygen atoms around an alcohol oxygen atom in a mixture of these components. This function has a strong experimental connection in the form of neutron and X-ray scattering patterns, (Head-Gordon and Hura, 2002) with their intense first maximum (i.e. occurring a shortest distance, typically in range 2.5-3.0 Å) interpreted as due to the presence of directly H-bonded neighbours; the function may be suitably integrated (typically up to the first minimum) in order to estimate the average number of such neighbours, also referred to as the coordination number (see Section 2.4.2).

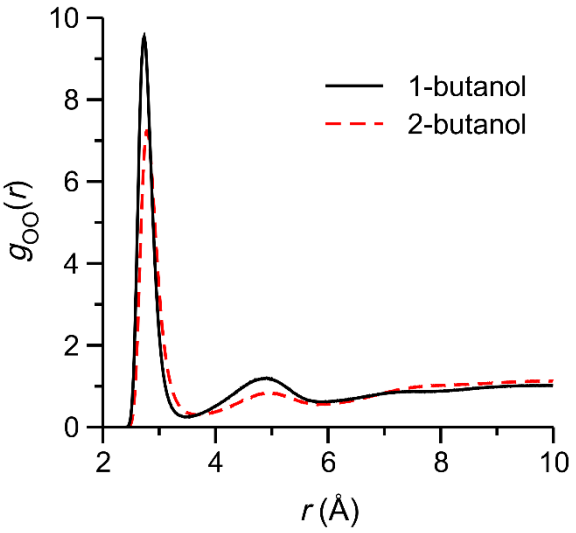

Figure 4.6 Radial distribution functions, $g_{OO}(r)$, (O_B-O_B RDFs) of simulated pure 1- and 2-butanol liquids (298.15 K; 0.1 MPa).

The RDFs describing the average distribution of butanol isomer oxygen atoms (O_B) around any given O_B for the simulated 1- and 2-butanol pure liquids and all DBE mixtures studied are shown in **Figure 4.6** & **Figure 4.7**, respectively. For all simulated mixtures studied, the first O_B-O_B RDF maxima for 1-butanol pure liquid and mixtures are more intense and consistently occur at shorter distances than those of corresponding 2-butanol systems at the same DBE molar fraction, x_{DBE}, indicative of a higher degree of alcohol self-association and more compact, stronger alcohol-alcohol H-bonds compared to the 2-butanol systems. (Rytting, Anderson and Higuchi, 1978) The O_B-O_B RDFs of the pure butanol isomers are essentially consistent with those presented by Mesele *et al.* (Mesele *et al.*, 2016) in their MD simulation study (temperature 298 K, using the OPLS-AA force field (Jorgensen, Maxwell and Tirado-Rives, 1996)) of the reorientational motions in pure liquid butanol isomers, though a slightly lower 1-butanol first maximum was reported by these authors. In fact, the pure 1-butanol O_B-O_B coordination number, n_{OO}, reported in **Table 4.3**, is notably higher than those reported from X-ray and neutron scattering experiments, n_{OO} = 1.54 – 1.8. (Shmyt'Ko *et al.*, 2010; Cuello *et al.*, 2014) These differences are discussed in greater detail below.

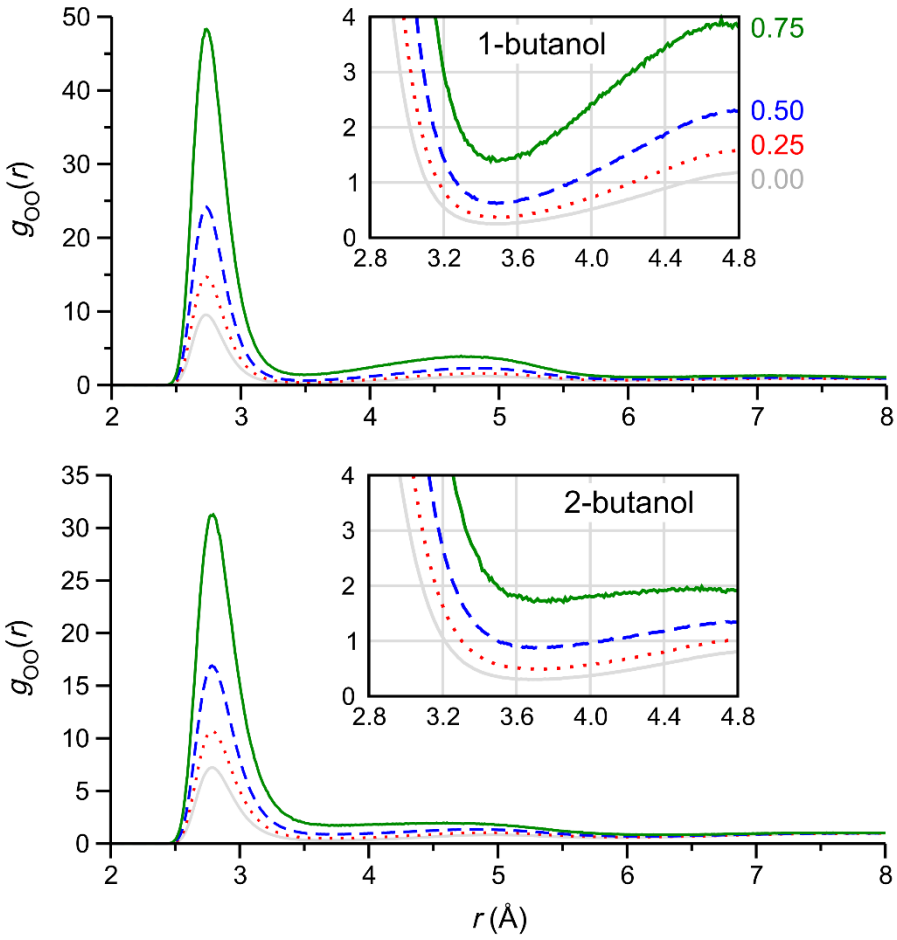

Figure 4.7 O_B-O_B RDFs computed for selected simulated 1- and 2-butanol – DBE mixtures. Insets show expansions of the respective first RDF minimum regions, which were used as cut-off distance for evaluation of H-bonded neighbours. Colour-coded numbers next to data trends in the top inset correspond to the mole fraction DBE, x_{DBE}, and serve as legend for the whole composite figure.

Table 4.3 Numerical data relating to the O_B-O_B RDFs for all simulated 1- and 2-butanol – DBE mixtures, at 298.15 K, 0.1 MPa; the position of the RDF first minima (R_{OO}) and corresponding coordination number (obtained by integration, n_{OO}). Numbers in brackets indicate estimated values where no clear first minimum could be identified

x_{DBE}	1-butanol		2-butanol	
	R_{OO}	n_{OO}	R_{OO}	n_{OO}
0.000	3.52	2.00	3.67	1.93
0.125	3.51	1.96	3.71	1.87
0.250	3.49	1.90	3.73	1.80
0.375	3.53	1.85	3.72	1.72
0.500	3.49	1.78	3.70	1.62
0.625	3.49	1.71	3.76	1.51
0.750	3.49	1.56	3.86	1.37
0.880	3.50	1.29	3.88	0.97
0.940	3.44	0.87	(3.88)	(0.56)

The O_B-O_B RDFs first maxima of the simulated 1- and 2-butanol - DBE mixtures increase with increasing DBE content, x_{DBE}, in **Figure 4.7**. Since RDFs are normalized to the bulk densities of the particles considered (in this case O_B), which decrease with increasing x_{DBE}, the observed RDF intensity increase does not necessarily correspond to an increase in the *number* of H-bonded neighbours. In fact, the O_B-O_B coordination numbers, n_{OO}, obtained by integration of these first RDF peaks (to their respective first minima, R_{OO}; **Table 4.3**) and plotted in **Figure 4.8**, show decrease, as may be expected, with increasing x_{DBE} for both mixture series, i.e. the average number of H-bonded alcohol neighbours of a given alcohol molecule decreases as the alcohol is increasingly diluted with DBE. The alcohol-alcohol n_{OO} values of the simulated 1-butanol mixtures are greater than those of corresponding 2-butanol mixtures, indicating a higher average number of such H-bonded alcohol-alcohol neighbours, as previously inferred from the O_B-O_B RDF first maxima intensity comparison.

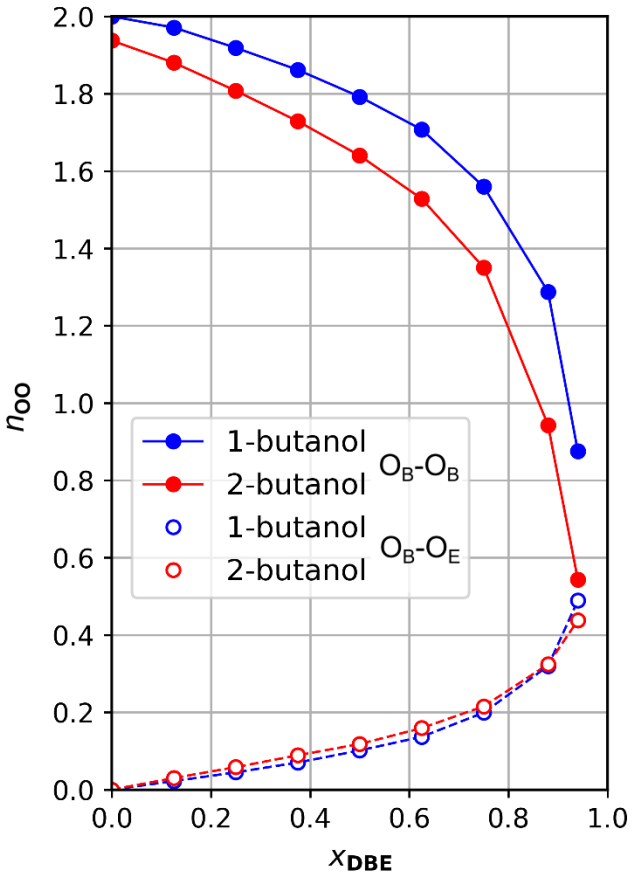

Figure 4.8 O-O coordination numbers, n_{OO}, obtained by RDF integration, plotted as a function of mixture composition, x_{DBE}. Data for 1-butanol (blue) and 2-butanol (red); O_B-O_B (alcohol-alcohol) coordination numbers plotted with solid circle data markers (solid line), and O_B-O_E (alcohol-ether) in open circle markers (dashed line). (Engelbrecht *et al.*, 2021)

RDFs may also be used to study the cross-species H-bonding between the butanol isomers and the ether, DBE, molecules (with ether oxygen atom O_E). The O_B-O_E RDFs and corresponding O_B-O_E coordination numbers are shown in **Figure 4.8** & **Figure 4.9**, respectively; pertinent numerical data are collected in **Table 4.4**. The O_B-O_E RDFs exhibit essentially similar shapes and variation with mixture composition compared to their O_A-O_A counterparts, with those of the 1-butanol mixtures consistently exhibiting more intense first minima, yet the coordination numbers in **Figure 4.8** reveal that the average numbers of O_E H-bonded to a given O_B are significantly lower than the corresponding O_B-O_B numbers and, interestingly, rather similar for the two butanol isomers. While the first of these observations is not unexpected (since an alcohol can donate only a single H-bond with a neighbouring DBE molecule), the similarity of the O_B-O_E coordination numbers for two butanol isomers is interesting in view of the fact that previous investigations have attributed the measured H^E differences of their mixtures to more pronounced 1-butanol – DBE H-bonding. (Kammerer and Lichtenthaler,

1998) However, considering the consistently higher 1-butanol O_B-O_B coordination numbers in **Figure 4.8**, and the consequent lower availability of 1-butanol molecules for H-bonding with DBE, it may indeed be concluded that a larger fraction of *available* 1-butanol molecules form H-bonds with DBE compared to the corresponding 2-butanol mixture.

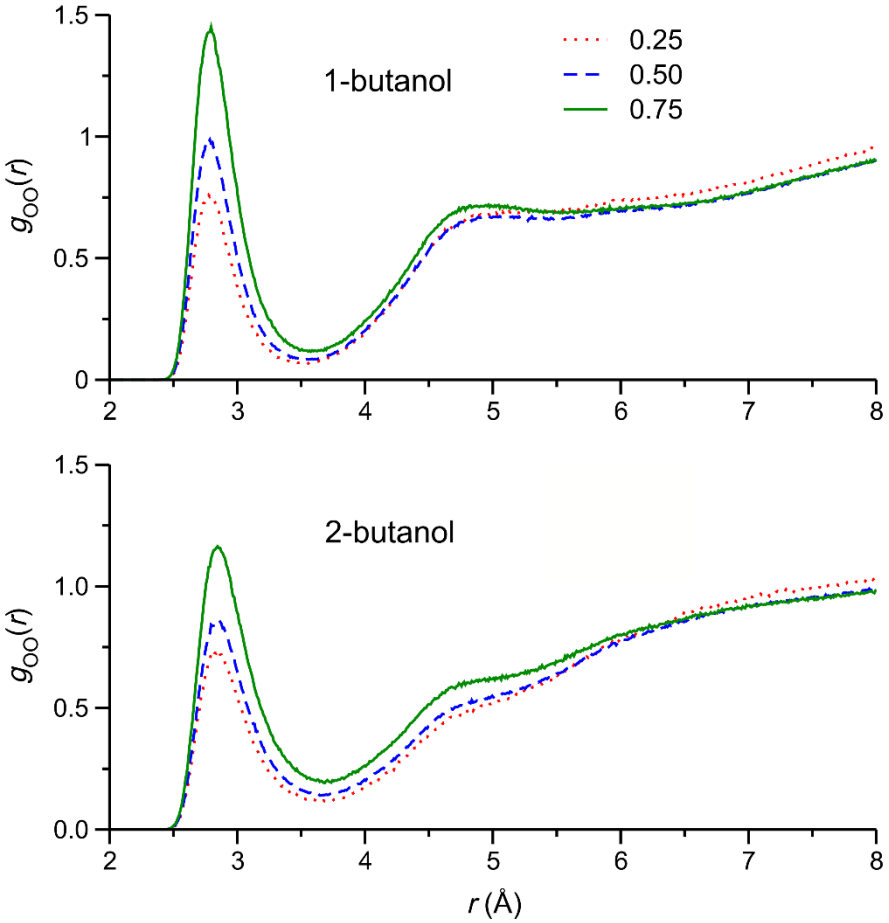

Figure 4.9 O_B-O_E RDFs computed for selected simulated 1- and 2-butanol – DBE mixtures. Pertinent numerical data reported in **Table 4.4**. (Engelbrecht *et al.*, 2021)

Table 4.4 Numerical data relating to the O_B-O_E RDFs for all simulated 1- and 2-butanol – DBE mixtures, at 298.15 K, 0.1 MPa, the position of the RDF first minima (R_{OO}) and corresponding coordination number (obtained by integration, n_{OO}) (Engelbrecht *et al.*, 2021)

x_{DBE}	1-butanol		2-butanol	
	R_{OO}	n_{OO}	R_{OO}	n_{OO}
0.125	3.49	0.02	3.65	0.03
0.250	3.46	0.04	3.65	0.06
0.375	3.50	0.07	3.69	0.09
0.500	3.53	0.10	3.65	0.12
0.625	3.61	0.14	3.66	0.16
0.750	3.58	0.20	3.69	0.22
0.880	3.69	0.32	3.69	0.32
0.940	3.70	0.49	3.74	0.44

4.5 Hydrogen bond analysis

While the analysis of O-O RDFs is extensively used to study H-bonded liquid systems, additional H-bond criteria have been proposed (Section 2.4.4) ; these may be energetic or geometric, (Stillinger, 1980; Rapaport, 1983; Luzar and Chandler, 1996; Kumar, Schmidt and Skinner, 2007) but the following set of three geometric H-bond criteria are widely cited: (Andanson *et al.*, 2005)

1. The distance between H-bond donor and acceptor oxygen atoms, O_D and O_A respectively, should be smaller than a certain value, typically chosen as the corresponding O_D-O_A RDF first minimum, R_{OO}.

2. The distance between donor H (H_D) and O_A should be smaller than a certain value, which is, similarly, taken as the H_D-O_A RDF first minimum, R_{OH}.

3. An angle criterion defining the relative orientations of donor and acceptor groups; in this study we define the H-bond O_D-H_D ··· O_A obtuse angle ≥ 135°.

In practical H-bond definitions, at least one of the above distance criteria (typically criterion 1) are combined with an angle criterion (3), allowing for the development of algorithms that provide detailed information on simulated H-bond topologies and dynamics. (DeBolt and Kollman, 1995; Mesele *et al.*, 2016) The above H-bond criteria are also incorporated into established software developments,

e.g. the *hbond* command of the CPPTRAJ program (combination of criteria 1 and 3) included in the Amber 18 simulation package, (Roe and Cheatham, 2013) which was used in the present study. The average numbers of butanol-butanol and butanol-DBE H-bonds per butanol isomer molecule (n_{HB}) for all simulated 1- and 2-butanol - DBE mixtures, computed using *hbond*, are plotted in **Figure 4.10**.

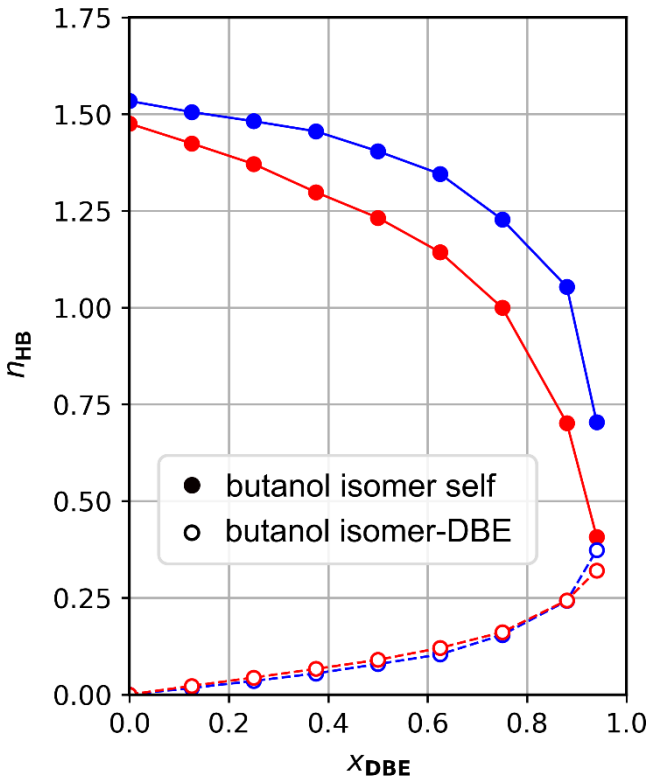

Figure 4.10 Average number of H-bonds for a given 1- or 2-butanol molecule with other butanol molecules of the same type (solid circle data markers, solid line), and with DBE (open circle, dashed line); colour code as in **Figure 4.8**: blue, 1-butanol; red, 2-butanol. (Engelbrecht *et al.*, 2021)

Comparison of the H-bond analysis results with those from RDF integration, **Figure 4.8** & **Figure 4.10**, confirms strong similarities between these analyses. As regarding the actual values, the average numbers of H-bonds per butanol isomer molecule obtained by the H-bond analysis are consistently lower than those obtained from RDF integration for both mixture series; this difference is due to application of the additional angle criterion in the former. We note that the average number of H-bonds per molecule in the simulated pure 1-butanol obtained using the *hbond* tool (1.53) agrees rather favourably with that reported by Cerar *et al.* (Cerar *et al.*, 2017) (1.56) employing the AMBER03 force field, as implemented in the GROMACS 5.1 simulation package (Van Der Spoel *et al.*, 2005),

though using a different set of H-bond criteria. The combined information from O_B-$O_{B/E}$ RDF integration and H-bond analysis indicate that 1-butanol is more extensively self-associated *via* H-bonding than 2-butanol, both in the respective pure liquids and in their mixtures with DBE. For the pure butanol isomer liquids, this finding is generally consistent with previous experimental (Rytting, Anderson and Higuchi, 1978) and simulation studies. (Mesele *et al.*, 2016) Moreover, while 1- and 2-butanol have on average similar numbers of DBE H-bonded neighbours in the mixtures, the more self-associated nature of 1-butanol indicates that it more effectively H-bonds with DBE under these conditions (as may be expected).

In the context of understanding the excess thermodynamic properties H^E and V^E, it is important to compare the extent to which the H-bonded structure of the pure butanol isomers are broken upon mixing with DBE; i.e. the *relative decrease* in the average number of H-bonds per butanol isomer molecule. Considering the butanol-butanol H-bond data plotted in **Figure 4.10**, a steeper decreasing trend in the average number of such H-bonds with increasing x_{DBE} may be noted for 2-butanol, suggesting a greater *relative* decrease in the number of such H-bonds. To facilitate comparison of the H-bond trends, the *normalized* average number of butanol-butanol H-bonds per butanol molecule for the 1- and 2-butanol mixtures, relative to that in the respective pure butanol isomer liquids, are plotted in **Figure 4.11**. This normalized number is lower for 2-butanol in all mixtures studied, confirming a greater degree of H-bond breakage for this isomer. This result also confirms that the H-bond breakage term, the positive contribution (1) to H^E and V^E described in Section 4.3.3, must play a role in determining these excess thermodynamic properties, especially considering the greater H-bond enthalpies of alcohol-alcohol *vs.* alcohol-ether H-bonds. (Murthy and Rao, 1968)

Before analysing the detailed structures of H-bonded butanol isomer self-associates, or clusters, a note on possible limitations of the current computational model is in order. Of the different systems considered here, comparable computer simulation results are available only for the pure liquids, primarily 1-butanol. (Lehtola, Hakala and Hämäläinen, 2010; Mesele *et al.*, 2016; Cerar *et al.*, 2017) While the average number of H-bonded neighbours in pure 1-butanol computed from our simulation agrees rather well with that presented by Cerar *et al.* (Cerar *et al.*, 2017) (using a different force field and H-bond criteria, the combined effects of which are unknown), the relevant O_B-O_B RDF first maximum is notably more intense, also than that reported by Mesele *et al.* (Mesele *et al.*, 2016) In fact, the 1-butanol O_B-O_B coordination number (2.00), is higher than those reported in X-ray and neutron scattering studies (1.54 and 1.88). (Shmyt'Ko *et al.*, 2010; Cuello *et al.*, 2014)

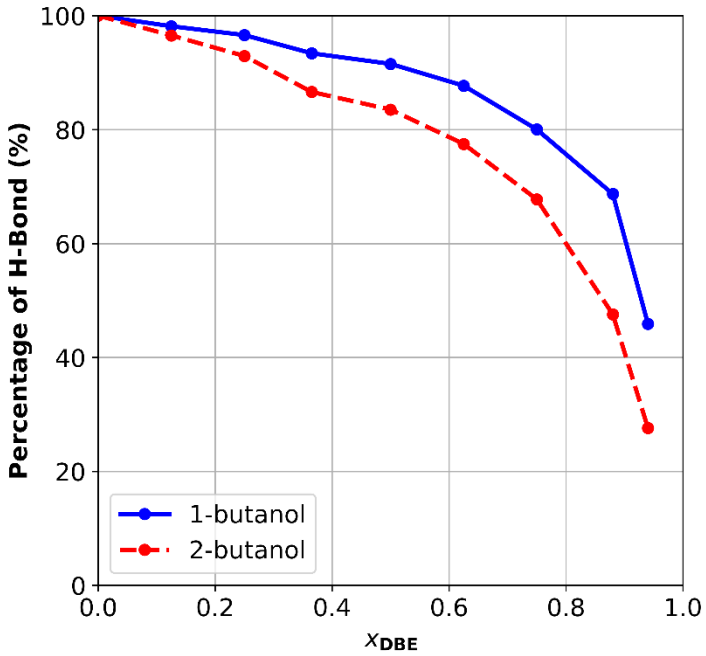

Figure 4.11 Normalized average numbers of butanol-butanol H-bonds, relative to those in the pure alcohols and expressed as a percentage, from MD simulations of 1- and 2-butanol-DBE mixtures, with DBE mole fraction x_{DBE}. Reproduced with permission from (Engelbrecht *et al.*, 2021). Copyright 2021 American Chemical Society.

In view of these differences, and considering also the too-low simulated *vs.* experimental H^E for the 1-butanol mixtures in **Figure 4.3**, it appears that the present 1-butanol model overestimates alcohol-alcohol H-bonding, both in the pure liquid and its DBE mixtures. Since H-bonding interactions are, within the present computational model, of a purely electrostatic nature, the above limitation points to the 1-butanol -OH group partial atomic charges (O: -0.71337 e; H: +0.43402 e) as possibly being too high (in an absolute sense). As described in the Section 4.2.1, these partial atomic charges were derived according to an electrostatic potential fitting protocol recommended for GAFF and are, in fact, in very good agreement with those of Caleman *et al.* (O: -0.7143 e; H: +0.4335 e), (Caleman *et al.*, 2012) which were similarly developed for use with GAFF parameters. Interestingly, Cerar *et al.* (Cerar *et al.*, 2017) made use of notably lower -OH group partial charges (O: -0.683 e; H: +0.418 e) in their comparative MD simulation and X-ray scattering study of pure 1-butanol, also in combination with the AMBER03 force field, which uses the same Lennard-Jones potential parameters as GAFF. Finally, the lower -OH group partial atomic charges derived for the present 2-butanol model (O: -0.69586 e; H: +0.397918 e) are generally consistent with the Compton scattering experiments and DFT calculations results of Hakala *et al.*, (Hakala *et al.*, 2009) that showed that the degree of charge delocalization is greater in the branched iso- and 2-butanol compared to the linear 1-butanol. Interestingly, this difference in charge distribution is not directly accounted for in the OPLS-AA force field used by Mesele *et al.*, (Mesele *et al.*, 2016) the only other reported MD simulation study comparing the liquid structures of butanol isomers, with all isomers having identical -OH group partial atomic charges.

4.6 Cluster analysis

MD simulations can provide detailed information on the size distributions and topologies of H-bonded alcohol self-associates (or *clusters*), (DeBolt and Kollman, 1995; MacCallum and Tieleman, 2002; Sillrén *et al.*, 2012; Janeček and Paricaud, 2013) differences and changes of which can affect the V^E of mixtures due to molecular packing effects, e.g. contribution (3) described in Section 4.3.3. In the present work, an algorithm was developed, employing H-bond criteria (1,2) described above, to identify such H-bonded alcohol clusters for the simulated 1- and 2-butanol-DBE mixtures. The computer script, written in tool command language ("tcl"), utilises the VMD program and its atom selection language. (Humphrey, Dalke and Schulten, 1996)

The script considers a single frame at time, iterating throughout all the alcohol molecules, creating nearest-neighbour lists based on the distance criteria of donor O (O_D)-acceptor O (O_A) (R_{OO}) and donor H (H_D)-O_A (R_{HO}) distances. These limiting distances were taken from the corresponding RDF first minima of the pure alcohols, which change only marginally upon mixing with DBE (**Table 4.3**). Finally, the nearest-neighbours lists are combined by a Python script (if the same alcohol molecules are presented in different lists), creating the final cluster lists. The clusters are saved as a list of molecule IDs ("resid" in VMD), that allows one to inspect the clusters by loading the frame in VMD and selecting the relevant cluster IDs. (Humphrey, Dalke and Schulten, 1996)

The H-bonded ring analysis script presents an additional H-bond criterion, which is the angle criterion ($\geq 135°$) for the O_D–H_D···O_A obtuse angle. However, the iteration is slightly different: the main iteration is the same as the cluster analysis but it is different for the presence of a sub-iteration; it starts from the selected molecule of the main iteration and follows with the nearest molecule that respects all distance and angle conditions (H-bonded). The sub-iteration continues to all the H-bonded molecules it finds, until no new nearest neighbours satisfying the criteria are found, or until it finds the initial (starting) molecule of the iteration, identifying the cluster as cyclic. Due to the fact that there are 2 iterations, it will find the same cyclic cluster as many times as the number of molecules in the ring; because of this, we used an "if" statement that identify for cyclic cluster replica and brake the sub-iteration. (Engelbrecht *et al.*, 2021)

The H-bonded cluster identification algorithm described above essentially produces, for each simulation configuration, a histogram of the count (occurrence) of H-bonded clusters of given size n_c; the algorithm may be applied to any number of trajectory frames and the results combined (averaged) in order to determine an average cluster size count distribution. Cluster count histograms for simulated pure 1-butanol obtained from analysis of a single configuration, 10 and 100

configurations are compared in **Figure 4.12** as example. The number of simulation frames to be analysed in order to obtain a converged cluster size distribution is an important consideration, since it not only affects the computational cost, but is also dependent on the system under investigation. Systems characterised by a wide cluster size distribution including large cluster sizes that occur only occasionally, e.g. pure 1-butanol, require the analysis and averaging of many more frames compared to systems having a narrower distribution, e.g. pure 2-butanol. The results for the two simulated pure butanol isomers, illustrating this effect, are shown in **Figure 4.13**; note that in the case of pure 1-butanol, the characteristic cluster size distribution of smaller clusters (e.g. $n_c \leq 10$) effectively converges even when considering only a modest number of simulation frames (100), while the long "tail" at larger cluster sizes only becomes regular when averaging over thousands of frames (e.g. $n_c > 100$, specific sizes having very low occurrence).

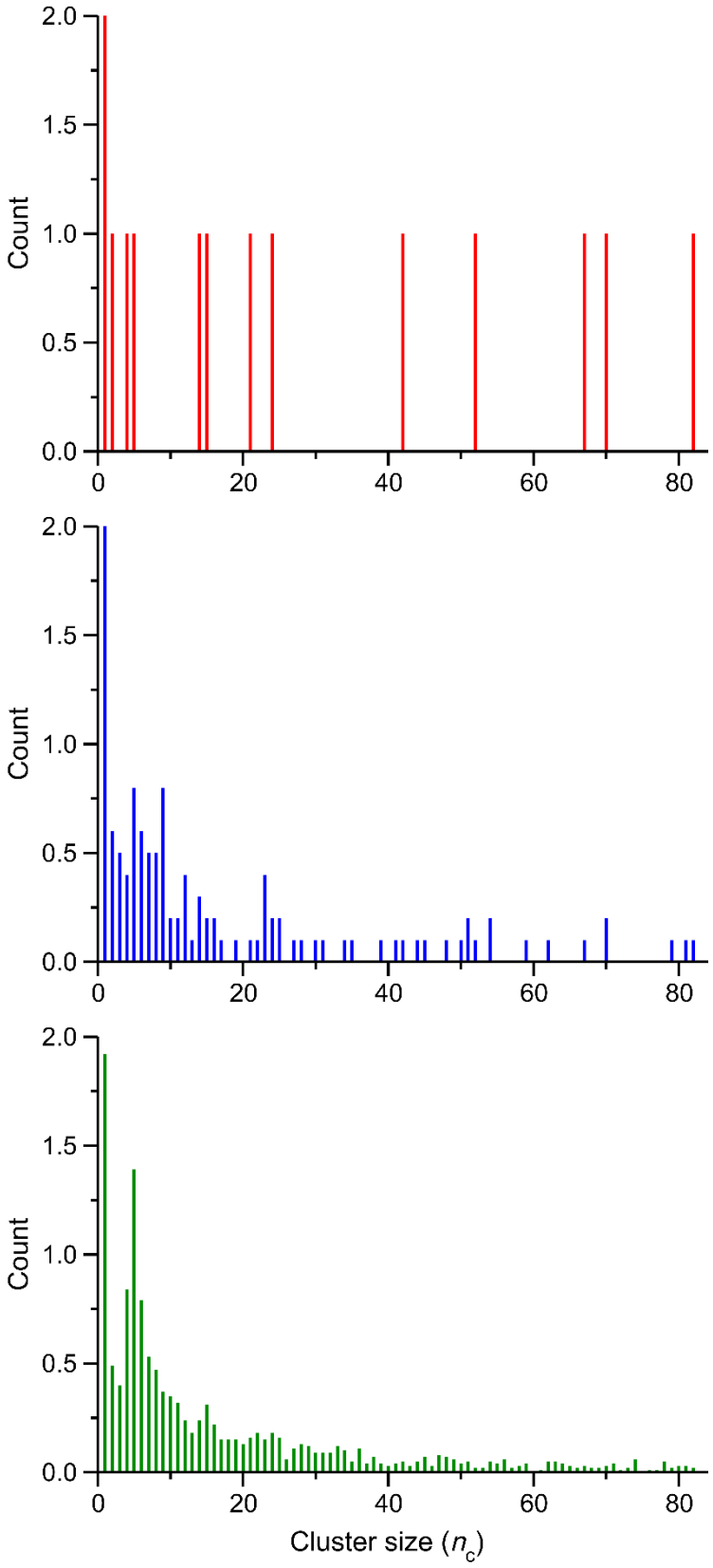

Figure 4.12 H-bonded 1-butanol cluster count histograms for clusters of size n_c from analysis of **1 (top)**, **10 (middle)** and **100 (bottom)** simulation configurations.

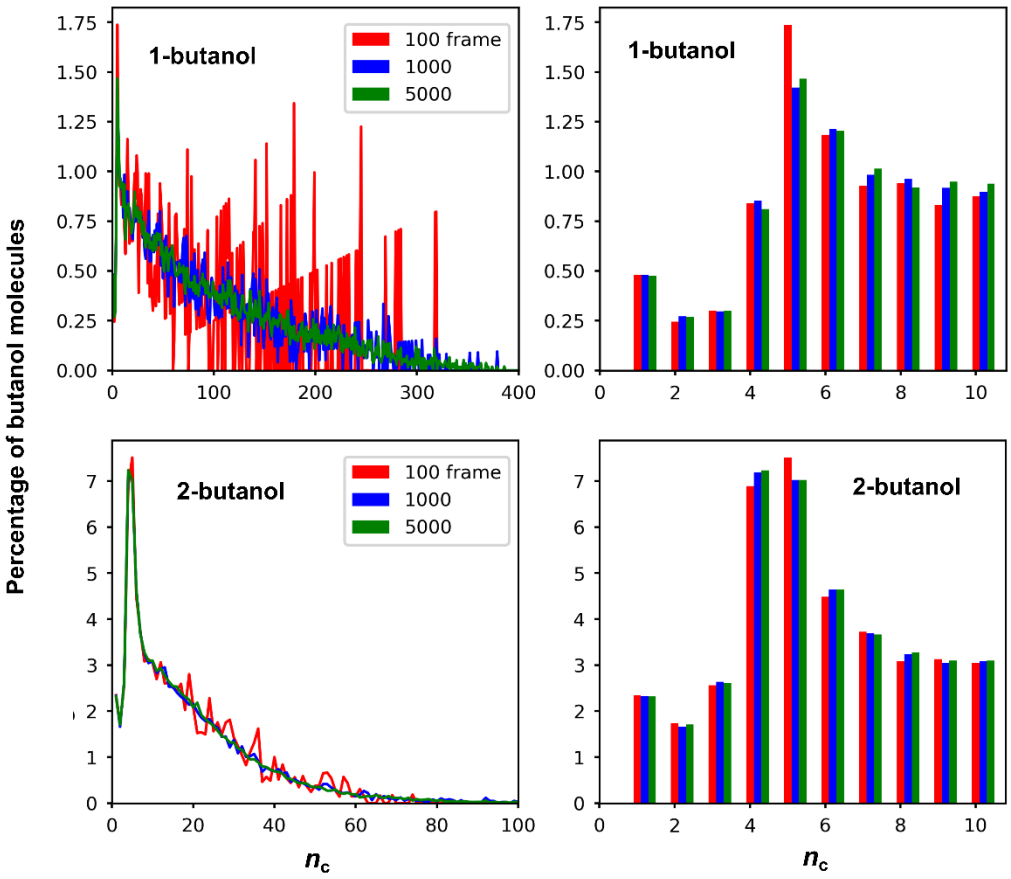

Figure 4.13 Convergence of H-bonded cluster analysis data for simulated pure 1-butanol (top) and 2-butanol (bottom). The graphs show the fraction of butanol isomers participating to clusters of size n_c for different numbers of simulation frames analysed.

In this study, 1,000 frames were used for all simulated systems as reasonable compromise, since the interest is primarily in the mixture systems which are characterised by much smaller H-bonded alcohol cluster sizes with a narrow distribution. Cerar *et al.*, (Cerar *et al.*, 2017) for example, considered only 100 frames in their MD simulations of pure 1-butanol, though using a different computational model (with a smaller average H-bonded cluster size).

The *average* H-bonded alcohol cluster sizes, $\langle n_c \rangle$, for all simulated 1- and 2-butanol – DBE mixtures are reported in **Table 4.5**. As inferred from the local H-bond analysis presented in the preceding section, the average cluster sizes in 1-butanol and its DBE mixtures are larger than those of corresponding 2-butanol systems at all compositions studied and decrease with increasing x_{DBE}. The $\langle n_c \rangle$ of simulated pure 1-butanol, 27.7, is significantly larger than that reported in previous computer simulation studies (< 4), (Sillrén *et al.*, 2012) estimated from near-IR measurements (7.5), (Iwahashi *et al.*, 2000) and estimated using a modified ERAS model (14). (Wandschneider, Michalik and Heintz, 2006) Previous computer simulation studies of pure 1-butanol used different force field

models and H-bonded neighbour search criteria, nevertheless, the discrepancy in $\langle n_c \rangle$ further supports the notion that the current GAFF model overestimates the extent of 1-butanol H-bonding.

Table 4.5 Average H-bonded butanol isomer cluster size, $\langle n_c \rangle$, for simulated 1- and 2-butanol-DBE mixtures.

x_{DBE}	Average cluster size $\langle n_c \rangle$	
	1-butanol	**2-butanol**
0.000	27.7	8.0
0.125	16.5	6.0
0.250	11.1	4.7
0.375	8.3	3.9
0.500	6.3	3.3
0.625	5.0	2.7
0.750	3.6	2.2
0.880	2.4	1.6
0.940	1.7	1.3

Computer simulation studies of alcohol self-association frequently represent the H-bonded cluster size distribution as a *fraction* (percentage) of alcohol molecules participating to clusters of given size n_c, e.g. **Figure 4.13**. (DeBolt and Kollman, 1995) Cluster count data, like that in **Figure 4.12**, are easily converted to this representation, which is shown for representative simulated mixtures in **Figure 4.14**. With the latter representation it is apparent that, while $n_c = 1$ is the most frequently occurring size in the simulated pure butanol isomers ($x_{DBE} = 0$; **Figure 4.12**), it accounts for only a small *fraction* of alcohol molecules: < 1 % for 1-butanol, < 3 % for 2-butanol For pure 1-butanol, a low maximum occurs at $n_c = 5$, while $n_c = 4$ (max.) and 5 are clearly prominent in 2-butanol. Nevertheless, most 1- and 2-butanol molecules participate in larger clusters, $n_c > 10$, suggesting that the properties of these pure liquids are primarily determined by the nature of their extensive H-bonded network structures. In fact, the smallest "cluster" size, $n_c = 1$, (no alcohol neighbours) has the highest *occurrence* (average count) in all simulated systems, followed by notably low counts of H-bonded dimers and trimers ($n_c = 2,3$), before increasing again for tetramers (prominent for 2-butanol), pentamers (prominent for 1-butanol) and hexamers. Similar H-bonded size distributions have been reported for simulations of 1-hexanol (Stubbs *et al.*, 2001; Stubbs and Siepmann, 2005) and 1-octanol, (DeBolt and Kollman, 1995; MacCallum and Tieleman, 2002) as well as for their aqueous and alkane binary mixtures; the higher occurrence of $n_c = 4$-6 has been attributed to the increased relative stability

of such clusters, especially since they are able to form energetically favourable cyclic H-bonded structures (additional H-bond compared to non-cyclic structures); larger clusters become increasingly entropically unfavourable, resulting in slowly decreasing "tails" for $n_c > 6$. In fact, for tert-butanol, the formation of tetrameric H-bonded cycles, or "rings", has been shown to be a characteristic feature of both the pure liquid and its alkane binary mixtures.(Rytting, Anderson and Higuchi, 1978; Andanson *et al.*, 2005; Sassi *et al.*, 2007)

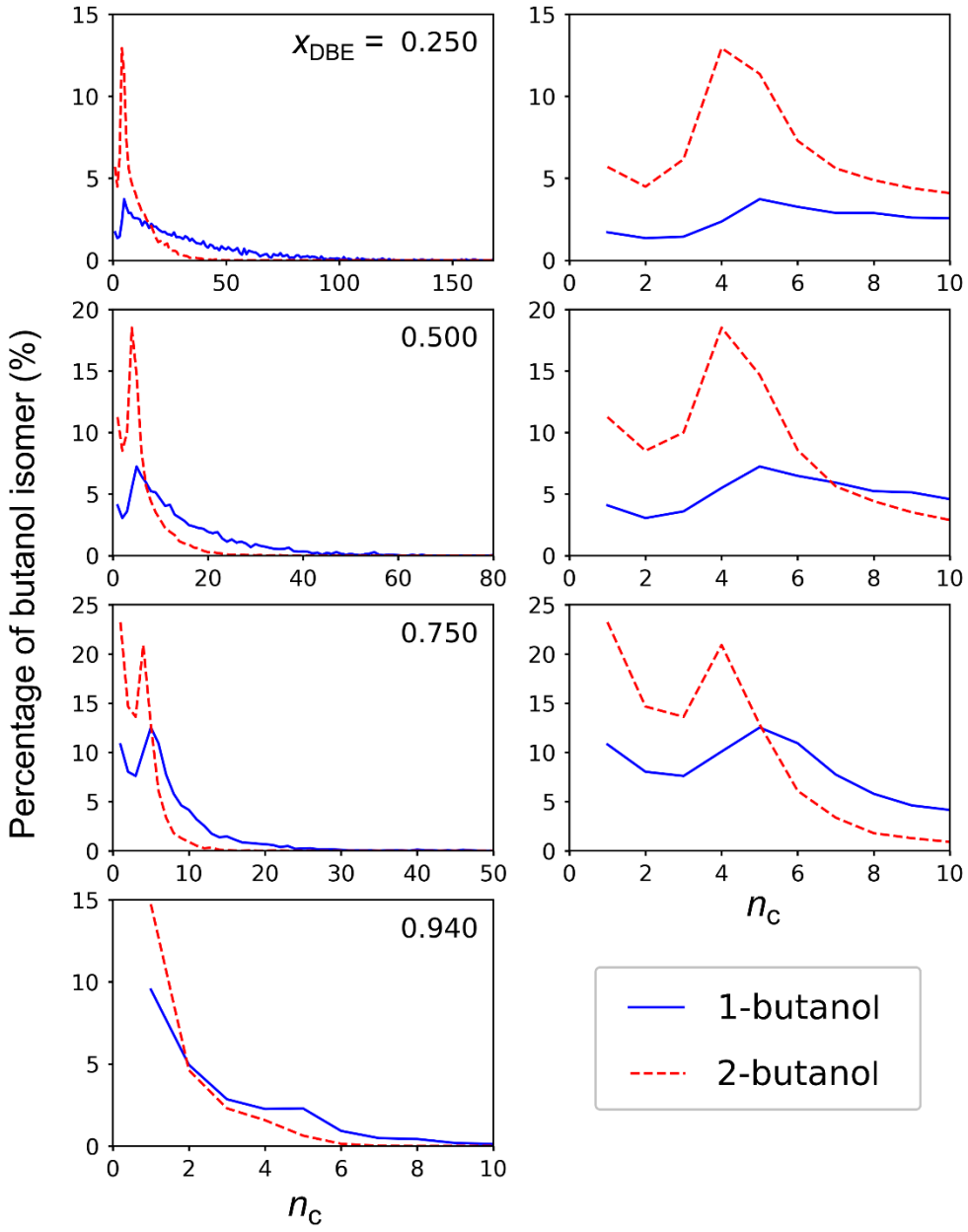

Figure 4.14 Percentage of 1- and 2-butanol molecules contributing to H-bonded clusters of size n_c. The number label in each panel in the column on the left corresponds to the mole fraction DBE, with corresponding panels on the right showing an expansion of the smaller cluster size range $n_c \leq 10$, as relevant to the discussion in the main text.

Upon dilution of the pure butanol isomers with DBE, the large H-bonded alcohol clusters are increasingly broken down, and smaller cluster sizes become more prominent in the mixtures. The H-bonded cluster size preferences observed for the pure butanol isomers, i.e. pentamers (n_c = 5) for 1-butanol and tetramers (n_c = 4) for 2-butanol, persist and intensify in the DBE mixtures, with non-self-associated (n_c = 1) molecules accounting for an increasingly larger butanol isomer fraction. For example, in the composition range x_{DBE} = 0.50 - 0.75, H-bonded tetramers and pentamers together account for > 30 % of 2-butanol molecules. The fractions of 1- and 2-butanol molecules participating in specific H-bonded cluster sizes n_c = 1-6, and > 6, are plotted as a function of x_{DBE} in **Figure 4.15**. The tendency of 1-butanol to strongly associate via H-bonding is evident in its fraction participating in larger clusters, n_c > 6, at all compositions studied, while for 2-butanol, tetramer (n_c = 4) is clearly important, with a maximum around $x_{DBE} \approx 0.7$. The H-bonded cluster topology differences may be illustrated by considering the simulation snapshots (x_{DBE} = 0.50) in **Figure 4.16**, where DBE molecules have been omitted from the representation in the interest of clarity. Here, 1-butanol molecules may be seen to engage in long chain-like H-bonded clusters, whereas 2-butanol tends to form smaller, more compact clusters with a larger number of single-molecule units (n_c = 1), i.e. not H-bonded to other 2-butanol molecules.

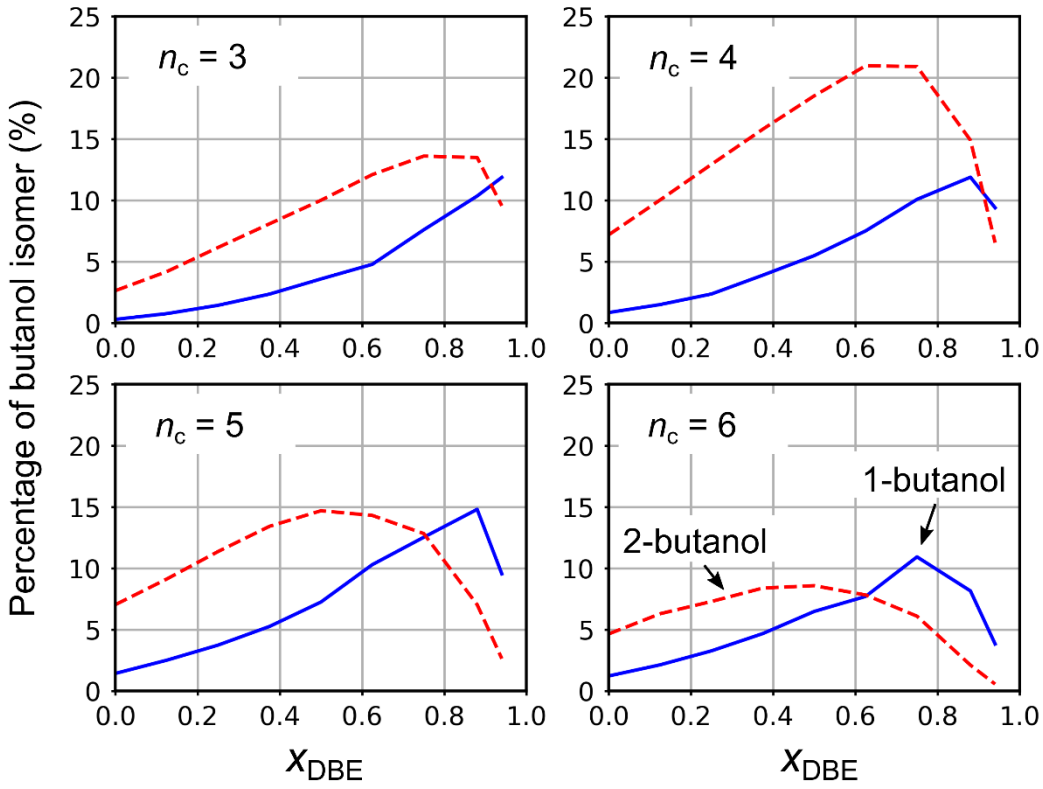

Figure 4.15 Percentage of 1- (blue solid line) and 2-butanol (red dashed line) molecules in H-bonded alcohol clusters of size n_c = 3, 4, 5, and 6, plotted as a function of mixture composition, x_{DBE}.

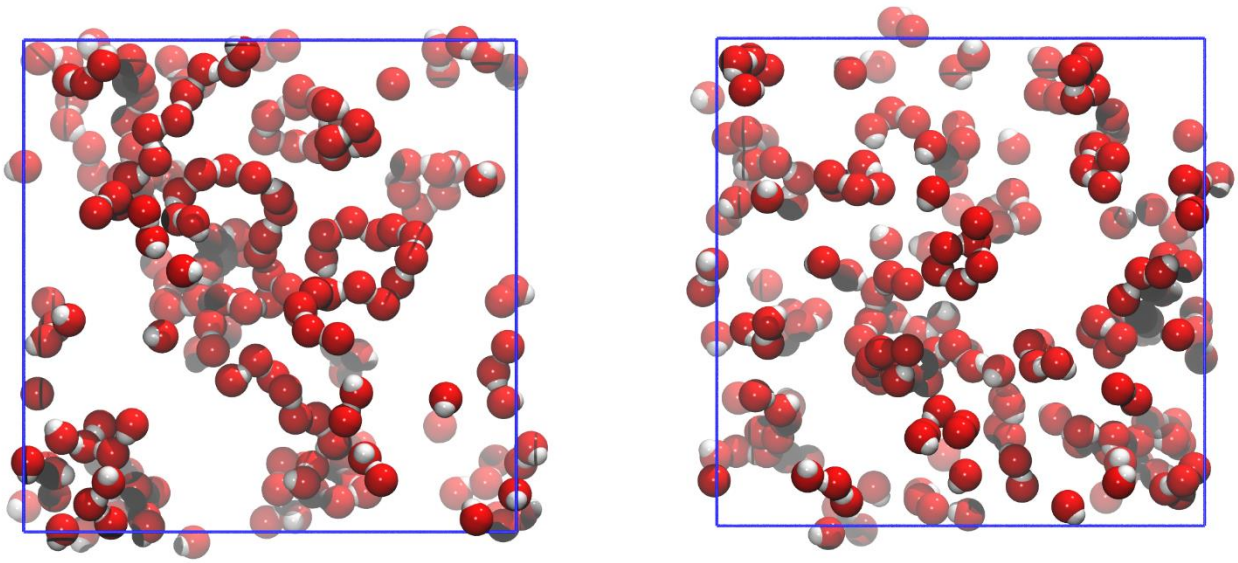

Figure 4.16 Representative configurations from MD simulations of (*left*) 1-butanol, and (*right*) 2-butanol-DBE equimolar mixtures (x_{DBE} = 0.5). DBE molecules and butanol isomer alkyl groups have been omitted in the interest of clarity, with butanol -OH groups shown using a space-filling representation (red and white spheres correspond to O and H atoms respectively).

As noted before, the increased prominence of n_c = 4 - 6 upon dilution of alcohols with alkanes has been explained as due to the formation of stable cyclic H-bonded alcohol clusters. (Stubbs and Siepmann, 2005; Wandschneider, Michalik and Heintz, 2006) Interestingly, Aida *et al.*, (Aida *et al.*, 2010) in their classical MD simulation study of volume expansion phenomena in various short chain alcohol - CO_2 binary mixtures, reported H-bonded alcohol cluster distribution histograms similar to those in **Figure 4.14**, notably for 1- and *tert*-butanol. For these butanol isomers it was also shown that a significant fraction of H-bonded tetramers (*tert*-butanol) and pentamers (1-butanol) are, in fact, simple ring structures, the formation of which also feature prominently in their proposed explanation of the observed volume expansion. Visual inspection of our simulation trajectories, e.g. **Figure 4.16**, also reveals the presence of such H-bonded butanol rings, with a notably higher occurrence in 2-butanol systems. A representative 4-membered H-bonded 2-butanol ring configuration, isolated from the simulation frame in **Figure 4.16**, is shown in **Figure 4.17 (a, b)**, where the alkyl groups of the ring members may be seen to adopt alternating up/down relative orientations, likely in order to minimize steric repulsion and consequent ring strain, as had been proposed for cyclic H-bonded tetramers in liquid *tert*-butanol, its alkane mixtures and vapors.(Fanourgakis *et al.*, 2003; Andanson *et al.*, 2005; Sassi *et al.*, 2007) A similar 1-butanol configuration shown in **Figure 4.17 (c, d)** notably does not exhibit this relative alkyl chain orientation (more below).

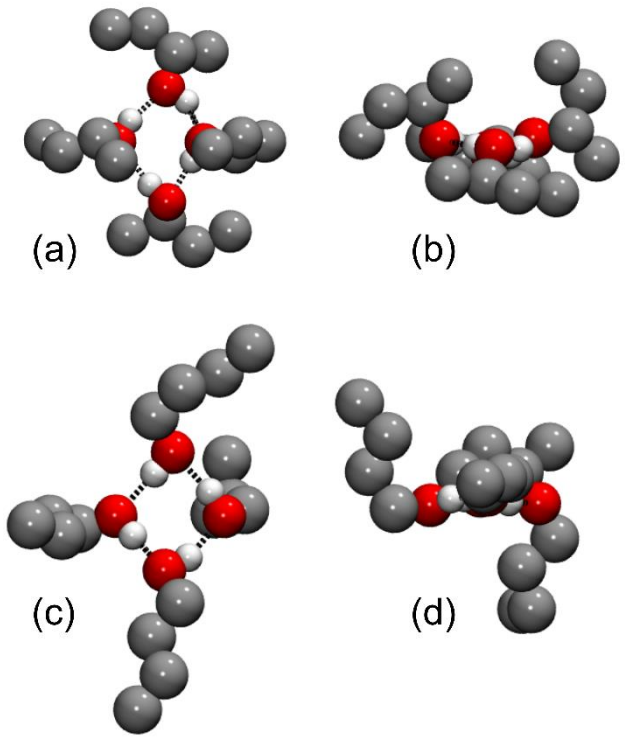

Figure 4.17 Representative 2-butanol (top row) and 1-butanol (bottom row) 4-membered H-bonded ring configuration: (a, c) top views of effective ring planes; (b, d) side views. Aliphatic H atoms have been omitted in the interest of clarity; O atoms in red, C atoms grey, and H white. The figures make use of a space-filling ("van der Waals") representation, with default van der Waals radii (VMD) scaled by a factor 0.5 in order to better show the H-bonded cluster core. (Humphrey, Dalke and Schulten, 1996) H-bonds are represented as dotted black lines. Reproduced with permission from (Engelbrecht *et al.*, 2021). Copyright 2021 American Chemical Society.

4.7 Analysis of cyclic H-bonded structures

In order to more effectively monitor the formation of cyclic H-bonded motifs, an additional algorithm was developed using the H-bond criteria (1-3) described in Section 4.5, that records *only* cyclic cluster counts. The results of this procedure, which initially provides histogram data similar to those in **Figure 4.12**, are plotted in **Figure 4.18** for selected H-bonded ring sizes, n_r. The smallest possible H-bonded ring size, $n_r = 3$, is notably absent in this figure; the reason for this omission is that the average fractions of both 1- and 2-butanol molecules participating in such small rings were found to be < 2 % in all systems studied, likely as a consequence of high ring strain, suggesting that this arrangement most likely does not significantly affect the physical properties of the mixtures studied.

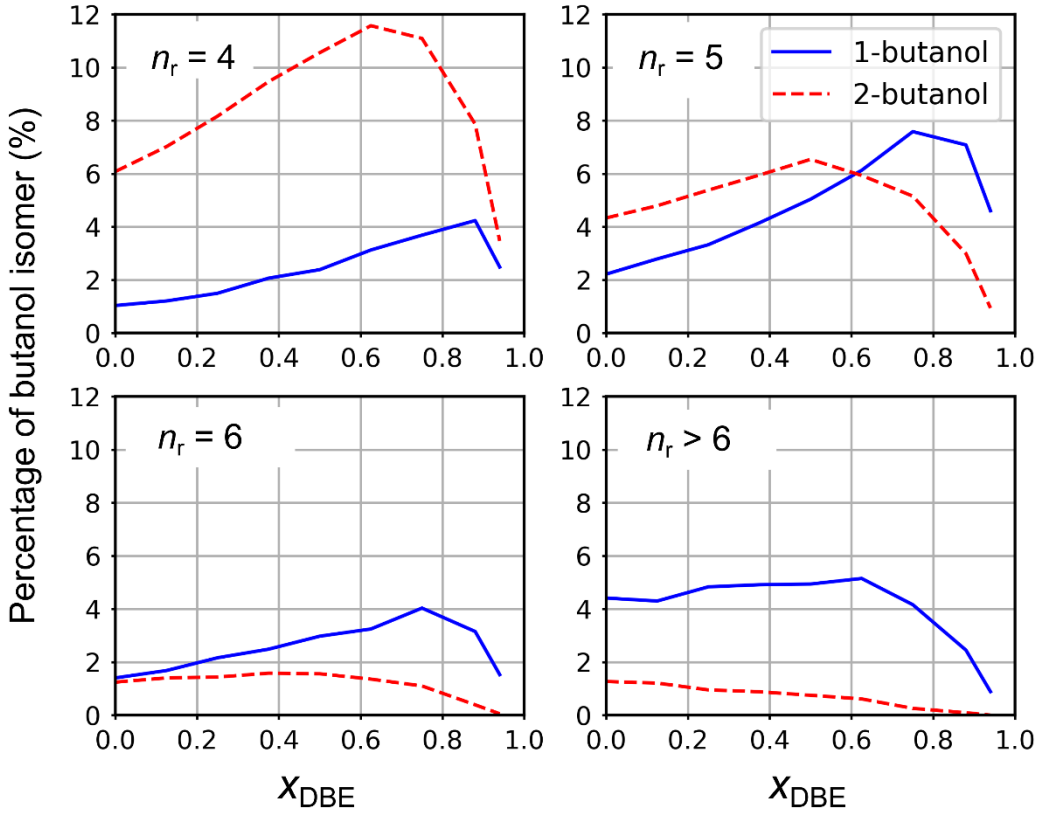

Figure 4.18 Percentage of 1- (blue solid line) and 2-butanol (red dashed line) molecules in cyclic H-bonded alcohol motifs of size n_r = 4 (a), 5 (b), 6 (c), and > 6 (d), plotted as a function of mixture composition, x_{DBE}.

For H-bonded ring sizes n_r = 4 and 5 in **Figure 4.18**, the butanol isomer fraction variations of both 1- and 2-butanol closely resemble those of the corresponding H-bonded cluster sizes, n_c = 4 and 5 in **Figure 4.15**, suggesting that a significant fraction of these H-bonded rings are, in fact, individual clusters of corresponding size, as opposed to being part of larger clusters. As noted in Section 4.6, similar findings were reported by Aida *et al.* (Aida *et al.*, 2010) for 1-butanol H-bonded pentamers

(*ca.* 70 % cyclic) and *tert*-butanol tetramers (80 % cyclic) in simulated binary mixtures of these butanol isomers with CO_2; the formation of such small H-bonded rings were proposed to play an important role in bringing about the lower-than-expected densities (volumetric expansion) occurring in these mixtures. In fact, considering the variation of 2-butanol molecules in H-bonded tetrameric rings ($n_r = 4$) in **Figure 4.18**, with its maximum at $x_{DBE} = 0.625$ (~ 12 % of 2-butanol molecules), and comparing this variation with the V^E trend of the simulated 2-butanol mixtures in **Figure 4.4**, similar symmetry and maxima positions may be noted, suggestive of a possible correlation between the presence of such ring configurations and the simulated system volume.

4.8 Preliminary investigation of structure-volume correlation

A preliminary investigation of selected simulation time blocks, spanning tens to hundreds of picoseconds, appears to support the above hypothesis: **Figure 4.19** compares the fluctuations in the simulated system volume with the variation of 2-butanol molecules in tetrameric H-bonded rings found by the algorithm over the final 150 of a DBE mixture ($x_{DBE} = 0.625$) simulation. While very "noisy" (high-frequency fluctuations), the running averages of these datasets, taken over 9 sequential datapoints (originally separated by 1 ps), appear to be correlated, even if somewhat offset considering minima/maxima features.

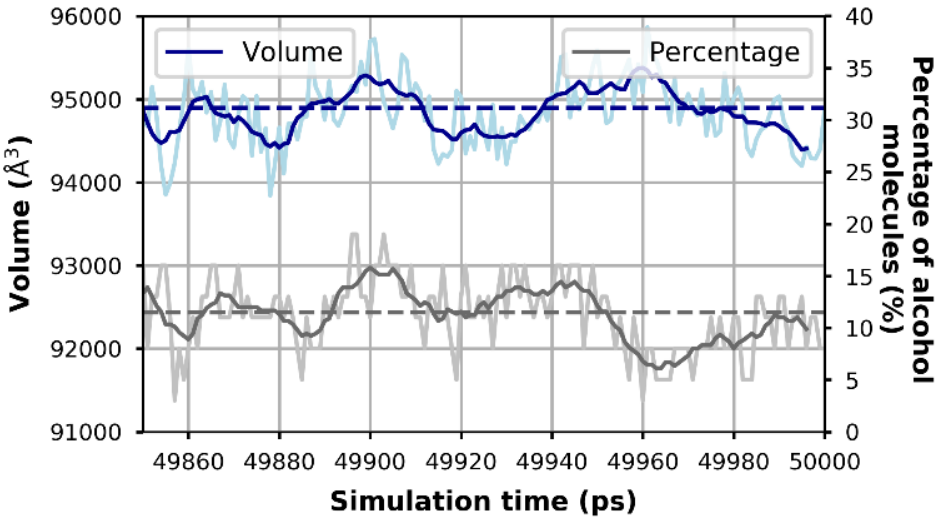

Figure 4.19 Variation of simulated system volume (blue, primary y-axis) and number of 4-membered ($n_r = 4$) 2-butanol rings (grey, secondary y-axis) over the final 150 ps for a selected 2-butanol - DBE mixture simulation trajectory ($x_{DBE} = 0.625$). In order to facilitate comparison of variation trends for the two datasets, 9-point running averages have been plotted in bold blue and grey lines for system volume and 4-membered ring fraction, respectively. Horizontal dashed lines show the trajectory average values. Reproduced with permission from (Engelbrecht *et al.*, 2021). Copyright 2021 American Chemical Society.

It must be stressed that the possible correlation described requires more dedicated computational study. For example, in **Figure 4.19**, not every time block recording higher-than-average volumes shows prominent tetrameric ring fractions, and it is highly likely other molecular configurations contribute to the volume expansion in such instances, e.g. pentameric rings or intermediate structures. Indeed, the 2-butanol tetrameric ring fraction plotted in this figure is dependent on the ring identification algorithm, with its particular H-bond criteria, and does not identify more deformed structures (e.g. intermediate) which may have similar volumetric properties.

On the other hand, for 1-butanol-DBE mixtures, which have negative V^E, there appears to be no apparent correlation between the simulated V^E trend shape and the presence of particular H-bonded 1-butanol rings (i.e. comparing **Figure 4.4** & **Figure 4.18**). The prominent tetrameric H-bonded rings of 2-butanol adopt the characteristic "up/down" alkyl group configuration shown in **Figure 4.17 (a, b)**, which likely serves to relieve the steric repulsion and ring strain produced by the bulky alkyl groups (this alternating up/down arrangement is not possible for cyclic pentamers). Such configurations prevent strong H-bonding or dipolar interactions of surrounding molecules with the H-bonded core, resulting in high-volume local arrangement. (Sassi *et al.*, 2007; Aida *et al.*, 2010) Conversely, 1-butanol tetrameric (and, importantly, pentameric) rings, shown in **Figure 4.17 (c, d)**, with their more mobile, linear alkyl groups are expected to allow for more favorable interactions with surrounding molecules. Nevertheless, the notably more asymmetric simulated V^E data for the 1-butanol mixtures compared to experiment, specifically the higher (more positive) simulated V^E values at high x_{DBE}, does suggest a contribution from the increased fraction of 1-butanol molecules in H-bonded rings of sizes n_r = 4-6 at these compositions, **Figure 4.18**.

Finally, considering the 6-membered (n_r = 6) and larger (n_r > 6) butanol isomer H-bonded ring size data in **Figure 4.18**, the fraction of 1-butanol molecules involved in such structures may be seen to be greater than for 2-butanol in all mixtures studied. This observation is consistent with the larger average H-bonded 1-butanol cluster sizes (**Table 4.5**); however, for these larger H-bonded ring sizes the variations as a function of x_{DBE} differ noticeably from those of the corresponding total H-bonded cluster size data (n_c) in **Figure 4.15**, unlike the case of n_c/n_r = 4 and 5 described above. For 1-butanol, larger H-bonded rings (n_r > 6) appear to be rather important motifs over most of the mixture composition range, with the percentage of 1-butanol molecules contributing to such rings remaining essentially constant at 4-6 % up to *ca.* x_{DBE} = 0.6. Regardless, the variation of H-bonded ring sizes $n_r \geq 6$ do not appear to correlate with the simulated V^E for the mixtures studied, with the possible exception of n_r = 6 in the case of 1-butanol, which shows a variation similar to that of n_r = 5 (see above); this observation seems reasonable considering that large cyclic H-bonded structures should

not occupy a significantly greater volume compared to a linear or branched H-bonded cluster having the same number of members (n_c).

4.9 Conclusions

The binary liquid mixtures of either 1- or 2-butanol with di-*n*-butyl ether (DBE) have been studied by MD computer simulations for the first time. The results were compared with newly performed calorimetric and densitometry measurements. (Engelbrecht *et al.*, 2021)

The simulations satisfactorily reproduce the experimentally extensively-studied differences in the excess molar enthalpies (H^E) and volumes (V^E) of these mixtures and directly demonstrate, for the first time, notable differences in butanol isomers self-association *via* H-bonding in these mixtures, as well as more subtle differences in butanol-DBE cross-species H-bonding, both of which have been implicated in previous explanations of the excess thermodynamic properties of alcohol-ether binary mixtures. Specifically,

- Pure 1-butanol and its DBE mixtures were found to be characterized by larger average H-bonded self-associate sizes and broader size distributions compared to corresponding 2-butanol mixtures, which prominently feature 4- and 5-membered H-bonded associates.

- The H-bonded clusters in 1-butanol and its DBE mixtures are more compact, with 1-butanol molecules interacting through shorter H-bonds than those between the 2-butanol isomers.

- The higher H^E experimentally observed for 2-butanol-DBE mixtures is explained by the greater relative disruption of H-bonds when DBE is added to 2-butanol with respect to adding it to 1-butanol, while the number of H-bonds to DBE is essentially the same for the two isomers at any concentration. Taken together, these two observations indicate a larger energetic counterbalance of the reduction in the alcohol self-association by the formation of butanol-DBE H-bonds in 1-butanol mixtures compared to those of 2-butanol.

- An H-bond topological analysis revealed a significant fraction of such small H-bonded 2-butanol clusters to be simple cyclic structures, and that the increased prominence of 4-membered H-bonded 2-butanol cycles, in particular, appears to show a correlation with the characteristic V^E variation of these mixtures. While a fuller understanding of the effect of small cyclic H-bonded self-associates on the volumetric properties of these mixtures must await a more comprehensive computational study, the present results show that MD

simulations can reasonably reproduce the excess thermodynamic properties of these mixtures and provide detailed information on the nature of molecular self-association phenomena.

A literature survey reveals very few computational reports describing correlations between specific H-bonded self-associated topologies, e.g. cyclic structures of given size, and anomalous liquid mixture densities, or V^E. (Sassi *et al.*, 2007; Aida *et al.*, 2010) On the other hand, the effects of cross-species H-bonding modes on binary liquid mixture excess thermodynamic properties, e.g. as leading to negative V^E by interstitial molecular accommodation phenomena, (Usula *et al.*, 2014; Kgagodi and Mbaiwa, 2017) have been studied in detail, notably for aqueous mixtures. In this context, while the computer simulation results presented here largely support existing interpretations of the different V^E of 1- and 2-butanol - DBE mixtures, namely as due to more prominent cross-species H-bonding in 1-butanol - DBE mixtures and greater retention of alcohol-alcohol H-bonds upon mixing with DBE, (Patil, Pathak and Pradhan, 1989; Kammerer and Lichtenthaler, 1998; Bernazzani *et al.*, 2006) we have shown that changes in the nature of H-bonded alcohol self-associates, e.g. increasing fraction of alcohol molecules in cyclic H-bonded clusters with increasing DBE content of the mixture, may indeed account for an important additional V^E contribution. As noted, more focused computational studies may reveal the precise importance of the presence of such cyclic H-bonded structures and the physical mechanism by which these affect the mixture density, e.g. reduced strength of interactions with surrounding molecules, poor molecular packing, or inherently high volume of such configurations.

5 Micro-heterogeneity in ethylammonium nitrate ionic liquid – acetonitrile mixtures

The work reported in this chapter has been included in a chapter of the book *Theoretical and Computational Approaches to Predicting Ionic Liquid Properties*, Elsevier, 2021. (Mariani *et al.*, 2021), and was performed, in part, using computational resources provided by the HPC-Europa3 transnational access programme (project code HPC170K5MD) at the PDC Center for High Performance Computing, KTH, Stockholm.

Most often, the size of the simulated systems used to model liquid mixtures can be kept relatively small compared to those of, e.g. of biological macromolecules and nucleic acids. However, as recently highlighted by X-ray scattering experiments, some liquid mixtures can be characterized by long-range ordering, revealed by the so-called "low q excess" (LqE) in SAXS patterns. In such cases, in order to accurately reproduce the large-scale structural organization of the liquid, the simulation box should be considerably larger than typical liquid mixtures simulation. The size of the system depends on the particular q value range of interest, but in general they are too big to be amenable with all-atom (atomistic) MD simulations, and coarse-grained (CG) models have to be developed. While CG models are becoming more and more popular, there is still no default, standard procedure to develop the CG model and its interaction parameters for highly charged particles such as ionic liquids (ILs).

The issues related to the study of liquid mixtures exhibiting the SAXS LqE are described in this chapter, which first introduces some important details of IL structure in Section 5.1, and information about the detection of the LqE in an IL-organic solvent binary mixture. The computational details, particularly important in this case, are described Section 5.2, while the analysis of the results, comprising also the calculations of the SAXS patterns from CG models, are described in Section 5.3. The main conclusions are summarised in Section 5.4.

5.1 Introduction

Ethylammonium nitrate (EAN, **Figure 5.1**) is a prototypical protic ionic liquid (IL), a diverse group of ionic substances formed typically by an organic cation and inorganic (or, less frequently, organic) anion, that are liquid at much lower temperatures (typically below 100 °C) than inorganic molten salts. EAN was discovered more than a century ago, (Walden, 1914) and has been identified as the earliest true room-temperature IL (RTIL), having a melting point of 12.5 °C; the related protic IL ethanolammonium nitrate, discovered already in 1888, (Gabriel and Weiner, 1888) has a melting point of 52-55 °C. (Greaves and Drummond, 2008) More recently, there has been a renewed interest in ILs in general as potential alternatives to conventional organic solvents in view of their low volatility (as pertains to environmental/health concerns) (Holbrey and Rogers, 2002) and highly-tuneable physicochemical properties.

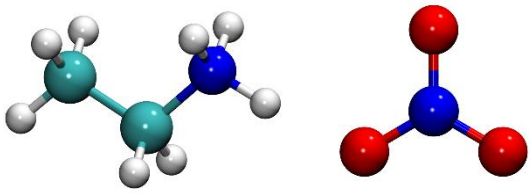

Figure 5.1 Molecular structure of ethylammonium (cation, left) nitrate (anion, right).

5.1.1 Ionic liquid structure

Neutron scattering experiments (SANS) have revealed the liquid structure of EAN to be characterized by nanometer-scale molecular segregation, consisting of percolating bi-continuous polar and non-polar regions (or "domains"), a "sponge-like" structure. (Atkin and Warr, 2008; Hayes *et al.*, 2011) Polar regions, consisting of nitrate anions and cationic ammonium groups (interacting through strong H-bonding interactions), and non-polar regions, in which the ethylammonium alkyl groups cluster together (see below), also have different average electron densities, resulting in electron density fluctuations which are repeated throughout the whole system, which, in turn, produce a characteristic neutron scattering peak. (Atkin and Warr, 2008) This dynamic micro-heterogeneous structure is also responsible for the characteristic low-*q* pre-peak (or "L*q*P", $q \approx 0.67$ Å^{-1}) in the small- and wide-angle X-ray scattering (SAXS/WAXS) pattern of EAN, shown in **Figure 5.2**, which, together with the intense main peak ($q = 1.66$ Å^{-1}), constitute a unique "fingerprint" for this liquid structure. (Russina *et al.*, 2014)

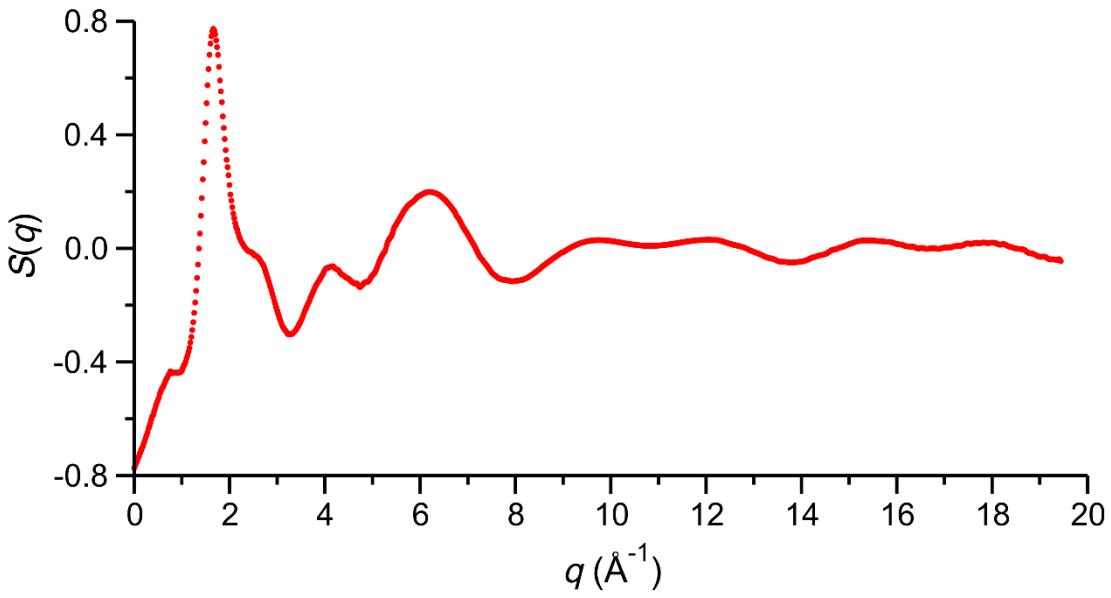

Figure 5.2 Experimental WAXS pattern of pure EAN ionic liquid at 298.15 K. The low-q pre-peak ("L*q*P", $q \approx 0.67$ Å^{-1}) is the first low shoulder on the low-q side of the intense main peak (1.66 Å^{-1}). Data kindly provided by A. Mariani.

Computer simulations, both MC and MD, have been instrumental in understanding the molecular-level structure of EAN (and many other ILs), especially since structure functions, $S(q)$, may be computed from the simulation configurations and compared with experiment as a means of validating the simulated structure. (Hayes *et al.*, 2011; Mariani *et al.*, 2016) Simulations also allow for the extraction of *partial structure functions*, which show the contributions of individual particle pair correlations to the total scattering pattern; such partial structure functions (which are not experimentally accessible) may be combined in order to evaluate the $S(q)$ contributions by specific IL components, e.g. anion-anion ($S(q)_{-,-}$), anion-cation ($S(q)_{+,-}$), etc. It follows that the total structure function of the IL may be expressed as a function of such contributions, $S(q) = S(q)_{+,+} + S(q)_{-,-} + S(q)_{+,-}$. (Mariani *et al.*, 2021) The partial structure functions computed from MD simulations of EAN, as well as the related propyl- (PAN) and butylammonium nitrate (BAN) ILs, have revealed the LqP to be primarily due to NO_3-NO_3 long-range correlations, i.e. $S(q)_{-,-}$. (Mariani *et al.*, 2016)

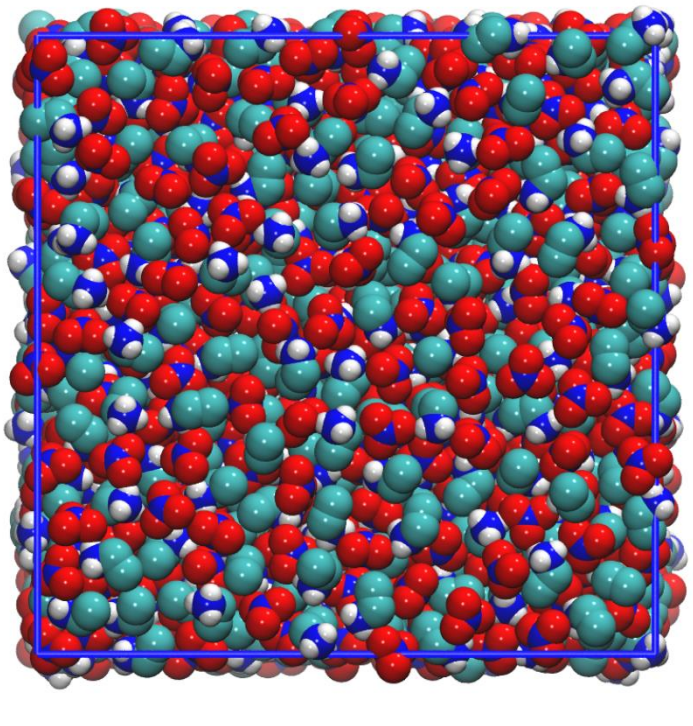

Figure 5.3 Simulation configuration (AA MD) of pure EAN liquid at 300 K. All components shown using a space-filling representation in VMD; (Humphrey, Dalke and Schulten, 1996) colour code: C cyan, H white, N blue and O red. Aliphatic H atoms have been omitted in the interest of clarity. The simulation cell edges are shown in blue. Data kindly provided by A. Mariani.

The local molecular structure and intermolecular interactions, e.g. H-bonding, in EAN have been extensively studied by analysis of radial and spatial distribution functions (RDFs and SDFs, introduced in Section 2.4), computed from computer simulation trajectories. (Umebayashi *et al.*, 2008; Huang *et al.*, 2016; Mariani *et al.*, 2021) The percolating "sponge-like" domain structure of liquid EAN (as well as PAN and BAN) under different pressures have been characterised by a Voronoi tessellation-based domain analysis method, (Mariani *et al.*, 2016) included in the TRAVIS trajectory analysis software package. (Brehm and Kirchner, 2011; Brehm *et al.*, 2015) This method has proven highly successful in studies of IL domain structures as it allows for the construction of particle neighbour lists without prior knowledge of the interaction type or its characteristic parameters (distances, angles etc.), i.e. it can be applied to study atomic contacts in a general sense. (Brehm *et al.*, 2015) A unique Voronoi polyhedron (VP) is assigned to each atom of the simulated system according to established rules, thus partitioning the entire simulation configuration into such polyhedra; any two atoms sharing a polyhedron face are now considered Voronoi neighbours. All atoms, in turn, are assigned to IL domains, i.e. atoms forming part of highly charged groups are assigned to the "polar/ionic" domain, whereas those forming aliphatic chains may be assigned to the "non-polar" domain. The unique Voronoi neighbour lists of all atoms may now be used in order to determine all "polar" and "non-polar" domains, such that the number of domains, their sizes and shapes may be determined. As for the H-bond cluster analysis described above, the procedure may be repeated for the remaining simulation trajectory frames in order to obtain time-averaged properties or their time evolution.

5.1.2 SAXS low-*q* excess

Addition of certain molecular solvents, notably *n*-alcohols, (Jiang *et al.*, 2014; Russina *et al.*, 2014) to EAN have been found to result in unexpectedly high SAXS pattern intensities at very low q values, in the so-called extreme low-q region (q < 0.5 Å^{-1}), indicative of the formation of large-scale molecular aggregates. This scattering, referred to as the low-q excess ("LqE", a term borrowed from the definition of excess thermodynamic properties), has also been observed for binary mixtures of EAN with acetonitrile; in fact, one such mixture, at low EAN content (x_{EAN} = 0.1, i.e. molar ratio 1:9), produces the most intense LqE scattering reported to date for mixtures of this type. (Mariani *et al.*, 2017) This LqE SAXS pattern is reproduced in **Figure 5.4**, has been interpreted as due to the presence of large molecular aggregates of effectively cylindrical ("rod") shape, as evaluated from the slope s of the SAXS signal decay ($s \propto q^{-1}$). (Mariani *et al.*, 2021) Atomic-resolution ("atomistic") MD simulations, showing nanometer-scale phase separation in these mixtures, further support the proposed liquid structure, characterised by worm-like EAN regions surrounded by acetonitrile. (Mariani *et al.*, 2017) A representative MD simulation configuration of the EAN-acetonitrile 1:9 mixture is shown in **Figure 5.5** (a).

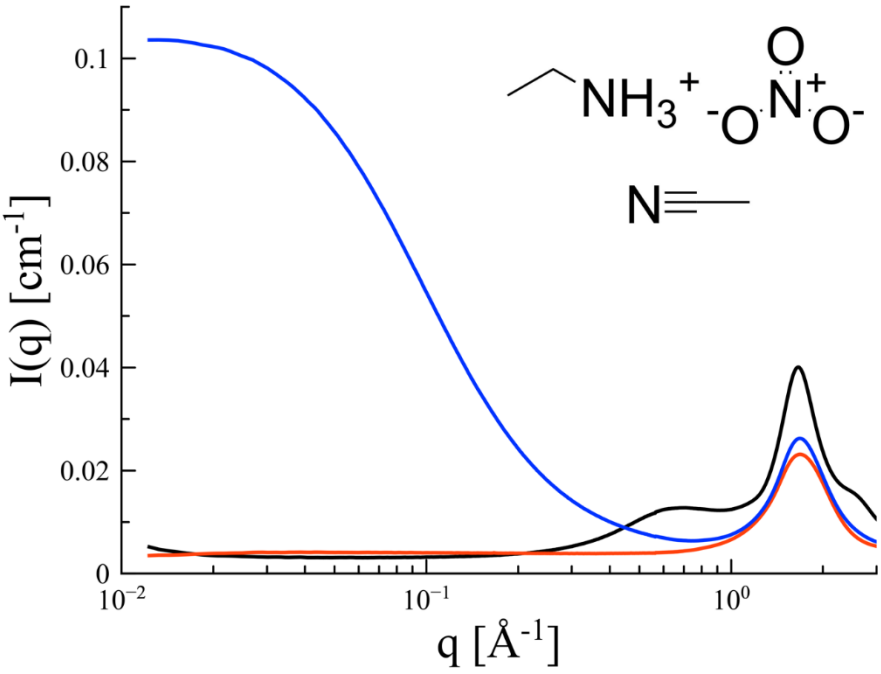

Figure 5.4 Experimental SAXS patterns of EAN (black), acetonitrile (red) and the EAN-acetonitrile 1:9 molar ratio mixture (blue), showing the LqE at low q < 0.5 Å^{-1}. Reproduced with permission from (Mariani *et al.*, 2021). Copyright 2021 Elsevier.

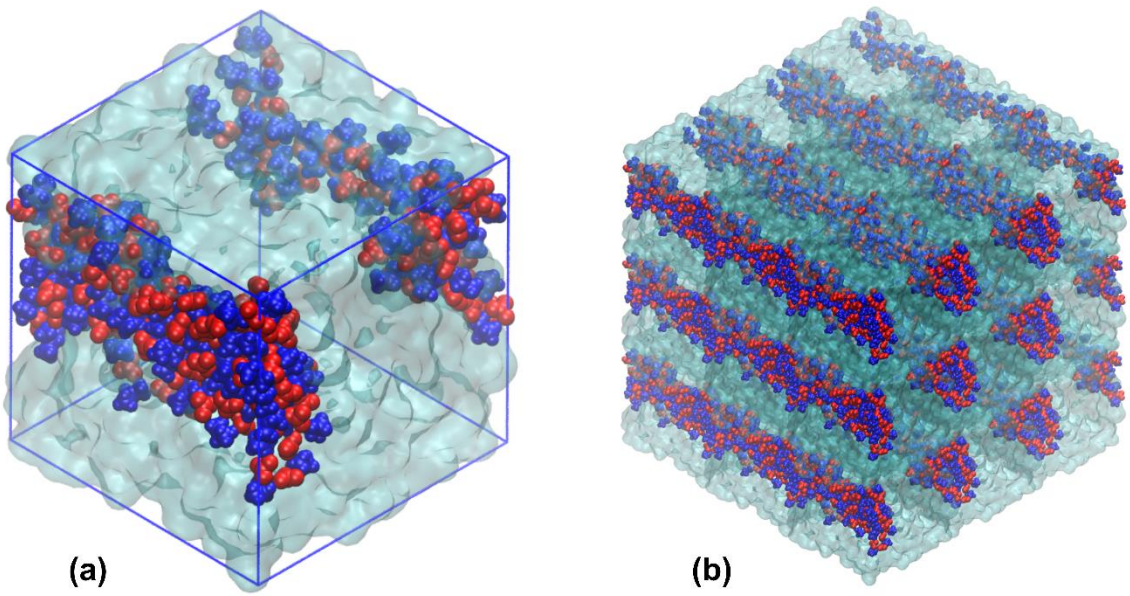

Figure 5.5 (a) Representative AA MD simulation configuration of the EAN-acetonitrile (1:9) mixture (T = 300 K) Ethylammonium cations (blue) and nitrate anions (red) make use of a space-filling ("van der Waals") representation, while the acetonitrile nano-phase is represented by a transparent cyan surface. The simulated system consists of 830 EAN ion pairs and 7470 acetonitrile molecules, with cubic simulation cell edge length *ca.* 53 Å. **(b)** Periodic representation (replicated 3 × 3 × 3). Reproduced with permission from (Mariani *et al.*, 2021). Copyright 2021 Elsevier.

The MD simulation represented in **Figure 5.5 (a)** provides a convincing picture of the nanometer-scale phase-separated structure of the macroscopically fully-miscible EAN-acetonitrile mixture. A periodic image representation, obtained by replicating this simulation configuration in three dimensions, is shown in **Figure 5.5 (b)** and represents an "idealised" larger-scale liquid structure exhibiting worm-like EAN aggregates. (Mariani *et al.*, 2017, 2021)

While atomistic MD simulations described above effectively reproduce the experimental WAXS patterns ($q \leq \sim 1$ Å^{-1}) of the EAN-acetonitrile mixtures, their proposed, "extrapolated" large-scale liquid structures, e.g. **Figure 5.5 (b)**, cannot be directly validated against the experimental LqE, because the highly-periodic nature of such "ideal" configurations results in a crystalline, highly order-type modulated $S(q)$, **Figure 5.6**. It follows that periodic representations, like that in **Figure 5.5 (b)**, while fitting the essential structural elements inferred from the experimental SAXS patterns, are not suitable for the study of the large-scale structure of such liquid systems. (Mariani *et al.*, 2017)

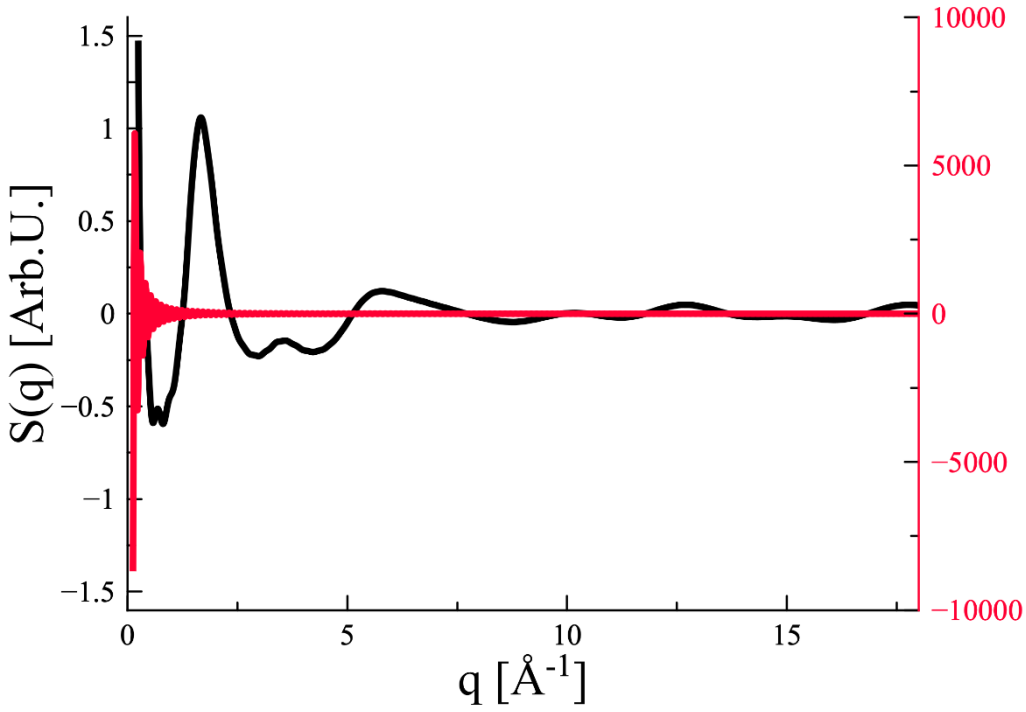

Figure 5.6 Experimental WAXS spectrum of EAN-acetonitrile (1:9) mixture (black, primary axis), compared with that calculated from periodic AA MD simulation configurations (red, secondary axis), e.g. **Figure 5.5 (b)**. Reproduced with permission from (Mariani *et al.*, 2021). Copyright 2021 Elsevier.

Accurate computational reproduction of the experimental L*q*E of the EAN-acetonitrile (1:9) system would require an exceedingly large model, having dimensions of up to 130 nm; such an extensive system would contain over *24 million* molecules, representing a prohibitively high computational cost considering a conventional atomistic model e.g. **Figure 5.5**. (Mariani *et al.*, 2017, 2021) The coarse-grained (CG) molecular modelling approach, introduced in Section 2.5, presents a computationally affordable approximation, allowing for the simulation of models representing hundreds of thousands to millions of atomic sites, and have been successfully applied in structural studies of ILs. (Wang *et al.*, 2013; Wang *et al.*, 2020) In the case of EAN, however, only a single CG MD study has been reported to date, that of Mehta and Levin, (Mehta and Levin, 2018) developed with the aim of studying electrospray propulsion emissions. The aim of the present study was to develop an appropriate CG model of the EAN-acetonitrile (1:9) mixture able to produce a more realistic picture of the nanoscale phase separation thought to be responsible for the intense L*q*E observed in the experimental SAXS pattern of this liquid mixture.

5.2 Computational details

5.2.1 Atomistic MD simulations

Atomistic MD simulations were previously performed (Mariani *et al.*, 2017) using the Amber 18 simulation package, (Case *et al.*, 2005) employing the GAFF (Wang *et al.*, 2004) force field, with atomic partial charges derived by electrostatic potential fitting using the RESP algorithm (Dupradeau *et al.*, 2010), based on quantum chemical calculations at the B3LYP/aug-cc-pVTZ level of theory using Gaussian09d. (Frisch *et al.*, 2009) The atomic partial charges for the EAN ions were scaled by a factor 0.74 (i.e. reduced by 26 %) in order to account for the effect of charge transfer from the nitrate anion to ethylammonium cation. (Mariani *et al.*, 2017) Starting configurations were prepared by random placement of EAN ions and acetonitrile molecules in cubic simulation cells, with periodic boundaries, using Packmol. (Martínez *et al.*, 2009)

The simulation equilibration was as follows: after a 10^7-step energy minimization, the system was first heated by a short (100 ps) NVT simulation at 50 K; this initial heating was followed by a 40 ns NPT MD simulation at the target temperature (300 K), and then by another 40 ns in the NVT ensemble, finally followed by the 10 ns NVT production phase. The X-ray scattering pattern was calculated from the simulation trajectory using the TRAVIS software. (Brehm and Kirchner, 2011)

5.2.2 CG model development

A CG model of the EAN-acetonitrile (1:9) mixture was developed using the systematic structure-based coarse-graining approach, (Lyubartsev and Laaksonen, 1995) as implemented in the MagiC (2.4) software package. (Mirzoev and Lyubartsev, 2013) The CG mapping scheme for the mixture components is shown in **Figure 5.7**, with each CG bead located at the centre of mass of the constituent atomic configuration. The partial electronic charges of the CG beads are similarly computed as the sum of the corresponding atomic partial charges. It should be noted that the only previously reported CG mapping of EAN employed a similar scheme, (Mehta and Levin, 2018) but with the ethylammonium cation represented by thee instead of two beads; acetonitrile has traditionally been represented using “united-atom” models, i.e. 3-site, or, more recently, as a single CG bead. (Wagner *et al.*, 2017)

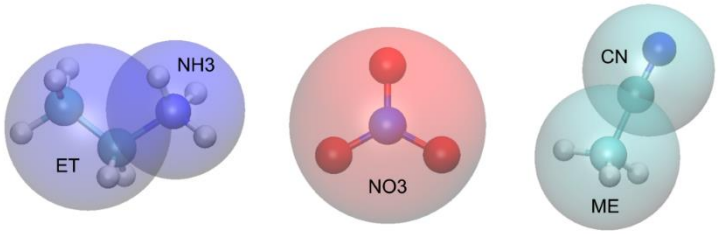

Figure 5.7 CG mapping scheme for EAN ions (ethylammonium left, nitrate centre) and acetonitrile (ACN, right). Atomic sites included the same transparent sphere are assigned to the same CG site, or "bead", the name of which is indicated (e.g. the ethylammonium cation ethyl group atoms are all assigned to a single CG bead with name "ET"). Reproduced with permission from (Mariani *et al.*, 2021). Copyright 2021 Elsevier.

The essential CG effective potential refinement procedure employed is described in Section 2.5.3, with the main steps for the present system as follows. (1) The IL mixture reference structure, described by a set of reference RDFs, was obtained from the AA MD simulation described in the Section 5.2.1: essentially, MagiC's *CGTRAJ* script applies the chosen CG mapping scheme to the reference atomistic trajectory, after which the *rdf.py* script operates on the newly-produced CG reference trajectory, computing the set of reference CG RDFs. (Mirzoev and Lyubartsev, 2013) (2) The initial trial CG effective potential set (all-zero starting potentials were chosen) was then refined using the Iterative Boltzmann Inversion (IBI) and Inverse Monte Carlo (IMC) algorithms implemented in MagiC's kernel, with starting configurations randomly taken from the CG mapped reference trajectory. Representative sets of CG RDFs (both reference and final iteration-MC sampled), with corresponding optimised CG effective potentials are plotted in **Figure 5.8** & **Figure 5.9**; these may be seen to be in very good agreement, and the results were deemed satisfactory for large-scale CG MD simulation. Original CG potentials were processed prior to use in MD simulations; this involved interpolation (more grid points added), smoothing and extension. (Mirzoev and Lyubartsev, 2013)

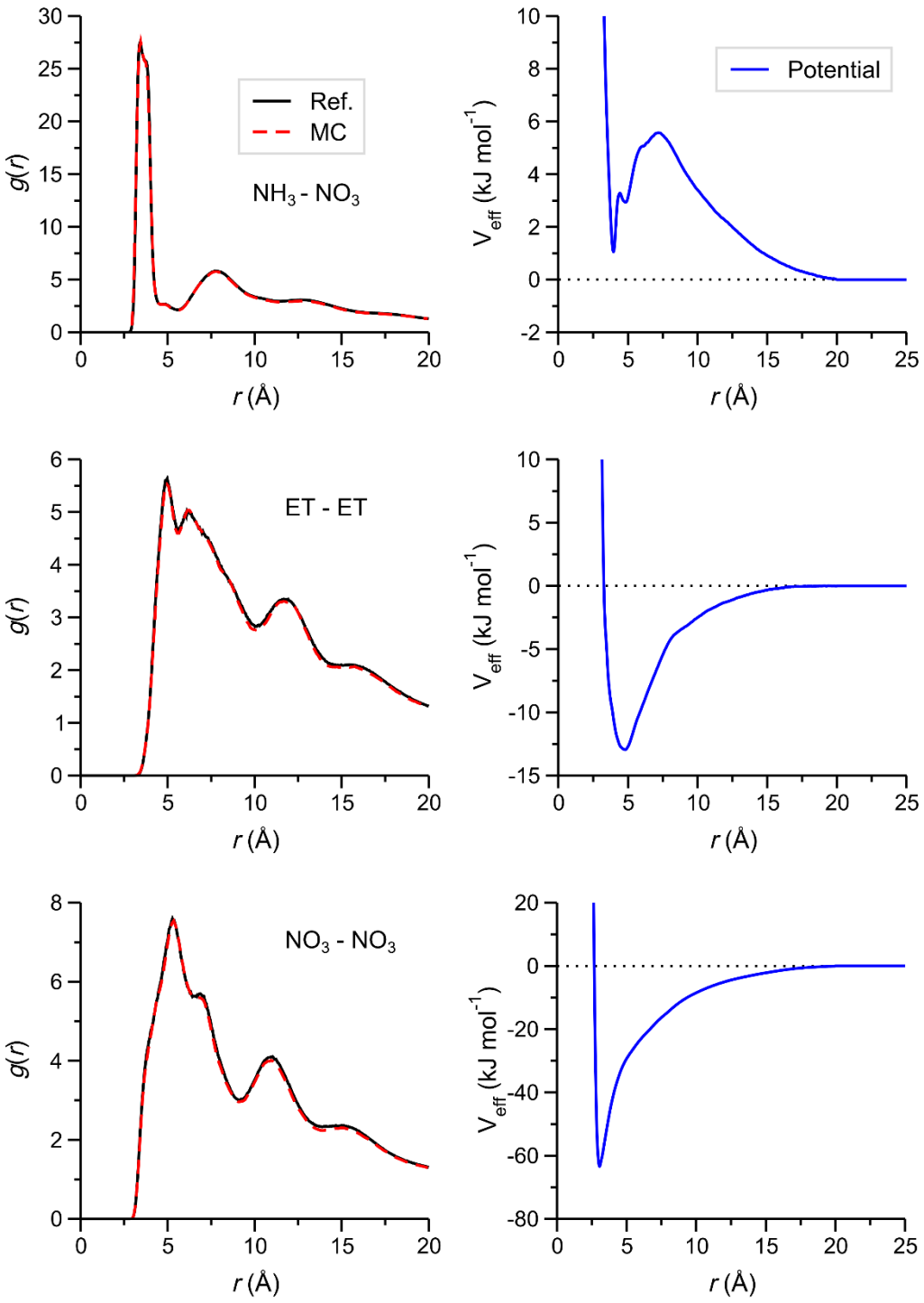

Figure 5.8 Left: Selected CG RDFs for the simulated EAN-acetonitrile (1:9) mixture, describing intermolecular interactions in the EAN phase: reference RDFs (obtained from CG representation of the AA MD reference simulation) in black solid line; CG RDFs from Monte Carlo simulation, final iteration of IMC procedure, red dashed line. **Right:** Corresponding final CG effective potentials, V_{eff}, blue solid line.

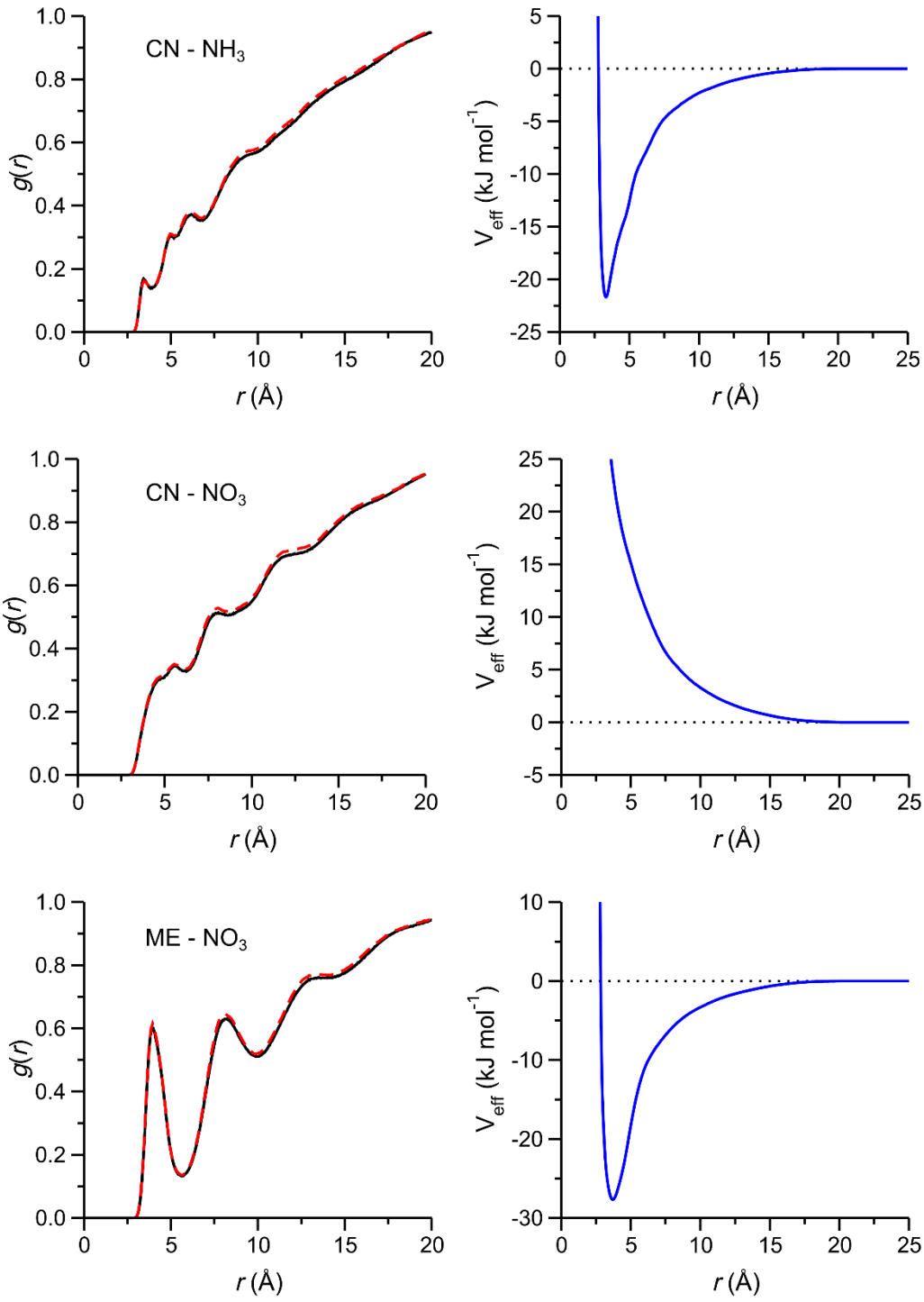

Figure 5.9 Left: Selected CG RDFs for the simulated EAN-acetonitrile (1:9) mixture, describing intermolecular interactions between EAN and acetonitrile CG beads: reference RDFs (obtained from CG representation of the AA MD reference simulation) in black solid line; CG RDFs from Monte Carlo simulation, final iteration of IMC procedure, red dashed line. **Right:** Corresponding final CG effective potentials, V_{eff}, blue solid line.

5.2.3 Large CG initial configuration preparation

The potentials governing the CG interactions are obtained as described in the previous section by optimizing the reproduction of structural reference properties of an AA system of the same size. Once the CG potentials are obtained, they can be applied to systems of any size. However, for the CG simulations the choice of the starting configurations is not straightforward, and some choices have to be made. In this investigation, the large CG starting configuration was prepared by replication of a single configuration taken from the CG-mapped reference trajectory four times in three dimensions (i.e. "4×4×4", 63 periodic images), resulting in a large cubic periodic system with edge lengths ~203 Å; **Figure 5.10 (a)**. While not sufficiently large to finely reproduce the entire L*q*E, this large CG model, consisting of 8,576 EAN ion pairs and 76,800 acetonitrile ("ACN") CG models (for a total of 179,328 CG beads, representing 589,440 atoms), allows for SAXS pattern calculation down to $q \approx 0.06$ Å^{-1} (provided, of course, system configurations can be appropriately sampled by e.g. MD simulation), compared to ~0.25 Å^{-1} using conventional AA MD. (Mariani *et al.*, 2021) While a highly periodic starting configuration may seem less than ideal, this approach has been used in previous large-scale CG MD simulations of IL systems (Bhargava and Klein, 2009); the systematic structure-based CG potential development approach used here technically allows for CG simulation of the system under identical conditions, and is intended to reproduce the structural features found in the equilibrium reference (AA MD) simulation on a large scale. It is not entirely clear if, or how (since CG dynamics differ from that of an atomistic model), the CG model structure will develop starting from a randomly-distributed configuration (i.e. a configuration that did not exist in the reference simulation), or under otherwise different physical conditions or ensembles. The investigation of these effects, including possible potential corrections to allow for accurate reproduction of thermodynamic properties, (Noid *et al.*, 2008; Wang, Junghans and Kremer, 2009; Lyubartsev *et al.*, 2010) require a more focused study, and in view of computer allocation limitations, a periodic representation of an existing simulation configuration was chosen as starting configuration, with all CG MD simulations performed under constant volume conditions (NVT).

5.2.4 CG MD simulations

All CG MD simulations were performed using the GROMACS 2016.4 software package. (Abraham *et al.*, 2015) Simulations were performed under constant volume (NVT), using Langevin dynamics with a 10 ps^{-1} friction coefficient and reference temperature 300 K. The MD time step was 2 fs. (Dunn and Noid, 2015) The non-bonded interaction cut-offs were set to 20 Å, with long range electrostatic interactions treated by the Particle Mesh Ewald (PME) method (using the default parameters in GROMACS); periodic boundary conditions were implemented throughout. The large CG system was simulated for a total simulation time of 50 ns, requiring about two days' allocation on 128 Xeon E5-2698v3 cores ("Beskow" supercomputer, KTH, Stockholm). A detailed performance comparison with the atomistic methodology was beyond the scope of the present study, though it is expected that an atomistic model of similar dimensions would require weeks of computer time using the same resources (Mariani *et al.*, 2021) Simulation trajectories were visualised and analysed (RDF calculation) using VMD. (Humphrey, Dalke and Schulten, 1996)

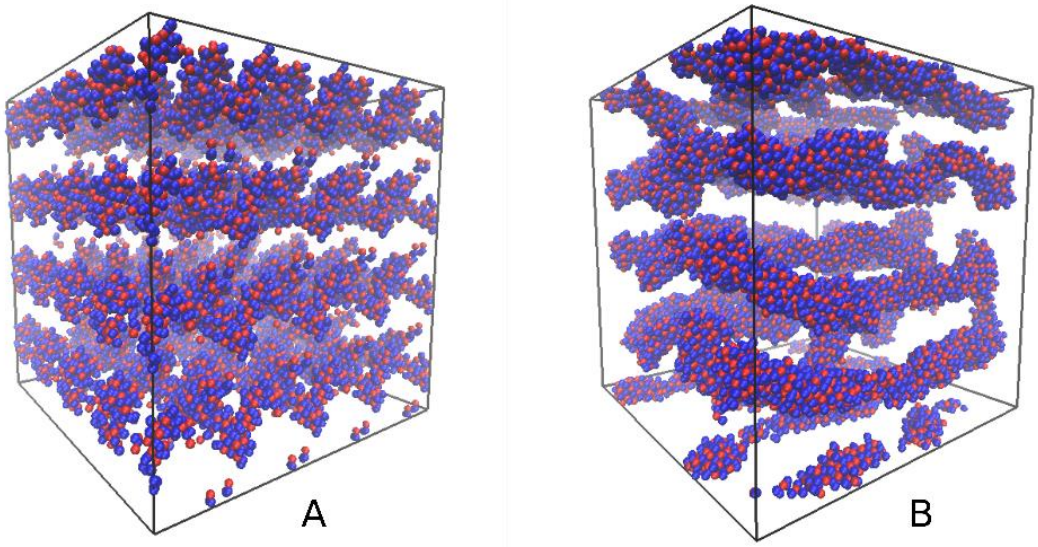

Figure 5.10 Large CG model configurations of the EAN-acetonitrile 1:9 mixture (300 K): **(a)** 4×4×4 (xyz) periodic representation (edge length ~ 203 Å) of CG-mapped atomistic configuration, used as starting structure for the large-scale CG MD simulation; **(b)** final configuration of the 50 ns-long CG MD simulation. In both panels, cations are shown in blue, anions in red, and acetonitrile molecules have been removed in order to better show the evolution of the EAN self-associates. (Mariani *et al.*, 2021)

5.3 Results

5.3.1 Visual inspection and note on system equilibration

The large CG periodic starting configuration is represented in **Figure 5.10 (a)**, with acetonitrile molecules removed so as to better show the development of EAN aggregates (cations blue; anions red). As demonstrated in **Figure 5.5**, EAN self-association is observed in AA MD simulations and, consequently, characterises the highly-periodic CG starting configuration, resulting in it having a "layered" appearance.

A representation of the final CG MD configuration (production time = 50 ns) is shown in **Figure 5.10 (b)**, where it may be compared with the periodic starting structure. The final configuration may be seen to contain effectively cylindrical, worm-like EAN aggregates, consistent with the essential average structure inferred from both the experimental SAXS signal slope ($\propto q^{-1}$; rod-like aggregates) in the extreme low-q region, and the periodic representations of AA MD configuration, e.g. **Figure 5.5 (b)**. (Mariani *et al.*, 2017) The EAN "worms" in **Figure 5.10 (b)** exhibit highly aligned, nearly parallel relative orientations, which are to some extent due to the periodic starting structure and relatively short simulation time (50 ns). Nevertheless, the CG MD simulation undoubtedly provides a more irregular, realistic liquid structure compared to a simple periodic representation.

5.3.2 RDFs

Selected RDFs, computed from the last 10 ns of the 50 ns-long CG MD simulation described above, are plotted in **Figure 5.11** & **Figure 5.12**. As was the case for the CG MC RDF in **Figure 5.8** & **Figure 5.9**, the RDFs from the large-scale CG MD simulation compare rather well with reference structure ($r \leq 20$ Å), confirming that the CG model does indeed reproduce the essential AA MD simulation structure at short distances. The CG MD RDFs, however, were calculated up to a distance of 100 Å (simulation cell edge = 203 Å) and it may be noted that at these longer distances the RDFs do not simply complete convergence to $g(r) = 1$, but instead show broad undulations around this value, indicative of long-range ordering and consequent density fluctuations.

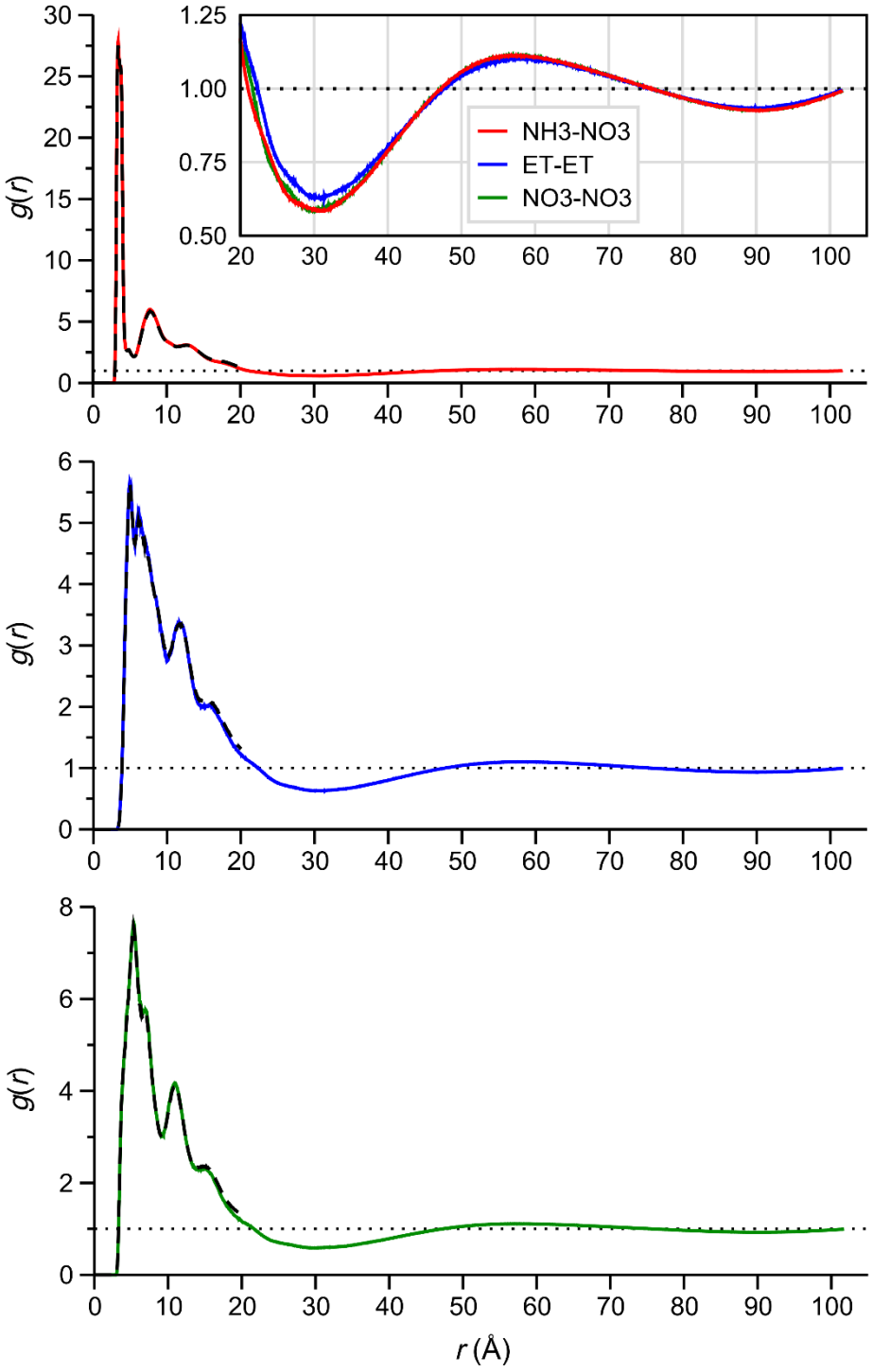

Figure 5.11 Selected CG RDFs computed for EAN CG bead pairs from the final 10 ns of the large-scale CG MD simulation of the 1:9 EAN-acetonitrile mixture (edge length = 203 Å, total simulation time = 50 ns). As shown in the legend, solid line colours correspond to specific bead pairs (NH_3-NO_3 red, ET-ET blue, and NO_3-NO_3 green), and in each panel the corresponding reference RDF *(*$r \leq 20$ Å) is plotted in dashed black line. The insert in the top panel shows the long-range ($r \geq 20$ Å) $g(r)$ structure for all three CG bead pairs, which may be seen to be rather similar. In all panels, the base value $g(r) = 1$ is indicated by a horizontal black dotted line. (Mariani *et al.*, 2021)

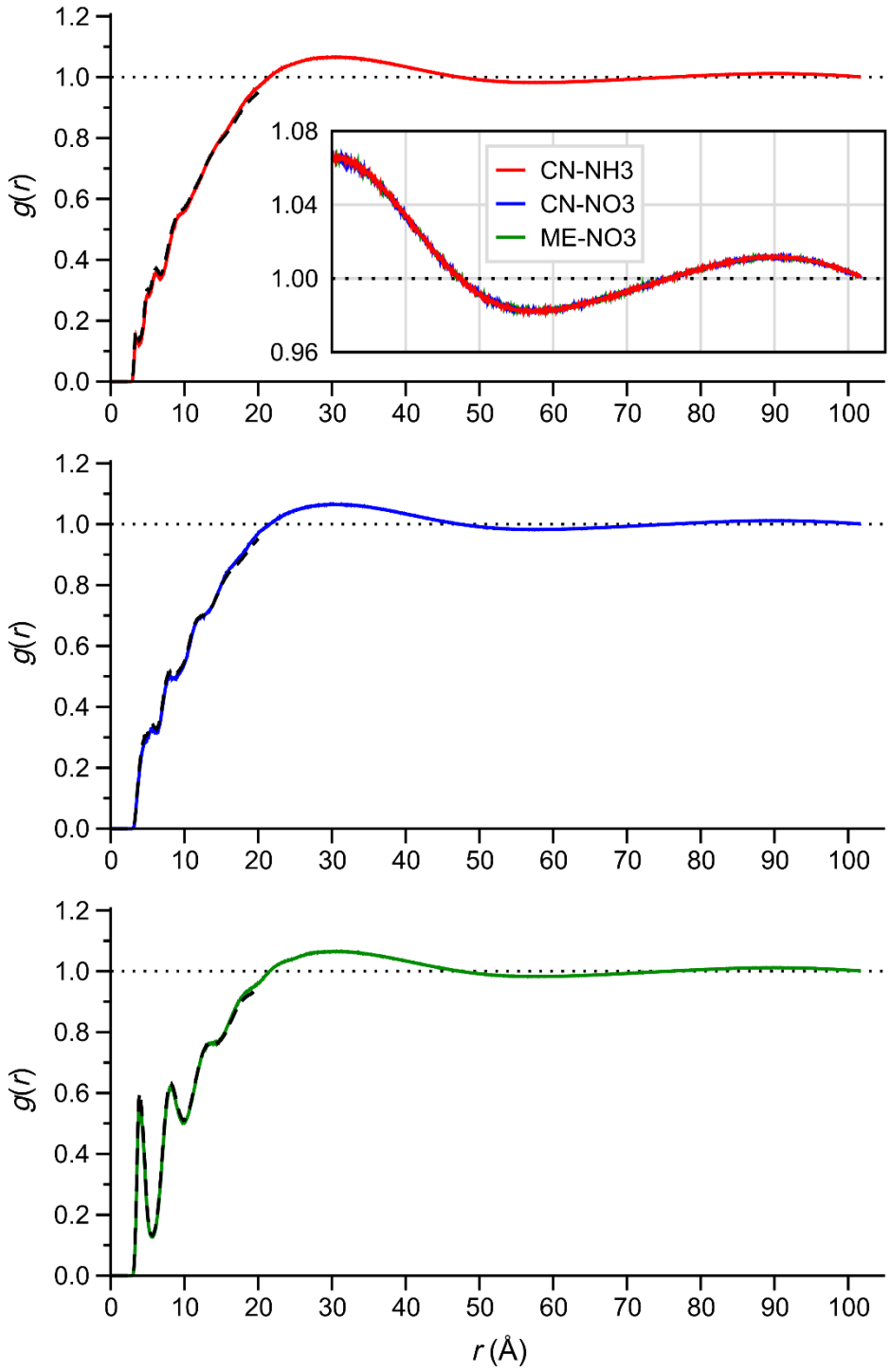

Figure 5.12 Selected CG RDFs for EAN and acetonitrile CG bead pairs, with other information as in the caption of **Figure 5.11**. Insert shows long-range undulations of $g(r)$, which may be noted to be similar to each other, yet different from the EAN CG bead pairs in **Figure 5.11**. (Mariani *et al.*, 2021)

5.3.3 SAXS pattern calculation

The scattering structure function, $S(q)$, may be computed for a simulated liquid system from the set of all atom-atom RDFs characterising the average system structure; the calculation of $S(q)$ proceeds through the calculation of *partial* structure factors, $H_{ij}(q)$, for all atomic pairs i,j, and employing established atomic scattering (or "form") factors f_i (e.g. for N, O, etc.). The calculation of $S(q)$ from computer simulation trajectories is described in detail by Mariani *et al.* (Mariani *et al.*, 2021), and is included in some trajectory analysis software packages. (Brehm and Kirchner, 2011) The simulated $S(q)$, obtained from AA MD simulation configurations of the EAN-acetonitrile (1:9) mixture by the approach described above, is show in **Figure 5.13**, where it is compared with the experimental pattern; these may be seen to be in good agreement, but deviate noticeably at low q. (Mariani *et al.*, 2021)

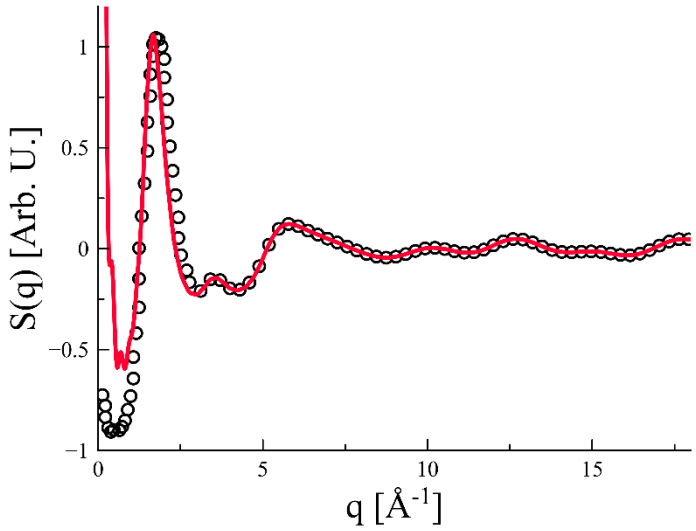

Figure 5.13 WAXS patterns for EAN-acetonitrile (1:9) mixture: Comparison between experimental (circles) and theoretical $S(q)$ extracted from the classical AA MD simulation (red line). Reproduced with permission from (Mariani *et al.*, 2021). Copyright 2021 Elsevier.

The calculation of $S(q)$ from CG models, however, is complicated by the fact that CG beads (which are often user-defined) do not have unique assigned form factors f. (Wang *et al.*, 2013) Nevertheless, it is possible to calculate approximate electronic form factors for the CG beads considered in this work by either of two approaches: (Mariani *et al.*, 2021) (1) the point-like approximation, within which a CG bead is assigned the established atomic scattering factor f_i of the atom i having atom number equal to the sum of *electron* charges of all constituent atoms; for example, the form factor of NO_3^- single CG bead (total electron charge Z = 31) can be approximated with the established scattering factor of the gallium atom (same Z). The validity of this approach (referred to as the "big-bead" approximation) depends on the extent to which the electron distribution of the atom group constituting the CG bead deviates from sphericity (i.e. more valid for groups having spherical distribution); (2) the form factor of CG bead m, F_m, is approximated as the square root of the structure factor of the isolated constituent atomic group (or "fragment"), (Niebling, Björling and Westenhoff, 2014) calculated in vacuo using the Debye formula:

$$F_m(q) = \sqrt{\sum_{k\in m}\sum_{l\in m} f_k \cdot f_l \frac{\sin(qr_{kl})}{qr_{kl}}} \tag{5.1}$$

where k and l are two scattering atoms, f_k and f_l are their respective scattering factors, and r_{kl} is the distance between them. (Mariani *et al.*, 2021) This approach can account for the contributions to the scattering from different conformers, provided a proper energy averaging of such contributions is performed. The form factors obtained with the two methods mostly differ in the high- to medium-q range, where differences in molecular shape and conformations play a major role. At low q, these internal structural differences can be neglected, and the two approaches tend to converge to the same value. (Mariani *et al.*, 2021) For the CG system considered here, the CG bead form factors were derived by approach (2) above, as described by Niebling *et al.*, (Niebling, Björling and Westenhoff, 2014) since the NO_3^- anion has a significantly non-spherical shape.

The overall and partial $S(q)$'s computed from the complete set of CG RDFs are shown in **Figure 5.14**. The position of the experimental $S(q)$ main peak ($q \approx 1.7$ Å^{-1}) is well reproduced by the simulated CG $S(q)$ in **Figure 5.14 (a)**, however, the CG peak is sharper, and the nearby minima deeper than those of the experimental $S(q)$.

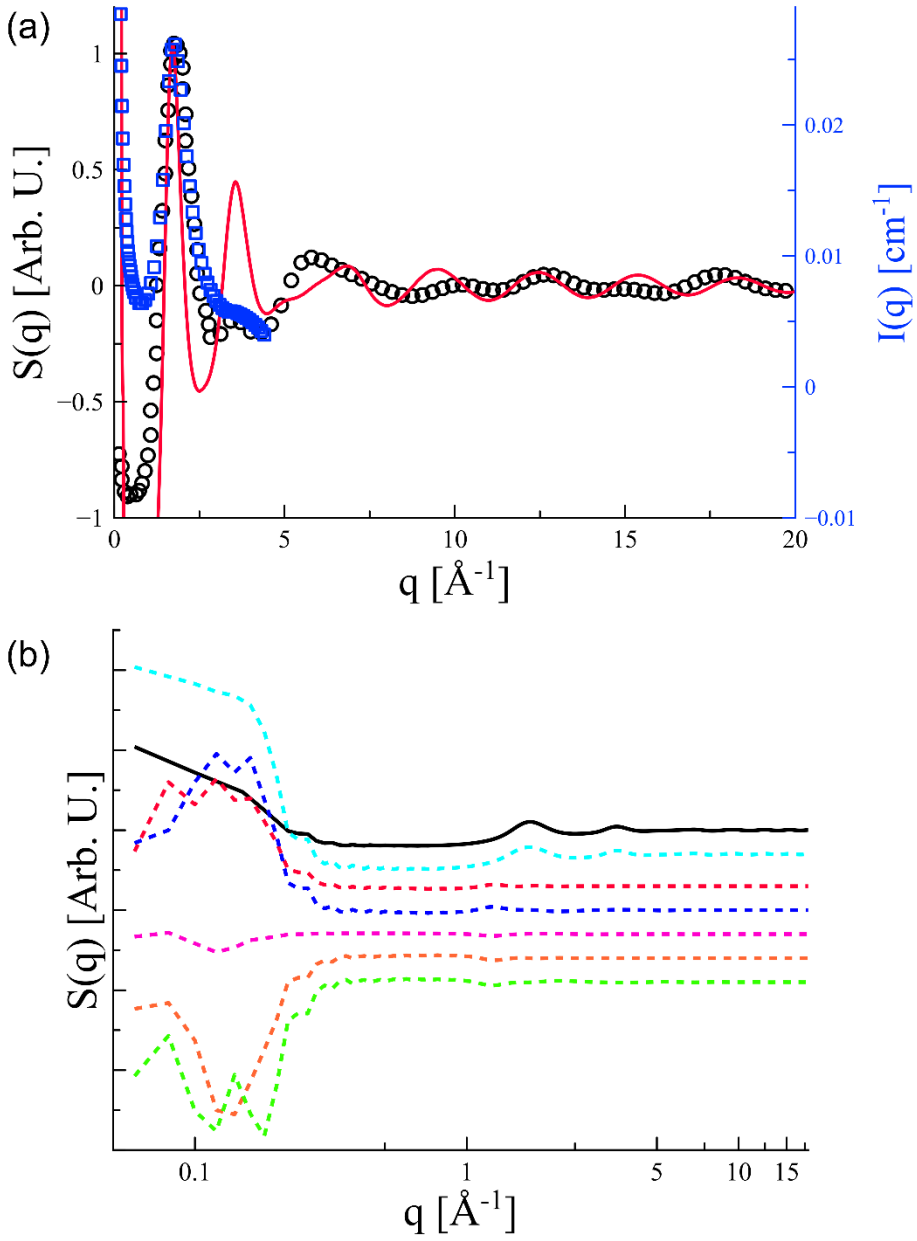

Figure 5.14 SWAXS patterns of the 1:9 molar-ratio EAN-acetonitrile (ACN) mixture. **(a)** Experimental S(q) (black circles, primary y-axis) and I(q) (blue squares, secondary y-axis) with S(q) obtained from the large-scale CG MD simulation (solid red line). **(b)** Representation with a logarithmic scale of the total (solid black line) and partial S(q) (coloured dashed lines) computed from CG simulation: ACN-ACN cyan, anion-anion red, cation-cation blue, cation-anion magenta, ACN-cation orange and ACN-anion green. Reproduced with permission from (Mariani *et al.*, 2021). Copyright 2021 Elsevier.

These differences can be attributed to the fact that the internal structures of real molecules, or atomistic molecular models, allow for a variety of interaction orientations, which are not accessible in simplified CG models. (Wang *et al.*, 2013) Indeed, features around the main $S(q)$ maxima have been found to be better reproduced by atomistic simulations. (Mariani *et al.*, 2021) At higher q,

corresponding to distances smaller than those of the CG beads (which have approximate radii > 2-3 Å), the CG model $S(q)$ does not follow the experimental pattern due to the lack of atomic resolution and, consequently, comparisons of $S(q)$ computed from CG simulations of ILs with experiment have been limited to a maximum $q = 2.5$ Å^{-1}. (Bhargava *et al.*, 2007; Wang *et al.*, 2013) On the other hand, CG models allow for reproduction of the features observed at low q in the experimental $I(q)$, specifically the LqE. Indeed, at $q < 1$ Å^{-1} the overall CG $S(q)$ increases sharply, consistent with the LqE observed in the experimental SWAXS patterns in **Figure 5.14 (a)**. It should be stressed that $S(q)$ and $I(q)$ are *not* equivalent: the former represents the structural information itself and typically ranges between $+1 < S(q) < -1$, oscillating around zero, i.e. assumes both positive and negative values; $I(q)$, on the other hand, is the *experimental scattered intensity*, i.e. $I(q) \geq 0$. It follows that the two functions are not directly comparable, though the positions and broadness of features may indeed be compared. (Mariani *et al.*, 2021)

Figure 5.14 (a) shows a good agreement between the shapes and positions of the simulated and experimental $S(q)/I(q)$ main peaks, suggesting a fine representation of the first solvation shells. More importantly, the CG model qualitatively reproduces the relative intensity and the shape of the experimental LqE. At $q >$ ~1 Å^{-1}, the partial $S(q)$s in **Figure 5.14 (b)** are generally consistent with those previously obtained from AA MD simulations: (Mariani *et al.*, 2021) $S(q)_{ACN,ACN}$ makes a dominant contribution to the overall $S(q)$ peak at $q \approx 1.7$ Å^{-1}. In contrast, the positive contributions of $S(q)_{+,+}$ and $S(q)_{-,-}$ at ~1.3 Å^{-1} are effectively cancelled in the overall $S(q)$ by negative $S(q)_{+,-}$ and $S(q)_{ACN,+/-}$. The homo-molecular functions, i.e., $S(q)_{ACN,ACN}$, $S(q)_{+,+}$, and $S(q)_{-,-}$ contribute positively to the LqE down to $q \approx 0.03$ Å^{-1}, though at lower q values, both $S(q)_{+,+}$, and $S(q)_{-,-}$ contributions decrease in intensity. Conversely, the correlations between acetonitrile (abbreviated "ACN") and EAN ions make a negative contribution to $S(q)$ down to 0.03 Å^{-1}, and then positively at lower q. The ion pair-function, $S(q)_{+,-}$, has little influence on the overall $S(q)$ structure, but qualitatively behaves similar to the latter group (EAN-ACN correlations). The dominant component, however, is clearly $S(q)_{ACN,ACN}$, suggesting the underlying structural phenomenon behind the LqE to be the formation of cylindrical cavities in the predominant acetonitrile component of the mixture (effectively the "solvent"). (Mariani *et al.*, 2021) These cavities are filled with the high-electron-density EAN component, resulting in a high contrast for passing X-rays. It is concluded that the SAXS LqE phenomenon in these mixtures is essentially driven by the following two factors: (1) the formation of strong, persistent interactions (H-bonding) between EAN ions, other than solely the Coulombic attraction, and (2) a co-solvent, acetonitrile, which only weakly interacts with the ions.

5.4 Conclusions

Coarse-Grained (CG) MD simulations were used for first time used to explain the low-*q* excess (LqE) experimentally observed in EAN-acetonitrile (1:9) mixture. The LqE cannot be properly reproduced with atomistic simulations because the system size required to verify the long-distance correlations responsible for this phenomenon are simply too large to obtain useful results in reasonable time. The use of a coarser description of the molecular components is thus necessary. The development of a proper CG model for charged entities, e.g. IL, are however still a challenging task, and no unique recipe exists that is valid for all types of systems. Moreover, in CG simulations, the choice of the initial configuration of system is still not obvious, and generating random configurations with standard program used for liquid mixture atomistic simulations might be either not feasible because of the large size of the system that can be modelled in CG simulations, or not a good starting point for fundamental reasons discussed this chapter.

In the real X-ray experiments, the scattering of the electromagnetic radiation is due to the electrons surrounding each individual atom. In CG models, on the other hand, the modelled particles represent several atoms, and in predicting the scattering effects it is necessary to approximate the sum of the individual atomic scattering factors with some function of those of the atoms belonging to each grain, and different approaches exist to this end. However, independently from the approximation used, it is not possible to properly describe the scattering at large *q*, due to distances between the scattering points that are smaller than the size of the beads (i.e. molecular detail), and in general the CG scattering prediction is of use for relative low *q*.

Overall, the development of CG models for ILs still require a considerable human effort and has to be based on very good atomistic models, which for some IL are often still challenging. However, as demonstrated by the work presented in this chapter, and published in (Mariani *et al.*, 2021), the required effort is justified by the possibility obtaining a convincing picture of the molecular organization originating the L*q*E.

6 Excess thermodynamic properties of mixtures of a choline chloride-based deep eutectic solvent with water or methanol

The work presented in this chapter was performed within a collaboration with Prof. Ji of the Luleå Technical University, who hosted me in her group for three months during my PhD period, and is currently being prepared for publication (Engelbrecht *et al.*, to be submitted).

As discussed in Chapter 4, MD simulations are largely employed to study the excess thermodynamic properties of solutions and liquid mixtures. However, to date, there has been no report of such study for the mixtures formed by a deep eutectic solvent and another solvent, despite the increasing attention to this class of mixtures.

In this chapter it is described the study of two DES - solvent mixture, with the solvent being either water or methanol. In Section 6.1 a general introduction to the studied systems is given, and in Section 6.2 are described the computational details concerning the performed simulations. The results concerning the excess thermodynamic properties and the structural properties as discussed in Sections 6.4 and 6.5 respectively.

6.1 Introduction

The deep eutectic solvents (DESs) are a diverse group of eutectic mixtures of two or more components, i.e. they have a lower melting point (mp) than expected for a corresponding ideal mixture of the components, and they exhibit a characteristic eutectic point (mp minimum). In fact, the "DES" assignment implies that the mixture composition is close to (or at) this eutectic point. (Smith, Abbott and Ryder, 2014) A schematic phase diagram for a two-component eutectic mixture, drawn after that of Smith *et al.* (Smith, Abbott and Ryder, 2014), is shown in **Figure 6.1**. DESs are typically composed of an ionic H-bond acceptor (HBA), e.g. quaternary ammonium halide salt, and a metal salt, or an electronically neutral H-bond donor (HBD) molecule. The choline chloride (ChCl)-based DESs involving neutral HBDs, for example, are a highly versatile and intensively studied class (often referred to as type III DESs). (Smith, Abbott and Ryder, 2014)

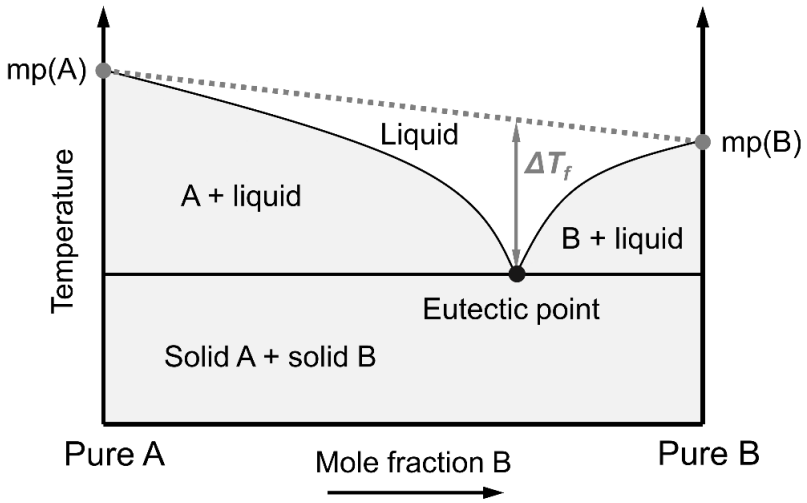

Figure 6.1 Schematic phase diagram for a binary eutectic mixture. The dotted grey line connecting the melting points of pure components A and B represents the ideal melting point variation of A+B mixtures as a function of composition; ΔT_f is the melting/freezing point difference between the ideal and actual mixture values (solid black curve), and reaches a maximum value at a certain composition, the eutectic point. Scheme draw after that of Smith et al. (Smith, Abbott and Ryder, 2014)

In such mixtures, HBDs strongly complex chloride anions, reducing the strength of electrostatic interactions with the organic cations and thus the melting point (**Figure 6.2**). Typical ChCl-based DES HBDs include urea, ethylene glycol, glycerol and malonic acid; in fact, these mixtures have become so frequently studied that they have been assigned unique names, e.g. the 1:2 molar ratio mixture of ChCl with urea is widely referred to as "reline", the corresponding mixture with ethylene glycol as "ethaline", and so on.

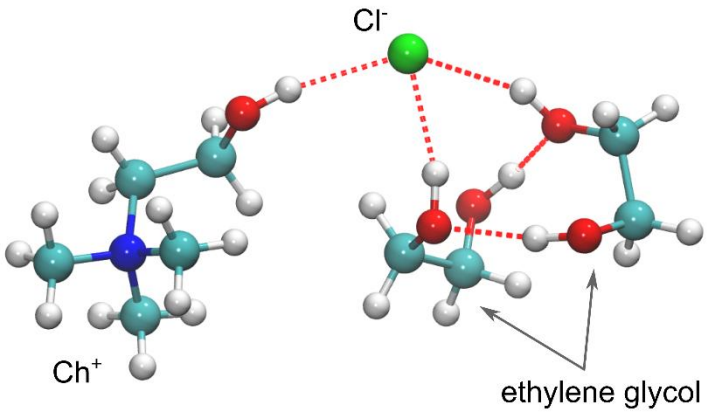

Figure 6.2 Choline chloride (ChCl) – ethylene glycol (1:2 molar ratio) configuration extracted from a computer simulation (temp. = 308.15 K). The two ethylene glycol molecules each form one H-bond (shown by dotted red lines) with the Cl^- anion (green sphere), with their other -OH group free to form H-bonds with surrounding molecules (in this case, each other). The Ch^+ cation forms a "doubly ionic" H-bond with Cl^-, (Ashworth et al., 2016) with its bulky cationic centre (blue N atomic site) pointing outwards. Other molecules participating in the Cl^- coordination shell have been omitted in the interest of clarity (i.e. a partial coordination shell only), and so as to represent the essential DES composition (1:2 ratio); clearly, many different coordination shell compositions and configurations are possible.

As may be inferred from the representative configuration of DES components in **Figure 6.2**, many different interaction modes are possible in such systems, resulting in a considerably complex liquid structure. While coordination *via* H-bonding of the anion by the HBD is a prominent structural feature, thought to be key to DES formation (note the common ChCl:HBD = 1:2 molar ratio of many ChCl-based DESs, at which the anion is thought to be effectively coordinated by HBD), many different configurations and other interactions are possible, including H-bonding between the cation and anion ("doubly ionic H-bonding"), and clustering of components; these complex structural features are exemplified by the extensive computational work of Ashworth *et al.* (Ashworth *et al.*, 2016)

DESs share many characteristics and properties with the ionic liquids (ILs), e.g. low vapour pressure, wide liquid temperature range and low flammability, and are widely regarded as IL analogues; (Ma *et al.*, 2018) in fact, DESs exhibit several additional, potentially favourable properties and advantages compared to ILs. (Smith, Abbott and Ryder, 2014) The ChCl-based DESs, in particular, may be prepared from inexpensive, readily-available starting materials under moderate conditions, and are thought to be non-toxic and environmentally benign. (Zhang *et al.*, 2012) However, as for ILs, the high viscosities of DESs under ambient conditions present a major obstacle for their practical

applications, e.g. as solvents or lubricants. (García *et al.*, 2015; Ma *et al.*, 2018) The addition of more highly-mobile co-solvents, e.g. water or alcohols, has been proposed as a possible solution to this problem. (Wang *et al.*, 2020) In fact, many DESs are hygroscopic (like ILs), readily absorbing atmospheric water. While the addition of co-solvents to DESs may be used to modify their macroscopic properties (e.g. viscosity, density), their introduction also affects the characteristic intermolecular interactions and molecular-level arrangements of the constituents of DESs, illustrated in **Figure 6.2**. (Gao *et al.*, 2018; Baz *et al.*, 2019; Celebi, Vlugt and Moultos, 2019) Information on such changes, which may have important implications for the applications of the DESs, notably their solvent characteristics, may be obtained from measurements of excess thermodynamic properties, e.g. the excess molar enthalpy/enthalpy of mixing (H^E); indeed, binary mixtures of DESs with co-solvents have been found to be significantly non-ideal, often exhibiting interesting variations of such excess thermodynamic properties as a function of mixture composition. (Ma *et al.*, 2018; Wang *et al.*, 2020)

Considering the binary (or "pseudo-binary")[1] mixtures of the ChCl-ethylene glycol (1:2 molar ratio), for example, it has been shown that addition of small amounts of either water or methanol dramatically decreases the room-temperature bulk dynamic viscosity, η, of the DES, as plotted in **Figure 6.3**. (Wang *et al.*, 2020) The DES-methanol mixtures have consistently lower viscosities, perhaps not unexpectedly, in view of the lower viscosity of pure methanol *vs.* water. In order to evaluate the intermolecular interactions in these mixtures, Wang *et al.* (Wang *et al.*, 2020) calculated for each "pseudo-binary" mixture the *viscosity deviation*, $\Delta\eta$, from that of the corresponding hypothetical ideal mixture

$$\Delta\eta = \eta_{mixture} - x_{DES}\eta_{DES} - x_{co-solvent}\eta_{co-solvent} \qquad (6.1)$$

where η_{mixture} is the viscosity of the mixture, and x_i, η_i the mole fractions and viscosities of the respective pure components, i.e. DES and co-solvent (water or methanol). The $\Delta\eta$ of both mixture series, also plotted in **Figure 6.3**, were found to be negative over the entire composition range, indicative of a lower-than-ideal η_{mixture} at all compositions, with that of methanol again lower.

[1] Considering that the DES has two components itself, the mixture with another solvent actually has three components, but is often referred as "pseudo-binary" because the composition of the DES is kept the same in all mixtures with the added solvent.

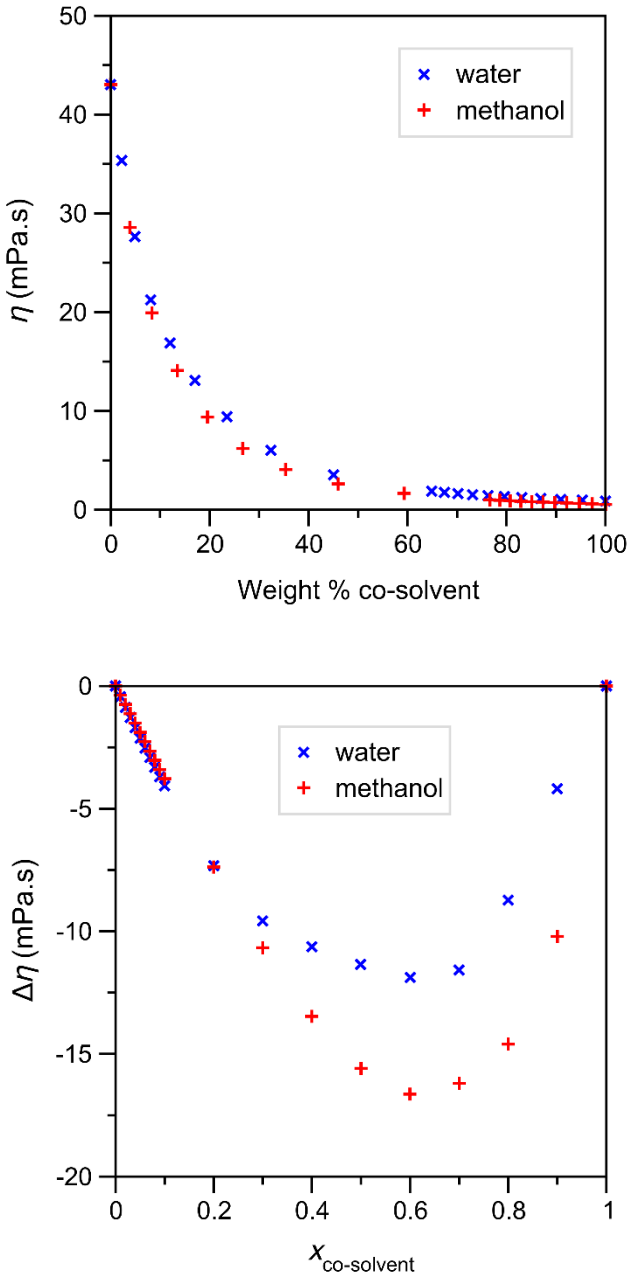

Figure 6.3 Top: Dynamic viscosities (η) of ChCl-ethylene glycol (1:2 molar ratio) DES binary mixtures with either water or methanol co-solvents as function of the weight percentage co-solvent at 298.15 K. **Bottom:** Viscosity deviations ($\Delta\eta$) of the DES-water/methanol mixtures as function of mole fraction co-solvent, $x_{co\text{-}solvent}$, at 298.15 K. Data from Wang et al. *(*Wang *et al.*, 2020)

Interestingly, the excess molar enthalpies, H^E, which directly concerns changes in intermolecular interactions upon mixing, were found to be of opposite sign for the two mixture series: those of the DES-water mixtures were substantially negative at all compositions, while those of methanol were smaller, but decidedly positive. (Wang *et al.*, 2020) The positive H^E of the methanol mixtures were taken as an indication of weak interactions between the DES components and methanol, i.e. the

interactions in the pure DES and pure methanol are, on average, stronger than those in the mixture. This contention seems reasonable considering that weaker intermolecular interactions in the methanol mixtures should lead to a lower dynamic viscosity. The formation of the pure DES from its components is associated with a large positive H^E (> 5000 J.mol^{-1}, at 323.15 K), which has been found to be largely due to melting of the pure ChCl salt. On the other hand, the actual molar enthalpy of mixing at the same temperature is significantly negative, $\Delta H^{mix} \approx$ -4500 J.mol^{-1}, due to strong interactions between the ions and HBD. (López-Porfiri, Brennecke and Gonzalez-Miquel, 2016) Moreover, the corresponding DES-water mixtures, while somewhat more viscous compared to those with methanol, also exhibit negative $\Delta\eta$ at all mixture compositions, indicating a lower-than-expected dynamic viscosity despite their substantial *negative* H^E (*ca.* -1100 J.mol^{-1} at $0.6 < x_{water} < 0.7$), suggesting the formation of strong intermolecular interactions in these water mixtures. (Ma *et al.*, 2017) Clearly, while the $\Delta\eta$ in these DES-water/methanol binary mixtures are likely due the further weakening of strong electrostatic interactions between ions by coordination of the co-solvent, the details of structural changes, e.g. the anion coordination shell composition (notably in the methanol mixtures), (Celebi, Vlugt and Moultos, 2019; Kaur *et al.*, 2020) the components self-association, and their exact roles in this phenomenon, have not been unambiguously established.

Unfortunately, detailed information on the structural changes upon mixing cannot be directly obtained from excess thermodynamic property measurements, and are difficult to obtain experimentally in general for these complex mixtures. (Celebi, Vlugt and Moultos, 2019) Computational molecular modelling, and classical MD computer simulations in particular, have been increasingly employed to study the complex liquid structures of ChCl-based DESs (Perkins, Painter and Colina, 2013, 2014; Ashworth *et al.*, 2016; Kaur, Sharma and Kashyap, 2017; Kaur, Malik and Kashyap, 2019) and, more recently, their mixtures with water. (Shah and Mjalli, 2014; Fetisov *et al.*, 2018; Gao *et al.*, 2018; Baz *et al.*, 2019; Celebi, Vlugt and Moultos, 2019) Such computational studies have provided detailed local structural information, typically though calculation of pair distribution functions (RDFs, SDFs), or analyses of the H-bonded networks; nevertheless, the sheer number of H-bonding interaction possible in these DES and their mixtures, described as an "alphabet soup of H-bonded interaction types", (Ashworth *et al.*, 2016) complicates structural analyses, and workers often resort to calculating simplified "centre-of-mass" (COM) distribution functions (e.g. average distribution of the cation centre of mass around the Cl^- anion). (Kaur, Sharma and Kashyap, 2017; Gao *et al.*, 2018)

Interestingly, it appears as though very few, if any, detailed structural studies of DES mixtures with co-solvents *other* than water (or absorbed gasses, e.g. CO_2) (Ullah *et al.*, 2015) have been reported. The aim of the present work is to perform classical MD simulations of the ChCl-ethylene glycol 1:2-

molar ratio DES (“ethaline”) and its pseudo-binary mixtures with both water and, for the first time, methanol to gain insight into the intermolecular interactions responsible for, in particular, the recently-reported differences in their H^E variations as a function of co-solvent content. (Y. Wang *et al.*, 2020)

6.2 Computational details

6.2.1 Force field details

The General Amber Force Field (GAFF) was used to model the ChCl-ethylene glycol DES and methanol. The DES partial atomic charges of Perkins *et al.*, (Perkins, Painter and Colina, 2014) developed specifically for use with GAFF parameters, was used (with ionic species charges scaled by a factor 0.9). For methanol, an established set of partial atomic charges was obtained from the online R.E.D database (R.E.DD.B project W-32), (Dupradeau, 2005) previously developed using the GAFF-consistent RESP (HF/6-31*) fitting procedure; (Dupradeau *et al.*, 2010) the SPC/E model was used for water. (Berendsen, Grigera and Straatsma, 1987).

6.2.2 Starting configurations

Starting configurations were prepared using the Packmol software, (Martínez *et al.*, 2009) randomly placing a total of 300 choline (Ch^+) and chloride (Cl^-) ions, and 600 ethylene glycol (EG) molecules in a periodic cubic simulation cell, with dimensions chosen such that the configuration is close to target density. For DES-co-solvent mixtures, an appropriate number of DES components and co-solvent molecules were placed in cubic cells of similar/reasonable dimensions, as detailed in **Table 6.1**.

Table 6.1 Details of simulated DES-co-solvent mixtures and respective pure solvents. The total number (N) of units (molecules) of each component (choline chloride ChCl, ethylene glycol EG, and water/methanol co-solvent) and the simulation average densities (308 K, 0.98 bar) are shown

System	$x_{\text{co-solvent}}$	N_{ChCl}	N_{EG}	$N_{\text{co-solvent}}$	Density (g.cm^{-3})
Pure DES	–	300	600	–	1.1044
Water mixtures	0.125	300	600	129	1.1041
	0.250	300	600	300	1.1029
	0.500	300	600	900	1.0953
	0.750	300	600	2700	1.0708
	0.875	150	300	3150	1.0430
	1.000	–	–	3000	0.9902

Methanol mixtures	0.125	300	600	129	1.0886
	0.250	300	600	300	1.0695
	0.500	300	600	900	1.0195
	0.750	150	300	1350	0.9400
	0.875	75	150	1575	0.8804
	1.000	–	–	1000	0.7976

6.2.3 MD simulation details

All MD simulations were performed using the Amber 16 software package. (Case *et al.*, 2005) The simulation procedure was essentially similar to that described by Perkins *et al.* (Perkins, Painter and Colina, 2014): following system equilibration (below), NPT simulations (308 K, 0.98 bar) were performed using Langevin dynamics (5 ps^{-1} time constant), with weak-coupling (Berendsen) pressure coupling (1 ps time constant), (Berendsen *et al.*, 1984) and a 2 fs simulation time step; bonds involving hydrogen atoms were constrained using the SHAKE algorithm. (Ryckaert, Ciccotti and Berendsen, 1977) The non-bonded interaction cut-off was set at 15 Å, with long-range electrostatic interactions computed using the PME procedure. (Darden, York and Pedersen, 1993) The equilibration of the system was performed through a combination of steepest-descent energy minimizations and NPT MD simulations. After the equilibration phase, the production trajectories were generated to obtain, for each mixture, 20 ns long NPT simulation.

6.3 Excess thermodynamic properties

The average densities of all simulated DES-co-solvent mixtures are plotted in **Figure 6.4**, along with experimental measurements of Wang *et al.*; (Wang *et al.*, 2020) corresponding numerical data are reported in **Table 6.1**. The reproduction of experimental densities constitutes a typical, yet key first step in the validation of DES models (as for many other liquid systems); in fact, the current DES model ionic charges, originally developed by Perkins *et al.*, (Perkins, Painter and Colina, 2014) were scaled by these authors (factor 0.9) to better reproduce experimental densities and transport properties compared to the model with full ionic charges (± 1 e).

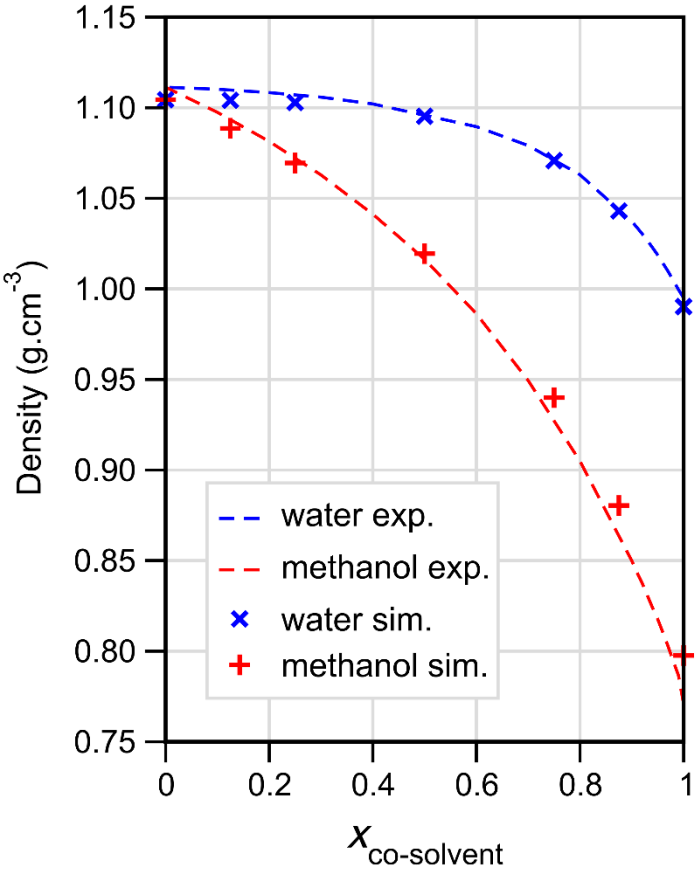

Figure 6.4 Average densities of ChCl-ethylene glycol (1:2) DES and selected mixtures with either water (blue crosses) or methanol (red plus signs) co-solvent from MD simulations at 308.15 K (*NPT* using Langevin dynamics; Berendsen (weak) pressure coupling). Dashed lines of corresponding colour connect experimental data of Wang et al. (Wang *et al.*, 2020) Density data plotted as a function of pseudo-binary mixture composition, expressed as mole fraction co-solvent, $x_{\text{co-solvent}}$.

The simulation average densities in **Figure 6.4** are in good agreement with the measurements of Wang *et al.*, (Wang *et al.*, 2020) with the methanol mixtures showing increasing deviation at higher methanol content. The average density of the pure methanol model is notably higher than experiment, 0.792 and 0.771 g.cm^{-3}, respectively; nevertheless, the discrepancies between simulated and experimental densities are in line with, and smaller than, those recently reported for these DES-water mixtures by Kaur *et al.*, (Kaur *et al.*, 2020) as well as for related DES-water mixtures, e.g. ChCl-urea (1:2; "reline") aqueous mixtures. (Shah and Mjalli, 2014)

The simulation excess molar enthalpies, H^{E}, are compared with experiment in **Figure 6.5** (Wang *et al.*, 2020) The simulated H^{E} were computed from the simulation average potential energies, as

described previously. While these deviate significantly from experiment, the experimental sign difference (water mixtures strongly negative, methanol mixtures low positive) and essential trend shapes are , in fact, reproduced. Interestingly, to the best of our knowledge, no H^E computed from MD simulations for DES-co-solvent (including, of course, water) mixtures have been reported in the literature for comparison, though the magnitude of H^E deviations from experiment in **Figure 6.5** is not uncommon for simulated neutral liquid mixtures, e.g. alcohols with water, using standard general-purpose force fields (e.g. the presently-employed GAFF), (Wang *et al.*, 2004; Dai *et al.*, 2010; Miroshnichenko and Vrabec, 2015) as discussed in the study described in Chapter 4. (Engelbrecht *et al.*, 2020)

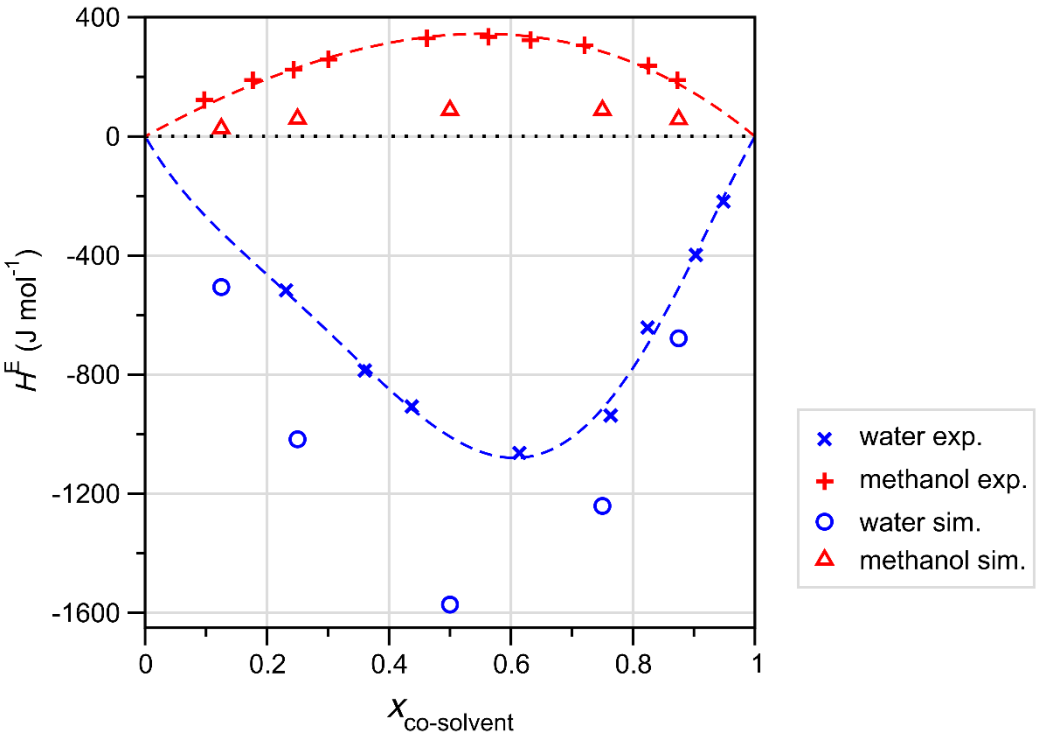

Figure 6.5 Experimental (crosses, plus signs) and simulated (circles, triangles) excess molar enthalpies, H^E, of binary mixtures of ChCl-ethylene glycol 1:2 DES ("ethaline") with either water (blue data markers/line) or methanol (red data markers/line) co-solvent at 308.15 K. Dashed lines, intended as a guides to the eye, are Redlich-Kister (RK, water) or "non-random two-liquid" (NRTL, methanol) model fits; all experimental data and model parameters taken from Wang et al. (Wang *et al.*, 2020) The horizontal dotted black line indicates H^E = 0 J.mol^{-1}, showing that for all simulated methanol mixtures H^E > 0 J.mol^{-1}.

6.4 Structural analysis and outlook

The liquid structure of ChCl-based DESs and their aqueous mixtures from computer simulations are routinely evaluated by the calculation of pair correlation functions, radial distribution functions (RDFs) in particular. These functions, introduced in Section 2.4.2, have a direct experimental connection in the form of neutron and X-ray scattering patterns, which have been reported for a few DES systems of this type, some only very recently. (Hammond, Bowron and Edler, 2016, 2017; Kaur, Malik and Kashyap, 2019; Kaur *et al.*, 2020) As shown in the previous chapters, RDFs are traditionally employed in studies of prototypical H-bonded liquids, e.g. water, with the first intense $g_{OO}(r)$ peak (i.e. at smallest particle pair separation, r) associated with directly H-bonded neighbours; this methodology is also applicable to multi-component liquid systems like DESs, with their "alphabet soup" of H-bonded interactions $X_D\text{-}H_D \cdots Y_A$, where X and Y are the H-bond donor and acceptor heavy (i.e. non-hydrogen) atoms. (Ashworth *et al.*, 2016)

It is widely accepted that the physical properties of typical ChCl-based DESs are primarily determined by strong ionic H-bonds involving the Cl^- anion acceptor; the ChCl:HBD = 1:2 molar ratio of many such DESs is, naturally, the prime example and is thought to be due to effective coordination of Cl^- by the HBD, thus disrupting strong electrostatic interactions between the anion and cation. (Ashworth *et al.*, 2016; Fetisov *et al.*, 2018) In fact, the Cl^- anion is considered to play a key role in the characteristic microstructural arrangements in ChCl-based DESs and their aqueous mixtures, (Celebi, Vlugt and Moultos, 2019) and, as such, the present structural analysis starts by considering the Cl^- anion coordination shell composition in the simulated DES and its water and methanol mixtures. The Cl-X RDFs, $g_{ClX}(r)$, where X are H-bond donors/heavy atoms of the DES components, for the pure ChCl-ethylene glycol (1:2) DES and selected water (left-column panels) or methanol (right) mixtures are shown in **Figure 6.6**.

The RDFs for the pure DES and its aqueous mixtures (**Figure 6.6, panels A, C & E**) have been reported and analysed before under different, but similar physical conditions. (Perkins, Painter and Colina, 2014; Ferreira *et al.*, 2016; Celebi, Vlugt and Moultos, 2019; Kaur, Malik and Kashyap, 2019) In those studies, the sharp first peaks (maxima) of the $g_{ClO}(r)$, shown in **Figure 6.6, panels A and C**, are identified with H-bonding interactions (Cl···H-O) of Cl^- with ethylene glycol and the choline cation (Ch^+), respectively. The intensity of these well-defined first maxima, occurring in the range r_{ClO} = 3.2 – 3.3 Å, decreases with increasing water content, consistent with water molecules entering the Cl^- coordination shell, displacing the DES components. (Celebi, Vlugt and Moultos, 2019)

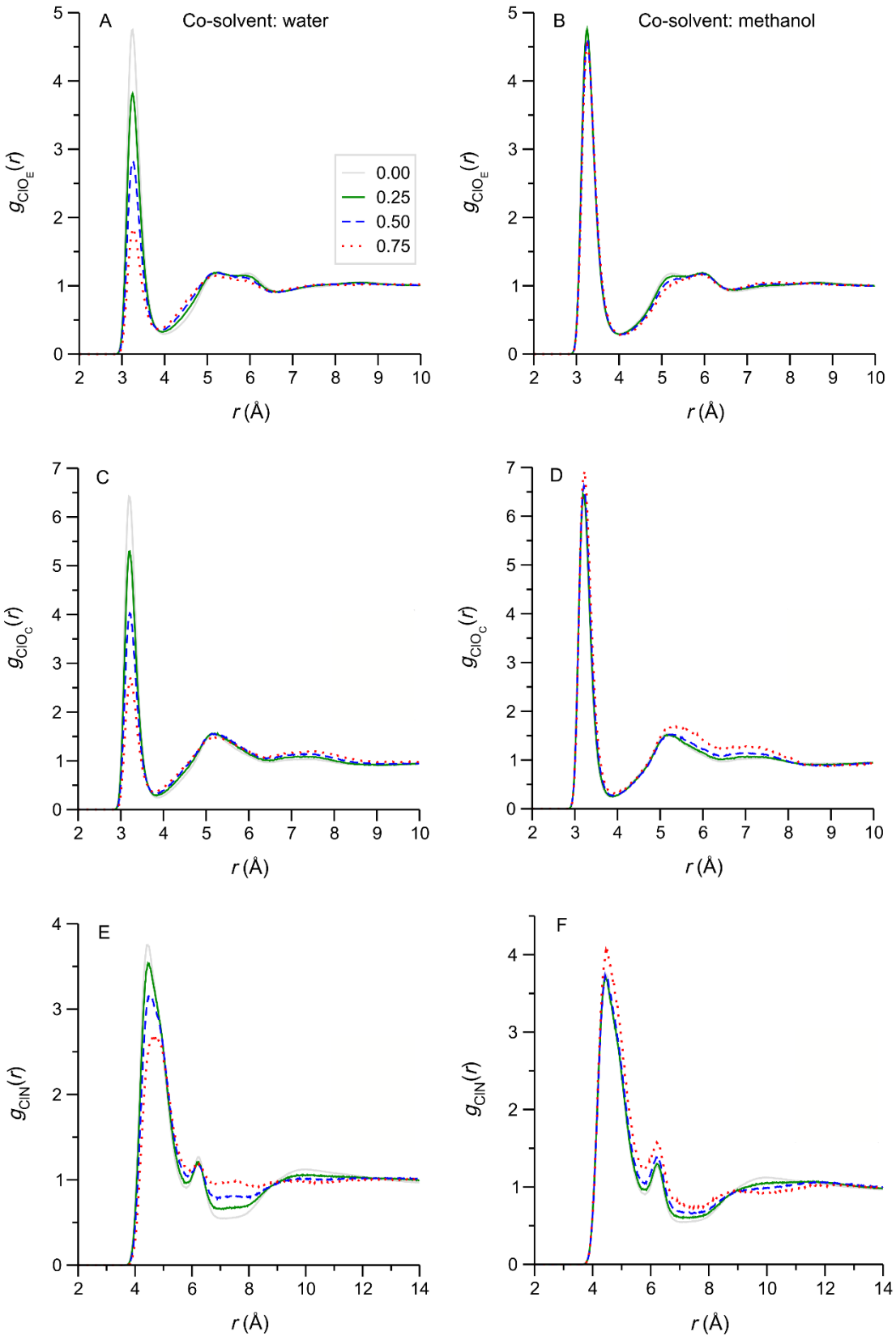

Figure 6.6 Cl-*X* (*X* = ethylene O, choline O or choline N) RDFs for the ChCl-ethylene glycol (1:2) DES and selected water (**left** panels) or methanol (**right**) co-solvent mixtures computed from *NPT* (308.15 K, 0.98 atm.) MD computer simulation trajectories. The numbers in the legend are co-solvent mole fractions.

The Cl-Ch^+ N RDFs in aqueous mixtures (**Figure 6.6, panel E**) exhibit broader first maxima at larger distances, r_{ClN} > 4 Å, resulting from electrostatic interactions between Cl^- and the bulky Ch^+ ammonium site; at all mixture compositions, the second maximum at $r_{ClN} \approx 6$ Å is due to Ch^+ cations interacting with Cl^- *via* H-bonding interactions O-H···Cl (panel C). In the pure DES, the $g_{ClN}(r)$ first maximum exhibits a noticeably asymmetric shape, suggesting various, energetically-similar, interaction configurations/modes between Cl^- and the bulky $(CH_3)_3N$-group of Ch^+. (Zahn, Kirchner and Mollenhauer, 2016; Stefanovic *et al.*, 2017) Indeed, a number of such interaction modes have been demonstrated by Ashworth *et al.*, (Ashworth *et al.*, 2016) and these are likely characterised by slightly different average r_{ClN}. The shape of the $g_{ClN}(r)$ first maximum gradually changes with increasing water content, the actual maximum position shifting from ~4.4 to 4.7 Å, suggesting a change in predominant Cl^- - Ch^+ interaction mode upon addition of water; this subtle change is also evident in the RDFs recently presented by Celebi *et al.* (Celebi, Vlugt and Moultos, 2019) (COM-COM RDFs) and Kaur *et al.* (Kaur *et al.*, 2020)

Considering the corresponding Cl-*X* RDFs for selected DES-methanol mixtures (**Figure 6.6, panels B, D & F**), it appears that these remain comparatively invariant with increasing methanol content, the first peak intensities *increasing* slightly, with more noticeable changes at higher $x_{methanol}$ (notably at larger r_{ClX} > 4 Å). Interestingly, the asymmetric $g_{ClN}(r)$ first peak profile of the pure DES largely persists in the methanol mixtures, even at high $x_{methanol}$, suggesting that the characteristic native DES Cl^- - Ch^+ interaction modes do not change appreciably upon dilution with methanol. This observation is in stark contrast to that for the water mixtures, described in the previous paragraph. It should be remarked at this stage that the effectively constant Cl-*X* RDF first peak intensities of the methanol mixtures do *not* necessarily imply a more stable Cl^- coordination shell *composition* upon addition of methanol (compared to water), since the RDF intensities are *normalised* to the corresponding bulk particle densities, which change with mixture composition/volumetric changes; this point will be addressed below with reference to the calculation of coordination numbers, obtained by appropriate RDF integration. Nevertheless, inspection of the RDF shapes in **Figure 6.6** has revealed interesting clues as to differences in configurational changes in the Cl^- coordination shell region between the DES-water and methanol mixtures.

Selected Cl-water oxygen (O_w) and methanol oxygen (O_m) RDFs are shown in **Figure 6.7**; these functions directly relate to H-bonding interactions between Cl^- and the co-solvent. Interestingly, as in **Figure 6.6**, the Cl-O_w RDFs show very noticeably changes with increasing water content, whereas those of methanol (Cl-O_m) remain more-or-less unchanged. In particular, the relative intensities of first ($r_{ClO} \approx 3.5$ Å) and broad second peaks ($r_{ClO} \approx$ 4-6 Å) in the water mixtures show an interesting

change with increasing water content, suggestive of changes in the liquid microstructure, and water self-association in particular. (Kaur *et al.*, 2020) Such changes are not observed for the methanol mixtures, i.e. for corresponding Cl-O_m RDFs.

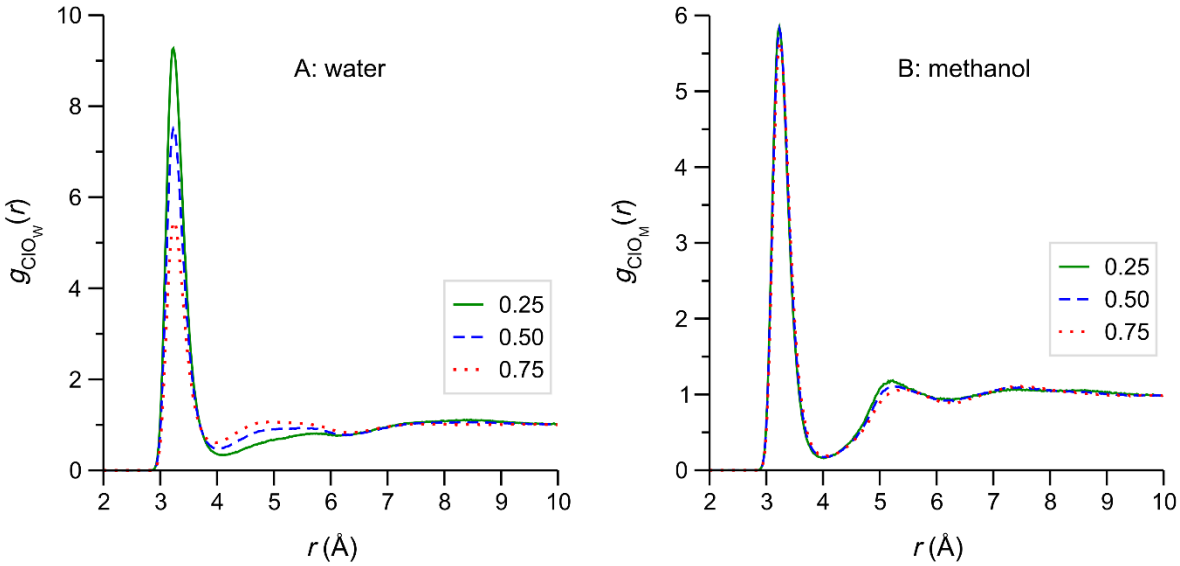

Figure 6.7 Cl-$O_{co\text{-}solvent}$ RDFs for selected ChCl-ethylene glycol (1:2) DES mixtures with either water (**A, left**) or methanol (**B, right**) co-solvent at 308.15 K, 0.1 MPa. Numbers in the legend refer to the mole fraction co-solvent.

The Cl-*X* RDFs in **Figure 6.6** & **Figure 6.7** may be integrated in order to determine Cl-*X* coordination numbers, n_{ClX}. (Ben-Naim, 1990) The results of this procedure show that, despite the clear $g_{ClX}(r)$ differences described above (intensities decrease with increasing water content, whereas those in methanol remain apparently unchanged), the corresponding coordination numbers, n_{ClX}, exhibit essentially similar behaviour as a function of $x_{co\text{-}solvent}$ for the water and methanol mixtures. Considering first the Cl-O coordination numbers (n_{ClO}), **Figure 6.8**, identified with strong ionic H-bonding interactions (-O-H ⋯ Cl^-) among DES components

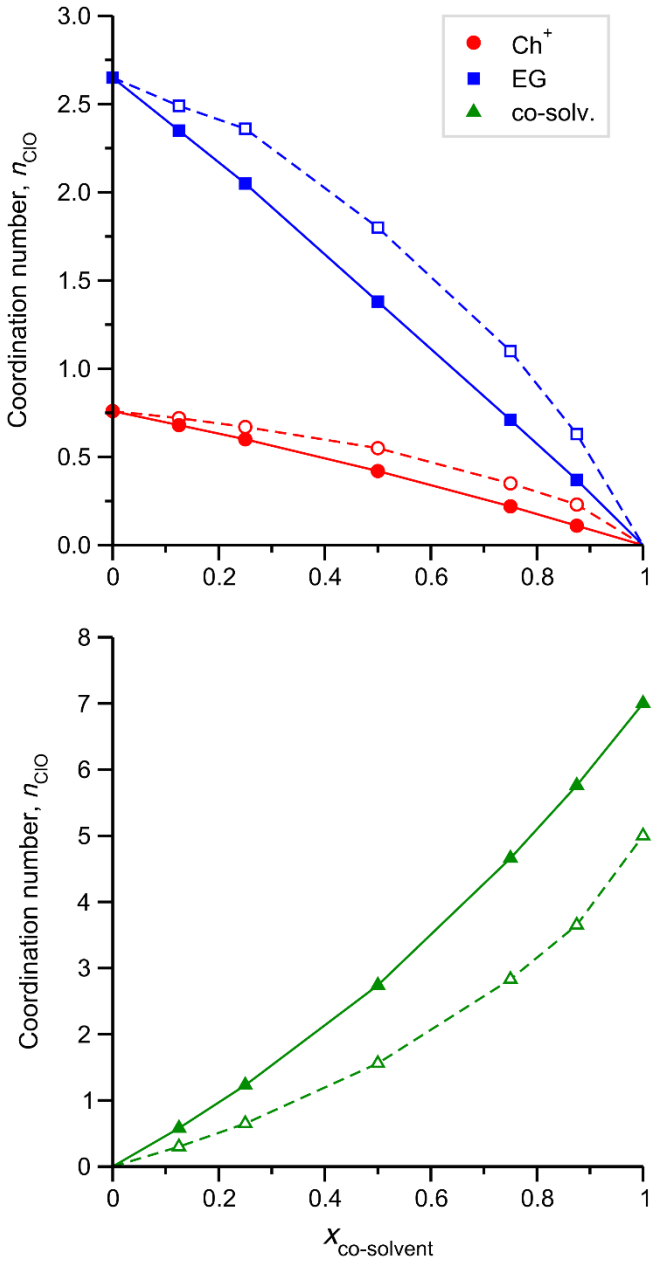

Figure 6.8 Cl-O coordination numbers, n_{ClO}, from RDF integration, plotted as a function of DES ("ethaline")-co-solvent composition expressed as mole fraction, $x_{co\text{-}solvent}$. Data markers are as follows: circle choline cation (Ch^+), squares ethylene glycol (EG), and triangles co-solvent (water or methanol). Solid data markers connected by solid line pertain to DES-water mixtures, whereas open markers and dashed lines correspond to DES-methanol mixtures.

Numerous particle-particle and COM-COM RDFs may be calculated for these complex systems; the ion-ion RDFs $g_{ChCl}(r)$, $g_{ChCh}(r)$, and $g_{ClCl}(r)$, for example, are frequently reported in computational studies of ChCl-based DESs. (Perkins, Painter and Colina, 2014; Ferreira *et al.*, 2016; Kaur, Malik and Kashyap, 2019) The Cl-Cl RDFs for selected mixtures are reported in **Figure 6.9**. The changes in these functions with increasing co-solvent content are intriguing, and clearly qualitatively very different for the water and methanol mixtures. In the pure DES, $g_{ClCl}(r)$ is characterised by a broad, apparently convoluted, first maximum at ca. $r_{ClCl} \approx$ 7-8 Å; these convoluted peaks are likely due to Cl^- anions located in characteristic "bridging" positions, i.e. acting as H-bonded bridges between Ch^+ and ethylene glycol, as was recently proposed, (Kaur *et al.*, 2020) and thus separated by either of these DES components, both of which are conformationally flexible.

In the DES-water mixtures, an interesting, well-defined, $g_{ClCl}(r)$ peak appears, first as a side-peak ("bump") around $r_{ClCl} \approx$ 5.5 Å (x_{water} = 0.125), then becoming sharp and gradually moving to r_{ClCl} = 5.0 Å (x_{water} = 0.875) with increasing water content. This $g_{ClCl}(r)$ peak also appears in recent simulation studies, (Celebi, Vlugt and Moultos, 2019; Kaur *et al.*, 2020) though apparently its significance has not received detailed consideration. In fact, this short-range $g_{ClCl}(r)$ peak is *completely absent* for the simulated DES-methanol mixtures; the broad pure-DES $g_{ClCl}(r)$ peak simply becomes less-defined and shifts gradually to greater r_{ClCl} with increasing methanol content, as expected due to dilution of the DES.

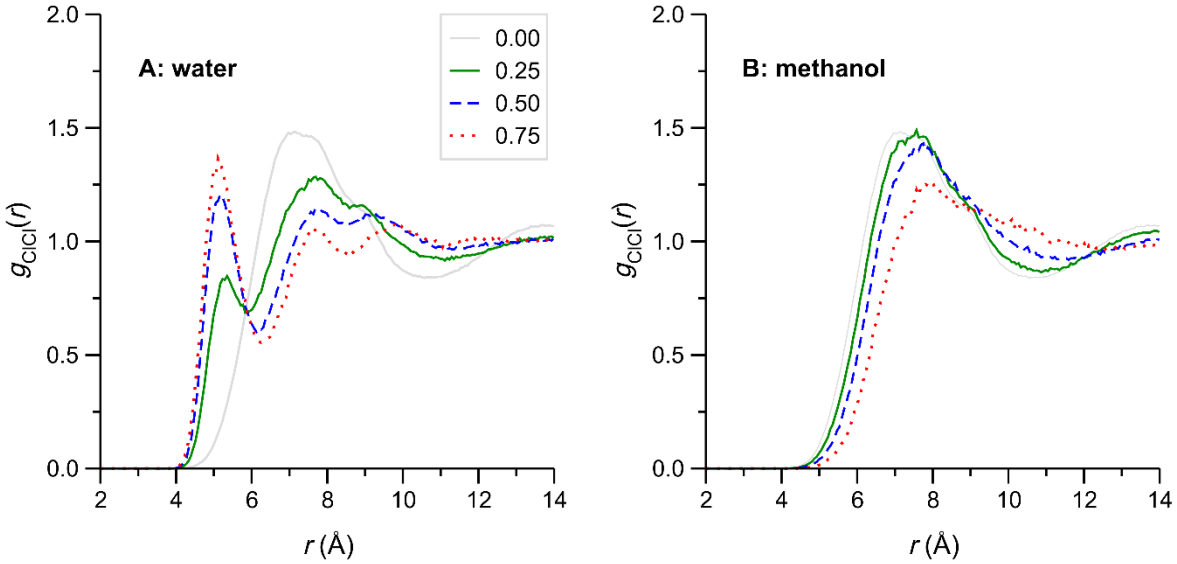

Figure 6.9 Cl-Cl RDFs, $g_{ClCl}(r)$, for selected simulated DES-water (A) and methanol (B) mixtures. As in **Figure 6.6** & **Figure 6.7**, the numbers in the legend indicates the mixture composition expressed as a mole fraction co-solvent (water or methanol).

The appearance of a new, short-range $g_{ClCl}(r)$ peak upon addition of water implies the formation of geometrically well-defined structures in which Cl^- anions are drawn closer together. Indeed, inspection of DES-water simulation configurations reveals an abundance of arrangements in which *two* water molecules form H-bonded bridges between connecting two Cl^- anions; a representative configuration is shown in **Figure 6.10, top**. Here, water molecules in the Cl^- coordination shell may also be seen to form part of larger H-bonded water self-associates, another prominent feature of these DES-water mixtures. The essential structural motif represented in **Figure 6.10, top** (two Cl^- anions and their two H-bonded bridging water molecules) are responsible for the new $g_{ClCl}(r)$ peak at r_{ClCl} = 5.0 – 5.5 Å, having a well-defined structure. Such arrangements are, of course, not possible for methanol as it can donate only a single H-bond, consistent with the complete absence of a similar short-range $g_{ClCl}(r)$ peak. A representative Cl^- coordination shell isolated from a DES-methanol mixture simulation is shown in **Figure 6.10, bottom** for comparison.

The observations described above, namely that water molecules form stable H-bonded bridge structures with Cl^-, and that they tend to self-associate through H-bonding, whereas methanol molecules are effectively unable to do so (or less extensively, in the case of H-bonded self-association), are consistent with H^E sign difference found for the DES-water and -methanol mixtures. (Wang *et al.*, 2020) In DES-methanol mixtures, the methanol molecules enter the Cl^- coordination shell, forming ionic H-bonds and displacing (partially) both Ch^+ and, more importantly, ethylene glycol molecules. The latter, in particular, engages in strong ionic H-bonding interactions with Cl^- in the pure DES, (Kaur, Malik and Kashyap, 2019) either effectively coordinating Cl^- in a "bi-dentate" H-bonded fashion (i.e. *gauche* conformation, forming two ionic H-bonds with Cl^-) or acting as an H-bonded bridge between Cl^- anions (or between Cl^- and Ch^+; it can also form H-bonds to other ethylene glycol molecules in the Cl^- coordination shell, as shown in **Figure 6.2** & **Figure 6.10, bottom.**

From these observations it follows that while the essential H-bonding interactions of methanol and ethylene glycol with Cl^- are similar (both being alcohols), the introduction of methanol should result in a reduction in the pure DES H-bonded network thus explaining the small positive H^E found for these. Conversely, water molecules are able to form strong and extensive H-bonded networks that involve Cl^- (through ionic H-bonding), with the notable formation of H-bonded "bridge" structures, as shown in **Figure 6.10, top**. Also, water self-association in the DES-water mixtures preserves, to some extent, the water-water H-bonds in pure water, the breakage of which upon mixing makes a positive contribution to H^E (energy required to break H-bonds); these two observations, i.e. strong Cl^- - water H-bonding and water self-association, are consistent with the decidedly negative H^E of the DES-water mixtures. (Ma *et al.*, 2017)

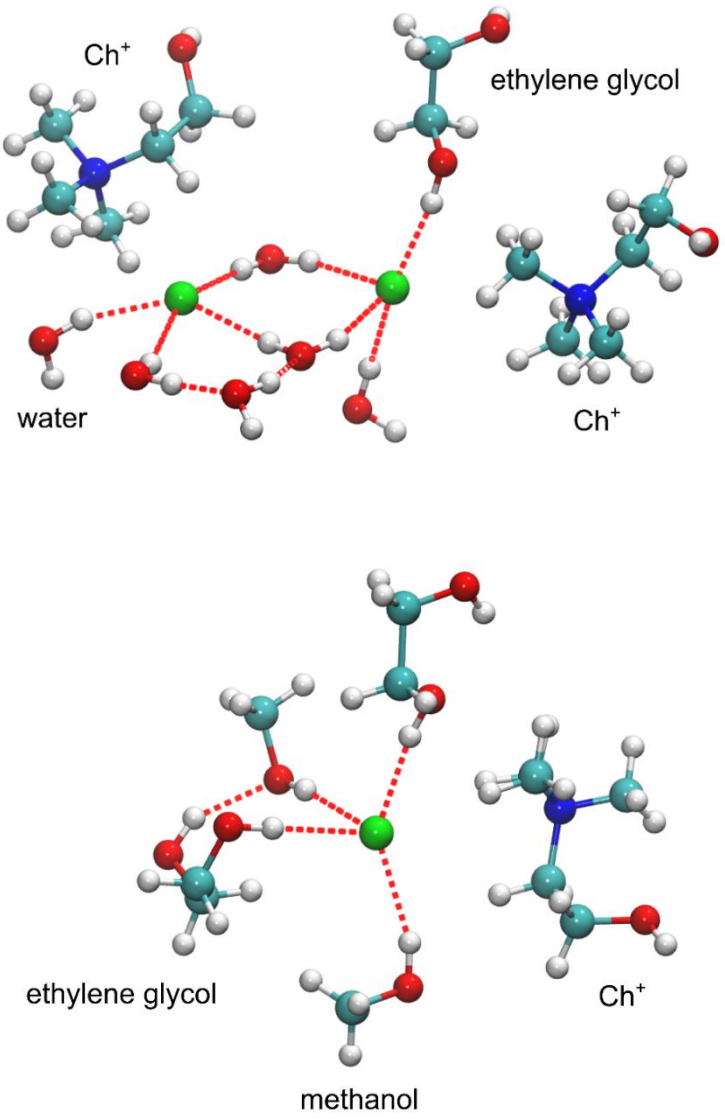

Figure 6.10 Representative Cl^- coordination shell configurations from simulations of equimolar DES-co-solvent mixtures: water (a, top) and methanol (b, bottom). Methanol molecules substitute DES components in the Cl^- coordination shell, forming -O-H···Cl H-bonds (dotted red lines), but are unable to donate further H-bonds. Water molecules, on the other hand, form strong H-bonded bridges between Cl^- anions, resulting in the appearance of a new $g_{ClCl}(r)$ peak at $r_{ClCl} \approx 5$ Å; water molecules also tend to self-associate through strong H-bonding interactions.

The characterisation of the structural features noted above, and how they relate to the viscosity deviations of these DES-co-solvent mixtures, requires detailed study; this work is currently in progress and in a future work will possibly include viscosity calculations. In fact, the structural complexity of these pseudo-binary mixtures must be stressed: considering the aqueous DES mixtures,

for example, it is relatively straightforward to study water self-association (e.g. by an iterative application of H-bond criteria, as done in Chapter 4, or by a Voronoi tessellation-based domain analysis). However, it is not clear how the second neutral component, ethylene glycol, interacts/contributes to these; the situation becomes even more complex for the methanol mixtures, where relatively free mixing of the two alcohols may be expected.

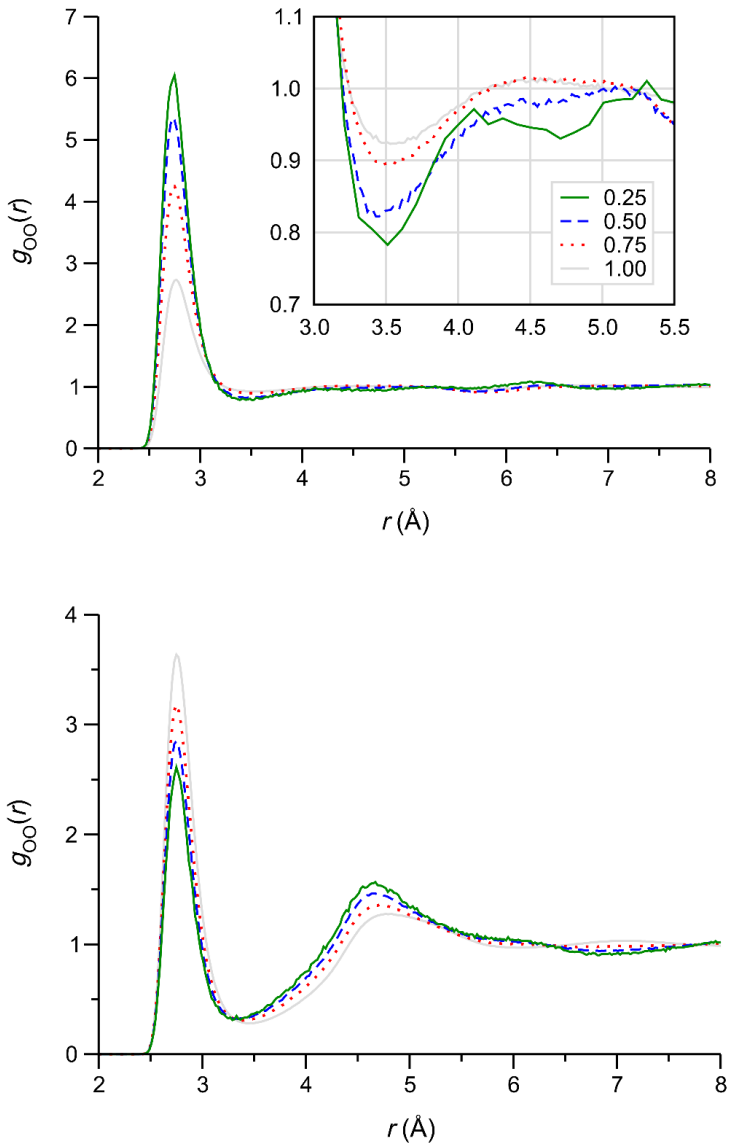

Figure 6.11 Water (top) and methanol (bottom) O-O RDFs in the pure liquids and selected DES mixtures at 308.15 K. Numbers in the legend refer to the mole fraction co-solvent (water or methanol). Inset in top panel shows $g_{OO}(r)$ first minima and partial second maxima more clearly.

6.5 Conclusions and future work

To the best of our knowledge, the excess enthalpy of mixing of pseudo binary mixtures has never been studied before by MD simulations. The work presented in this chapter shows clearly how, even using a standard force field as GAFF with a simple minor adjustment of the charges, MD simulations are capable of reproducing the most important features of the excess molar enthalpy of mixing for the pseudo binary mixtures of ethaline (ChCl-ethylene glycol in the 1:2 ratio) with water or methanol. In agreement with recent experimental results obtained by the group where I spent 3 months of my PhD period, the reported simulations predict a positive mixing enthalpy for any composition of the ethaline/methanol pseudo-binary mixture, and a negative mixing enthalpy with methanol.

Inspection of the RDFs, a standard liquid mixture MD simulation analysis tool, together with visual inspection of the complex structural organization of the four components of the pseudo-binary mixtures, allows for rationalization of the very different behaviour between water and its most similar organic analogue, methanol. Indeed, marked difference are observed in most of the RDF, with the most striking differences involving the Cl^- anion. The differences comprise:

- a marked difference in the number of solvent molecules in Cl^- first solvation shell, with a remarkable higher number of solvating molecules in water mixtures compare to methanol
- a remarkable difference in the added solvent structure when solvating Cl^- anion: while water can maintain its self-association when solvating chlorine, this Is not possible for methanol. Simulations reveals further details on the peculiar hydration of chlorine in these mixtures, with an expected decrease, with water concentration, of the first maximum of Cl^- - Cl^- RDF . Interestingly, while this behaviour has been observed before, it has never been explained in detail. The configurations observed in the trajectory indicate that this behaviour is due to two water molecules bridging the anions. On the other hand, the anion while coordinating the water molecules, keep their strong interactions with either ethylene glycol or choline.

These findings indicate that, differently from methanol, water can reorganize to solvate Cl^- while keeping its network of H-bond interactions with other water molecule, and at the same time Cl^- can keep its solvation structure with the other DES components. Such differences in the molecular aggregates nicely explain while the mixing of the DES with water is much more favourable than with methanol, as indicated by the negative excess enthalpy of mixing of the former, and slightly positive for the latter.

7 Conclusions

Molecular dynamics simulation is an ideal tool to study liquid mixtures, and indeed it has been widely applied since its early development, to rationalize the complex structures of liquids, their mixtures, solutions and solvation phenomena. Over the years, more and more complex systems are being studying with MD simulations. Relatively recent classes of solvents such as the highly charged Ionic Liquids and the Deep Eutectic Solvents, and their mixtures with organic solvents, are currently the subject of intensive experimental and also computational studies.

The work included in the present PhD thesis shows how even with relatively simple organic solvent mixtures with large applicative interest, many phenomena, albeit extensively studied experimentally have received limited attention from the computational point of view and have yet to be fully clarified. These include the understanding of the underlying molecular interactions which induce large differences in the excess thermodynamic molar properties, either in relatively simple mixtures of two organic solvent, or even more, in mixtures with four components as the DES-solvent "pseudo binary mixtures"; no MD study of the excess thermodynamic properties of such mixtures has been published. Also, the solvation of ions, while extensively studied at the interface of macroscopically immiscible solvents, has received very limited attention for ions solvated in miscible liquid mixtures where the inherent structural micro-heterogenity can play an important role. The presented investigation, on the atomistic level, shows how even with highly complex mixtures standard MD simulations, with limited adjustments of the atomic charges, can give important information concerning solvation and are an invaluable tool in rationalizing the experimental findings.

While atomistic simulations are necessary to investigate key interactions driving many mixtures properties, i.e. hydrogen bonding, when the micro-heterogeneity of the system leads to long range structural correlations, the model description should have a lower resolution, i.e. to the coarse-grained (CG) level. The work presented here shows – for the first time - how the development of proper CG models can give a clear indication of the structural features from which the experimental low-q excess (LqE) originates.

The presented studies unavoidably also show some limitations in the use of general force field parameters, like those obtained following the standard GAFF parameterizations, and certainly improved results could be obtained with further fine-tuning of the charges, and probably even more, if polarizable force fields are used. However, when considering the overall cost-to-benefit ratio, it

seems that this simple approach is still very valuable, able to provide results good enough to explain many unusual experimental observations.

Concerning the CG level simulations, and particularly the parameterization, it has to be noted that it is still a very human, time-consuming activity. While the obtained results are highly satisfactory, since it is the only published CG model used to reproduce the L*q*E, it is important to note that such model development took most part of my PhD work, although this is not entirely reflected in the publications outcome. Hopefully, this type of parameterization will become easier in the future to allow larger applications in the solvents world, and to be used also by non-experts in the CG parameter developments.

8 References

Abdel Hamid, A. R. *et al.* (2013) 'Solvation effects on self-association and segregation processes in *tert* -butanol-aprotic solvent binary mixtures', *Journal of Physical Chemistry B*, 117(35), pp. 10221–10230. doi: 10.1021/jp402380f.

Abraham, M. J. *et al.* (2015) 'Gromacs: High performance molecular simulations through multi-level parallelism from laptops to supercomputers', *SoftwareX*, 1–2, pp. 19–25. doi: 10.1016/j.softx.2015.06.001.

Aida, T. *et al.* (2010) 'Relation between volume expansion and hydrogen bond networks for CO_2-alcohol mixtures at 40 °C', *Journal of Physical Chemistry B*, 114(43), pp. 13628–13636. doi: 10.1021/jp1017339.

Aidas, K. *et al.* (2013) 'A quantum mechanics/molecular dynamics study of electric field gradient fluctuations in the liquid phase. The case of Na^+ in aqueous solution', *Phys. Chem. Chem. Phys.*, 15, pp. 1621–1631. doi: 10.1039/c2cp41993a.

Alaoui, F. *et al.* (2011) 'Liquid density of 1-butanol at pressures up to 140MPa and from 293.15K to 403.15K', *Fluid Phase Equilibria*, 301(2), pp. 131–136. doi: 10.1016/j.fluid.2010.11.020.

Alaoui, F. *et al.* (2011) 'Liquid density of biofuel additives: 1-butoxybutane at pressures up to 140 MPa and from (293.15 to 393.15) K', *Journal of Chemical and Engineering Data*, 56(3), pp. 595–600. doi: 10.1021/je101286a.

Alaoui, F. *et al.* (2011) 'Liquid density of biofuel mixtures: (Dibutyl ether+1-butanol) system at pressures up to 140MPa and temperatures from (293.15 to 393.15)K', *The Journal of Chemical Thermodynamics*. Elsevier Ltd, 43(11), pp. 1768–1774. doi: 10.1016/j.jct.2011.06.006

Allen, M. P. and Tildesley, D. J. (1987) *Computer Simulations of Liquids*. Clarendon Press.

Andanson, J. M. *et al.* (2005) 'Hydrogen bonding in supercritical *tert*-butanol assessed by vibrational spectroscopies and molecular-dynamics simulations', *Journal of Chemical Physics*, 122, p. 174512. doi: 10.1063/1.1886730.

Aono, S., Mori, T. and Sakaki, S. (2016) '3D-RISM-MP2 Approach to Hydration Structure of Pt(II) and Pd(II) Complexes: Unusual H-Ahead Mode vs Usual O-Ahead One', *Journal of Chemical Theory and Computation*, 12(3), pp. 1189–1206. doi: 10.1021/acs.jctc.5b01137.

Ashworth, C. R. *et al.* (2016) 'Doubly ionic hydrogen bond interactions within the choline chloride-urea deep eutectic solvent', *Physical Chemistry Chemical Physics*. Royal Society of Chemistry, 18(27), pp. 18145–18160. doi: 10.1039/c6cp02815b.

Atkin, R. and Warr, G. G. (2008) 'The smallest amphiphiles: Nanostructure in protic room-temperature ionic liquids with short alkyl groups', *Journal of Physical Chemistry B*, 112(14), pp. 4164–4166. doi: 10.1021/jp801190u.

Awwad, A. M. and Pethrick, R. A. (1982) 'Ultrasonic Investigations of Mixtures of *n*-Octane with Isomeric Octanols', *Journal of Chemical Society, Faraday Transactions*, 78(Dma 60), pp. 3203–3212. doi: 10.1039/F19827803203.

Bagno, A. (2002) 'Probing the solvation shell of organic molecules by intermolecular ^{1}H NOESY', *Journal of Physical Organic Chemistry*, 15(12), pp. 790–795. doi: 10.1002/poc.543.

Balanay, M. P., Kim, D. H. and Fan, H. (2016) 'Revisiting the formation of cyclic clusters in liquid ethanol', *Journal of Chemical Physics*, 144, p. 154302. doi: 10.1063/1.4945809.

Barker, J. A. and Watts, R. O. (1969) 'Structure of water; A Monte Carlo calculation', *Chemical Physics Letters*, 3(3), pp. 144–145. doi: 10.1016/0009-2614(69)80119-3.

Bayly, C. I. *et al.* (1993) 'A well-behaved electrostatic potential based method using charge restraints for deriving atomic charges: The RESP model', *Journal of Physical Chemistry*, 97, pp. 10269–10280. doi: 10.1021/j100142a004.

Baz, J. *et al.* (2019) 'Thermophysical properties of glyceline-water mixtures investigated by molecular modelling', *Physical Chemistry Chemical Physics*, 21(12), pp. 6467–6476. doi: 10.1039/c9cp00036d.

Bedrov, D. *et al.* (2000) 'Simulation and QENS Studies of Molecular Dynamics in Aqueous Solutions of 1,2-Dimethoxyethane', *Journal of Physical Chemistry B*, 104(21), pp. 5151–5154. doi: 10.1021/jp994167u.

Bedrov, D., Borodin, O. and Smith, G. D. (1998) 'Molecular dynamics simulations of 1,2-dimethoxyethane/water solutions. 1. Conformational and structural properties', *Journal of Physical Chemistry B*, 102(29), pp. 5683–5690. doi: 10.1021/jp981009e.

Bedrov, D., Pekny, M. and Smith, G. D. (1998) 'Quantum-chemistry-based force field for 1,2-dimethoxyethane and poly(ethylene oxide) in aqueous solution', *Journal of Physical Chemistry B*, 102(6), pp. 996–1001. doi: 10.1021/jp972545u.

Ben-Naim, A. (1990) 'Preferential Solvation in two- and in Three-Component Systems', *Pure and Applied Chemistry*, 62(1), pp. 25–34. doi: 10.1351/pac199062010025.

Berendsen, H. J. C. *et al.* (1984) 'Molecular dynamics with coupling to an external bath', *J. Chem. Phys.*, 81(8), pp. 3684–3690. doi: 10.1063/1.448118.

Berendsen, H. J. C. (2011) *A student's guide to data and error analysis*. Cambridge: Cambridge University Press.

Berendsen, H. J. C., Grigera, J. R. and Straatsma, T. P. (1987) 'The missing term in effective pair potentials', *Journal of Physical Chemistry*, 91(24), pp. 6269–6271. doi: 10.1021/j100308a038.

Beret, E. C. *et al.* (2008) 'Explaining asymmetric solvation of Pt(II) versus Pd(II) in aqueous solution revealed by ab initio molecular dynamics simulations', *Journal of Chemical Theory and Computation*, 4(12), pp. 2108–2121. doi: 10.1021/ct800010q.

Berfeld, G. J., Bird, A. J. and Edwards, R. I. (1986) *Gmelin Handbook of Inorganic Chemistry*. 8th edn, *Polyhedron*. 8th edn. Springer-Verlag: Berlin.

Bergman, D. and Laaksonen, A. (1998) 'Topological and spatial structure in the liquid-water–acetonitrile mixture', *Physical Review E*, 58(4), pp. 4706–4715. doi: 10.1103/PhysRevE.58.4706.

Bernardis, F. L., Grant, R. A. and Sherrington, D. C. (2005) 'A review of methods of separation of the platinum-group metals through their chloro-complexes', *Reactive and Functional Polymers*, 65(3), pp. 205–217. doi:10.1016/j.reactfunctpolym.2005.05.011.

Bernazzani, L. *et al.* (2006) 'Volumetric properties of binary mixtures of isomeric butanols and C8 solvents at 298.15 K', *Journal of Solution Chemistry*, 35(11), pp. 1567–1585. doi: 10.1007/s10953-006-9079-0.

Bertie, J. E. and Lan, Z. (1997) 'Liquid water-acetonitrile mixtures at 25 °C: The hydrogen-bonded structure studied through infrared absolute integrated absorption intensities', *Journal of Physical Chemistry B*, 101(20), pp. 4111–4119. doi: 10.1021/jp9639511.

Bhargava, B. L. *et al.* (2007) 'Nanoscale organization in room temperature ionic liquids: A coarse grained molecular dynamics simulation study', *Soft Matter*, 3(11), pp. 1395–1400. doi: 10.1039/b710801j.

Bhargava, B. L. and Klein, M. L. (2009) 'Formation of micelles in aqueous solutions of a room temperature ionic liquid: A study using coarse grained molecular dynamics', *Molecular Physics*, 107(4–6), pp. 393–401. doi: 10.1080/00268970902810283.

Bjelkmar, P. *et al.* (2010) 'Implementation of the CHARMM Force Field in GROMACS: Analysis of Protein

Stability Effects from Correction Maps, Virtual Interaction Sites, and Water Models', *Journal of Chemical Theory and Computation*, 6, pp. 459–466. doi: 10.1021/ct900549r.

Bowron, D. T. *et al.* (2012) 'Axial structure of the Pd(II) aqua ion in solution', *Journal of the American Chemical Society*, 134(2), pp. 962–967. doi: 10.1021/ja206422w.

Bragg, A. E., Kanu, G. U. and Schwartz, B. J. (2011) 'Nanometer-Scale Phase Separation and Preferential Solvation in', *The Journal of Physical Chemistry Letters*, (2), pp. 2797–2804. doi: 10.1021/jz201295a.

Brehm, M. *et al.* (2015) 'Domain Analysis in Nanostructured Liquids: A Post-Molecular Dynamics Study at the Example of Ionic Liquids', *ChemPhysChem*, 16(15), pp. 3271–3277. doi: 10.1002/cphc.201500471.

Brehm, M. and Kirchner, B. (2011) 'TRAVIS - A Free Analyzer and Visualizer for Monte Carlo and Molecular Dynamics Trajectories', *Journal of Chemical Information and Modeling*, 51(8), pp. 2007–2023. doi: 10.1021/ci200217w.

Brini, E. and Van Der Vegt, N. F. A. (2012) 'Chemically transferable coarse-grained potentials from conditional reversible work calculations', *Journal of Chemical Physics*, 137(15). doi: 10.1063/1.4758936.

Brooks, B. R. *et al.* (1983) 'CHARMM: A program for macromolecular energy, minimization, and dynamics calculations', *Journal of Computational Chemistry*, 4(2), pp. 187–217. doi: 10.1002/jcc.540040211.

Bühl, M. *et al.* (2005) 'Simulation of59Co NMR chemical shifts in aqueous solution', *Chemistry - A European Journal*, 12(2), pp. 477–488. doi: 10.1002/chem.200500285.

Burgess, J. (1978) *Metal Ions in Solution*. Chichester: Ellis Horwood Limited.

Burikov, S. *et al.* (2010) 'Raman and IR spectroscopy research on hydrogen bonding in water-ethanol systems', *Molecular Physics*, 108(18), pp. 2427–2436. doi: 10.1080/00268976.2010.516277.

Caleman, C. *et al.* (2011) 'Atomistic simulation of ion solvation in water explains surface preference of halides', *Proceedings of the National Academy of Sciences of the United States of America*, 108(17), pp. 6838–6842. doi: 10.1073/pnas.1017903108.

Caleman, C. *et al.* (2012) 'Force field benchmark of organic liquids: Density, enthalpy of vaporization, heat capacities, surface tension, isothermal compressibility, volumetric expansion coefficient, and dielectric constant', *Journal of Chemical Theory and Computation*, 8(1), pp. 61–74. doi: 10.1073/pnas.1017903108.

Case, D. A. *et al.* (2018) 'AMBER 2018, University of California, San Francisco'.

Case, D. a *et al.* (2005) 'The Amber biomolecular simulation programs', *Journal of Computational Chemistry*, 26(16), pp. 1668–1688. doi: 10.1002/jcc.20290.

Castiglione, F. *et al.* (2020) 'Xenon Dynamics in Ionic Liquids: A Combined NMR and MD Simulation Study', *Journal of Physical Chemistry B*, 124(30), pp. 6617–6627. doi: 10.1021/acs.jpcb.0c03357.

Celebi, A. T., Vlugt, T. J. H. and Moultos, O. A. (2019) 'Structural, Thermodynamic, and Transport Properties of Aqueous Reline and Ethaline Solutions from Molecular Dynamics Simulations', *Journal of Physical Chemistry B*. American Chemical Society, 123(51), pp. 11014–11025. doi: 10.1021/acs.jpcb.9b09729.

Cerar, J. *et al.* (2017) 'Performance of various models in structural characterization of *n*-butanol: Molecular dynamics and X-ray scattering studies', *Journal of Molecular Liquids*, 229, pp. 346–357. doi: 10.1016/j.molliq.2016.12.057.

Chaimovich, A. and Shell, M. S. (2011) 'Coarse-graining errors and numerical optimization using a relative entropy framework', *Journal of Chemical Physics*, 134(9). doi: 10.1063/1.3557038.

Chaudhari, S. K. and Katti, S. S. (1985) 'Excess volumes of (an isomer of butanol + *n*-octane) at 298.15 K, measured with a continuous-dilution dilatometer', *The Journal of Chemical Thermodynamics*, 17(2), pp. 101–

104. doi: 10.1016/0021-9614(85)90060-6.

Cieplak, P. *et al.* (2000) 'How well does a restrained electrostatic potential (RESP) model perform in calculating conformational energies of organic and biological molecules?', *Journal of Computational Chemistry*, 21(12), pp. 1049–1074. doi: 10.1002/1096-987.

Cohen, S. M. and Brown, T. H. (1974) 'Temperature dependence of ^{195}Pt nuclear resonance chemical shifts', *The Journal of Chemical Physics*, 61(7), pp. 2985–2986. doi: 10.1063/1.1682446.

Corsaro, C. *et al.* (2008) 'Clustering dynamics in water/methanol mixtures: A nuclear magnetic resonance study at 205 K < T < 295 K', *Journal of Physical Chemistry B*, 112(34), pp. 10449–10454. doi: 10.1021/jp803456p.

Corsaro, C. *et al.* (2018) 'Contrasting microscopic interactions determine the properties of water/methanol solutions', *Frontiers of Physics*, 13(1), pp. 1–6. doi: 10.1007/s11467-017-0685-7.

Cuello, G. J. *et al.* (2014) 'Structure factor of liquid *n*-butanol at room temperature', *Journal of Physics: Conference Series*, 549(1), 012015. doi:10.1088/1742-6596/549/1/012015.

Dai, J. *et al.* (2010) 'Enthalpies of mixing predicted using molecular dynamics simulations and OPLS force field', *Fluid Phase Equilibria*, 289(2), pp. 156–165. doi: doi:10.1016/j.fluid.2009.11.028.

Dakkach, M. *et al.* (2015) 'Liquid density of oxygenated additives to biofuels: 2-Butanol at pressures up to 140 MPa and temperatures from (293.15 to 393.27) K', *Journal of Chemical Thermodynamics*. Elsevier Ltd, 89, pp. 278–285. doi: 10.1016/j.jct.2015.05.027.

Dakkach, M. *et al.* (2017) 'Liquid densities and excess volumes of biofuel mixtures: (2-butanol + di-isopropyl ether) system at pressures up to 140 MPa and temperatures from 293.15 K to 393.28 K', *Journal of Chemical Thermodynamics*. Elsevier Ltd, 105, pp. 123–132. doi: 10.1016/j.jct.2016.10.009.

Darden, T., York, D. and Pedersen, L. (1993) 'Particle mesh Ewald : An N · log (N) method for Ewald sums in large systems in large systems', *Journal of Chemical Physics*, 98(April 1993), pp. 10089–10092. doi: 10.1063/1.464397.

Dauber-Osguthorpe, P. and Hagler, A. T. (2019) 'Biomolecular force fields: where have we been, where are we now, where do we need to go and how do we get there?', *J. Comput. Aided Mol. Des.*, 33(2), pp. 133–203. doi: 10.1007/s10822-018-0111-4.

DeBolt, S. E. and Kollman, P. A. (1995) 'Investigation of Structure, Dynamics, and Solvation in 1-Octanol and Its Water-Saturated Solution: Molecular Dynamics and Free-Energy Perturbation Studies', *Journal of the American Chemical Society*, 117(19), pp. 5316–5340. doi: 10.1021/ja00124a015.

Dechter, J. J. and Zink, J. I. (1975) 'Solvent Dependence of the ^{205}Tl(I) Nuclear Magnetic Resonance Chemical Shift', *Journal of the American Chemical Society*, 97(11), pp. 2937–2942. doi: 10.1021/ja00844a001.

Directive 2009/28/EC of the European Parliament and of the Council of 23 April 2009 on the promotion of the use of energy from renewable sources and amending and subsequently repealing Directives 2001/77/EC and 2003/30/EC (2015).

Dixit, S. *et al.* (2002) 'Molecular Segregation in a Concnetrated Alcohol-Water Solution', *Nature*, 416, pp. 829–832. doi: 10.1038/416829a.

Dougan, L. *et al.* (2004) 'Methanol-water solutions: A bi-percolating liquid mixture', *Journal of Chemical Physics*, 121(13), pp. 6456–6462. doi: 10.1063/1.1789951.

Douhéret, G. *et al.* (2004) 'Aggregative processes in aqueous solutions of mono- to tetra-ethylene glycol dimethyl ether at 298.15 K', *Physical Chemistry Chemical Physics*, pp. 784–792. doi: 10.1039/b315286c.

Dunn, N. J. H. and Noid, W. G. (2015) 'Bottom-up coarse-grained models with predictive accuracy and

transferability for both structural and thermodynamic properties of heptane-toluene mixtures', *Journal of Chemical Physics*, 144(November), p. 204124. doi: 10.1063/1.4937383.

Dunn, N. J. H. and Noid, W. G. (2016) 'Bottom-up coarse-grained models with predictive accuracy and transferability for both structural and thermodynamic properties of heptane-toluene mixtures', *Journal of Chemical Physics*, 144(20). doi: 10.1063/1.4952422.

Dupradeau, F. Y. (2005) *R.E.DD.B. Project W-32*. Available at: https://upjv.q4md-forcefieldtools.org/REDDB/projects/W-32/.

Dupradeau, F. Y. *et al.* (2010) 'The R.E.D. tools: Advances in RESP and ESP charge derivation and force field library building', *Physical Chemistry Chemical Physics*, 12(28), pp. 7821–7839. doi: 10.1039/c0cp00111b.

Engelbrecht, L. *et al.* (2018) '^{195}Pt NMR and Molecular Dynamics Simulation Study of the Solvation of $[PtCl_6]^{2-}$ in Water-Methanol and Water-Dimethoxyethane Binary Mixtures', *Inorganic Chemistry*, 57(19), pp. 12025–12037. doi: 10.1021/acs.inorgchem.8b01554.

Engelbrecht, L. de V. *et al.* (2021) 'Theoretical and Experimental Study of the Excess Thermo-dynamic Properties of Highly Non-Ideal Liquid Mixtures of Butanol Isomers + DBE' *Journal of Physical Chemistry B*, 2021, 125, pp. 587−600. doi: 10.1021/acs.jpcb.0c10076.

Engelbrecht, L., Murray, P. and Koch, K. R. (2015) 'Isotope effects in ^{195}Pt NMR spectroscopy: Unique $^{35/37}$Cl- and $^{16/18}$O-resolved "fingerprints" for all $[PtCl_{6-n}(OH)_n]^{2-}$ (n = 1-5) anions in an alkaline solution and the implications of the trans influence', *Inorganic Chemistry*, 54(6), pp. 2752–2764. doi: 10.1021/ic502901d.

Essafri, I. and Ghoufi, A. (2019) 'Microstructure of nonideal methanol binary liquid mixtures', *Physical Review E*. American Physical Society, 99(6), pp. 1–12. doi: 10.1103/PhysRevE.99.062607.

Essmann, U. *et al.* (1995) 'A smooth particle mesh Ewald method', *The Journal of Chemical Physics*, 103(19), pp. 8577–8593. doi: 10.1063/1.470117.

Fanourgakis, G. S. *et al.* (2003) 'A spectroscopic and computer simulation study of butanol vapors', *Journal of Chemical Physics*, 119(13), pp. 6597–6608. doi: 10.1063/1.1605384.

Farrar, T. C. and Becker, E. D. (1971) *Pulse and Fourier Transform NMR. Introduction to Theory and Methods*. Academic Press.

Ferreira, E. S. C. *et al.* (2016) 'Improved force field model for the deep eutectic solvent ethaline: Reliable physicochemical properties', *Journal of Physical Chemistry B*, 120(38), pp. 10124–10137. doi: 10.1021/acs.jpcb.6b07233.

Fetisov, E. O. *et al.* (2018) 'First-Principles Molecular Dynamics Study of a Deep Eutectic Solvent: Choline Chloride/Urea and Its Mixture with Water', *Journal of Physical Chemistry B*, 122(3), pp. 1245–1254. doi: 10.1021/acs.jpcb.7b10422.

Flores, M. E. *et al.* (2014) 'N-Hexanol association in cyclohexane studied by NMR and NIR spectroscopies', *Journal of Molecular Liquids*. Elsevier B.V., 199, pp. 301–308. doi: 10.1016/j.molliq.2014.09.012.

Flyvbjerg, H. and Petersen, H. G. (1989) 'Error estimates on averages of correlated data', *The Journal of Chemical Physics*, 91(1), p. 461. doi: 10.1063/1.457480.

Fouad, W. A. *et al.* (2015) 'Understanding the Thermodynamics of Hydrogen Bonding in Alcohol-Containing Mixtures: Self Association', *Journal of Physical Chemistry B*, 119(44), pp. 14086–14101. doi: 10.1021/acs.jpcb.5b08285

Frank, H. S. and Evans, M. W. (1945) 'Free volume and entropy in condensed systems III. Entropy in binary liquid mixtures; Partial molal entropy in dilute solutions; Structure and thermodynamics in aqueous electrolytes', *The Journal of Chemical Physics*, 13(11), pp. 507–532. doi: 10.1063/1.1723985.

Frankel, L. S., Langford, C. H. and Stengle, T. R. (1970) 'Nuclear magnetic resonance techniques for the study of preferential solvation and the thermodynamics of preferential solvation', *Journal of Physical Chemistry*, 74(6), pp. 1376–1381. doi: 10.1021/j100701a039.

Frankel, L. S., Stengle, T. R. and Langford, C. H. (1965) 'A study of preferential solvation utilizing nuclear magnetic resonance', *Chemical Communications (London)*, (17), pp. 393–394. doi: 10.1039/C19650000393.

Freeman, W. *et al.* (1976) 'Platinum-195 NMR using Fourier transform techniques. The $PtCl_4^{2-}$ ion', *Journal of Magnetic Resonance (1969)*, 22(3), pp. 473–478. doi: 10.1016/0022-2364(76)90010-X.

Frisch, M. J. *et al.* (2009) 'Gaussian09, Revision C.01', *Gaussian 09*.

Fu, C. F. and Tian, S. X. (2010) 'Molecular dynamics study of solvation differences between cis- and transplatin molecules in water', *Journal of Chemical Physics*, 132(17), pp. 1–8. doi: 10.1063/1.3426029.

Gabriel, S. and Weiner, J. (1888) *Ber.*, 21(2), pp. 2669–2679. doi: 10.1002/cber.18880210288.

Gao, Q. *et al.* (2018) 'Effect of water concentration on the microstructures of choline chloride/urea (1:2) /water mixture', *Fluid Phase Equilibria*. Elsevier Ltd, 470, pp. 134–139. doi: 10.1016/j.fluid.2018.01.031.

García, G. *et al.* (2015) 'Deep eutectic solvents: Physicochemical properties and gas separation applications', *Energy and Fuels*, 29(4), pp. 2616–2644. doi: 10.1021/ef5028873.

Gibson, R. E. (1935) 'The Compressions and Specific Volumes of Aqueous Solutions of Resorcinol and Methanol at 25° and the Behavior of Water in these Solutions', *Journal of the American Chemical Society*, 57(9), pp. 1551–1557. doi: 10.1021/ja01312a013.

Giner, B. *et al.* (2003) 'Excess Thermodynamic properties of isomeric butanols with 2-methyl-tetrahydrofuran', *J. Mol. Liq.*, 108/1–3(March), pp. 303–311. doi: 10.1016/S0167-7322(03)00188-0.

Glaister, B. J. and Mudd, G. M. (2010) 'The environmental costs of platinum-PGM mining and sustainability: Is the glass half-full or half-empty?', *Minerals Engineering*. Elsevier Ltd, 23(5), pp. 438–450. doi: 10.1016/j.mineng.2009.12.007.

Gómez-Álvarez, P., Romaní, L. and González-Salgado, D. (2013) 'Association effects in the {methanol + inert solvent} system via Monte Carlo simulations. I. Structure', *Journal of Chemical Physics*, 138(20), p. 204505. doi: 10.1063/1.4807309.

González, J. A. *et al.* (2000) 'Thermodynamics of mixtures containing ethers. Part I. DISQUAC characterization of systems of MTBE, TAME or ETBE with n-alkanes, cyclohexane, benzene, alkan-1-ols or alkan-2-ols. Comparison with Dortmund UNIFAC results', *Physical Chemistry Chemical Physics*, 2(11), pp. 2587–2597. doi: 10.1039/b001025l.

Le Grand, S., Götz, A. W. and Walker, R. C. (2013) 'SPFP: Speed without compromise - A mixed precision model for GPU accelerated molecular dynamics simulations', *Comput. Phys. Commun.* Elsevier B.V., 184(2), pp. 374–380. Available at: http://dx.doi.org/10.1016/j.cpc.2012.09.022.

Greaves, T. L. and Drummond, C. J. (2008) 'Protic ionic liquids: Properties and applications', *Chemical Reviews*, 108(1), pp. 206–237. doi: 10.1021/cr068040u.

Gubskaya, A. V. and Kusalik, P. G. (2004) 'Molecular Dynamics Simulation Study of Ethylene Glycol, Ethylenediamine, and 2-Aminoethanol. 2. Structure in Aqueous Solutions', *The Journal of Physical Chemistry A*, 108(35), pp. 7165–7178. doi: 10.1021/jp048921+.

Gujt, J. *et al.* (2017) 'Isobaric-isothermal molecular dynamics computer simulations of the properties of water-1,2-dimethoxyethane model mixtures', *Condensed Matter Physics*, 20(3), pp. 1–14. doi: 10.5488/CMP.20.33603.

Hakala, M. *et al.* (2009) 'Charge localization in alcohol isomers studied by Compton scattering', *Journal of*

Chemical Physics, 130(3), p. 034506. doi: 10.1063/1.3059421.

Hammond, O. S., Bowron, D. T. and Edler, K. J. (2016) 'Liquid structure of the choline chloride-urea deep eutectic solvent (reline) from neutron diffraction and atomistic modelling', *Green Chemistry*. Royal Society of Chemistry, 18(9), pp. 2736–2744. doi: 10.1039/c5gc02914g.

Hammond, O. S., Bowron, D. T. and Edler, K. J. (2017) 'The Effect of Water upon Deep Eutectic Solvent Nanostructure: An Unusual Transition from Ionic Mixture to Aqueous Solution', *Angewandte Chemie - International Edition*, 56(33), pp. 9782–9785. doi: 10.1002/anie.201702486.

Harp, G. D. and Berne, B. J. (1968) 'Linear- and Angular-Momentum Autocorrelation Functions in Diatomic Liquids', *Journal of Chemical Physics*, 49(2), pp. 1249–1254. doi: 10.1063/1.1670216.

Harp, G. D. and Berne, B. J. (1970) 'Time-Correlation Functions, Memory Functions, and Molecular Dynamics', *Phys. Rev. A*, 2(3), pp. 975–996. doi: 10.1103/PhysRevA.2.975.

Harris, R. K. and Mann, B. E. (1978) *NMR and the Periodic Table*. London: Academic Press Inc.

Haughney, M., Ferrario, M. and McDonald, I. R. (1987) 'Molecular-dynamics simulation of liquid methanol', *Journal of Physical Chemistry*, 91(19), pp. 4934–4940. doi: 10.1021/j100303a011.

Hawlicka, E. and Swiatla-Wojcik, D. (1998) 'Solvation of ions in binary solvents - Experimental and MD simulation studies', *Journal of Molecular Liquids*, 78(1–2), pp. 7–18. doi: 10.1016/s0167-7322(98)00079-8.

Hayes, R. *et al.* (2011) 'Amphiphilicity determines nanostructure in protic ionic liquids', *Physical Chemistry Chemical Physics*, 13(8), pp. 3237–3247. doi: 10.1039/c0cp01137a.

Head-Gordon, T. and Hura, G. (2002) 'Water structure from scattering experiments and simulation', *Chemical Reviews*, 102(8), pp. 2651–2670. doi: 10.1021/cr0006831.

Hess, B. *et al.* (1997) 'LINCS: A linear constraint solver for molecular simulations.', *J. Comp. Chem.*, 18, pp. 1463–1472. doi: 10.1002/(SICI)1096-987X(199709)18:12<1463::AID-JCC4>3.0.CO;2-H.

Hezaveh, S. *et al.* (2011) 'Structure and dynamics of 1,2-dimethoxyethane and 1,2-dimethoxypropane in aqueous and non-aqueous solutions: A molecular dynamics study', *Journal of Chemical Physics*, 135(16), p. 164501. doi: 10.1063/1.3643417.

Holbrey, J. D. and Rogers, R. D. (2002) 'Green Chemistry and Ionic Liquids: Synergies and Ironies', in *Ionic Liquids*. Washington, DC: American Chemical Society, pp. 2–14.

Hoover, W. G. (1985) 'Canonical dynamics: equilibrium phase-space distributions.', *Phys. Rev. A*, 31, pp. 1695–1697. doi: 10.1103/PhysRevA.31.1695.

Huang, Y. *et al.* (2016) 'Molecular dynamics simulations of temperature-dependent structures and dynamics of ethylammonium nitrate protic ionic liquid: The role of hydrogen bond', *Chemical Physics*. Elsevier B.V., 472, pp. 105–111. doi: 10.1016/j.chemphys.2016.03.020.

Humphrey, W., Dalke, A. and Schulten, K. (1996) 'VMD - Visual Molecular Dynamics', *J. Mol. Graphics*, 14(1), pp. 33–38. doi: 10.1016/0263-7855(96)00018-5.

Iwahashi, M. *et al.* (2000) 'Molecular self-assembling of butan-1-ol, butan-2-ol, and 2-methylpropan-2-ol in carbon tetrachloride solutions as observed by near-infrared spectroscopic measurements', *Applied Spectroscopy*, 54(2), pp. 268–276. doi: 10.1366/0003702001949203.

Jameson, C. J. (1996) 'Understanding NMR Chemical Shifts', *Annual Reviews of Physical Chemistry*, 47, pp. 135-169. doi: 10.1146/annurev.physchem.47.1.135.

Jameson, C. J., Sears, D. N. and Murad, S. (2004) 'Molecular dynamics averaging of Xe chemical shifts in liquids', *Journal of Chemical Physics*, 121(19), pp. 9581–9592. doi: 10.1063/1.1807817.

Janeček, J. and Paricaud, P. (2013) 'Size distribution of associated clusters in liquid alcohols: Interpretation of simulation results in the frame of SAFT approach', *Journal of Chemical Physics*, 139, p. 174502. doi: 10.1063/1.4827107.

Jiang, H. J. *et al.* (2014) 'Amphiphilic self-assembly of alkanols in protic ionic liquids', *Journal of Physical Chemistry B*, 118(33), pp. 9983–9990. doi: 10.1021/jp504998t.

Jorgensen, W. L. *et al.* (1983) 'Comparison of simple potential functions for simulating liquid water', *The Journal of Chemical Physics*, 79(2), pp. 926–935. doi: 10.1063/1.445869.

Jorgensen, W. L. (1986) 'Optimized intermolecular potential functions for liquid alcohols', *Journal of Physical Chemistry*, 90(7), pp. 1276–1284. doi: 10.1021/j100398a015.

Jorgensen, W. L., Maxwell, D. S. and Tirado-Rives, J. (1996) 'Development and testing of the OPLS all-atom force field on conformational energetics and properties of organic liquids', *Journal of the American Chemical Society*, 118(45), pp. 11225–11236. doi: 10.1021/ja9621760.

Jorgensen, W. L. and Tirado-Rives, J. (1988) 'The OPLS potential functions for proteins. Energy minimizations for crystals of cyclic peptides and crambin.', *Journal of the American Chemical Society*, 110, pp. 1657–1666. doi: 10.1021/ja00214a001.

Joshi, Y. S. and Kumbharkhane, A. C. (2011) 'Study of heterogeneous interaction in binary mixtures of 2-methoxyethanol-water using dielectric relaxation spectroscopy', *J. Mol. Liq.*, 161(3), pp. 120–124. doi: 10.1016/j.molliq.2011.05.003.

Jungwirth, P. and Tobias, D. J. (2006) 'Specific ion effects at the air/water interface', *Chemical Reviews*, 106(4), pp. 1259–1281. doi: 10.1021/cr0403741.

Kammerer, K. and Lichtenthaler, R. N. (1998) 'Excess properties of binary alkanol-ether mixtures and the application of the ERAS model', *Thermochimica Acta*, 310(1–2), pp. 61–67. doi: 10.1016/S0040-6031(97)00227-X.

Kaur, S. *et al.* (2020) 'How Hydration Affects the Microscopic Structural Morphology in a Deep Eutectic Solvent', *Journal of Physical Chemistry B*, 124(11), pp. 2230–2237. doi: 10.1021/acs.jpcb.9b11753.

Kaur, S., Malik, A. and Kashyap, H. K. (2019) 'Anatomy of Microscopic Structure of Ethaline Deep Eutectic Solvent Decoded through Molecular Dynamics Simulations', *Journal of Physical Chemistry B*, 123(39), pp. 8291–8299. doi: 10.1021/acs.jpcb.9b06624.

Kaur, S., Sharma, S. and Kashyap, H. K. (2017) 'Bulk and interfacial structures of reline deep eutectic solvent: A molecular dynamics study', *Journal of Chemical Physics*, 147(19). doi: 10.1063/1.4996644.

Kgagodi, O. W. and Mbaiwa, F. (2017) 'Molecular dynamics study of 2,2′-difurylmethane and *n*-propanol binary mixture', *Journal of Molecular Liquids*. Elsevier B.V., 227, pp. 366–372. doi: 10.1016/j.molliq.2016.10.128.

Koch, K. R. *et al.* (2006) '^{195}Pt NMR and DFT computational methods as tools towards the understanding of speciation and hydration/solvation of $[PtX_6]^{2-}$(X = Cl^-, Br^-) anions in solution', *Journal of the Chemical Society. Dalton Transactions*, (27), pp. 3277–3284. doi: 10.1039/b605182k.

Koch, K. R. and Engelbrecht, L. (2017) 'Intrinsic $^{37/35}$Cl and $^{18/16}$O isotope shifts in ^{195}Pt and ^{103}Rh NMR of purely inorganic Pt and Rh complexes as unique spectroscopic fingerprints for unambiguous assignment of structure', *Dalton Transactions*. Royal Society of Chemistry, 46(29), pp. 9303–9315. doi: 10.1039/c7dt01722g.

Kramer, J. and Koch, K. R. (2006) '^{195}Pt NMR study of the speciation and preferential extraction of Pt(IV)-mixed halide complexes by diethylenetriamine-modified silica-based anion exchangers', *Inorganic Chemistry*, 45(19), pp. 7843–7855. doi: 10.1021/ic0609655.

Kramer, J. and Koch, K. R. (2007) '195Pt NMR chemical shift trend analysis as a method to assign new Pt(IV)-halohydroxo complexes', *Inorganic Chemistry*, 46(18), pp. 7466–7476. doi: 10.1021/ic700804t.

Kudin, K. N. and Car, R. (2008) 'Why are water-hydrophobic interfaces charged?', *Journal of the American Chemical Society*, 130(12), pp. 3915–3919. doi: 10.1021/ja077205t.

Kumar, R., Schmidt, J. R. and Skinner, J. L. (2007) 'Hydrogen bonding definitions and dynamics in liquid water', *Journal of Chemical Physics*, 126(20), p. 4107. doi: 10.1063/1.2742385.

Kusalik, P. G. and Svishchev, I. M. (1994) 'The Spatial Structure in Liquid Water', *Science*, 265, pp. 1219–1221. doi: 10.1126/science.265.5176.1219.

Laaksonen, A., Kusalik, P. G. and Svishchev, I. M. (1997) 'Three-dimensional structure in water-methanol mixtures', *Journal of Physical Chemistry A*, 101(33), pp. 5910–5918. doi: 10.1021/jp970673c.

Lee, H. *et al.* (2008) 'Molecular dynamics studies of polyethylene oxide and polyethylene glycol: Hydrodynamic radius and shape anisotropy', *Biophysical Journal*, 95(4), pp. 1590–1599. doi: 10.1529/biophysj.108.133025.

Lee, J. *et al.* (2016) 'CHARMM-GUI Input Generator for NAMD, GROMACS, AMBER, OpenMM, and CHARMM/OpenMM Simulations Using the CHARMM36 Additive Force Field', *Journal of Chemical Theory and Computation*, 12(1), pp. 405–413. doi: 10.1021/acs.jctc.5b00935.

Lehtola, J., Hakala, M. and Hämäläinen, K. (2010) 'Structure of liquid linear alcohols', *Journal of Physical Chemistry B*, 114(19), pp. 6426–6436. doi: 10.1021/jp909894y.

Leontyev, I. V. and Stuchebrukhov, A. A. (2009) 'Electronic continuum model for molecular dynamics simulations', *Journal of Chemical Physics*, 130(8). doi: 10.1063/1.3060164.

Leontyev, I. V. and Stuchebrukhov, A. A. (2010) 'Electronic continuum model for molecular dynamics simulations of biological molecules', *Journal of Chemical Theory and Computation*, 6(5), pp. 1498–1508. doi: 10.1021/ct9005807.

Leontyev, I. V. and Stuchebrukhov, A. A. (2011) 'Accounting for electronic polarizability in non-polarizable force fields', *Phys. Chem. Chem. Phys.*, 13, pp. 2613–2626. doi: 10.1039/C0CP01971B.

Lienke, A. *et al.* (2001) 'Modeling platinum group metal complexes in aqueous solution', *Inorganic Chemistry*, 40(10), pp. 2352–2357. doi: 10.1021/ic0005745.

Lin, B., He, X. and MacKerell, A. D. (2013) 'A comparative Kirkwood-Buff study of aqueous methanol solutions modeled by the charmm additive and drude polarizable force fields', *Journal of Physical Chemistry B*, 117(36), pp. 10572–10580. doi: 10.1021/jp4061889.

Lindgren, M., Laaksonen, A. and Westlund, P. O. (2009) 'A theoretical spin relaxation and molecular dynamics simulation study of the Gd(H2O)93+ complex', *Physical Chemistry Chemical Physics*, 11(44), pp. 10368–10376. doi: 10.1039/b907099k.

López-Porfiri, P., Brennecke, J. F. and Gonzalez-Miquel, M. (2016) 'Excess molar enthalpies of deep eutectic solvents (DESs) composed of quaternary ammonium salts and glycerol or ethylene glycol', *Journal of Chemical and Engineering Data*, 61(12), pp. 4245–4251. doi: 10.1021/acs.jced.6b00608.

Luzar, A. and Chandler, D. (1996) 'Effect of environment on hydrogen bond dynamics in liquid water', *Physical Review Letters*, 76(6), pp. 928–931. doi: 10.1103/PhysRevLett.76.928.

Lyubartsev, A. *et al.* (2010) 'Systematic coarse-graining of molecular models by the Newton inversion method', *Faraday Discussions*, 144, pp. 43–56. doi: 10.1039/b919800h.

Lyubartsev, A. P. and Laaksonen, A. (1995) 'Calculation of effective interaction potentials from radial distribution functions: A reverse Monte Carlo approach', *Phys. Rev. E*, 52(4), pp. 3730–3737. doi:

10.1103/PhysRevE.52.3730.

Ma, C. *et al.* (2017) 'Molar enthalpy of mixing and refractive indices of choline chloride-based deep eutectic solvents with water', *Journal of Chemical Thermodynamics*. Elsevier Ltd, 105, pp. 30–36. doi: 10.1016/j.jct.2016.10.002.

Ma, C. *et al.* (2018) 'The peculiar effect of water on ionic liquids and deep eutectic solvents', *Chemical Society Reviews*. Royal Society of Chemistry, 47(23), pp. 8685–8720. doi: 10.1039/c8cs00325d.

MacCallum, J. L. and Tieleman, D. P. (2002) 'Structures of neat and hydrated 1-octanol from computer simulations', *Journal of the American Chemical Society*, 124(50), pp. 15085–15093. doi: 10.1021/ja027422o.

Das Mahanta, D. *et al.* (2016) 'Non-monotonic dynamics of water in its binary mixture with 1,2-dimethoxy ethane: A combined THz spectroscopic and MD simulation study', *Journal of Chemical Physics*, 145(16). doi: 10.1063/1.4964857.

Marcus, Y. (1985) *Ion Solvation*. Chichester: Wiley-Interscience.

Marcus, Y. (1990) 'Preferential Solvation in Mixed Solvents. Part 5. Binary Mixtures of Water and Organic Solvents', *J. Chem. Soc. Faraday Trans.*, 86(12), pp. 2215–2224. doi: 10.1039/FT9908602215.

Marcus, Y. (2002) *Solvent Mixtures: Properties and Selective Solvation*. New York: Marcel Dekker, Inc.

Mariani, A. *et al.* (2016) 'Pressure-induced mesoscopic disorder in protic ionic liquids: First computational study', *Physical Chemistry Chemical Physics*, 18(4), pp. 2297–2302. doi: 10.1039/c5cp06800b.

Mariani, A. *et al.* (2017) 'Inhomogeneity in Ethylammonium Nitrate–Acetonitrile Binary Mixtures: The Highest "Low q Excess" Reported to Date', *The Journal of Physical Chemistry Letters*. American Chemical Society, 8(15), pp. 3512–3522. doi: 10.1021/acs.jpclett.7b01244.

Mariani, A. *et al.* (2021) 'Disclosing the hierarchical structure of ionic liquid mixtures by multiscale computational methods', in Joseph, A. and Mathew, S. (eds) *Theoretical and Computational Approaches to predicting ionic liquid propertiess*. Elsevier, pp. 1–63.

Mark, P. and Nilsson, L. (2001) 'Structure and dynamics of the TIP3P, SPC, and SPC/E water models at 298 K', *Journal of Physical Chemistry A*, 105(43), pp. 9954–9960. doi: 10.1021/jp003020w.

Marrink, S. J. and Tieleman, D. P. (2013) 'Perspective on the martini model', *Chemical Society Reviews*, 42(16), pp. 6801–6822. doi: 10.1039/c3cs60093a.

Martínez, L. *et al.* (2009) 'PACKMOL: A package for building initial configurations for molecular dynamics simulations', *Journal of Computational Chemistry*, 30(13), pp. 2157–2164. doi: 10.1002/jcc.21224.

Matthews, R. P., Venter, G. A. and Naidoo, K. J. (2011) 'Using solvent binding and dielectric friction to interpret the hydration behavior of complex anions', *Journal of Physical Chemistry B*, 115(5), pp. 1045–1055. doi: 10.1021/jp109976p.

McDonald, I. R. (1972) 'NpT-ensemble Monte Carlo calculations for binary liquid mixtures', *Molecular Physics*, 23(1), pp. 41–58. doi: 10.1080/00268977200100031.

McGlashan, M. L. and Williamson, A. G. (1976) 'Isothermal Liquid-Vapor Equilibria for System Methanol-Water', *Journal of Chemical and Engineering Data*, 21(2), pp. 196–199. doi: 10.1021/je60069a019.

Mehta, N. A. and Levin, D. A. (2018) 'Molecular dynamics electrospray simulations of coarse-grained ethylammonium nitrate (EAN) and 1-ethyl-3-methylimidazolium tetrafluoroborate (EMIM-BF4)', *Aerospace*, 5(1), pp. 1–18. doi: 10.3390/aerospace5010001.

Melchior, A. *et al.* (2015) 'Hydration of two cisplatin aqua-derivatives studied by quantum mechanics and molecular dynamics simulations', *Journal of Chemical Theory and Computation*, 11(4), pp. 1735–1744. doi:

10.1021/ct500975a.

Mesele, O. O. *et al.* (2016) 'Reorientation of Isomeric Butanols: The Multiple Effects of Steric Bulk Arrangement on Hydrogen-Bond Dynamics', *Journal of Physical Chemistry B*, 120(8), pp. 1546–1559. doi: 10.1021/acs.jpcb.5b07692.

Metropolis, N. *et al.* (1953) 'Equation of state calculations by fast computing machines', *The Journal of Chemical Physics*, 21(6), pp. 1087–1092. doi: 10.1063/1.1699114.

Mhanna, R. *et al.* (2016) 'Microstructure and concentration fluctuations in alcohol-Toluene and alcohol-Cyclohexane binary liquids: A small angle neutron scattering study', *Journal of Molecular Liquids*. Elsevier B.V., 218, pp. 198–207. doi: 10.1016/j.molliq.2016.02.070.

Mikhail, S. Z. and Kimel, W. R. (1961) 'Densities and Viscosities of Methanol-Water Mixtures', *Journal of Chemical and Engineering Data*, 6(4), pp. 533–537. doi: 10.1021/je60011a015.

Miroshnichenko, S. and Vrabec, J. (2015) 'Excess properties of non-ideal binary mixtures containing water, methanol and ethanol by molecular simulation', *Journal of Molecular Liquids*. Elsevier B.V., 212, pp. 90–95. Available at: http://dx.doi.org/10.1016/j.molliq.2015.08.058.

Mirzoev, A. and Lyubartsev, A. P. (2013) 'MagiC: Software package for multiscale modeling', *Journal of Chemical Theory and Computation*, 9(3), pp. 1512–1520. doi: 10.1021/ct301019v.

Miyamoto, S. and Kollman, P. A. (1992) 'Settle: An analytical version of the SHAKE and RATTLE algorithm for rigid water models', *Journal of Computational Chemistry*, 13(8), pp. 952–962. doi: 10.1002/jcc.540130805.

Mocci, F. and Laaksonen, A. (2015) 'Combining MD simulations and NMR spectroscopy for molecular insight and methodological synergy: The integrated MD-NMR method', in *Nuclear Magnetic Resonance*, pp. 592–616. doi: 10.1039/9781782622758-00592.

Morgado, P. *et al.* (2013) 'Probing the structure of liquids with ^{129}Xe NMR spectroscopy: N -Alkanes, cycloalkanes, and branched alkanes', *Journal of Physical Chemistry B*, 117(30), pp. 9014–9024. doi: 10.1021/jp4060507.

Morgado, P., Martins, L. F. G. and Filipe, E. J. M. (2019) 'From nano-emulsions to phase separation: Evidence of nano-segregation in (alkane + perfluoroalkane) mixtures using ^{129}Xe NMR Spectroscopy', *Physical Chemistry Chemical Physics*, 21(7), pp. 3742–3751. doi: 10.1039/c8cp06509h.

Murdoch, K. M. *et al.* (2002) 'Infrared spectroscopy of ethanol clusters in ethanol-hexane binary solutions', *Journal of Chemical Physics*, 116(13), pp. 5717–5724. doi: 10.1063/1.1458931.

Murthy, A. S. N. and Rao, C. N. R. (1968) 'Spectroscopic Studies of the Hydrogen Bond', *Applied Spectroscopy Reviews*, 2(1), pp. 69–191. doi: 10.1080/05704926808050887.

Naidoo, K. J. *et al.* (2002) 'Geometric hydration shells for anionic platinum group metal chloro complexes', *Inorganic Chemistry*, 41(7), pp. 1845–1849. doi: 10.1021/ic010719n.

Naidoo, K. J. *et al.* (2003) 'Contact Ion Pair between Na^+ and $PtCl_6^{2-}$ Favored in Methanol', *Journal of the American Chemical Society*, 125(44), pp. 13330–13331. doi: 10.1021/ja035326x.

Nickolov, Z. S., Goutev, N. and Matsuura, H. (2001) 'Hydrogen bonding in concentrated aqueous solutions of 1,2-dimethoxyethane: Formation of water clusters', *Journal of Physical Chemistry A*, 105(48), pp. 10884–10889. doi: 10.1021/jp011384y.

Niebling, S., Björling, A. and Westenhoff, S. (2014) 'MARTINI bead form factors for the analysis of time-resolved X-ray scattering of proteins', *Journal of Applied Crystallography*, 47(4), pp. 1190–1198. doi: 10.1107/S1600576714009959.

Nishikawa, K. and Iijima, T. (1993) 'Small-angle X-ray scattering study of fluctuations in ethanol and water mixtures', *Journal of Physical Chemistry*, 97(41), pp. 10824–10828. doi: 10.1021/j100143a049.

Nishikawa, K., Kasahara, Y. and Ichioka, T. (2002) 'Inhomogeneity of Mixing in Acetonitrile Aqueous Solution Studied by Small-Angle X-ray Scattering', *The Journal of Physical Chemistry B*, 106(3), pp. 693–700. doi: 10.1021/jp011964v.

Noid, W. G. *et al.* (2008) 'The multiscale coarse-graining method. I. A rigorous bridge between atomistic and coarse-grained models', *Journal of Chemical Physics*, 128(24). doi: 10.1063/1.2938860.

Noid, W. G. (2013) 'Perspective: Coarse-grained models for biomolecular systems', *Journal of Chemical Physics*, 139(9). doi: 10.1063/1.4818908.

Nosé, S. (1984) 'A molecular dynamics method for simulations in the canonical ensemble', *Molecular Physics*, 52, pp. 255–268. doi: 10.1063/1.447334.

Odelius, M., Holz, M. and Laaksonen, A. (1997) 'Quadrupolar relaxation of ^{21}Ne, ^{83}Kr, and ^{131}Xe dissolved in acetonitrile. A molecular dynamics study', *Journal of Physical Chemistry A*, 101(49), pp. 9537–9544. doi: 10.1021/jp972506i.

Parrinello, M. and Rahman, A. (1981) 'Polymorphic transitions in single crystals: A new molecular dynamics method.', *J. Appl. Phys.*, 52, pp. 7182–7190. doi: 10.1063/1.328693.

Pathak, G. and Pradhan, S. (1988) 'Enthalpies of mixing of di-*n*-butyl ether with isomeric butanols: Enthalpies of hydrogen-bonded complexes', *Proceedings of the Indian Academy of Sciences - Chemical Sciences*, 100(6), pp. 519–523.

Patil, K. R., Pathak, G. and Pradhan, S. D. (1989) 'Excess volumes of isomeric butanols with di-*n*-butyl ether', *Proceedings of the Indian Academy of Sciences - Chemical Sciences*, 101(5), pp. 443–447.

Pegado, L. *et al.* (2012) 'Solvation and ion-pairing properties of the aqueous sulfate anion: Explicit versus effective electronic polarization', *Physical Chemistry Chemical Physics*, 14(29), pp. 10248–10257. doi: 10.1039/c2cp40711f.

Perkins, S. L., Painter, P. and Colina, C. M. (2013) 'Molecular dynamic simulations and vibrational analysis of an ionic liquid analogue', *Journal of Physical Chemistry B*, 117(35), pp. 10250–10260. doi: 10.1021/jp404619x.

Perkins, S. L., Painter, P. and Colina, C. M. (2014) 'Experimental and computational studies of choline chloride-based deep eutectic solvents', *Journal of Chemical and Engineering Data*, 59(11), pp. 3652–3662. doi: 10.1021/je500520h.

Pesek, J. J. and Mason, W. R. (1977) 'Platinum-195 magnetic resonance spectra of some platinum(II) and platinum(IV) complexes', *Journal of Magnetic Resonance*, 25(3), pp. 519–529. doi: 10.1016/0022-2364(77)90217-7.

Petersen, P. B. *et al.* (2005) 'Enhanced concentration of polarizable anions at the liquid water surface: SHG spectroscopy and MD simulations of sodium thiocyanide', *Journal of Physical Chemistry B*, 109(21), pp. 10915–10921. doi: 10.1021/jp050864c.

Pluhařová, E., Mason, P. E. and Jungwirth, P. (2013) 'Ion pairing in aqueous lithium salt solutions with monovalent and divalent counter-anions', *Journal of Physical Chemistry A*, 117(46), pp. 11766–11773. doi: 10.1021/jp402532e.

Požar, M. *et al.* (2016) 'Micro-heterogeneity: Versus clustering in binary mixtures of ethanol with water or alkanes', *Physical Chemistry Chemical Physics*, 18(34), pp. 23971–23979. doi: 10.1039/c6cp04676b

Preetz, W., Peters, G. and Bublitz, D. (1996) 'Preparation and spectroscopic investigations of mixed octahedral complexes and clusters', *Chemical Reviews*, 96(3), pp. 977–1025. doi: 10.1021/cr940393i.

Pronk, S. *et al.* (2013) 'GROMACS 4.5: A high-throughput and highly parallel open source molecular simulation toolkit', *Bioinformatics*, 29(7), pp. 845–854. doi: 10.1093/bioinformatics/btt055.

Rahman, A. and Stillinger, F. H. (1971) 'Molecular Dynamics Study of Liquid Water', *The Journal of Chemical Physics*, 55(7), pp. 3336–3359. doi: 10.1063/1.1676585.

Rapaport, D. C. (1983) 'Hydrogen bonds in water network organization and lifetimes', *Molecular Physics*, 50(5), pp. 1151–1162. doi: 10.1080/00268978300102931.

Rebič, M. *et al.* (2017) 'Coarse-Grained Simulation of Rodlike Higher-Order Quadruplex Structures at Different Salt Concentrations', *ACS Omega*, 2(2), pp. 386–396. doi: 10.1021/acsomega.6b00419.

Rezanova, E. N., Kammerer, K. and Lichtenthaler, R. N. (1999) 'Excess properties of binary alkanol + diisopropyl ether (DIPE) or + dibutyl ether (DBE) mixtures and the application of the extended real associated solution model', *Journal of Chemical and Engineering Data*, 44(6), pp. 1235–1239. doi: 10.1021/je990084v.

Roe, D. R. and Cheatham, T. E. (2013) 'PTRAJ and CPPTRAJ: Software for processing and analysis of molecular dynamics trajectory data', *Journal of Chemical Theory and Computation*, 9(7), pp. 3084–3095. doi: 10.1021/ct400341p.

Russina, O. *et al.* (2014) 'Amphiphile meets amphiphile: Beyond the polar-apolar dualism in ionic liquid/alcohol mixtures', *The Journal of Physical Chemistry Letters*, 5(10), pp. 1738–1742. doi: 10.1021/jz500743v.

Ryckaert, J. P., Ciccotti, G. and Berendsen, H. J. C. (1977) 'Numerical integration of the cartesian equations of motion of a system with constraints: molecular dynamics of n-alkanes', *Journal of Computational Physics*, 23(3), pp. 327–341. doi: 10.1016/0021-9991(77)90098-5.

Rytting, J. H., Anderson, B. D. and Higuchi, T. (1978) 'Vapor pressure studies of the self-association of alcohols in isooctane. 2. The effect of chain branching', *Journal of Physical Chemistry*, 82(20), pp. 2240–2245. doi: 10.1021/j100509a018.

Sagnella, D. E. and Voth, G. A. (1996) 'Structure and Dynamics of Hydronium in the Ion Channel Gramicidin A' *Biophysical Journal*, 70, pp. 2043-2051. doi: 10.1016/S0006-3495(96)79773-4

Saielli, G. *et al.* (2005) 'Solvation of tetraalkylammonium chlorides in acetonitrile-water mixtures: Mass spectrometry and molecular dynamics simulations', *ChemPhysChem*, 6(7), pp. 1307–1315. doi: 10.1002/cphc.200500050.

Sando, G. M., Dahl, K. and Owrutsky, J. C. (2007) 'Vibrational spectroscopy and dynamics of azide ion in ionic liquid and dimethyl sulfoxide water mixtures', *Journal of Physical Chemistry B*, 111(18), pp. 4901–4909. doi: 10.1021/jp067143d.

Sassi, P. *et al.* (2007) 'Distributions of H-bonding aggregates in *tert*-butyl alcohol: The pure liquid and its alkane mixtures', *Journal of Physical Chemistry A*, 111(27), pp. 6020–6027. doi: 10.1021/jp071609q.

Schmuckler, G. and Limoni-Relis, B. (1995) 'Interseparation of Platinum Metals in Concentrated Solution by Gel Permeation Chromatography', *Separation Science and Technology*, 30(3), pp. 337–346. doi: 10.1080/01496399508013875.

Schnabel, T., Vrabec, J. and Hasse, H. (2007) 'Unlike Lennard-Jones parameters for vapor-liquid equilibria', *Journal of Molecular Liquids*, 135(1–3), pp. 170–178. doi: 10.1016/j.molliq.2006.12.024.

Shah, D. and Mjalli, F. S. (2014) 'Effect of water on the thermo-physical properties of Reline: An experimental and molecular simulation based approach', *Physical Chemistry Chemical Physics*. Royal Society of Chemistry, 16(43), pp. 23900–23907. doi: 10.1039/c4cp02600d.

Shih, J. P., Sheu, S. Y. and Mou, C. Y. (1994) 'A Voronoi polyhedra analysis of structures of liquid water', *The Journal of Chemical Physics*, 100(3), pp. 2202–2212. doi: 10.1063/1.466517.

Shmyt'Ko, I. M. *et al.* (2010) 'Structural and thermodynamic studies of *n*-butanol', *Journal of Physics Condensed Matter*, 22(19). doi:10.1088/0953-8984/22/19/195102.

Sillrén, P. *et al.* (2012) 'A statistical model of hydrogen bond networks in liquid alcohols', *Journal of Chemical Physics*, 136(9), p. 094514. doi: 10.1063/1.3690137.

Smith, E. L., Abbott, A. P. and Ryder, K. S. (2014) 'Deep Eutectic Solvents (DESs) and Their Applications', *Chemical Reviews*, 114(21), pp. 11060–11082. doi: 10.1021/cr300162p.

Smith, L. J., Berendsen, H. J. C. and Van Gunsteren, W. F. (2004) 'Computer simulation of urea-water mixtures: A test of force field parameters for use in biomolecular simulation', *Journal of Physical Chemistry B*, 108(3), pp. 1065–1071. doi: 10.1021/jp030534x.

Soper, A. K. and Phillips, M. G. (1986) 'A new determination of the structure of water at 25°C', *Chemical Physics*, 107(1), pp. 47–60. doi: 10.1016/0301-0104(86)85058-3.

Van Der Spoel, D. *et al.* (2005) 'GROMACS: Fast, flexible, and free', *Journal of Computational Chemistry*, 26(16), pp. 1701–1718. doi: 10.1002/jcc.20291.

Stefanovic, R. *et al.* (2017) 'Nanostructure, hydrogen bonding and rheology in choline chloride deep eutectic solvents as a function of the hydrogen bond donor', *Physical Chemistry Chemical Physics*. Royal Society of Chemistry, 19(4), pp. 3297–3306. doi: 10.1039/c6cp07932f.

Stengle, T. R. *et al.* (1984) 'NMR chemical shifts of xenon in aqueous solutions of amphiphiles: A new probe of the hydrophobic environment', *Journal of Solution Chemistry*, 13, pp. 779–787. doi: 10.1007/BF00647693.

Sterzel, M. and Autschbach, J. (2006) 'Toward an accurate determination of 195Pt chemical shifts by density functional computations: The importance of unspecific solvent effects and the dependence of Pt magnetic shielding constants on structural parameters', *Inorganic Chemistry*, 45(8), pp. 3316–3324. doi: 10.1021/ic052143y.

Stillinger, F. H. (1980) 'Water Revised', *Science*, 209(4455), pp. 451–457. doi: 10.1126/science.209.4455.451

Stouten, P. F. W. and Kroon, J. (1990) 'Computation confirms contraction: A molecular dynamics study of liquid methanol, water and a methanol-water mixture', *Molecular Simulation*, 5(3–4), pp. 175–179. doi: 10.1080/08927029008022129.

Stubbs, J. M. *et al.* (2001) 'Monte Carlo calculations for the phase equilibria of alkanes, alcohols, water, and their mixtures', *Fluid Phase Equilibria*, 183–184, pp. 301–309. doi: 10.1016/S0378-3812(01)00442-3.

Stubbs, J. M. and Siepmann, J. I. (2005) 'Elucidating the vibrational spectra of hydrogen-bonded aggregates in solution: Electronic structure calculations with implicit solvent and first-principles molecular dynamics simulations with explicit solvent for 1-hexanol in n-hexane', *Journal of the American Chemical Society*, 127(13), pp. 4722–4729. doi: 10.1021/ja044380q.

Svishchev, I. M. and Kusalik, P. G. (1993) 'Structure in liquid water: a study of spatial distribution functions', *Journal of Chemical Physics*, 99, pp. 3049–3058. doi: 10.1063/1.465158.

Takamuku, T. *et al.* (2005) 'X-ray diffraction studies on methanol-water, ethanol-water, and 2-propanol-water mixtures at low temperatures', *Journal of Molecular Liquids*, 119(1–3), pp. 133–146. doi: 10.1016/j.molliq.2004.10.020.

Tanaka, H. and Gubbins, K. E. (1992) 'Structure and thermodynamic properties of water-methanol mixtures: Role of the water-water interaction', *The Journal of Chemical Physics*, 97(4), pp. 2626–2634. doi: 10.1063/1.463051.

Treszczanowicz, A. J. and Benson, G. C. (1977) 'Excess volumes for *n*-alkanols + *n*-alkanes I. Binary mixtures of methanol, ethanol, n-propanol, and n-butanol + n-heptane', *The Journal of Chemical Thermodynamics*, 9(12), pp. 1189–1197. doi: 10.1016/0021-9614(77)90119-7.

Truflandier, L. A. and Autschbach, J. (2010) 'Probing the solvent shell with ^{195}Pt chemical shifts: Density functional theory molecular dynamics study of PtII and Pt IV Anionic Complexes in Aqueous Solution', *Journal of the American Chemical Society*, 132(10), pp. 3472–3483. doi: 10.1021/ja9096863.

Truflandier, L. A., Sutter, K. and Autschbach, J. (2011) 'Solvent effects and dynamic averaging of ^{195}Pt NMR shielding in cisplatin derivatives', *Inorganic Chemistry*, 50(5), pp. 1723–1732. doi: 10.1021/ic102174b.

Ullah, R. *et al.* (2015) 'A detailed study of cholinium chloride and levulinic acid deep eutectic solvent system for CO_2 capture via experimental and molecular simulation approaches', *Physical Chemistry Chemical Physics*, 17(32), pp. 20941–20960. doi: 10.1039/c5cp03364k.

Umebayashi, Y. *et al.* (2008) 'Liquid Structure and the Ion-Ion Interactions of Ethylammonium Nitrate Ionic Liquid Studied by Large Angle X-Ray Scattering and Molecular Dynamics Simulations', *Journal of Computer Chemistry, Japan*, 7(4), pp. 125–134. doi: 10.2477/jccj.h2013.

Usula, M. *et al.* (2014) 'The structural organization of *N*-methyl-2-pyrrolidone + water mixtures: A densitometry, x-ray diffraction, and molecular dynamics study', *Journal of Chemical Physics*, 140(12), p. 124503. doi: 10.1063/1.4869235.

Valén, A. *et al.* (2002) 'Thermodynamic study of mixtures containing oxygenated compounds', *J. Mol. Liq.*, 95, pp. 157–165. doi: 10.1016/S0167-7322(01)00279-3.

Vanommeslaeghe, K. *et al.* (2010) 'CHARMM General Force Field: A Force Field for Drug-Like Molecules Compatible with the CHARMM All-Atom Additive Biological Force Fields', *Journal of Computational Chemistry*, 31(4), pp. 671–690. doi: 10.1002/jcc.21367.

Vazdar, M. *et al.* (2012) 'Ions at hydrophobic aqueous interfaces: Molecular dynamics with effective polarization', *Journal of Physical Chemistry Letters*, 3(15), pp. 2087–2091. doi: 10.1021/jz300805b.

Vorobyov, I. *et al.* (2007) 'Additive and classical drude polarizable force fields for linear and cyclic ethers', *Journal of Chemical Theory and Computation*, 3(3), pp. 1120–1133. doi: 10.1021/ct600350s.

Wagner, J. W. *et al.* (2017) 'Extending the range and physical accuracy of coarse-grained models: Order parameter dependent interactions', *Journal of Chemical Physics*, 147(4). doi: 10.1063/1.4995946.

Walden, P. (1914) 'Molecular weights and electrical conductivity of several fused salts', *Bull. Acad. Imp. Sci.*, pp. 405–42.

Wandschneider, D., Michalik, M. and Heintz, A. (2006) 'Spectroscopic and thermodynamic studies of liquid *n*-butanol + *n*-hexane and + cyclohexane mixtures based on quantum mechanical ab initio calculations of *n*-butanol clusters', *Journal of Molecular Liquids*, 125(1), pp. 2–13. doi:10.1016/j.molliq.2005.11.011.

Wang, H., Junghans, C. and Kremer, K. (2009) 'Comparative atomistic and coarse-grained study of water: What do we lose by coarse-graining?', *European Physical Journal E*, 28(2), pp. 221–229. doi: 10.1140/epje/i2008-10413-5.

Wang, J. *et al.* (2004) 'Development and testing of a general Amber force field', *Journal of Computational Chemistry*, 25(9), pp. 1157–1174. doi: 10.1002/jcc.20035.

Wang, Y. *et al.* (2020) 'Thermodynamic Study of Choline Chloride-Based Deep Eutectic Solvents with Water and Methanol', *Journal of Chemical and Engineering Data*, 65(5), pp. 2446–2457. doi: 10.1021/acs.jced.9b01113.

Wang, Y. L. *et al.* (2013) 'Multiscale coarse-grained simulations of ionic liquids: Comparison of three approaches to derive effective potentials', *Physical Chemistry Chemical Physics*, 15(20), pp. 7701–7712. doi: 10.1039/c3cp44108c.

Wang, Y. L. *et al.* (2018) 'Electrostatic interactions in soft particle systems: Mesoscale simulations of ionic liquids', *Soft Matter*, 14(21), pp. 4252–4267. doi: 10.1039/c8sm00387d.

Wang, Y. L. *et al.* (2020) 'Microstructural and Dynamical Heterogeneities in Ionic Liquids', *Chemical Reviews*, 120, pp. 5798–5877. doi: 10.1021/acs.jced.9b01113.

Washburn, E. W. (ed.) (2003) *International Critical Tables of Numerical Data, Physics, Chemistry and Technology*. New York: Knovel.

Weiner, P. K. and Kollman, P. A. (1981) 'AMBER: Assisted model building with energy refinement. A general program for modeling molecules and their interactions', *Journal of Computational Chemistry*, 2(3), pp. 287–303. doi: 10.1002/jcc.540020311.

Wensink, E. J. W. *et al.* (2003) 'Dynamic properties of water/alcohol mixtures studied by computer simulation', *Journal of Chemical Physics*, 119(14), pp. 7308–7317. doi: 10.1063/1.1607918.

Westra, A. N. (2005) *High Resolution NMR Studies Concerning the Solvation/Hydration and Coordination Chemistry of Pt(II/IV) Compounds*. University of Stellenbosch.

Yang, L. *et al.* (2006) 'New-generation Amber united-atom force field', *Journal of Physical Chemistry B*, 110(26), pp. 13166–13176. doi: 10.1021/jp060163v.

Yoshida, K., Kitajo, A. and Yamaguchi, T. (2006) '^{17}O NMR relaxation study of dynamics of water molecules in aqueous mixtures of methanol, ethanol, and 1-propanol over a temperature range of 283-403 K', *Journal of Molecular Liquids*, 125(2–3), pp. 158–163. doi: 10.1016/j.molliq.2005.11.009.

Zahn, S., Kirchner, B. and Mollenhauer, D. (2016) 'Charge Spreading in Deep Eutectic Solvents', *ChemPhysChem*, 17(21), pp. 3354–3358. doi: 10.1002/cphc.201600348.

Zhang, N. *et al.* (2013) 'Molecular dynamics study on water self-diffusion in aqueous mixtures of methanol, ethylene glycol and glycerol: Investigations from the point of view of hydrogen bonding', *Molecular Physics*, 111(7), pp. 939–949. doi: 10.1080/00268976.2012.760050.

Zhang, Q. *et al.* (2012) 'Deep eutectic solvents: Syntheses, properties and applications', *Chemical Society Reviews*, 41(21), pp. 7108–7146. doi: 10.1039/c2cs35178a.

9 List of Publications

I. ^{195}Pt NMR and Molecular Dynamics Simulation Study of the Solvation of $[PtCl_6]^{2-}$ in Water-Methanol and Water-Dimethoxyethane Binary Mixtures. Leon Engelbrecht, Francesca Mocci, Aatto Laaksonen and Klaus R. Koch. *Inorganic Chemistry*, 2018, *57*, 12025-12037.

II. Theoretical and Experimental Study of the Excess Thermodynamic Properties of Highly Nonideal Liquid Mixtures of Butanol Isomers + DBE. Leon de Villiers Engelbrecht, Riccardo Farris, Tudor Vasiliu, Monica Demurtas, Alessandra Piras, Flaminia Cesare Marincola, Aatto Laaksonen, Silvia Porcedda and Francesca Mocci. *Journal of Physical Chemistry B*, 2021, *125*(2), 587-600.

III. Disclosing the hierarchical structure of ionic liquid mixtures by multiscale computational methods. Alessandro Mariani, Leon Engelbrecht, Andrea Le Donne, Francesca Mocci, Enrico Bodo and Stefano Passerini. Book chapter in *Theoretical and Computational Approaches to Predicting Ionic Liquid Properties*, 2021, pp. 1-67, Elsevier Inc.

IV. Cholinium-based Ionic Liquids from hydroxycinnamic acids as new promising bioactive agents: a combined experimental and theoretical investigation. Monica Demurtas, Valentina Onnis, Paolo Zucca, Antonio Rescigno, Joanna Izabela Lachowicz, Leon Engelbrecht, Mariella Nieddu, Guido Ennas, Alessandra Scano, Francesca Mocci and Flaminia Cesare Marincola. Accepted for publication in *ACS Sustainable Chemistry & Engineering*, 2021, *9*(7), 2975-2986.

Accepted for publication (peer-reviewed book chapters)

V. Molecular Perspective on Solutions and Liquid Mixtures from Modelling & Experiment. Leon de Villiers Engelbrecht, Francesca Mocci, Yonglei Wang, Sergiy Perepelytsya, Tudor Vasiliu, Aatto Laaksonen. Chapter 3 of the book: *Soft Matter Systems for Biomedical Applications*, *Springer Proceedings in Physics* © Springer Nature Switzerland AG, 2021

VI. DNA-polyamine interactions: Insight from Molecular Dynamics simulations on the sequence-specific binding of spermidine3+. Francesca Mocci, Aatto Laaksonen, Leon Engelbrecht, Tudor Vasiliu, Sergiy Perepelytsya. Chapter 4 of the book: *Soft Matter Systems for Biomedical Applications*, Springer Proceedings in Physics © Springer Nature Switzerland AG, 2021

Manuscript in preparation

VII. Excess thermodynamic properties of mixtures of a choline chloride-based deep eutectic solvent with water or methanol. Leon de Villiers Engelbrecht et al. (first name), *Manuscript in preparation.*